713 | September 2019

SCHRIFTENREIHE SCHIFFBAU

Robinson Perić

Minimizing undesired wave reflection at the domain boundaries in flow simulations with forcing zones

TUHH
Technische Universität Hamburg

Minimizing undesired wave reflection at the domain boundaries in flow simulations with forcing zones

Vom Promotionsausschuss der
Technischen Universität Hamburg

zur Erlangung des akademischen Grades
Doktor-Ingenieur (Dr.-Ing.)

genehmigte Dissertation

von
Robinson Perić

aus
Erlangen

2019

1. Gutachter: Prof. Dr.-Ing. Moustafa Abdel-Maksoud
2. Gutachter: Prof. Dr.-Ing. Otto von Estorff
Prüfungsvorsitzender: Prof. Dr.-Ing. Stefan Krüger

Tag der mündlichen Prüfung: 7. Juni 2019

Publisher
Schriftenreihe Schiffbau der
Technischen Universität Hamburg
Am Schwarzenberg-Campus 4(C)
D-21073 Hamburg
www.tuhh.de/vss

Bericht Nr. 713
ISBN 978-3-89220-713-9

Digital Object Identifier (DOI): https://doi.org/10.15480/882.2394

Summary

In this thesis, a theory is presented which predicts the reflection coefficients and the flow within forcing zones in finite-volume-based flow simulations with (hydro-)acoustic waves and free-surface waves. Forcing zones (such as absorbing layers, damping zones, sponge layers, relaxation zones, etc.) can be used to reduce undesired wave reflections at the domain boundaries. They introduce source terms to one or several of the governing equations in a zone adjacent to the corresponding boundaries, with the intention of gradually forcing the solution within the zone towards some reference solution.

The theory is intended to be used to optimize the forcing zone's case-dependent parameters before performing the flow simulation. It is derived based on a generic forcing zone formulation, thus the present findings can be applied to different forcing zone formulations in different flow solvers in a straightforward manner.

The theory is validated against results from 1D- to 3D-flow simulations with (hydro-)acoustic waves and free-surface waves, including irregular and highly nonlinear waves. A novel forcing zone arrangement for strongly-reflecting floating bodies subjected to long-crested far-field waves is proposed. The mechanisms by which forcing zones reduce undesired wave reflections are investigated. The influence of the case-dependent parameters of forcing zones are discussed, resulting in recommendations for engineering practice.

When the forcing zone was tuned using the developed theory, the simulation results for the reflection coefficient were in most cases smaller or nearly equal to those predicted by theory, but never more than 3.4% larger. The developed theory is therefore suitable for optimization of the forcing zone parameters in flow simulations with (hydro-)acoustic or free-surface waves.

Acknowledgments

The present thesis is the result of five years of work at the Institute for Fluid Dynamics and Ship Theory at the Hamburg University of Technology. I am grateful for all the support I received during this time.

I am especially thankful to Prof. Dr.-Ing. Moustafa Abdel-Maksoud for supervising this thesis with continuous support and encouragement. I am grateful for the many interesting opportunities, such as assisting in teaching the ‘Energy from the Ocean’ lecture and in the organization of the 32nd Symposium on Naval Hydrodynamics, for the insightful discussions, and for all that I have learned from him during this time.

I thank Prof. Dr.-Ing. Otto von Estorff and Prof. Dr.-Ing. Stefan Krüger for thoroughly reading the thesis and the interesting discussions during its defense.

I thank all my collaborators in research: Prof. Dr.-Ing. Jovan Jovanović, for allowing me to accompany him a little bit further on the search for the holy grail of turbulent drag reduction, Prof. Dr. Hrvoje Jasak, Dr. Inno Gatin, and Dr. Vuko Vukčević, for inviting me to work together with them in Zagreb and sharing their expertise, especially regarding the `foam-extend` flow solver.

I thank all those who taught me about teaching: Prof. Dr.-Ing. Michael Schlüter and his team, for the enjoyable collaboration concerning the lecture module ‘Fluid Mechanics and Ocean Energy’, Katrin Billerbeck, Dr. Mirjam Glessmer, Dr. Timo Lüth and Uta Riedel at the Center for Teaching and Learning (ZLL), for being enthusiastic about active teaching approaches and their help in implementing these in the lecture ‘Energy from the Ocean’, and all my students, who taught me a lot through their questions and creativity.

I thank Prof. Dr.-Ing. Volker Bertram for interesting and humorous discussions, and for sending me to the Numerical Towing Tank Symposium in 2013; I learned a lot from the presentations on different research topics in ship hydrodynamics and the discussions in a friendly community, which made me come back year after year.

Many thanks go to my colleagues at the institute, who were always helpful and made my time at the institute a very pleasant one.

I thank Hamburgs public transport association (HVV) and the Deutsche Bahn (DB); most of the analytical derivations in this work were done on their trains, which provide just the right amount of noise and not-too-comfortable seats to generate a surprisingly productive working climate.

I am very thankful to my family and friends for all their support and the good times.

Most of all, I thank my wonderful wife Isabell for her love, patience and support. This thesis is dedicated to you!

Contents

Nomenclature

Wave parameters with index '$_0$' denote deep water conditions. Deviations from the following nomenclature are mentioned in the text.

1D	one-dimensional
2D	two-dimensional
3D	three-dimensional
CFD	computational fluid dynamics
CV	control volume
DOF	degree(s) of freedom
FFT	fast Fourier transform
FVM	finite volume method
HRIC	high resolution interface capturing
KCS	Kriso container ship
LES	large eddy simulation
RANS	Reynolds-averaged Navier-Stokes
SIMPLE	semi-implicit method for pressure linked equations
VOF	volume of fluid
A	analytical solution for an infinite number of constant-blending zones in a forcing zone; area
A_h	analytical solution for a forcing zone subdivided into constant-blending zones with thickness h
A_0	displacement amplitude for fluid particles in a (hydro-)acoustic wave
a	wave amplitude
a_n	Fourier amplitude of the wave component with frequency f_n
a_{refl}	amplitude of the wave reflected at forcing zone and domain boundary
$b'(t)$	blending function for generation of irregular (hydro-)acoustic waves
$b(\mathbf{x})$	blending function
C_{R}	reflection coefficient
$C_{\mathrm{R},j}$	reflection coefficient at the interface between zones j and $j+1$
$C_{\mathrm{R,opt}}$	optimum reflection coefficient for given $b(\mathbf{x})$ and x_{d}
$C_{\mathrm{R,sim}}$	simulation result for reflection coefficient
$C_{\mathrm{R,theory}}$	theory prediction for reflection coefficient
C_{R,θ_i}	reflection coefficient for wave incidence angle θ_i
$C_{\mathrm{T},j}$	transmission coefficient at interface between zones j and $j+1$
c	phase velocity
c_{g}	group velocity
D	diameter
E	energy
E_{A}, E_{R}, E_{T}	absorbed, reflected, and transmitted part of the total wave energy
E_{gen}	energy of the generated wave
E_{kin}	kinetic wave energy
E_{kin,x_i}	kinetic wave energy component in x_i-direction
E_{pot}	potential wave energy
E_{refl}	energy of the reflected wave
E_{tot}	total wave energy
$F_{x_i,p}$	pressure forces in x_i-direction, integrated over the body surface
f_1	parameter from Appendix B equal to forcing strength γ
f_n	frequency of wave component n
f_{peak}	peak frequency for irregular waves
Δf_n	frequency interval between wave components n and $n-1$
Fr	Froude number
$\mathbf{g} = (0, 0, -g)^{\mathrm{T}}$	vector for the gravitational acceleration
g	gravitational acceleration
H	wave height

H_{break}	breaking wave height
$H_{\max}$	largest wave height recorded in the vicinity of the forcing zone
$H_{\min}$	smallest wave height recorded in the vicinity of the forcing zone
H_{refl}	height of the wave reflected at forcing zone and domain boundary
H_{s}	significant wave height
h	water depth
h_e	enthalpy
$\mathbf{i}_j$	unit vector in x_j-direction
k	wave number; turbulent kinetic energy
k_j	wave number within zone j
L	characteristic length scale; waterline length of the ship in Appendix B
L_{model}, L_{full}	characteristic length scale for model and full scale
L_x, L_y, L_z	dimensions of the simulation domain in x-, y-, and z-direction
$\mathbf{n}$	unit vector normal to surface S
n	blending exponent; scaling factor; number of constant-blending zones in a forcing zone
p	pressure; order of convergence in Richardson extrapolation in Sect. 4.4
p_{a}	pressure amplitude
$p_{\mathrm{a,s}}$	significant pressure amplitude
q	forcing term in wave equation
q_c	source term for mass
q_i	source term for momentum in x_i-direction; forcing term in zone i
q_α	source term for volume fraction α
q_ϕ	source term for transport quantity ϕ
R	gas constant
r	radius
S	closed surface of control volume CV
T	wave period
T_{peak}	peak wave period for irregular waves
T_{ref}	wave period in reference simulation
t	time
t_{end}	end of a simulated time interval
t_{start}	start of a simulated time interval
Δt	time step; time interval
U	characteristic velocity; ship speed
U_{model}, U_{full}	characteristic velocity for model and full scale
u_{a}	velocity amplitude
$u_{i,\mathrm{ref}}$	reference velocity component in x_i-direction
$u_{\max}$	largest velocity amplitude recorded in the vicinity of the forcing zone
$u_{\min}$	smallest velocity amplitude recorded in the vicinity of the forcing zone
V	volume of a control volume CV; volume occupied by a fluid
V_θ	volume along a thin slice along the wave path with incidence angle θ
$\mathbf{v} = \begin{pmatrix} u \\ v \\ w \end{pmatrix} = \begin{pmatrix} u_1 \\ u_2 \\ u_3 \end{pmatrix}$	velocity vector with components u, v, w in x_i-direction, also denoted as u_1, u_2, u_3
$\mathbf{v}_g$	velocity vector of the moving CV surface
$\Delta x, \Delta y, \Delta z$	cell size in x-, y- and z-direction
$\mathbf{x} = \begin{pmatrix} x \\ y \\ z \end{pmatrix} = \begin{pmatrix} x_1 \\ x_2 \\ x_3 \end{pmatrix}$	vector with Cartesian coordinates x, y, z, also denoted as x_1, x_2, x_3
$\tilde{x}$	shortest distance of $\mathbf{x}$ to the closest domain boundary to which a forcing zone is attached
$\tilde{x}$, $\tilde{y}$, $\tilde{z}$	shortest distance to closest x-, y-, or z-normal domain boundary in Sect. 5.4
x_{d}	forcing zone thickness
x_{d_j}	forcing zone thickness for zone j

$x_{\mathrm{d}_{j,\mathrm{1D}}}$	forcing zone thickness for zone j and normal wave incidence
$x_{\mathrm{d}_{j,\mathrm{2D}}}$	effective forcing zone thickness for zone j and oblique wave incidence
$x_{\mathrm{d,ref}}$	forcing zone thickness in reference simulation
z_{b},z_{fs}	locations of domain bottom and free-surface in Eq. 115
α	volume fraction of water
α_{ref}	reference solution for volume fraction α
β_{j+1}	part of the equation for C_{R_j} at interface between zones j and $j+1$
Γ	diffusion coefficient
γ	forcing strength
γ_j	forcing strength introduced in the conservation equation denoted by j (cf. Sect. 4.1.2)
γ_{opt}	optimum forcing strength γ_{opt}, at which for given $b(\mathbf{x})$ and x_{d} a minimum of C_{R} occurs
$\gamma_{\mathrm{opt,sim}}$	simulation results for optimum forcing strength γ_{opt} for given $b(\mathbf{x})$ and x_{d}
$\gamma_{\mathrm{opt,theory}}$	theory prediction for optimum forcing strength γ_{opt} for given $b(\mathbf{x})$ and x_{d}
γ_{ref}	forcing strength in reference simulation
$\tilde{\gamma}$	forcing strength for forcing $\propto \omega\|\omega\|$
ϵ	turbulent dissipation
ε_{h}	error estimate for grid spacing h in Richardson extrapolation
η	free-surface elevation, measured from the location of the calm surface
ϑ	temperature
Θ	phase shift
θ	wave incidence angle
λ	wavelength
λ_{peak}	peak wavelength for irregular waves
λ_{ref}	wavelength in reference simulation
μ	primary wave propagation direction
ρ	density
ρ_{ref}	reference density
τ	relaxation parameter for relaxation zones
τ_{opt}	optimum relaxation parameter τ_{opt}, at which for given $b(\mathbf{x})$ and x_{d} a minimum of C_{R} occurs
$\tau_{\mathrm{opt,sim}}$	simulation results for optimum relaxation parameter τ_{opt} for given $b(\mathbf{x})$ and x_{d}
$\tau_{\mathrm{opt,theory}}$	theory prediction for optimum relaxation parameter τ_{opt} for given $b(\mathbf{x})$ and x_{d}
τ_{ref}	relaxation parameter in reference simulation
τ_{ij}	component of the viscous stress tensor
Υ	generic transport equation
ϕ	a generic transport quantity; velocity potential
ϕ_{ref}	reference solution for generic transport quantity ϕ
χ	fluid particle displacement in a (hydro-)acoustic wave
ψ	velocity stream function
ψ_j	velocity stream function in zone j
ψ_{ref}	reference solution for velocity stream function
ω	angular wave frequency; specific dissipation
ω_{full}	angular wave frequency in full scale
ω_{model}	angular wave frequency in model scale
ω_{ref}	angular wave frequency in reference simulation
$\mathcal{R}$	corresponds to the term $\int_V (\phi - \phi_{\mathrm{ref}})\ \mathrm{d}V$ in Eq. 22
$\mathcal{X}$	horizontal fluid particle displacement in a free-surface wave
$\mathcal{Z}$	vertical fluid particle displacement in a free-surface wave

1 Introduction

Key findings

- In flow simulations, undesired wave reflections at domain boundaries can produce significant errors
- An overview over techniques to reduce such undesired reflections is given
- Forcing zones can reduce undesired reflections by applying source terms in the vicinity of domain boundaries, but contain case-dependent parameters
- In this thesis, an analytical approach is developed to optimally tune the case-dependent parameters of forcing zones
- This work focuses on finite-volume-based flow simulations with free-surface waves for typical ocean engineering and shipbuilding applications
- Further, (hydro-)acoustic flow simulations will be performed as a computationally efficient model of shallow water waves

In flow simulations, it is usually desired to choose the computational domain as small as possible to reduce the computational effort. Thus when simulating free-surface wave propagation, undesired wave reflections at the domain boundaries must be minimized. If this is not achieved, the reflections travel back into the solution domain and can lead to large errors in the results.

For finite-volume-based flow solvers there are many unresolved problems, especially

- reliable reduction of reflections at the domain boundaries,
- prediction of the amount of undesired wave reflection *before performing the simulation*.

This work aims to provide further insight to solve these problems for flow simulations based on Navier-Stokes-type equations (Reynolds-averaged Navier-Stokes (RANS), Euler equations, Large Eddy Simulations (LES), etc.) discretized via the finite volume method.

In Sect. 1.1, different techniques to reduce undesired wave reflections at domain boundaries are compared. Subsequently, the aim of the present thesis is outlined in Sect. 1.2, followed by an overview of the thesis structure in Sect. 1.3.

1.1 Comparison of techniques to reduce undesired wave reflections

Undesired wave reflections at domain boundaries[1] can be reduced via *increasing the domain size*, *beaches*, *active wave absorption techniques*, *grid stretching*, *absorbing boundary conditions*, and/or *forcing zones*. Some of these approaches are shown in Fig. 1.

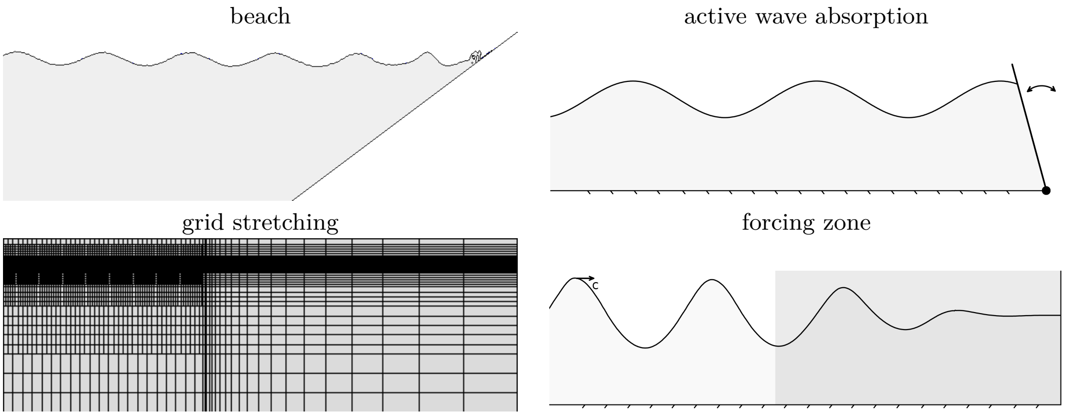

Figure 1: Illustration of wave damping for a right-going wave via wave breaking at a beach, flap-like motion of a domain boundary for an active wave absorber, intentional increase of discretization errors due to grid stretching, and gradual decrease of wave height due to source terms inside a forcing zone (shaded gray)

[1] Most common boundary conditions such as wall boundary, symmetry boundary, velocity inlet, and pressure outlet are nearly perfectly reflecting. Detailed information on the implementation of these boundary conditions can be found in Ferziger and Perić (2002).

Increasing the domain size delays the time at which undesired wave reflections reach the domain part of interest. This approach substantially increases the computational effort: First, because the number of cells increases. Second, because the waves have to travel a larger distance to the domain part of interest, so the time-step and the mesh size may have to be refined, or else numerical dissipation and dispersion errors could lead to a change in wave height or phase. Thus in practice this approach is rarely suitable, except perhaps for very short simulations (e.g. a single wave impact on a structure).

Beaches trigger wave breaking via a gradual decrease of water depth. As in experiments, even when the beach slope is optimally tuned to the incidence wave, reflection coefficients[2] of 5% to 10% must be expected (Cruz, 2008; Lloyd, 1998; Ursell et al., 1960). Note that in wave tank experiments, measurements are usually stopped when the first reflections from the beach reach the measurement location. The role of the beach is to decrease the 'waiting' time between two experiments; with the beach it typically takes $\mathcal{O}(20\,\mathrm{min})$ until there is again a calm water surface in the tank, without the beach it can take several hours. Thus beach reflection coefficients are seldom reported for experiments (Lloyd, 1998). In flow simulations however, the solution domain is usually small compared to real wave tank dimensions. Thus to avoid the accumulation of undesired wave reflections, flow simulations require lower reflection coefficients than beaches can typically provide.

Active wave absorption techniques are available in the world's most expensive wave basins, and the approach can also be used in flow simulations. Active wave absorbers detect approaching waves and move the domain boundary (or in the wave basin: the wave-maker flap/piston) so that it eliminates wave reflections via destructive interference (e.g. Cruz, 2008; Higuera et al., 2013; Schäffer and Klopman, 2000). While for selected wave periods and steepnesses reflection coefficients well below 5% can be obtained (Schäffer and Skourup, 1997), in general reflection coefficients of 10% or more may occur (Higuera et al., 2013; Troch and De Rouck, 1999). Further, the reflection coefficient increases with increasing wave incidence angle (Schäffer and Skourup, 1997). Depending on the implementation, the necessity to move the whole domain boundary may especially in 3D increase the computational effort. In principle though, it seems possible that correctly tuned active wave absorption could be capable of providing satisfactory (say $C_\mathrm{R} \lesssim 2\%$) reduction of undesired wave reflection, as long as the waves are not too steep and do not break. A drawback of the approach is that (at least in experiments) it does not permit flow through the wave-maker boundary.

Grid stretching (also called grid extrusion, numerical beach, etc.) gradually decreases the resolution of the computational grid towards the corresponding boundaries, so that the waves are damped by numerical diffusion and other numerical errors. The approach is easy to implement, but increases the size of the computational domain and the number of grid cells. Further, it cannot be applied to wave generating boundaries. Since the main mechanisms behind the wave damping are discretization and iteration errors, the reflection coefficient depends on the discretization scheme and on its order, on the mesh size, and on the time step. Thus when conducting grid- and time-step-dependence studies, the reflection coefficient changes for each simulation, which is undesired. Additionally, it is not known how to reliably predict the reflection coefficients before performing the simulation (Colonius, 2004; Perić and Abdel-Maksoud, 2016).

Absorbing boundary conditions (also called non-reflecting boundary conditions, artificial boundary conditions, radiation boundary condition, Dirichlet to Neumann boundary condition, etc.) are applied at the boundary, i.e. they require no increase of the domain size or of the number of grid cells. They can be implemented by prescribing suitable values for the solution at the boundary, which may be derived e.g. from the analytical solution of the exterior problem. Such boundary conditions were shown to work successfully for many problems where linearization of the wave field near the boundary is possible and where the far-field solution is known. Although much is known regarding their stability and accuracy, there are still unsolved problems, e.g. compatibility conditions at the domain corners. Moreover, applying the analytical formulations for the boundary conditions to discretized equations may produce undesired reflections. Thus the resulting reflection coefficients cannot always be reliably predicted before the simulations. Further, the theory behind many advanced absorbing boundary conditions can be quite complex, so that the choice and the implementation may be time-consuming, especially for non-experts in this field. The main drawback though is that when significant nonlinear effects occur close to the boundary, it may either be impossible to formulate such boundary conditions, or boundary conditions of such a high order may be required that the computational effort becomes too large for practical purposes. This is typically the case for flows where turbulence occurs close to the boundaries. For steep free-surface waves, especially for irregular, short-crested, or breaking waves, no satisfactory absorbing boundaries conditions have been presented so far; indeed, it seems unlikely that it is possible to find a theoretical solution that satisfactorily describes all relevant

[2] The reflection coefficient $C_\mathrm{R} = H_\mathrm{refl}/H$ is the ratio of the reflected wave height H_refl to the generated wave height H, as described in detail in Sect. 3.

aspects of such complicated, nonlinear flows. However, for simpler flows such as linear sound wave propagation they can be applied with success. Further information on absorbing boundary conditions can be found e.g. in Colonius (2004), Givoli (2004), Hu (2004), Israeli and Orszag (1981), Marburg and Nolte (2008), Novak and Bonazzola (2004), or Romate (1992).

Forcing zones (also called absorbing layers, damping zones, dissipation zones, numerical beach, sponge layers, Euler overlay method, coupling or relaxation zones) introduce source terms to one or several of the governing equations in a zone adjacent to the corresponding domain boundaries, with the intention of gradually forcing the solution towards some reference solution within the forcing zone, as described in Sect. 2. Prescribing a steady far-field solution often simply corresponds to a damping of the waves which enter the layer (e.g. Arai et al., 1993; Choi and Yoon, 2009; Israeli and Orszag, 1981; Park et al., 1999). Prescribing an unsteady far-field solution can be used to generate waves which travel from the forcing zone into the domain, while simultaneously damping waves which enter the forcing zone (e.g. Jacobsen et al., 2012; Kim et al., 2012; Vukčević et al., 2016, 2016b). Forcing zones can also be used to couple two different flow solvers, e.g. a finite-volume-based flow solver, which resolves the viscous near-field of a structure, to a boundary-element-based flow solver, which resolves the inviscid far-field (Guignard et al., 1999); the blending between the two solvers can be achieved by applying two forcing zones, one for each solver, in-between the near- and the far-field domains. Forcing zones usually have a thickness of one to two wavelengths, and thus moderately increase the computational effort. Apart from this, they have none of the aforementioned drawbacks. However, there is one aspect which is critical to their successful application: the forcing function contains case-dependent parameters, which must be tuned for every simulation (Berenger, 1996; Mani, 2012; Perić and Abdel-Maksoud, 2016; Romate, 1992). Prior to the work presented in this thesis, forcing zones were usually considered 'ad-hoc' approaches (Benacchio and Bonaventura, 2013); the case-dependent parameters were tuned by trial and error or kept at default values, resulting in unreliable reduction of undesired wave reflections (Bodony, 2006; Colonius, 2004; Perić and Abdel-Maksoud, 2016). When correctly tuned though, they have been demonstrated to reliably provide low reflection coefficients (say $C_\mathrm{R} \lesssim 2\%$) for a wide range of wave conditions (Perić and Abdel-Maksoud 2016, 2018, 2018b; Perić et al., 2018).

In summary, forcing zones appear to be the most promising candidate to achieve the desired minimization of undesired wave reflections at domain boundaries, to enable flow simulations of free-surface waves without any restriction of the simulated time interval and without restrictions of application to steep waves, breaking waves, or waves with superposed currents. Further, forcing zones enable the coupling to reference flow solutions. Thus the rest of this work focuses exclusively on forcing zones.

1.2 Aim of this thesis

The aim of this thesis is to develop an analytical approach to optimally tune the case-dependent parameters of forcing zones *before performing the flow simulations*, with focus on finite-volume-based flow simulations with free-surface waves for typical ocean engineering and shipbuilding applications. The approach should be 'practical' in the sense that it should be as simple as possible and as accurate as necessary to enable wide use in industrial practice; thus this theory is intended to predict the flow features relevant for determining optimum or close-to-optimum tuning, but not all flow details in the forcing zone need to be fully captured.

In this thesis, the theory is validated[3] via results from two-dimensional (2D) and three-dimensional (3D) finite-volume-based flow simulations, with regard to typical ocean engineering and shipbuilding applications. Simulations are performed for regular and irregular waves in deep water to shallow water conditions. Further, simulations are carried out to determine the influence of the wave steepness, of the forcing zone parameters, of the choice of governing equations to which forcing is applied, and of the decision which forcing zones to apply at which domain boundaries.

Although the focus of this thesis is on free-surface flows, also (hydro-)acoustic flow simulations with forcing zones are performed, with sound waves used as a computationally efficient model of shallow-water waves, because in both cases dispersion[4] is approximately zero. The advantage of performing flow simulations with sound waves is that it reduces the complexity of the flow problem by one dimension: In free-surface waves, fluid particles travel on orbital paths (Clauss et al., 1992), so their motion is both longitudinal (i.e. in wave propagation direction) and transverse (i.e. perpendicular

[3]In this work, the term 'validation' is used based on the definition in Eça et al. (2010), i.e. that validation aims at identifying modeling errors via comparison to results from experiments or, in the present case, flow simulations.

[4]If a medium is dispersive, the wave's phase velocity depends on the wavelength. Free-surface waves become non-dispersive in the shallow water limit, since then the phase velocity is $c|_{h\leq 0.05\lambda} = \sqrt{\frac{g}{k}\tanh(kh)}|_{h\leq 0.05\lambda} \approx \sqrt{gh}$ with water depth h, wavelength $\lambda = 2\pi/k$, and gravitational acceleration $g \approx 9.81\,\mathrm{m/s^2}$ according to linear wave theory (cf. Clauss et al., 1992).

to the wave propagation direction). Thus '1D-wave-propagation', e.g. a long-crested wave traveling in one direction, requires a 2D-flow simulation to resolve the flow below the free surface, and '2D-wave-propagation' requires a 3D-flow simulation. In contrast, the particle motion in sound waves is only longitudinal. Thus '1D-' and '2D-wave-propagation' can be computed in 1D or 2D, which drastically reduces the computational effort and enables the simulation of larger wave propagation distances. Further, for free-surface waves it was found that reflection coefficients smaller than $\approx 1\%$ could not be reliably detected (Perić and Abdel-Maksoud, 2018), since the approach to account for the two fluid phases, i.e. the volume of fluid (VOF; Hirt and Nichols, 1981) method with interface sharpening (Muzaferija and Perić, 1999), can create a slight background noise in the approaches to determine reflection coefficient C_{R} (Larsen et al., 2019; Perić and Abdel-Maksoud, 2018). Such schemes are not required when simulating sound wave propagation in a single phase medium, so then reflection coefficient C_{R} can be calculated much more accurately, as demonstrated in Sect. 5. Finally, the (hydro-)acoustic flow simulations demonstrate that the theory is not restricted to free-surface waves, but can be extended to waves in other mediums in a straight-forward manner.

To facilitate the use of the presented theory for other researchers, computer programs to evaluate the theory for free-surface and sound waves have been published as free software. The download links can be found in Sects. 4.1, 4.2, and 4.3.

1.3 Thesis structure

In Sect. 2, a generic formulation of forcing zones is presented, of which the forcing-zone-type approaches listed in Sect. 1.1 are special cases. Thus the present findings can be applied to all these approaches in a straight-forward manner. It is shown how the case-dependent parameters scale so that similar forcing can be obtained when up-/down-scaling the waves. 'Relaxation zones', a special case of forcing zones, are discussed, as well as forcing zones for (hydro-) acoustic waves.

In Sect. 3, an overview over techniques to calculate reflection coefficient C_{R} is given. In the present work, only approaches with low background noise ($\lesssim 1\%$) are used.

In Sect. 4, the derivation of the theory for predicting reflection coefficients for forcing zones in flows with free-surface waves and flows with (hydro-)acoustic waves is given. The theory is presented for the case of long-crested (1D) wave propagation, and then extended to 2D and 3D to cover oblique wave incidence.

In Sect. 5, the theory is validated via simulation results for flows with (hydro-)acoustic waves and forcing zones. The investigations include a grid- and time-step-dependence study, damping of regular and irregular sound waves with different periods, amplitudes and forcing zone parameters in 1D-/2D-/3D-flows, damping of highly nonlinear waves, forcing towards an unsteady reference solution, and prediction of reflection coefficients for oblique wave incidence.

In Sects. 6 to 8, the theory is validated via simulation results for flows with free-surface waves and typical ocean engineering and shipbuilding applications. The investigations include grid- and time-step-dependence studies, damping of regular and irregular free-surface waves with different periods, wave steepnesses, water depths and forcing zone parameters in 2D-/3D-flows, relaxation zones using two different flow solvers, forcing towards an unsteady reference solution, source terms in different governing equations, and the choice of forcing zones for 3D-flow simulations. A recommended forcing zone arrangement for 3D-flow simulations with strongly reflecting bodies in long-crested far-field waves is proposed.

In Sect. 9, the findings, the benefits, and the limitations of the theory are discussed and an outlook for possible future research is given. After a brief conclusion in Sect. 10 two appendices present flow simulations results for (hydro-)acoustic wave propagation through thin forcing zones in Appendix A and the use of forcing zones for improving the convergence in ship resistance computations in Appendix B.

2 Forcing zones

Key findings

- A generic formulation of forcing zones is presented
- Forcing zones contain three case-dependent parameters:
  - forcing strength γ, which regulates the source term magnitude,
  - blending function $b(\mathbf{x})$, which regulates how the source term magnitude varies within the zone
  - and zone thickness x_{d}
- It is shown how these parameters scale with the wave
- The application of forcing zones to the governing equations for flow simulations with free-surface waves or (hydro-)acoustic waves is described, as well as 'relaxation zones', a special case of forcing zones

Forcing zones apply source terms to the governing equations in a zone adjacent to the corresponding domain boundaries as illustrated in Fig. 2. Such approaches have been presented under many different names, such as absorbing layers (Wei et al., 1999), damping zones (Cao et al., 1993; Jose et al., 2017; Kim et al., 2014; Park et al., 1999; Perić and Abdel-Maksoud, 2016), dissipation zones (Park et al., 1993), numerical beach (Clément, 1996), sponge layers (Brorsen and Helm-Petersen, 1999; Choi and Yoon, 2009; Ha et al. 2013; Hu et al., 2015; Israeli and Orszag, 1981; Larsen and Dancy, 1983; Zhang et al., 2014), Euler overlay method (Kim et al., 2012; Kim et al., 2013), forcing zones (Perić, 2015; Siemens STAR-CCM+ manual version 11.06), and coupling or relaxation zones (Jacobsen et al., 2012; Jasak et al., 2015; Meyer et al., 2017; Schmitt and Elsaesser, 2015; Vukčević et al., 2016, 2016b; Wöckner-Kluwe, 2013).

The general principle behind all these approaches is that they apply source terms to one, to several, or to all[5] of the governing equations, with the intention of gradually forcing the solution towards some reference solution within a zone (layer) attached to the domain boundary. This damps waves which travel into the zone, but it can also be used to generate waves or to couple different flow solvers (e.g. a viscous solver for the near-field and an inviscid solver for the far-field).

A possible distinction could be that terms like *forcing zone* and *relaxation zone* are more general, while others are more specific; for example, the *Euler overlay method* forces the flow towards the analytical solution of an undisturbed wave. *Damping zones*, *absorbing layers* and *sponge layers* often apply source terms only in a single governing equation, with the forcing term formulated so that it can be interpreted as a damping term. Yet in several cases there seems to be no clear distinction and some of the names are used synonymously.

Thus in the following, the term *forcing zone* will be used to highlight that the results in this work are applicable to all of the above approaches. To illustrate this, a generic formulation of forcing zones is presented in Sect. 2.1. Section 2.2 shows how the case-dependent parameters of forcing zones scale. In Sects. 2.3 to 2.5, the generic forcing zone formulation is applied to flows with free-surface waves and (hydro-)acoustic waves; further, the application to 'relaxation zones', a special case of forcing zones, is presented.

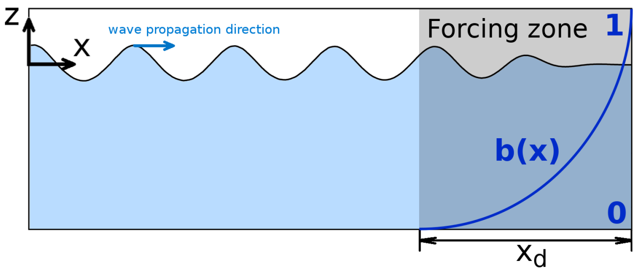

Figure 2: Qualitative sketch of a flow simulations with free-surface wave propagation, using a forcing zone (shaded gray) with zone thickness x_{d} and blending function $b(x)$ to minimize undesired wave reflections at a domain boundary

[5] With one exception: no forcing source terms are applied in the pressure-correction equation, since it is derived from the continuity equation with the intention to achieve that velocities and densities fulfill both the continuity and the momentum conservation equations (cf. Patankar, 1980). In the case of incompressible flows, velocities are the only variables in the continuity equation and they are forced through their corresponding momentum equations. In the case of compressible flows, one can additionally apply forcing to the energy equation and/or the equation from which the density is computed (depending on whether a density-based or a pressure-based algorithm is used). Thus additional forcing of the pressures could impair convergence of the pressure correction.

2.1 A generic formulation of forcing zones

The following generic formulation of forcing zones is given for the generic transport equation for transport quantity ϕ, which is described e.g. in Ferziger and Perić (2002)

$$\frac{\partial}{\partial t}\int_V \rho\phi \ \mathrm{d}V + \int_S \rho\phi\mathbf{v}\cdot\mathbf{n} \ \mathrm{d}S = \int_S \Gamma\nabla\phi\cdot\mathbf{n} \ \mathrm{d}S + \int_V \rho q_\phi \ \mathrm{d}V \quad , \tag{1}$$

with time t, density ρ, volume V of the control volume (CV) bounded by the closed surface S, velocity vector $\mathbf{v} = (u_1, u_2, u_3)^{\mathrm{T}} = (u, v, w)^{\mathrm{T}}$ with Cartesian components u_i (equivalent to u, v, w), unit vector $\mathbf{n}$ normal to S and pointing outwards, diffusion coefficient Γ, and source term q_ϕ.

Within the forcing zone, the following source term is introduced in Eq. (1)

$$q_\phi = \gamma b(\mathbf{x})\left(\phi_{\mathrm{ref}} - \phi\right) \quad , \tag{2}$$

with forcing strength γ, blending function $b(\mathbf{x})$ and reference transport quantity ϕ_{ref}.

Forcing strength γ regulates the magnitude of the source term, i.e. how strongly the solution for ϕ at a given cell is forced against the reference solution ϕ_{ref}.

Blending function $b(\mathbf{x})$ regulates how the magnitude of the source term varies within the forcing zone. Outside the forcing zone holds $b(\mathbf{x}) = 0$, and inside the forcing zone holds $0 \leq b(\mathbf{x}) \leq 1$. Usually, $b(\mathbf{x})$ is ≈ 0 at the entrance to the forcing zone and gradually increases within the zone as illustrated in Fig. 3.

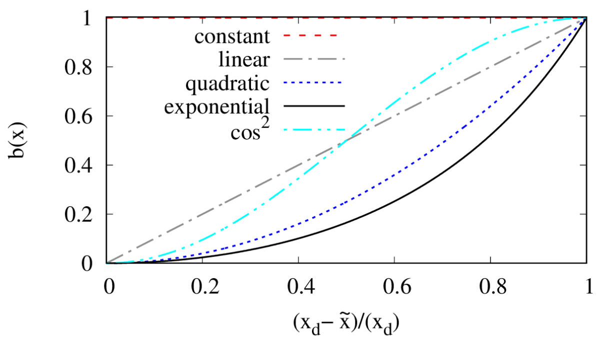

Figure 3: Different blending functions $b(\mathbf{x})$ as a function of $\mathbf{x}$-location in the forcing zone; $\tilde{x}$ is the shortest distance of $\mathbf{x}$ to the closest domain boundary to which a forcing zone of thickness x_{d} is attached; waves enter the zone at $(x_{\mathrm{d}} - \tilde{x})/x_{\mathrm{d}} = 0$, and the boundary to which the zone is attached lies at $(x_{\mathrm{d}} - \tilde{x})/x_{\mathrm{d}} = 1$; for constant (Eq. (3)), linear (Eq. (4)), quadratic (Eq. (5)), exponential (Eq. (9)), and $\cos^2$ (Eq. (7)) blending

In this work, the following blending functions are used:

Constant blending

$$b(\mathbf{x}) = 1 \quad , \tag{3}$$

linear blending

$$b(\mathbf{x}) = \left(\frac{x_{\mathrm{d}} - \tilde{x}}{x_{\mathrm{d}}}\right) \quad , \tag{4}$$

quadratic blending

$$b(\mathbf{x}) = \left(\frac{x_{\mathrm{d}} - \tilde{x}}{x_{\mathrm{d}}}\right)^2 \quad , \tag{5}$$

power blending

$$b(\mathbf{x}) = \left(\frac{x_{\mathrm{d}} - \tilde{x}}{x_{\mathrm{d}}}\right)^n \quad , \tag{6}$$

$\cos^2$-blending

$$b(\mathbf{x}) = \cos^2\left(\frac{\pi}{2} + \frac{\pi}{2}\left(\frac{x_{\mathrm{d}} - \tilde{x}}{x_{\mathrm{d}}}\right)\right) \quad , \tag{7}$$

$\cos^{2n}$-blending

$$b(\mathbf{x}) = \left[\cos^2\left(\frac{\pi}{2} + \frac{\pi}{2}\left(\frac{x_{\mathrm{d}} - \tilde{x}}{x_{\mathrm{d}}}\right)\right)\right]^n \quad , \tag{8}$$

exponential blending

$$b(\mathbf{x}) = \left(\frac{e^{((x_\mathrm{d}-\tilde{x})/x_\mathrm{d})^2} - 1}{e^1 - 1} \right) \quad , \tag{9}$$

and exponential blending with power n

$$b(\mathbf{x}) = \left(\frac{e^{((x_\mathrm{d}-\tilde{x})/x_\mathrm{d})^n} - 1}{e^1 - 1} \right) \quad , \tag{10}$$

where $\tilde{x}$ is the shortest distance of location $\mathbf{x}$ to the closest domain boundary to which a forcing zone of thickness x_d is attached (cf. Fig. 2), and n regulates the shape of the blending function.

The problem with forcing zones is to find optimum values for the case-dependent parameters forcing strength γ, blending function $b(\mathbf{x})$, and zone thickness x_d, before performing the simulation. These parameters must be tuned for every simulation. Using default coefficients can lead to large errors in the simulation results as shown in Perić and Abdel-Maksoud (2016).

2.2 Scaling of case-dependent parameters in forcing zones

In engineering practice, flow simulations are often performed both for model and for full scale. Then it is desired to have the same reflection coefficients in both cases. To achieve this, the case-dependent parameters of the forcing zone described in Sect. 2.1 need to be scaled accordingly.

Geometric similarity requires that the zone thickness x_d must scale with the wavelength λ. The blending function $b(\mathbf{x})$ is non-dimensionalized by x_d and thus requires no further scaling. Kinematic similarity and dimensional analysis of Eqs. (1) and (2) show that forcing strength γ has the unit $[1/s]$, so γ scales with the inverse of the wave period.

Let the scaling factor be

$$n = \frac{L_\mathrm{model}}{L_\mathrm{full}} \quad ,$$

with characteristic lengths L_model and L_full in model and full scale. Geometric similarity requires the wavelength λ to scale as $\lambda \propto n$. Kinematic and dynamic similarity require the Froude number Fr, which denotes the ratio of inertia force to gravity force, to be identical in model and full scale, with

$$\mathrm{Fr} = \frac{U}{\sqrt{gL}} \quad , \tag{11}$$

with characteristic velocity U, gravitational acceleration g, and characteristic length L. It follows that $U_\mathrm{model}/U_\mathrm{full} \propto \sqrt{n}$. Since the velocity can be interpreted as a characteristic length scale over a characteristic time scale, it follows that the characteristic time scale and thus the wave period T scale with $T \propto \sqrt{n}$; a detailed derivation can be found e.g. in McCormick (2007).

Thus forcing strength γ and forcing zone thickness x_d scale as

$$\gamma \propto T^{-1}, \quad x_\mathrm{d} \propto \lambda \quad , \tag{12}$$

with wave period T and wavelength λ.

Therefore, to achieve the same reflection coefficient and similar free-surface elevations within the forcing zones when performing two flow simulations, the parameters γ and x_d for the second simulation have to be adjusted as

$$x_\mathrm{d} = x_\mathrm{d,ref} \cdot \frac{\lambda}{\lambda_\mathrm{ref}} \quad , \tag{13}$$

$$\gamma = \gamma_\mathrm{ref} \cdot \frac{T_\mathrm{ref}}{T} \quad , \tag{14}$$

where $x_\mathrm{d,ref}$, λ_ref, T_ref and γ_ref are the corresponding parameters from the first simulation.

Note that equivalently γ could be scaled with the angular wave frequency $\omega = \frac{2\pi}{T}$ via

$$\gamma \propto \omega \quad , \tag{15}$$

and thus instead of Eq. (14) one obtains

$$\gamma = \gamma_{\mathrm{ref}} \cdot \frac{\omega}{\omega_{\mathrm{ref}}} \quad . \tag{16}$$

Therefore, both [1/s] and [rad/s] are used as unit for γ in the following.

2.3 Governing equations and forcing zones for flows with free-surface waves

In this work, the flow simulations with free-surface waves are governed by the equation for mass conservation, the three equations for momentum conservation and the equation for the volume fraction, which describes the distribution of the phases:

$$\frac{\mathrm{d}}{\mathrm{d}t} \int_V \rho \ \mathrm{d}V + \int_S \rho(\mathbf{v} - \mathbf{v}_g) \cdot \mathbf{n} \ \mathrm{d}S = 0 \quad , \tag{17}$$

$$\frac{\mathrm{d}}{\mathrm{d}t} \int_V \rho u_i \ \mathrm{d}V + \int_S \rho u_i(\mathbf{v} - \mathbf{v}_g) \cdot \mathbf{n} \ \mathrm{d}S = \int_S (\tau_{ij}\mathbf{i}_j - p\mathbf{i}_i) \cdot \mathbf{n} \ \mathrm{d}S + \int_V \rho\mathbf{g} \cdot \mathbf{i}_i \ \mathrm{d}V + \int_V \rho q_i \ \mathrm{d}V \quad , \tag{18}$$

$$\frac{\mathrm{d}}{\mathrm{d}t} \int_V \alpha \ \mathrm{d}V + \int_S \alpha(\mathbf{v} - \mathbf{v}_{\mathrm{g}}) \cdot \mathbf{n} \ \mathrm{d}S = \int_V q_\alpha \ \mathrm{d}V \quad . \tag{19}$$

Here V is the control volume (CV) bounded by the closed surface S, $\mathbf{v}$ is the velocity vector of the fluid with the Cartesian components u_i, $\mathbf{v}_g$ is the grid velocity, $\mathbf{n}$ is the unit vector normal to S and pointing outwards, t is time, p is the pressure, ρ are fluid density, τ_{ij} are the components of the viscous stress tensor, $\mathbf{i}_j$ is the unit vector in direction x_j, with volume fraction α of water. The results in this work apply regardless which formulation for τ_{ij} is chosen or whether it is neglected altogether, since, unless wave breaking occurs, the propagation of ocean waves is an approximately inviscid phenomenon.

Based on the forcing zone formulation in Eq. (2) from Sect. 2.1, undesired wave reflections can be minimized by applying source terms for momentum, q_i, and volume fraction, q_α, as

$$q_{\mathrm{i}} = \gamma b(\mathbf{x})(u_{i,\mathrm{ref}} - u_i) \quad , \tag{20}$$

$$q_\alpha = \gamma b(\mathbf{x}) \left(\alpha_{\mathrm{ref}} - \alpha\right) \quad , \tag{21}$$

with reference velocity component $u_{i,\mathrm{ref}}$, reference volume fraction α_{ref}, forcing strength γ and blending function $b(\mathbf{x})$. As before, γ regulates the source term magnitude and $b(\mathbf{x})$ can e.g. be selected from Eqs. (3) to (10). Forcing may be applied only for horizontal momentum (q_x, q_y), or for vertical momentum (q_z), or for volume fraction (q_α), or for any combination of these. If the reference solution is the hydrostatic solution for the undisturbed free surface (e.g. $u_{i,\mathrm{ref}} = 0$), then the forcing can be interpreted as '*wave damping*'.

Apart from Eq. (20), some forcing-zone-type approaches have been proposed in which the source terms are not directly proportional to the forced quantity; these are discussed in Sect. 6.9.

Empirical approaches to tuning the case-dependent parameters of forcing zones, such as Carmigniani and Violeau (2018) and Perić and Abdel-Maksoud (2016), demonstrated that the optimum forcing strength γ_{opt} and the corresponding reflection coefficient $C_{\mathrm{R,opt}}$ can be determined with comparatively low computational effort for a given blending function $b(\mathbf{x})$, zone thickness x_{d}, and wave period T, by performing 2D-flow simulations for different forcing strength γ. For waves with a different period T, the reflection coefficient can be expected to be $C_{\mathrm{R}} \approx C_{\mathrm{R,opt}}$ if zone thickness x_{d} and forcing strength γ_{opt} are scaled via Eqs. (13) and (14), given that the waves are roughly similar and the same blending function $b(x)$ is used. Then γ_{opt} can for practical purposes be considered independent of the wave steepness, independent of the discretization (time step, mesh size, order and choice of discretization scheme), and roughly independent of zone thickness x_{d} within some interval such as $1\lambda \lesssim x_{\mathrm{d}} \lesssim 2\lambda$; for example for blending according to Eq. (9), Perić and Abdel-Maksoud (2016) obtained $\gamma_{\mathrm{opt}} \approx \pi\omega$, which gives $C_{\mathrm{R}} < 1\%$ for $x_{\mathrm{d}} = 2\lambda$. A drawback of this approach is that, for a different blending function $b(x)$ or zone thickness (i.e. $x_{\mathrm{d}} < 1\lambda$ or $x_{\mathrm{d}} > 2\lambda$), the above calibration process has to be carried out again. Thus a more efficient approach to tuning forcing zones is required, which was the motivation for the present work.

2.4 Governing equations and relaxation zones for flows with free-surface waves

Relaxation zones blend, say a generic transport equation Υ for transport quantity ϕ, over to a reference solution via

$$(1-b(\mathbf{x}))\,\Upsilon + \frac{b(\mathbf{x})}{\tau}\mathcal{R} = 0 \quad , \tag{22}$$

where $b(\mathbf{x})$ is a blending function such as e.g. Eqs. (3) to (10), Υ corresponds e.g. to Eqs. (18) and (19), and $\mathcal{R}$ corresponds to $\int_V (\phi - \phi_{\mathrm{ref}})\ \mathrm{d}V$ with reference solution ϕ_{ref} for transport quantity ϕ.

The relaxation parameter τ has unit[6] [s], scales with the wave period T as $\tau \propto T$, and regulates the magnitude of the source term in such a way that a large value of τ implicates a small source term and vice versa.

Hence the conservation equations for momentum and volume fraction take the form

$$\begin{aligned}(1-b(\mathbf{x}))\Bigg[\frac{\mathrm{d}}{\mathrm{d}t}\int_V \rho u_i\ \mathrm{d}V + \int_S \rho u_i(\mathbf{v}-\mathbf{v}_g)\cdot\mathbf{n}\ \mathrm{d}S \\ - \int_S (\tau_{ij}\mathbf{i}_j - p\mathbf{i}_i)\cdot\mathbf{n}\ \mathrm{d}S - \int_V \rho\mathbf{g}\cdot\mathbf{i}_i\ \mathrm{d}V\Bigg] \\ + \frac{b(\mathbf{x})}{\tau}\left[\int_V \rho\,(u_i - u_{i,\mathrm{ref}})\ \mathrm{d}V\right] = 0 \quad ,\end{aligned} \tag{23}$$

$$\begin{aligned}(1-b(\mathbf{x}))\left[\frac{\mathrm{d}}{\mathrm{d}t}\int_V \alpha\ \mathrm{d}V + \int_S \alpha(\mathbf{v}-\mathbf{v}_{\mathrm{g}})\cdot\mathbf{n}\ \mathrm{d}S\right] \\ + \frac{b(\mathbf{x})}{\tau}\left[\int_V (\alpha - \alpha_{\mathrm{ref}})\ \mathrm{d}V\right] = 0\end{aligned} \tag{24}$$

with reference velocities $u_{i,\mathrm{ref}}$ and reference volume fraction α_{ref}.

Relaxation zones can be interpreted as a special case of the forcing zones as shown in Sect. 4.2. Whereas the forcing zones from Sect. 2.3 are frequently applied to just a single governing equation in literature, relaxation zones usually blend all governing equations except for the pressure-correction equation. Further, relaxation zones 'blend out' all terms except the source terms in the governing equations via the factor $(1-b(\mathbf{x}))$; as illustrated in Fig. 4, forcing zones do not have this factor, thus with forcing zones the whole governing equations remain active in the whole domain, whereas within relaxation zones as in Eqs. (23) and (24), the terms from the governing equations that are active in the solution domain of interest are faded out and the reference solution is faded in[7].

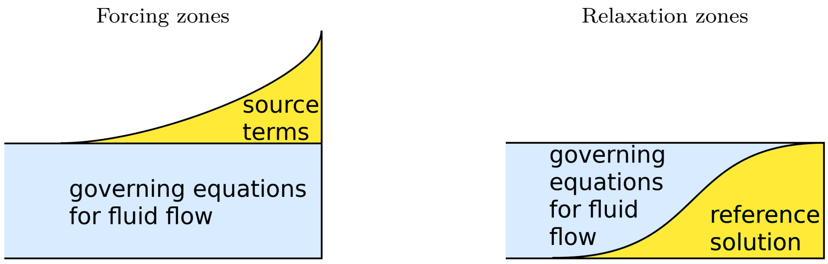

Figure 4: Illustration of the difference in implementation between forcing zones from Sect. 2.3 and relaxation zones; in forcing zones, the governing equations are active in the whole solution domain and the forcing source terms are added to them; in relaxation zones, the governing equations are blended-out inside the forcing zone while the reference solution is blended-in

In this work, the relaxation is implemented implicitly as described in Jasak et al. (2015) and Vukčević et al. (2016, 2016b). Note that also explicit implementations as in Jacobsen et al. (2012) are possible.

As with the forcing zones from Sect. 2.3, also relaxation zones have three case-dependent parameters, i.e. relaxation parameter τ, blending function $b(\mathbf{x})$, and relaxation zone thickness x_{d}. Therefore, to achieve the same reflection coefficient and similar free-surface elevations within the relaxation zones when performing two flow simulations, the relaxation

[6]Note that τ has sometimes been interpreted as a numerical stability parameter, and thus has occasionally been omitted from Eq. (22) in literature. However, dimensional analysis shows that it has a unit and requires scaling as described in Sects. 2.2 and 2.4.

[7]A distinct behavior of relaxation zones appears when relaxation parameter $\tau \to \infty$, so that the term with the reference solution vanishes, i.e. $(b(\mathbf{x})/\tau)\mathcal{R} \to 0$. At the same time, the governing equations are blended out in the vicinity of the boundary to which the zone is attached, since $(1-b(\mathbf{x}))\,\Upsilon \to 0$ for $\tilde{x} \to 0$. Thus all terms in Eq. (22) go to zero. In this case the reference solution (e.g. the far-field wave) cannot be maintained as shown in Fig. 140, which underlines the necessity of correctly tuning relaxation parameter τ.

parameter τ and the relaxation zone thickness x_{d} for the second simulation have to be adjusted as

$$\tau = \tau_{\mathrm{ref}} \cdot \frac{T}{T_{\mathrm{ref}}} \quad , \tag{25}$$

where T_{ref} and τ_{ref} are the corresponding parameters from the first simulation, and x_{d} is adjusted via Eq. (13).

2.5 Governing equations and forcing zones for flows with (hydro-)acoustic waves

The governing equations for the single-phase flow simulations with (hydro-)acoustic waves are the equation for mass conservation and the three equations for momentum conservation:

$$\frac{\partial}{\partial t}\int_V \rho \ \mathrm{d}V + \int_S \rho \mathbf{v}\cdot\mathbf{n} \ \mathrm{d}S = \int_V q_{\mathrm{c}} \ \mathrm{d}V \quad , \tag{26}$$

$$\frac{\partial}{\partial t}\int_V \rho u_i \ \mathrm{d}V + \int_S \rho u_i \mathbf{v}\cdot\mathbf{n} \ \mathrm{d}S = \int_S (\tau_{ij}\mathbf{i}_j - p\mathbf{i}_i)\cdot\mathbf{n} \ \mathrm{d}S + \int_V \rho\mathbf{g}\cdot\mathbf{i}_i \ \mathrm{d}V + \int_V \rho q_i \ \mathrm{d}V \quad , \tag{27}$$

with volume V of control volume (CV) bounded by the closed surface S, fluid velocity vector $\mathbf{v}$ with the Cartesian components u_i, unit vector $\mathbf{n}$ normal to S and pointing outwards, time t, pressure p, fluid density ρ, components τ_{ij} of the viscous stress tensor, unit vector $\mathbf{i}_j$ in direction x_j, mass source terms q_c, and momentum source terms q_i.

Since many acoustic wave phenomena are approximately inviscid, the results in this work apply regardless which formulation for τ_{ij} is chosen or whether it is neglected altogether; this was verified by performing selected simulations from Sect. 5 first with the standard k-ω turbulence model (see. e.g. Wilcox, 1993), then as laminar simulation (i.e. without any modeling in Eq. (18)), and as inviscid simulation; as expected, no significant differences in wave absorption were encountered.

The energy equation is

$$\frac{\partial}{\partial t}\int_V \rho E \ \mathrm{d}V + \int_S \rho h_e \mathbf{v}\cdot\mathbf{n} \ \mathrm{d}S = -\int_S \dot{q}\cdot\mathbf{n} \ \mathrm{d}S \quad , \tag{28}$$

with total energy $E = h_e - p/\rho$, total enthalpy $h_e = c_{\mathrm{p}}\vartheta + \frac{1}{2}|\mathbf{v}|^2$, heat capacity c_{p} at constant pressure, temperature ϑ and heat flux vector $\dot{q}$.

The fluid mediums investigated in this work are liquid water using the IAPWS (1997) model and ideal gases using the ideal gas law

$$pV = nR\vartheta \quad , \tag{29}$$

with pressure p, volume V, amount of gas substance n in moles, gas constant $R = 8.314JK^{-1}\mathrm{mol}^{-1}$, and absolute temperature ϑ.

Forcing zones can be implemented using the following source terms in Eqs. (26) and (27)

$$q_{\mathrm{c}} = \gamma b(\mathbf{x})\left(\rho_{\mathrm{ref}} - \rho\right) \quad , \tag{30}$$

$$q_{\mathrm{i}} = \gamma b(\mathbf{x})\left(u_{i,\mathrm{ref}} - u_i\right) \quad , \tag{31}$$

with reference density ρ_{ref}, density ρ, reference velocity component $u_{i,\mathrm{ref}}$, velocity component u_i, forcing strength γ, and blending function $b(\mathbf{x})$ such as Eqs. (3) to (10). As in Sect. 2.3, forcing may be applied to a single or a combination of several governing equations. Unless mentioned otherwise, the reference solution is the medium at rest, so $u_{i,\mathrm{ref}} = 0\,\frac{\mathrm{m}}{\mathrm{s}}$.

3 Calculating reflection coefficient C_R

Key findings

- Approaches for calculating reflection coefficient C_R are presented
- In this work, only approaches with low background noise ($C_\mathrm{R} \lesssim 1\%$) are used
- Different approaches are used for different flows

The reflection coefficient for free-surface waves is defined as the ratio of reflected wave height H_refl to the generated wave height H as

$$C_\mathrm{R} = \frac{H_\mathrm{refl}}{H} \quad . \tag{32}$$

For harmonic waves, the reflection coefficient may equivalently be written as

$$C_\mathrm{R} = \frac{a_\mathrm{refl}}{a} \quad . \tag{33}$$

with amplitude a_refl of the reflected and amplitude a of the generated wave; for example for linear sound waves, these could be velocity or pressure amplitudes u_a and p_a. It holds $0 \leq C_\mathrm{R} \leq 1$, with $C_\mathrm{R} = 1$ for perfect wave reflection and $C_\mathrm{R} = 0$ for no wave reflection.

In flows with free-surface waves or sound waves, the ratio of the energies of the reflected wave (E_refl) to the generated wave (E_gen) is $E_\mathrm{refl}/E_\mathrm{gen} = C_\mathrm{R}^2$, since according to linear wave theory the wave energy E is $E \propto H^2$ (for free-surface waves with wave height H) or $E \propto u_\mathrm{a}^2$ and $E \propto p_\mathrm{a}^2$ (for sound waves with velocity and pressure amplitudes u_a and p_a). Thus a reflection coefficient of $C_\mathrm{R} = 10\%$ means that the forcing zone reflects 1% of the wave's energy.

For regular monochromatic waves, the superposition of the generated wave and the wave which is partially reflected at the forcing zone creates a so-called 'partial' standing wave, which can be recognized by the 'bumps' in the wave height envelope as shown in Fig. 5. The height of these 'bumps' can be used to calculate the reflection coefficient. The domain size and simulation duration should be chosen so that wave reflections have fully developed in the evaluation interval, while possible wave re-reflections (e.g. at the inlet boundary) have not yet traveled back into the evaluation interval, which was fulfilled in all simulations in this work. The approach works equally well for dispersive and non-dispersive mediums as shown in Sects. 3.1 and 3.2.

For irregular waves in non- or weakly-dispersive mediums, a wave packet can be generated. After the wave packet has fully encountered the forcing zone, the energy in the wave packet for forcing with forcing strength γ can be related to the energy for the case of perfect reflection to obtain a reflection coefficient.

For irregular waves in dispersive mediums, accurate calculation of reflection coefficients C_R requires larger computational effort for the following reasons. Due to dispersion, waves of different wavelengths travel at different speeds; thus a wave packet in a dispersive medium will not remain compact. It holds for all approaches for calculating the reflection coefficient C_R for irregular waves that the domain size and simulation duration should be chosen so that all waves of interest have passed through the forcing zone once and have fully traveled into the evaluation interval, while possible wave re-reflections (e.g. at the inlet boundary) have not yet traveled back into the evaluation interval, which was fulfilled in all simulations in this work. Thus a significantly larger domain must be used to avoid that, in the time in which the slowest wave component has traveled the desired distance, the fastest wave component has crossed the whole domain, was re-reflected at the wave-maker and enters the evaluation interval again. The larger domain size requires possibly a finer discretization to ensure that numerical discretization and iteration errors do not lead to a substantial decay of the height of the shorter wave components.

The calculation of reflection coefficients C_R according to Sects. 3.1 and 3.2 in this work is based on the above approaches, since these are comparatively simple and have a low background noise of $\approx 1\%$ for reflection coefficients with free-surface waves (see Sects. 6 to 8) and $\ll 1\%$ for flows with sound waves (see Sect. 5).

Apart from the approaches used in this work, various other methods to calculate C_R have been presented in literature. For example, in wave tank experiments it is common to record the surface elevation using two (e.g. Goda and Suzuki, 1977) or more (e.g. Mansard and Funke, 1980) wave probes, usually positioned in-line in wave propagation direction. From data analysis in the frequency domain, reflection coefficient C_R can be estimated. However, such approaches were reported to exhibit errors in the measurement of C_R of up to $8\% - 10\%$ or more (Hughes, 1993; Isaacson, 1991; Mansard

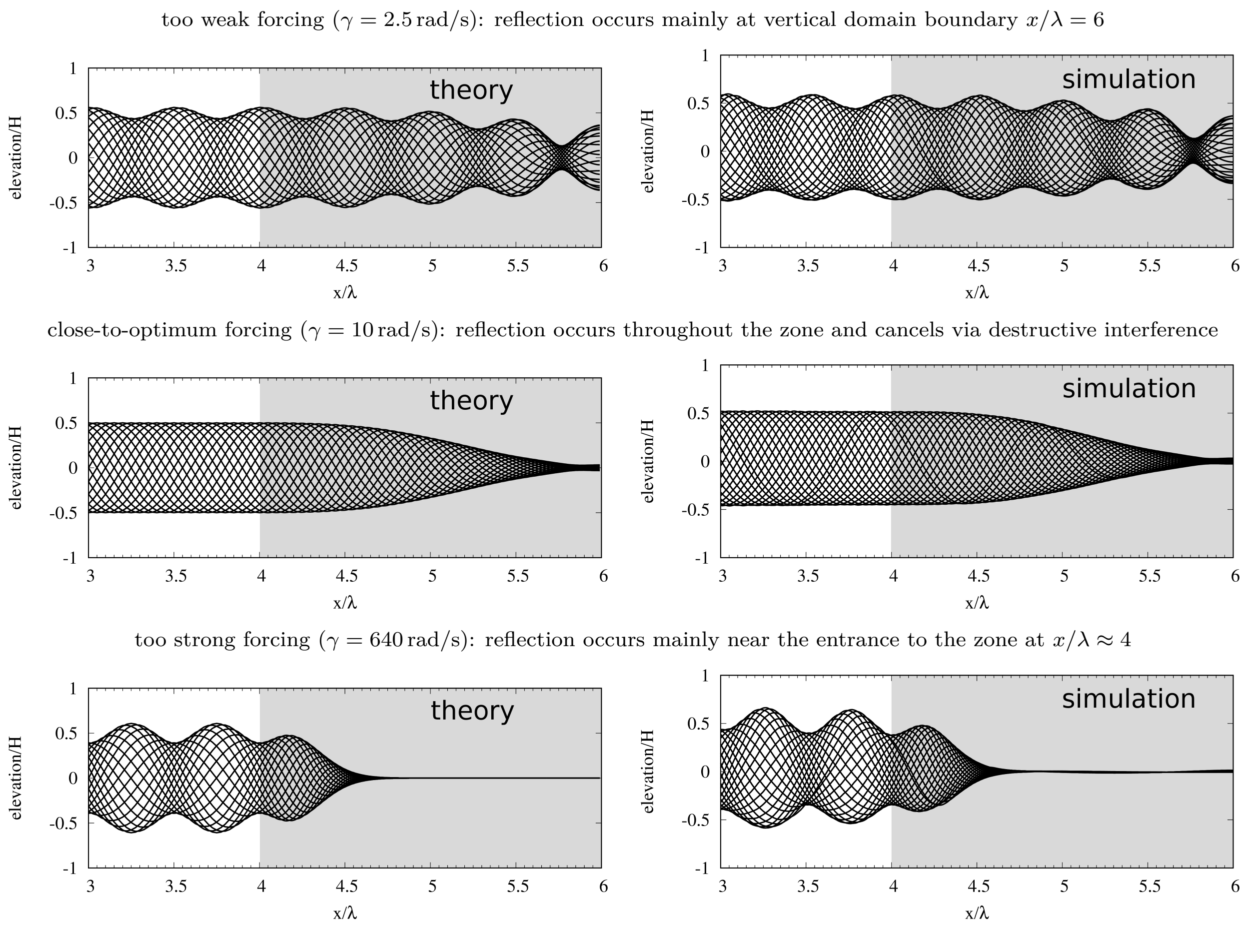

Figure 5: Theory predictions and simulation results for free-surface elevation as a function of x-location according to the results from Sect. 6.2, plotted for several equally spaced time-instances during the last simulated period; for regular waves with period $T = 1.6\,\mathrm{s}$ and wavelength $\lambda = 4\,\mathrm{m}$; with forcing zone (shaded gray area) for exponential blending via Eq. (9), zone thickness $x_\mathrm{d} = 2\lambda$ and forcing of horizontal momentum

and Funke, 1980; McKee et al., 2018), and are thus not used in the present work. For further details, the reader is referred to the above references and the references therein.

3.1 Calculating reflection coefficient C_R for free-surface waves

To calculate reflection coefficient C_R for long-crested monochromatic free-surface waves, the surface elevation in the whole domain is recorded at a sufficient number (say 80) of evenly spaced time intervals during the last simulated wave period. The evaluation interval contains all cells outside the forcing zone which are within a distance of slightly more than one wavelength to the forcing zone. The overall highest and lowest wave heights recorded in this interval are determined as H_max and H_min. From H_max and H_min, the reflection coefficient is calculated as in Ursell et al. (1960) via

$$C_\mathrm{R} = (H_\mathrm{max} - H_\mathrm{min}) \,/\, (H_\mathrm{max} + H_\mathrm{min}) \quad . \tag{34}$$

This approach contains only a small background noise of $\approx 1\%$ as seen from the results in Sects. 6 to 8, which was considered accurate enough for the present purposes.

To calculate reflection coefficient C_R for irregular free-surface-wave packets, the surface elevation in the whole domain is recorded after each simulation. Then a Fourier analysis is performed of the recording, e.g. via a fast Fourier transform (see e.g. Cooley and Tukey, 1965; Moin, 2010), to obtain the amplitudes and frequencies of the wave components.

The overall reflection coefficient C_R is then computed from the Fourier analysis results for the given forcing strength γ in relation to the Fourier analysis results for the case without forcing, i.e. $\gamma = 0$, by

$$C_\mathrm{R} = \frac{\sum_{n=1}^{N} a_n \Delta f_n|_\gamma}{\sum_{n=1}^{N} a_n \Delta f_n|_{\gamma=0}} \quad , \tag{35}$$

with the total number of frequencies N, Fourier amplitude a_n of the wave component with frequency f_n, and frequency interval $\Delta f_n = f_n - f_{n-1}$.

3.2 Calculating reflection coefficient C_R for (hydro-)acoustic waves

For regular monochromatic (hydro-)acoustic waves in 1D, reflection coefficient C_R can be computed as in Eq. (34) via maximum and minimum velocities u_max and u_min, which occur during the last simulated period for all cells outside the forcing zone which are within a given distance (here: slightly more than one wavelength) to the forcing zone:

$$C_\mathrm{R} = \frac{|u_\mathrm{max}| - |u_\mathrm{min}|}{|u_\mathrm{max}| + |u_\mathrm{min}|} \quad . \tag{36}$$

Alternatively, for cases with wave packets in 1D, 2D, or 3D, reflection coefficient C_R can be determined based on the energy in the domain at time $t = t_\mathrm{end}$ when the simulation is finished, by relating it to the energy in the domain after repeating the simulation without forcing (i.e. for $\gamma = 0$)

$$C_\mathrm{R} = \sqrt{\frac{(E_\mathrm{kin} + E_\mathrm{pot})|_{\gamma=\gamma_i,\ t=t_\mathrm{end}}}{(E_\mathrm{kin} + E_\mathrm{pot})|_{\gamma=0\ \ t=t_\mathrm{end}}}} \quad , \tag{37}$$

where γ_i is the forcing strength used in the simulation, and the kinetic and potential energies are

$$E_\mathrm{kin} = \int_V \frac{1}{2}\rho|\mathbf{v}|^2 \ \mathrm{d}V \quad , \quad E_\mathrm{pot} = \int_V \frac{1}{2}\frac{p^2}{\rho c^2} \ \mathrm{d}V \quad , \tag{38}$$

with density ρ, velocity vector $\mathbf{v} = (u, v, w)^\mathrm{T}$, pressure p relative to reference pressure, phase velocity $c = \lambda/T$ of the wave, and control volume V; see e.g. Lerch et al. (2009) for a detailed derivation. The domain size and simulation duration should be chosen so that at $t = t_\mathrm{end}$ the whole wave packet has passed through the forcing zone once, which was fulfilled in all calculations in this work.

For wave trains of arbitrary length in 1D, 2D, or 3D, another option is to obtain reflection coefficient C_R based on the maximum energy inside a certain domain part in a time interval after the wave train has passed once through the forcing zone (e.g. $\Delta t_1 = \{t \in \mathbb{R}\,|\,t_{1,\mathrm{start}} \leq t \leq t_{1,\mathrm{end}}\}$), by relating it to the energy in the same domain part during some earlier time interval of the simulation (e.g. $\Delta t_0 = \{t \in \mathbb{R}\,|\,t_{0,\mathrm{start}} \leq t \leq t_{0,\mathrm{end}}\}$), when the wave train has been fully generated but has not yet encountered any forcing zone. The domain part used for evaluation can e.g. comprise all cells outside the forcing zone which are within a given distance to the forcing zone, e.g. when investigating forcing zones which simultaneously generate out-going waves and damp waves that enter the zone as in Sect. 5.7, but it can also comprise the whole domain[8] which would be an option e.g. for short wave packets. Thus the reflection coefficient is

$$C_\mathrm{R} = \sqrt{\frac{\max\left(E_\mathrm{kin} + E_\mathrm{pot}|_{\gamma,\,\Delta t_1}\right)}{\max\left(E_\mathrm{kin} + E_\mathrm{pot}|_{\gamma=0,\,\Delta t_0}\right)}} \quad , \tag{39}$$

with E_kin and E_pot according to Eq. (38).

[8]It is recommended to use Eq. (39) only when using Eq. (37) is not feasible. This is because in flow simulations, discretization and iteration errors can accumulate over time, and thus dissipate wave energy. Therefore, Eq. (39) requires a sufficiently fine discretization, so that the energy loss due to numerical errors is negligible between the first and the second time interval used for evaluation of the energies; assume e.g. that a coarse discretization is used, so that there is a 10% loss of wave energy in the domain between these time intervals, then for full reflection the approach would give $C_\mathrm{R} = 0.99$ instead of the correct value $C_\mathrm{R} = 1$. Since Eq. (37) evaluates all energies at the same time, the effects of discretization and iteration errors are similar in all simulations and hence do not affect the calculation of reflection coefficient C_R.

4 Theory for predicting reflection coefficients for forcing zones

Key findings

- Waves are reflected at every location within the forcing zone where $\nabla b(\mathbf{x}) \neq 0$
- A theory is derived which predicts reflection coefficients for forcing zones for 1D-wave-propagation of free-surface waves and (hydro-)acoustic waves
- The theory is derived to hold for all continuous or discontinuous blending functions $b(\mathbf{x})$
- This is achieved by converting continuous blending to a piece-wise constant blending; with decreasing piece-size the theory solution converges quickly towards the solution for continuous blending
- The theory is extended to cover oblique wave incidence into the forcing zone for 2D- and 3D-wave-propagation

In this section, an analytical solution to predict reflection coefficients for forcing zones is derived. This theory can be used to optimally tune the case-dependent parameters of forcing zones before performing the flow simulations. The theory is based on the assumptions that waves are reflected *everywhere within the forcing zone* where $\nabla b(\mathbf{x}) \neq 0$, which was confirmed by the results from flow simulations in Sects. 5 to 8, and Appendix A.

In practice, many different blending functions $b(\mathbf{x})$ can be used as indicated in Sect. 2. Instead of deriving analytical solutions for each possible continuous blending function $b(\mathbf{x})$, the following theory is derived to hold with good approximation for every continuous or discontinuous blending function $b(\mathbf{x})$. This is achieved by replacing the possibly continuous blending function $b(\mathbf{x})$ by a piece-wise constant blending function $b(\mathbf{x})$, as illustrated in Fig. 6.

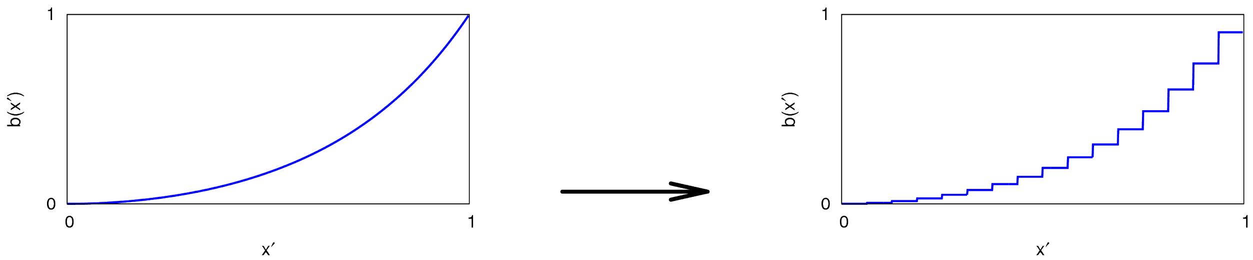

Figure 6: Replace continuous by piece-wise constant blending function $b(x')$; x' is the location in wave propagation direction, with $x' = 0$ at the entrance to the forcing zone and $x' = 1$ at the domain boundary to which the forcing zone is attached

Sections 4.1 to 4.3 derive the theory for long-crested (or 1D-) wave propagation for free-surface waves and (hydro-)acoustic waves. Section 4.4 demonstrates that the theory solution for piece-wise constant blending $b(\mathbf{x})$ quickly converges towards the solution for the continuous blending function $b(\mathbf{x})$, which agrees with findings from Sects. 5 to 8 that, for practical discretizations, the forcing zone behavior in the flow simulations was found to be independent of the time-step size, the mesh size, as well as the choice and order of the discretization scheme. Finally, Sect. 4.5 extends the 1D-theory to 2D and 3D to cover oblique wave incidence into the forcing zone.

4.1 1D-theory for predicting forcing zone behavior in flows with free-surface waves

This section considers the propagation of long-crested free-surface waves. As illustrated in Fig. 7, the waves are generated at $x = 0$, and travel towards boundary $x = L_x$, to which a forcing zone with thickness x_d is attached. The coordinate system origin lies at the level of the undisturbed free surface on the wave generating boundary as illustrated in Fig. 7. The x-direction points in wave propagation direction and the z-direction is normal to the undisturbed free surface pointing away from the liquid phase.

Outside the forcing zone, the waves fulfill the one-dimensional wave equation

$$\psi_{tt} = c^2 \psi_{xx} \quad , \tag{40}$$

with location x in wave propagation direction, velocity stream function ψ, and phase velocity c.

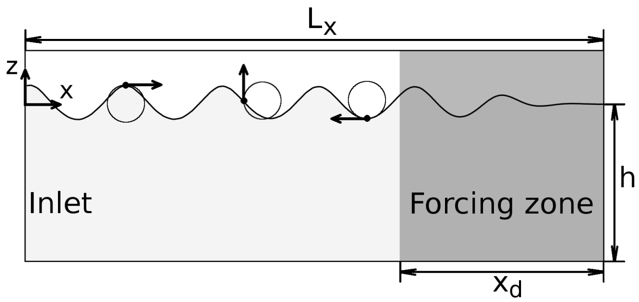

Figure 7: Solution domain filled with air (white) and water (light gray, water depth h), wave-maker at $x = 0$ and forcing zone (shaded dark gray) with thickness x_d; three fluid particles (black dots) are sketched with their particle paths (circles) and velocity vectors (arrows)

According to linear wave theory in the complex plane, the velocity stream function for an undamped wave is

$$\psi = \frac{H\omega}{2k}\frac{\sinh(k(z+h))}{\sinh(kh)}\mathrm{e}^{i(-\omega t+kx)} \quad , \tag{41}$$

with wave height H, angular wave frequency $\omega = 2\pi/T$, wave period T, wave number $k = 2\pi/\lambda$, wavelength λ, and water depth h. Horizontal and vertical velocity components u and w are

$$u = \psi_z \quad ,$$

$$w = -\psi_x \quad .$$

Horizontal and vertical particle displacements $\mathcal{X}$ and $\mathcal{Z}$ are

$$\mathcal{X} = i\frac{H}{2}\frac{\cosh(k(z+h))}{\sinh(kh)}\mathrm{e}^{i(-\omega t+kx)} \quad , \tag{42}$$

$$\mathcal{Z} = \frac{H}{2}\frac{\sinh(k(z+h))}{\sinh(kh)}\mathrm{e}^{i(-\omega t+kx)} \quad . \tag{43}$$

Thus outside the forcing zone, Eq. (40) is equivalent to

$$\mathcal{X}_{tt} = c^2\mathcal{X}_{xx} \quad . \tag{44}$$

A detailed discussion of linear wave theory can be found e.g. in Clauss et al. (1992), McCormick (2007), and Mei et al. (1989).

4.1.1 Forcing of x-momentum

Undesired wave reflections at a domain boundary can be reduced by attaching a forcing zone to the boundary, where the horizontal particle velocity $u = \mathcal{X}_t$ is forced to a reference velocity $u = \mathcal{X}_{t,\mathrm{ref}}$

$$\mathcal{X}_{tt} = c^2\mathcal{X}_{xx} + \underbrace{\gamma b(x)(\mathcal{X}_{t,\mathrm{ref}} - \mathcal{X}_t)}_{q} \quad , \tag{45}$$

with forcing strength γ and blending function $b(x)$. The last term in Eq. (45), q, is equivalent to the forcing source term in Eq. (20). In the following, $\mathcal{X}_{t,\mathrm{ref}} = 0$ so that Eq. (45) corresponds to a wave damping zone. Further, Eq. (45) is equivalent to

$$\psi_{tt} = c^2\psi_{xx} + \gamma b(x)(\psi_{t,\mathrm{ref}} - \psi_t) \quad , \tag{46}$$

with temporal derivative of the reference stream function $\psi_{t,\mathrm{ref}} = 0$.

Inserting Eq. (41) into Eq. (40) gives the wave number *outside the forcing zone*

$$k = \sqrt{\frac{\omega^2}{c^2}} = \frac{\omega}{c} \quad . \tag{47}$$

Inserting Eq. (41) for piecewise-constant blending $b(x)$ into Eq. (46) gives the wave number *inside the forcing zone*

$$k = \sqrt{\frac{\omega^2}{c^2} + i\frac{\omega\gamma b(x)}{c^2}} \quad . \tag{48}$$

Thus inside the forcing zone, the wave number contains an additional imaginary part which damps the wave amplitude but does not change the wavelength.

The following procedure is taken to analytically determine the reflection coefficient for a wave entering a forcing zone according to Eqs. (40) and (46); the approach is somewhat analogous to the way in which forcing source terms are applied in numerical flow simulations on finite grids.

The solution domain is discretized into a finite number of cells as illustrated in Fig. 8. Each cell j corresponds to a forcing zone, within which the stream function is given by ψ_j, and the complex wave number k_j has a constant value. For this, $b(x)$ is evaluated at the cell center:

$$k_j = \sqrt{\frac{\omega^2 + i\omega\gamma b\left(\sum_{n=1}^{j-1} x_{\mathrm{d}_n} + \frac{1}{2}x_{\mathrm{d}_j}\right)}{c^2}} \quad , \tag{49}$$

with thickness $x_{\mathrm{d},j}$ of zone j; $x_{\mathrm{d},j}$ is equivalent to the size of the cell in x-direction. Thus the damping is constant within every zone. Reflection and transmission may occur at every interface between two cells.

The benefit of this approach is that even non-continuous blending functions and the influence of the discretization can be considered. With increasing resolution, the theoretical results are expected to converge to the solution of the continuous problem. The latter is not derived here, since for practical purposes only the analytical solution to the discretized problem is of interest. In this manner, the problem remains linear and the solution can be derived as follows.

Consider a wave propagating in positive x-direction. The wave is generated at $x = 0$ following the coordinate system in Fig. 8. Let the stream function at $x = 0$ be

$$\psi_0 = \frac{H\omega}{2k_0}\frac{\sinh(k_0(z+h))}{\sinh(k_0 h)}\mathrm{e}^{i(-\omega t)} \quad , \tag{50}$$

with wave height H, angular wave frequency ω, wave number k_0, vertical coordinate z, and time t. Set the transmission coefficient $C_{\mathrm{T}_0} = 1$ and the reflection coefficient $C_{\mathrm{R}_0} = 0$, thus the 'inlet' boundary is perfectly transparent, and waves propagating through it in negative x-direction will be fully transmitted without reflection.

For illustration, a domain with 4 zones is depicted in Fig. 8. Let the wave number $k_1 = 2\pi/\lambda_1$ within zone 1 equal the wave number $k_0 = 2\pi/\lambda_0$ of the wave generated at $x = 0$, where λ_0 and λ_1 are the corresponding wavelengths. Thus within the first zone $0 \leq x \leq x_{\mathrm{d}_1}$, there is no wave damping, i.e. $q(x) = 0$. At the end of the domain, i.e. at $x = \sum_{n=1}^{4} x_{\mathrm{d}_n}$, the boundary is perfectly reflecting (a typical 'wall boundary condition' in computational fluid dynamics), so the transmission coefficient $C_{\mathrm{T}_4} = 0$ and the reflection coefficient $C_{\mathrm{R}_4} = 1$. Within each zone in zones 2 to 4, the damping is constant, i.e. $q(x) = q_j = -\gamma b(\sum_{n=1}^{j-1} x_{\mathrm{d}_n} + \frac{1}{2}x_{\mathrm{d}_j})\mathcal{X}_t$, yet q_2 to q_4 may be of different magnitude, which is indicated through the different shading of the zones in Fig. 8.

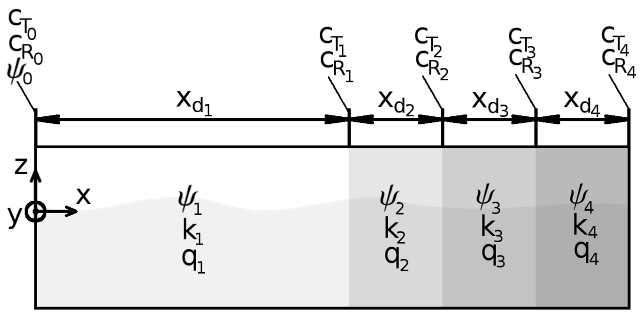

Figure 8: Example of a solution domain decomposed into 4 zones; within each zone j of thickness $x_{\mathrm{d},j}$ holds stream function ψ_j, wave number k_j and damping term q_j; at each interface j between two zones, transmission and reflection coefficients are C_{T_j} and C_{R_j}

By requiring that the particle displacements and velocities must be continuous at every interface between two zones, as they should be at the interfaces between two cells in a flow simulation, the periodic solution is obtained. As Eqs. (59) to (62) show, this requirement is equivalent to requiring that the velocity stream function ψ and its spatial derivative

ψ_x are continuous in the whole forcing zone.

For a domain with j zones, the solution for the velocity stream function $\psi(x)$ within zone $j > 0$ can be written as a sum of a right-going (incoming) and a left-going (reflected) wave component

$$\psi_j = \psi_0 \left(\prod_{n=0}^{j-1} C_{\mathrm{T}_n} \right) \cdot \left[\mathrm{e}^{i\left(\sum_{n=1}^{j-1} k_n x_{\mathrm{d}_n} + k_j \left(x - \sum_{n=1}^{j-1} x_{\mathrm{d}_n}\right)\right)} \right.$$
$$\left. - C_{\mathrm{R}_j} \mathrm{e}^{i\left(\sum_{n=1}^{j-1} k_n x_{\mathrm{d}_n} + k_j 2 x_{\mathrm{d}_j} - k_j \left(x - \sum_{n=1}^{j-1} x_{\mathrm{d}_n}\right)\right)} \right] \quad , \tag{51}$$

with ψ_0 according to Eq. (50). The derivative of ψ_j with respect to wave propagation direction x is thus

$$\psi_{x,j} = i k_j \psi_0 \left(\prod_{n=0}^{j-1} C_{\mathrm{T}_n} \right) \cdot \left[\mathrm{e}^{i\left(\sum_{n=1}^{j-1} k_n x_{\mathrm{d}_n} + k_j \left(x - \sum_{n=1}^{j-1} x_{\mathrm{d}_n}\right)\right)} \right.$$
$$\left. + C_{\mathrm{R}_j} \mathrm{e}^{i\left(\sum_{n=1}^{j-1} k_n x_{\mathrm{d}_n} + k_j 2 x_{\mathrm{d}_j} - k_j \left(x - \sum_{n=1}^{j-1} x_{\mathrm{d}_n}\right)\right)} \right] \quad . \tag{52}$$

Requirement 1: At the interface between zones j and $j+1$, the solution for the zone on the left, i.e. ψ_j, must equal the solution for the zone on the right, i.e. ψ_{j+1}:

$$\left[\psi_j = \psi_{j+1}\right]_{x=\sum_{n=1}^{j} x_{\mathrm{d}_n}} \quad . \tag{53}$$

Inserting Eq. (51) into Eq. (53), dividing by

$$\psi_0 \left(\prod_{n=0}^{j-1} C_{\mathrm{T}_n} \right) \left[\mathrm{e}^{i\left(\sum_{n=1}^{j-1} k_n x_{\mathrm{d}_n}\right)} \right] \quad ,$$

inserting

$$x - \sum_{n=1}^{j-1} x_{\mathrm{d}_n} = x_{\mathrm{d}_j} \quad , \quad x - \sum_{n=1}^{j} x_{\mathrm{d}_n} = 0 \quad ,$$

and rearranging for C_{T_j} gives

$$\boxed{C_{\mathrm{T}_j} = \frac{1 - C_{\mathrm{R}_j}}{1 - C_{\mathrm{R}_{j+1}} \mathrm{e}^{i\left(k_{j+1} 2 x_{\mathrm{d}_{j+1}}\right)}} \quad .} \tag{54}$$

Requirement 2: At the interface between zones j and $j+1$, the spatial derivative with respect to x of the solution for the zone on the left, i.e. $\partial\psi_j/\partial x = \psi_{x,j}$, must equal the spatial derivative with respect to x of the solution for the zone on the right, i.e. $\partial\psi_{j+1}/\partial x = \psi_{x,j+1}$:

$$\left[\psi_{x,j} = \psi_{x,j+1}\right]_{x=\sum_{n=1}^{j} x_{\mathrm{d}_n}} \quad . \tag{55}$$

Inserting Eq. (52) into Eq. (55), dividing by

$$i\psi_0 \left(\prod_{n=0}^{j-1} C_{\mathrm{T}_n} \right) \left[\mathrm{e}^{i\left(\sum_{n=1}^{j-1} k_n x_{\mathrm{d}_n}\right)} \right] \quad ,$$

inserting C_{T_j}, and setting

$$\beta_{j+1} = \frac{1 + C_{\mathrm{R}_{j+1}} \mathrm{e}^{i\left(k_{j+1} 2 x_{\mathrm{d}_{j+1}}\right)}}{1 - C_{\mathrm{R}_{j+1}} \mathrm{e}^{i\left(k_{j+1} 2 x_{\mathrm{d}_{j+1}}\right)}} \quad . \tag{56}$$

gives

$$C_{\mathrm{R}_j} = \frac{k_{j+1}\beta_{j+1} - k_j}{k_{j+1}\beta_{j+1} + k_j} \quad , \tag{57}$$

For practical purposes, mainly the 'global' reflection coefficient C_R is of interest, which is the ratio of the amplitude of the wave, which is reflected back into the solution domain, to the amplitude of the wave, which enters the forcing zone. The global reflection coefficient C_R corresponds to the magnitude of C_{R_j} at the interface to the forcing zone, which depends on all C_{R_j} inside the whole forcing zone. So if the forcing zone starts at zone 1, then

$$C_\mathrm{R} = |C_{\mathrm{R}_1}| = \sqrt{\mathrm{Re}\{C_{\mathrm{R}_1}\}^2 + \mathrm{Im}\{C_{\mathrm{R}_1}\}^2} \quad , \tag{58}$$

where $\mathrm{Re}\{X\}$ and $\mathrm{Im}\{X\}$ denote the real and the imaginary part of the complex number X.

Since for the complex exponential functions in this case the order of derivatives and integrals can be exchanged, when setting integration constants to zero one obtains

$$u_j = \psi_{z,j} = k_0 \frac{\cosh(k_0(z+h))}{\sinh(k_0(z+h))}\psi_j \quad , \tag{59}$$

$$\mathcal{X}_j = \int \psi_{z,j}\,\mathrm{d}t = \frac{k_0}{-i\omega}\frac{\cosh(k_0(z+h))}{\sinh(k_0(z+h))}\psi_j \quad , \tag{60}$$

$$w_j = -\psi_{x,j} \quad , \tag{61}$$

$$\mathcal{Z}_j = \int -\psi_{x,j}\,\mathrm{d}t = \frac{1}{i\omega}\psi_{x,j} \quad . \tag{62}$$

Thus ψ_j, $\psi_{x,j}$ and and all particle displacements and velocities are continuous throughout the domain.

The theory is implemented in a computer program, which is made publicly available as free software. The source code and manual can be downloaded from:
`https://github.com/wave-absorbing-layers/absorbing-layer-for-free-surface-waves`

4.1.2 Forcing of volume fraction α, x-, y- or z-momentum and combinations thereof

In Sect. 4.1, the theory for predicting reflection coefficients for forcing zones was derived for forcing of x-momentum[9]. The present section extends the theory to hold for applying forcing source terms in the equations for volume fraction α as well as y- and z-momentum, and combinations thereof. This is achieved by relating the forcing strength γ to the wave energy component(s) associated with the governing equations to which the source terms are applied: forcing of x-momentum acts directly on the horizontal component $E_{\mathrm{kin},x}$ of the kinetic wave energy, forcing of z-momentum acts directly on the vertical component $E_{\mathrm{kin},z}$ of the kinetic wave energy, and forcing of volume fraction α acts directly on the potential wave energy E_pot.

According to linear wave theory, the average energy $\bar{E} = \int_0^\lambda \int_{-h}^\eta \int_0^{1\,\mathrm{m}} E\,\mathrm{d}y\mathrm{d}z\mathrm{d}x$ in a regular free-surface wave traveling in x-direction can be subdivided as

$$\bar{E} = \bar{E}_\mathrm{pot} + \underbrace{\bar{E}_\mathrm{kin}}_{=\bar{E}_{\mathrm{kin},x}+\bar{E}_{\mathrm{kin},z}} \quad , \tag{63}$$

with free-surface elevation η measured from the still water level $z = 0$, water depth h, average potential and kinetic energy $\bar{E}_\mathrm{pot}$ and $\bar{E}_\mathrm{kin}$, and the x- and z-component $\bar{E}_{\mathrm{kin},x}$ and $\bar{E}_{\mathrm{kin},z}$ of the average kinetic energy.

[9] In this thesis, the following terms will be used synonymously: forcing of x_i-momentum, forcing of velocity component u_i, applying forcing source terms in the governing equation for momentum conservation in x_i-direction.

Then, for all water depths holds[10]

$$\bar{E}_{\text{pot}} = \bar{E}_{\text{kin}} \quad , \tag{64}$$

$$\bar{E}_{\text{kin},x} = \left(\frac{\sinh(2kh) + 2kh}{\sinh(2kh) - 2kh}\right) \bar{E}_{\text{kin},z} \quad , \tag{65}$$

with wave number k and water depth h.

For deep-water conditions (water depth $h \geq 0.5\lambda$), Eq. (65) simplifies to

$$\bar{E}_{\text{kin},x} = \bar{E}_{\text{kin},z} = \frac{1}{2}\bar{E}_{\text{kin}} \quad , \tag{66}$$

while for shallow-water conditions ($h \leq 0.05\lambda$) holds[11]

$$\bar{E}_{\text{kin},x} \gg \bar{E}_{\text{kin},z} \quad , \quad \text{so} \quad \bar{E}_{\text{kin},x} \approx \bar{E}_{\text{kin}} \quad . \tag{67}$$

The equations for volume fraction α and fluid momentum in horizontal and vertical directions x and z are coupled, so assume that forcing of one equation acts on the other equations immediately[12]. Thus for example the whole wave can be damped by applying forcing source terms to just a single governing equation, as demonstrated e.g. in Sect. 6.2 and 6.3.

To obtain the same reflection coefficient C_{R} when applying forcing source terms to different governing equations, require

$$\gamma_j \sum E_j = \text{const.} \quad , \tag{68}$$

where j denotes the equations to which forcing is applied (here: x for forcing of x-momentum, z for forcing of z-momentum, α for forcing of volume fraction α, or combinations of these), forcing strength γ_j, and $\sum E_j$ is the sum of the wave energy components associated with these equations (here: $\bar{E}_{\text{kin},x}$ for forcing of x-momentum, $\bar{E}_{\text{kin},z}$ for forcing of z-momentum, and $\bar{E}_{\text{pot}}$ for forcing of volume fraction α).

As an example for the application of Eq. (68), forcing of x-momentum with forcing strength γ is equivalent to forcing of volume fraction α, x-, and z-momentum with a forcing strength $\gamma_{\alpha xz}$, when holds

$$\gamma = \left(\frac{\bar{E}_{\text{kin},x} + \bar{E}_{\text{kin},z} + \bar{E}_{\text{pot}}}{\bar{E}_{\text{kin},x}}\right) \gamma_{\alpha xz} \quad . \tag{69}$$

From Eq. (69) follows that in *deep water*, forcing of volume fraction α, x-, and z-momentum with a forcing strength $\gamma_{\alpha xz}$ is equivalent to forcing of x-momentum with forcing strength γ when

$$\gamma = 4\gamma_{\alpha xz} \quad , \tag{70}$$

since in deep water $\left(\bar{E}_{\text{kin},x} + \bar{E}_{\text{kin},z} + \bar{E}_{\text{pot}}\right) = 4\bar{E}_{\text{kin},x}$.

[10] The linear wave theory solution for arbitrary water depth h of horizontal and vertical velocity amplitudes are $u_a = \omega \frac{H}{2} \frac{\cosh(kz+kh)}{\sinh(kh)}$ and $w_a = \omega \frac{H}{2} \frac{\sinh(kz+kh)}{\sinh(kh)}$, with wave height H, angular wave frequency ω, and wave number k. Therefore the ratio of the average kinetic energy components in vertical and horizontal direction is

$$\frac{\bar{E}_{\text{kin},z}}{\bar{E}_{\text{kin},x}} \propto \frac{\frac{1}{h}\int_{-h}^{0} w_{\text{a}}^2 \,\text{d}z}{\frac{1}{h}\int_{-h}^{0} u_{\text{a}}^2 \,\text{d}z} = \frac{\frac{1}{h}\int_{-h}^{0} \left(\omega \frac{H}{2} \frac{\sinh(kz+kh)}{\sinh(kh)}\right)^2 \text{d}z}{\frac{1}{h}\int_{-h}^{0} \left(\omega \frac{H}{2} \frac{\cosh(kz+kh)}{\sinh(kh)}\right)^2 \text{d}z} = \frac{\sinh(2kh) - 2kh}{\sinh(2kh) + 2kh} \quad .$$

[11] According to linear wave theory, the horizontal and vertical velocity components in a shallow water wave are $u = \omega \frac{H}{2} \frac{1}{kh} \sin(kx - \omega t)$ and $w = -\omega \frac{H}{2} \left(\frac{z+h}{h}\right) \cos(kx - \omega t)$, with wave height H, wavelength λ, wave period T, water depth $h \leq 0.05\lambda$, angular wave frequency $\omega = 2\pi/T$, wave number $k = 2\pi/\lambda$, time t and horizontal and vertical coordinates x and z. Further holds for the kinetic energy components $\bar{E}_{\text{kin},x_i} \propto \int_{-h}^{0} u_{i,\text{a}}^2 \,\text{d}z$. The squared velocity amplitudes u_{a} and w_{a} averaged over the water depth h are $\frac{1}{h}\int_{-h}^{0} u_{\text{a}}^2 \,\text{d}z = \frac{1}{h}\int_{-h}^{0} \left(\omega \frac{H}{2} \frac{1}{kh}\right)^2 \text{d}z \geq \frac{\omega^2 H^2}{0.04\pi^2}$ and $\frac{1}{h}\int_{-h}^{0} w_{\text{a}}^2 \,\text{d}z = \frac{1}{h}\int_{-h}^{0} \left(\omega \frac{H}{2}\left(\frac{z+h}{h}\right)\right)^2 \text{d}z = \frac{\omega^2 H^2}{12}$. Thus integrated over one wavelength holds

$$\frac{\bar{E}_{\text{kin},z}}{\bar{E}_{\text{kin},x}} = \frac{\int_{-h}^{0} w_{\text{a}}^2 \,\text{d}z}{\int_{-h}^{0} u_{\text{a}}^2 \,\text{d}z} \leq \frac{\omega^2 H^2 0.04\pi^2}{12\omega^2 H^2} < 3.3\% \quad ,$$

so $\bar{E}_{\text{kin},x} \gg \bar{E}_{\text{kin},z}$ and $\bar{E}_{\text{kin},x} \approx \bar{E}_{\text{pot}}$.

[12] The results in Sects. 6 to 8 demonstrate that this assumption holds with good approximation. An exception is forcing of z-momentum if the forcing source terms change rapidly within the forcing zone, i.e. for comparatively thin forcing zones (say $x_{\text{d}} < 0.5\lambda$) or for significantly larger-than-optimum forcing strength γ (when most of the wave is reflected close to the entrance of the forcing zone, see e.g. Fig. 5 bottom); in this case, the assumption is not entirely fulfilled and reflection coefficients C_{R} were lower than theory predictions, cf. Sects. 6.3 and 6.5.

In contrast, in *shallow water* holds

$$\gamma = 2\gamma_{\alpha x z} \quad , \tag{71}$$

since in shallow water $\left(\bar{E}_{\mathrm{kin},x} + \bar{E}_{\mathrm{kin},z} + \bar{E}_{\mathrm{pot}}\right) = 2\bar{E}_{\mathrm{kin},x}$, as follows from Eqs. (63) to (67). Thus when simultaneously forcing α, x- and z-momentum, e.g. each with forcing strength $\gamma = 20\,\mathrm{rad/s}$, then the theoretical prediction for the reflection coefficient C_{R} is the same as when using the theory from Sect. 4.1.1 with $\gamma = 80\,\mathrm{rad/s}$ for deep-water conditions or $\gamma = 40\,\mathrm{rad/s}$ for shallow-water conditions.

Following the same procedure yields[13]

$$\gamma = \left(\frac{\bar{E}_{\mathrm{kin},x}}{\bar{E}_{\mathrm{kin},x}}\right)\gamma_x = \left(\frac{\bar{E}_{\mathrm{kin},z}}{\bar{E}_{\mathrm{kin},x}}\right)\gamma_z = \left(\frac{\bar{E}_{\mathrm{kin},x} + \bar{E}_{\mathrm{kin},z}}{\bar{E}_{\mathrm{kin},x}}\right)\gamma_{xz} = \left(\frac{\bar{E}_{\mathrm{pot}}}{\bar{E}_{\mathrm{kin},x}}\right)\gamma_\alpha = \left(\frac{\bar{E}_{\mathrm{kin},x} + \bar{E}_{\mathrm{kin},z} + \bar{E}_{\mathrm{pot}}}{\bar{E}_{\mathrm{kin},x}}\right)\gamma_{\alpha x z} \quad . \tag{72}$$

For deep water conditions, this corresponds to

$$\gamma = \gamma_x = \gamma_z = 2\gamma_{xz} = 2\gamma_\alpha = 4\gamma_{\alpha x z} \quad , \tag{73}$$

whereas for shallow water conditions, this corresponds to

$$\gamma = \gamma_x = \gamma_{xz} = \gamma_\alpha = 2\gamma_{\alpha x z} \quad . \tag{74}$$

The case of forcing of z-momentum deserves special attention, since it is the default approach for wave damping zones in several flow solvers at the time of writing: In shallower water depths, the optimum value for forcing strength γ_z can then be several orders of magnitude larger than the optimum value of forcing strength γ for forcing of x-momentum (cf. Eq. (72)), since the vertical kinetic wave energy becomes small compared to the horizontal kinetic energy as visualized in Fig. 9. This is discussed in more detail in Sect. 6.7.

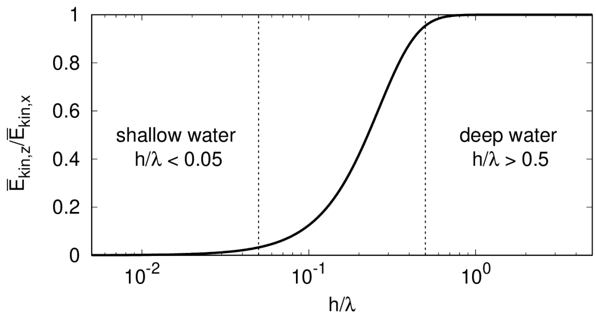

Figure 9: Ratio of vertical ($\bar{E}_{\mathrm{kin},z}$) to horizontal ($\bar{E}_{\mathrm{kin},x}$) components of the average kinetic wave energy as a function of water depth h per wavelength λ, calculated based on linear wave theory via Eq. (65)

To sum up, the optimum value of forcing strength γ can depend on which governing equations the forcing is applied to[14]. This is considered in the open-source computer program for evaluating the theory, mentioned in Sect. 4.1.

4.2 Extension of 1D-theory to relaxation zones

To extend the theory from Sect. 4.1 to *relaxation zones* as described in Sect. 2.3, multiply Eqs. (23) and (24) by the factor $1/\left(1 - b(\mathbf{x})\right)$. Then the relaxation can be interpreted as a forcing, where the source terms in Eqs. (18) and (19) are

$$q_i = \frac{b(\mathbf{x})}{\tau(1 - b(\mathbf{x}))}(u_{i,\mathrm{ref}} - u_i) \quad , \tag{75}$$

[13] When rotating the coordinate system around the z-axis from (x, y, z) to (x', y', z) so that the wave propagation direction has both an x'- and y'-component, then replace $\bar{E}_{\mathrm{kin},x}$ by $\bar{E}_{\mathrm{kin},x'} + \bar{E}_{\mathrm{kin},y'}$ in the numerator in Eq. (72), for example via $\gamma = \left(\frac{\bar{E}_{\mathrm{kin},x'} + \bar{E}_{\mathrm{kin},y'} + \bar{E}_{\mathrm{kin},z} + \bar{E}_{\mathrm{pot}}}{\bar{E}_{\mathrm{kin},x}}\right)\gamma_{\alpha x' y' z}$, and therefore $\gamma_{\alpha x' y' z} = \gamma_{\alpha x z}$ since $\bar{E}_{\mathrm{kin},x'} + \bar{E}_{\mathrm{kin},y'} = \bar{E}_{\mathrm{kin},x}$.

[14] It is not recommended to apply forcing in a governing equation which is associated with a wave energy component which is zero or negligible compared to the other energy components. For example, a long-crested wave traveling in x-direction has no velocity components in y-direction and thus no corresponding kinetic energy $\bar{E}_{\mathrm{kin},y} = 0$. Therefore, forcing of y-momentum towards zero (i.e. $v_{\mathrm{ref}} = 0$ in Eq. (20)) with the intention of damping these waves would have no effect. Another example is forcing of vertical (i.e. z-) momentum in shallow water; when $\bar{E}_{\mathrm{kin},z}/\bar{E}_{\mathrm{kin},x}$ approaches zero (cf. Fig. 9), at some point the optimum forcing strength γ becomes so large (cf. Eq. (72)) that stability problems or simulation blow-up might occur.

$$q_\alpha = \frac{b(\mathbf{x})}{\tau(1-b(\mathbf{x}))}(\alpha_{\mathrm{ref}} - \alpha) \quad , \tag{76}$$

with blending function $b(\mathbf{x})$, relaxation parameter τ, velocity u_i, reference velocity $u_{i,\mathrm{ref}}$, volume fraction α, and reference volume fraction α_{ref}. Thus by setting γ in Eqs. (46) to (58) to

$$\gamma = \frac{1}{\tau(1-b(\mathbf{x}))} \quad , \tag{77}$$

the theory is extended to relaxation zones.

Note that unless $\tau = 0$, Eqs. (75) to (77) do not become singular, since for the piecewise-constant blending in Eq. (49) $b(\mathbf{x})$ is evaluated at the center of each segment and thus is always < 1. The exception to this statement is $b(\mathbf{x}) = 1$, which is the only case for which relaxation zones according to Eqs. (23) and (24) behave differently from the otherwise equivalent formulation in Eqs. (75) to (77). However, this case is not of practical interest, since $b(\mathbf{x}) = 1$ would mean that within the relaxation zone there is no interaction between the reference solution and the governing equations for fluid flow, since the latter equal zero and the solution inside the relaxation zone equals the prescribed reference solution. Thus the entrance to the relaxation zone would behave like a fully reflective velocity inlet boundary condition, but with an increased computational effort.

A simple computer program to evaluate the theory for predicting the relaxation zone behavior has been published as free software.

The source code and manual can be downloaded from the following link:
`https://github.com/wave-absorbing-layers/relaxation-zones-for-free-surface-waves`

4.3 1D-theory for predicting forcing zone behavior in flows with (hydro-)acoustic waves

(Hydro-)acoustic, one-dimensional wave propagation with forcing of fluid momentum follows with good approximation the wave equation

$$\chi_{tt} = c^2 \chi_{xx} + \gamma b(x)(\chi_{t,\mathrm{ref}} - \chi_t) \quad . \tag{78}$$

with particle displacement χ, velocity $u = \chi_t$, and speed of sound c. The wave equation describes waves e.g. in an ideal gas, liquid or solid under isothermal conditions and is derived e.g. in Feynman et al. (2011). The forcing term is formulated in analogy to Eq. (45) with forcing strength γ, blending function $b(x)$ and reference velocity $u_{\mathrm{ref}} = \chi_{t,\mathrm{ref}}$. In the following, set $\chi_{t,\mathrm{ref}} = 0\,\frac{\mathrm{m}}{\mathrm{s}}$ to damp the waves within the zone.

The derivation of the 1D-theory for (hydro-)acoustic waves follows the derivation in Sect. 4.1 except that instead of the velocity stream function, the equations for particle displacement χ_j are used to obtain the analytical solution for the reflection coefficient. Thus for a domain with j zones, the solution for the particle displacement $\chi_j(x)$ within zone $j > 0$ can be written as a sum of a right-going (incoming) and a left-going (reflected) wave component

$$\begin{aligned}\chi_j = \chi_0 \left(\prod_{n=0}^{j-1} C_{\mathrm{T}_n}\right) \Bigg[& \mathrm{e}^{i\left(\sum_{n=1}^{j-1} k_n x_{\mathrm{d}_n} + k_j \left(x - \sum_{n=1}^{j-1} x_{\mathrm{d}_n}\right)\right)} \\ & - C_{\mathrm{R}_j} \mathrm{e}^{i\left(\sum_{n=1}^{j-1} k_n x_{\mathrm{d}_n} + k_j 2 x_{\mathrm{d}_j} - k_j \left(x - \sum_{n=1}^{j-1} x_{\mathrm{d}_n}\right)\right)} \Bigg] \quad ,\end{aligned} \tag{79}$$

with the particle displacement at $x = 0$ set to

$$\chi_0 = A_0 \mathrm{e}^{-i\omega t} \quad , \tag{80}$$

with wave number k_j in zone j with thickness x_{d_j}, transmission and reflection coefficients C_{T_j} and C_{R_j}, displacement amplitude A_0, angular wave frequency $\omega = 2\pi/T$, wave period T, and time t.

Requiring that the particle displacements, their spatial derivatives, and velocities must be continuous at every interface between two adjacent zones, as they should be at the interfaces between two zones in a flow simulation, the analytical solution is obtained. This can be achieved by requiring that at the interface between zones j and $j+1$, the solution for the zone on the left, i.e. χ_j, and its spatial derivative, $\partial \chi_j / \partial x = \chi_{x,j}$, must equal the solution for the zone on the right, i.e. χ_{j+1}, and its spatial derivative, $\partial\chi_{j+1}/\partial x = \chi_{x,j+1}$, so

$$\left[\chi_j = \chi_{j+1}\right]_{x=\sum_{n=1}^{j} x_{\mathrm{d}n}} \quad , \tag{81}$$

$$\left[\chi_{x,j} = \chi_{x,j+1}\right]_{x=\sum_{n=1}^{j} x_{\mathrm{d}n}} \quad . \tag{82}$$

Thus the same equations for transmission and reflection coefficients as in Sect. 4.1 are obtained, i.e.

$$\boxed{C_{\mathrm{T}_j} = \frac{1 - C_{\mathrm{R}_j}}{1 - C_{\mathrm{R}_{j+1}} \mathrm{e}^{i\left(k_{j+1} 2 x_{\mathrm{d}_{j+1}}\right)}} \quad ,} \tag{83}$$

and

$$\boxed{C_{\mathrm{R}_j} = \frac{k_{j+1}\beta_{j+1} - k_j}{k_{j+1}\beta_{j+1} + k_j} \quad , \quad \text{with} \quad \beta_{j+1} = \frac{1 + C_{\mathrm{R}_{j+1}} \mathrm{e}^{i\left(k_{j+1} 2 x_{\mathrm{d}_{j+1}}\right)}}{1 - C_{\mathrm{R}_{j+1}} \mathrm{e}^{i\left(k_{j+1} 2 x_{\mathrm{d}_{j+1}}\right)}} \quad .} \tag{84}$$

Therefore, the particle displacements χ, their spatial derivatives χ_x, the velocity $u = \chi_t$, and the velocity potential ϕ are continuous throughout the forcing zone.

The theory is implemented in a computer program, which is made publicly available as free software. The source code and manual can be downloaded from:
`https://github.com/wave-absorbing-layers/pressure-wave-absorption`.

4.4 Convergence of the theory solution for piecewise-constant blending to the solution for continuous blending

The theory from Sects. 4.1 to 4.3 was derived by subdividing the forcing zone into n zones with constant blending $b(\mathbf{x})$ as illustrated in Fig. 10. This section demonstrates that, if n is larger than a certain threshold, then the theory results can be considered independent of n. Thus also the forcing zone behavior in flow simulations can be expected to be basically grid-independent, if the number n of grid cells, by which the forcing zone is discretized in wave propagation direction, is above the same threshold.

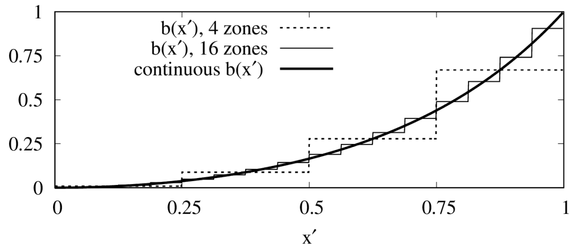

Figure 10: Blending function $b(x')$ according to Eq. (9) as a function of x'-coordinate; x' is directed in wave propagation direction and linearly scaled such that it is 0 at the entrance to the forcing zone and 1 at the boundary to which the zone is attached; for forcing zones consisting of 4 and 16 zones with piece-wise constant blending $b(x')$ and for continuous blending $b(x')$

Figure 11 shows for a subdivision into 32 zones, that the results are barely distinguishable from subdivisions into larger numbers of zones. This agrees well with findings from Fig. 16, where the wave damping was observed to be grid-independent for practical flow simulation setups (i.e. grids with at least 30 cells per wavelength).

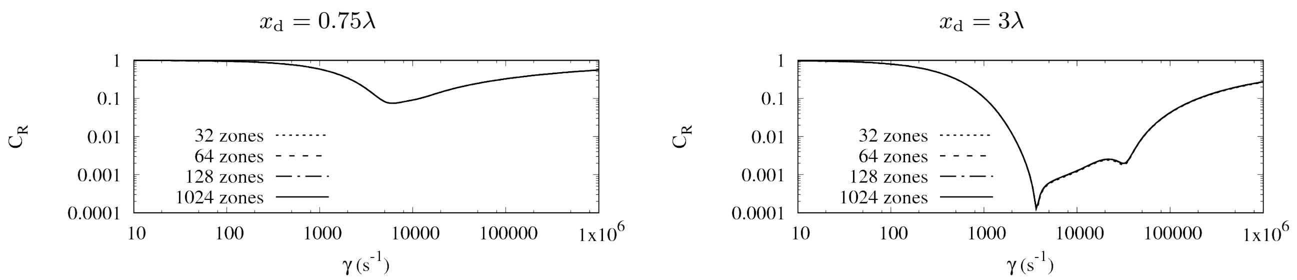

Figure 11: Theory prediction for reflection coefficient C_R as a function of forcing strength γ for waves with period $T = 0.00\overline{227}\,\mathrm{s}$; for a forcing zone according to Eq. (31) with exponential blending (Eq. (9)), zone thickness $x_\mathrm{d} = 0.75\lambda$, and $x_\mathrm{d} = 3.0\lambda$; for $b(x)$ subdivided into $n = 32$, 64, 128 and 1024 zones the average difference between the results is $< 0.08\%$ and the largest deviation from the results for $n = 1024$ is $< 0.9\%$

Figure 12 shows that for subdivision into less than 16 zones, the results differ significantly from the results for > 32 zones. This is relevant when assessing flow simulations, in which a combination of grid stretching and forcing zones is used to damp the waves; in industrial practice, these two wave damping approaches are sometimes combined with the intention to lower the computational effort and to improve the damping. However, Figs. 11 and 12 show that, if due to the grid stretching the number of grid cells per zone thickness drops below a certain threshold, then grid stretching can significantly increase reflection coefficient C_R. Based on the present results, it is recommended to have cell sizes of at most $\lambda/10$ when combining grid stretching and forcing zones.

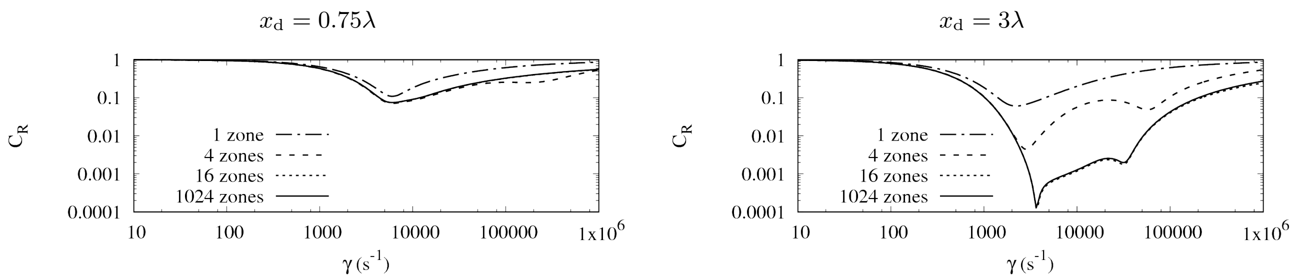

Figure 12: As Fig. 11, except that $b(x)$ is subdivided into $n = 1$, 4, 16 and 1024 zones; the average difference between the results is $< 0.23\%$ ($n = 16$), $< 4.2\%$ ($n = 4$), and $< 20\%$ ($n = 1$); the largest deviation from the results for $n = 1024$ is $< 3.4\%$ ($n = 16$), $< 27\%$ ($n = 4$), and $< 63\%$ ($n = 1$); for a subdivision into $n = 1$ and $n = 4$ zones, the results differ significantly compared to subdivisions into 16 or more zones, and reflection coefficients C_R for optimum tuning increase substantially

If the forcing zone is subdivided into a sufficient number of zones n, then the difference between the theory solutions for different n can be estimated by a Richardson-type extrapolation. Detailed information on Richardson extrapolation can be found e.g. in Ferziger and Perić (2002), Richardson (1911), or Richardson and Gaunt (1927). Say

$$A = A_\mathrm{h} + \varepsilon_\mathrm{h} \quad , \tag{85}$$

where A is the analytical solution for $n = \infty$, A_h is the analytical solution for $n = x_\mathrm{d}/h$, and ε_h is the error. Let all zones have the same thickness $x_{\mathrm{d},j} = h$, with a total forcing zone thickness of $x_\mathrm{d} = \sum_{j=1}^{n} x_{\mathrm{d},j}$. Thus when using zones of twice the thickness, i.e. $x_{\mathrm{d},j} = 2h$, one obtains

$$A = A_\mathrm{2h} + \varepsilon_\mathrm{2h} \quad , \tag{86}$$

and similar for further refinement or coarsening.

Taylor-series analysis of truncation errors suggests that the error ε_h is proportional to some power p of the zone thickness h, i.e. $\varepsilon_h \propto h^p$. It follows that the error with a twice coarser spacing is

$$\varepsilon_\mathrm{2h} = 2^p \varepsilon_\mathrm{h} \quad , \tag{87}$$

where p is the order of convergence. Setting Eqs. (85) and (86) as equal and inserting Eq. (87) leads to

$$\varepsilon_\mathrm{h} = \frac{A_\mathrm{h} - A_\mathrm{2h}}{2^p - 1} \quad . \tag{88}$$

Insert Eq. (87) into Eq. (88) written for $\varepsilon_{2\mathrm{h}}$ finally gives

$$p = \frac{\log\left(\frac{A_{2\mathrm{h}}-A_{4\mathrm{h}}}{A_{\mathrm{h}}-A_{2\mathrm{h}}}\right)}{\log(2)} \quad . \tag{89}$$

Figures 11 and 12 show that the deviation of C_{R} can differ depending on γ. Thus to estimate ε_{h} and p in Eqs. (88) and (89), set

$$A_{2\mathrm{h}} - A_{4\mathrm{h}} \approx \max\{C_{\mathrm{R},2\mathrm{h}}(\gamma) - C_{\mathrm{R},4\mathrm{h}}(\gamma)\} \quad , \tag{90}$$

$$A_{\mathrm{h}} - A_{2\mathrm{h}} \approx \max\{C_{\mathrm{R,h}}(\gamma) - C_{\mathrm{R},2\mathrm{h}}(\gamma)\} \quad , \tag{91}$$

where $C_{\mathrm{R,h}}(\gamma)$ is the reflection coefficient for zone thickness $x_{\mathrm{d},j} = h$ and forcing strength γ, and the $\max\{X(\gamma)\}$-function delivers the maximum value of X of all γ-values in the considered range (here: $10\,\mathrm{s}^{-1} \leq \gamma \leq 10^6\,\mathrm{s}^{-1}$).

Figure 13 shows, exemplarily for $b(x)$ according to Eq. (9), that the analytical solution converges with 2$^{\mathrm{nd}}$-order to the analytical solution for $n = \infty$. For the blending functions investigated in Sect. 5.3, all curves showed 2$^{\mathrm{nd}}$-order convergence (i.e. $p \to 2$ if $n \to \infty$), except constant blending ($b(x) = 1$), for which the solution naturally must be exact independent of the number of zones. It is out of the scope of this work to rigorously prove that for all possible $b(x)$ the order of convergence will be at least $p = 2$, so this is left for future research; however, the present results suggest that this is the case. Figure 13 also shows that the error estimate ε_{h} for different n decays accordingly. Thus for practical grids in flow simulations, as well as for the theory results plotted in this work, the forcing zone behavior can be assumed to be independent of the number n of zones or grid cells.

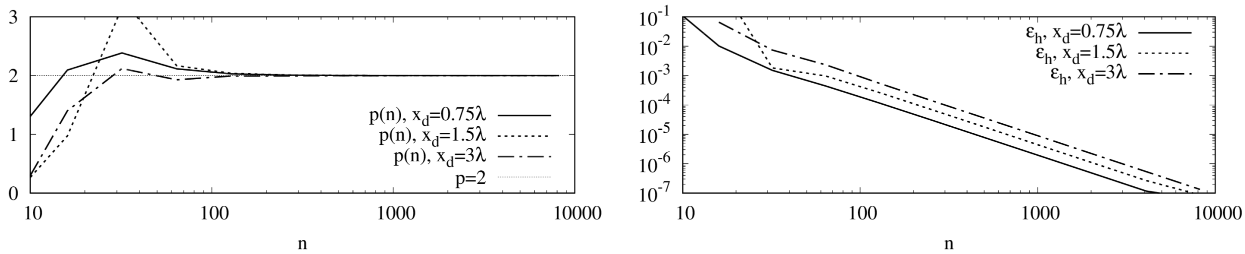

Figure 13: Order of convergence p (left) and error estimate ε_{h} (right) as a function of the number of zones n, for the forcing zones in Figs. 11 and 12

Given the simulation setups in Sects. 5 to 8 it is expected that, when the grid resolution increases, the wave damping behavior in the flow simulation will converge towards the solution for the specified continuous blending function $b(x)$. Since Sects. 5 to 8 show that the theory from Sect. 4 predicts flow simulation results with high accuracy, it is expected that the results of the theory from Sect. 4, which is based on discontinuous piece-wise constant blending $b(x)$, will converge towards the analytical solution for any given continuous blending function $b(x)$, if the forcing zone is subdivided into a sufficient number of zones n.

In the following, the theory will be evaluated for a subdivision into $n = 200$ zones, so that for practical purposes the theory predictions can be considered discretization-independent.

4.5 2D-/3D-theory for predicting forcing zone behavior in flows with oblique wave incidence

In 2D- and 3D-flows, the reflection coefficient may differ locally, for example due to different wave incidence angles as discussed in Sect. 5.4. To accurately predict both the global reflection coefficient C_{R} and the flow inside the domain as for the 1D-case, the theory would need to take into account the wave evolution in the whole domain, including the influence of reflecting and possibly moving bodies placed within the domain. This makes an accurate theoretical description for every possible 2D-case difficult.

Therefore this section follows a more practical approach: The 1D-theory is modified to describe 2D- and 3D-waves that enter the forcing zone at an angle θ as shown in Fig. 14. Thus the influence of θ on C_{R} is obtained, and it is possible to judge whether 1D-theory predictions can be used with confidence for the 2D- and 3D-case as Sect. 5.4 suggests, and roughly to what extent the 1D-theory predictions will be conservative or not.

To extend the 1D-theory to 2D and 3D, the 1D-theory is modified as follows. The incoming waves are approximated as plane waves, assuming that the waves are generated sufficiently far from the forcing zone and that a comparatively thin segment of the forcing zone is considered. The waves enter the forcing zone at an incidence angle θ between wave propagation direction and the layer-normal vector as shown in Fig. 14; by looking at the plane spanned by these two vectors, every 3D-problem is reduced to a 2D problem. Hence in the following, the subscript '$_{2D}$' denotes the modified theory which is applicable to 2D- and 3D-flows. As in the 1D-case in Sects. 4.1 to 4.3, the forcing zone is composed of several zones with constant blending $b(\mathbf{x})$, and the shortest distance between two neighboring zone interfaces j and $j+1$ is $x_{\mathrm{d}_{j,1\mathrm{D}}}$. Waves can be partially reflected at each interface between two zones, and interference occurs between those reflected wave components which travel along the same path.

Two mechanisms modify the reflection behavior in contrast to the 1D-case. First, the wave travels a larger distance through the forcing zone, which acts like an increase of the layer thickness x_d proportional to the increase in propagation distance within the layer; thus each zone acts on the wave as if it had thickness

$$x_{\mathrm{d}_{j,2\mathrm{D}}} = \frac{x_{\mathrm{d}_{j,1\mathrm{D}}}}{\cos(\theta)} \quad , \tag{92}$$

with thickness $x_{\mathrm{d}_{j,1\mathrm{D}}}$ of zone j and incidence angle $|\theta| \leq 90\,\mathrm{deg}$.

Second, the amount of destructive interference depends on the phase shift between the reflected waves. In 1D-theory the distance shift between the crests of waves reflected at two adjacent zone interfaces j and $j+1$ is always $2x_{\mathrm{d}_{j,1\mathrm{D}}}$; for the 2D-case, the distance shift is $\leq 2x_{\mathrm{d}_{j,2\mathrm{D}}}$, since a wave reflected at a certain location will interfere with wave reflections which occur at neighboring positions as illustrated in Fig. 14.

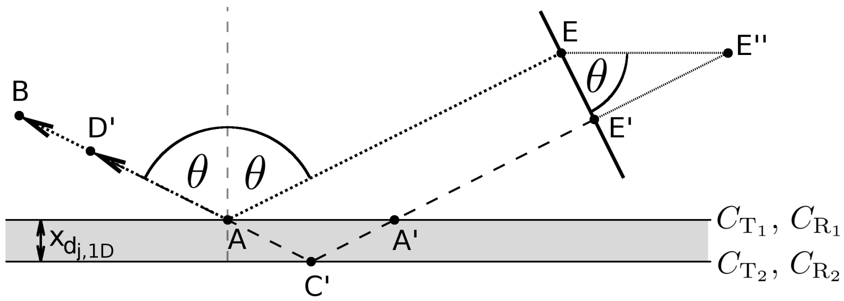

Figure 14: Wave crest ($\overline{EE'}$) propagates with incidence angle θ towards a forcing zone (shaded gray, only the first zone is depicted); given are the paths for reflection at the layer entrance for the crest segment close to E (path $\overline{EAB}$) and for reflection at the interface to the second zone for the crest segment close to E' (path $\overline{E'C'D'}$); both reflected paths lie on top of each other and create interference; distances $\overline{AC'} = x_{\mathrm{d}_{j,2\mathrm{D}}}$ and $\overline{AA'} = \overline{EE''} = 2x_{\mathrm{d}_{j,2\mathrm{D}}} \sin\theta$ give the distance shift between reflected waves at two adjacent layer interfaces as $\overline{E'E''} = 2x_{\mathrm{d}_{j,2\mathrm{D}}} \sin^2\theta$

Trigonometric considerations (see Fig. 14) show that the distance shift is

$$\Delta x = 2x_{\mathrm{d}_{j,2\mathrm{D}}} \sin^2\theta \quad . \tag{93}$$

For reflections at the interface between zones j and $j+1$, this leads to a phase shift for the reflected wave component in zone $j+1$ by factor

$$\Theta = \mathrm{e}^{ik_0(-\Delta x)} \quad , \tag{94}$$

where k_0 is the wave number outside the forcing zone.

Therefore, the 2D-problem can be reduced to a 1D-problem to save computational effort: The reflection coefficients for the 2D-case in Fig. 14 are equivalent to those obtained using 1D-theory, if the thickness of the zones is set to $x_{\mathrm{d}_{j,2\mathrm{D}}}$ instead of $x_{\mathrm{d}_{j,1\mathrm{D}}}$, and additionally the phase shift between waves reflected at adjacent zones is adjusted according to Eq. (94).

Consider two adjacent zones j and $j+1$. For example for (hydro-)acoustic waves, the particle displacements for the equivalent 1D-case are

$$\chi_j = \chi_0 \left(\prod_{n=0}^{j-1} C_{\mathrm{T}_n}\right) \left[\mathrm{e}^{i\left(\sum_{n=1}^{j-1} k_n x_{\mathrm{d}_{n,2\mathrm{D}}} + k_j\left(x - \sum_{n=1}^{j-1} x_{\mathrm{d}_{n,2\mathrm{D}}}\right)\right)} \right.$$

$$\left. - C_{\mathrm{R}_j} \mathrm{e}^{i\left(\sum_{n=1}^{j-1} k_n x_{\mathrm{d}_{n,2\mathrm{D}}} + k_j 2 x_{\mathrm{d}_{j,2\mathrm{D}}} - k_j\left(x - \sum_{n=1}^{j-1} x_{\mathrm{d}_{n,2\mathrm{D}}}\right)\right)}\right] \quad , \tag{95}$$

$$\chi_{j+1} = \chi_0 \left(\prod_{n=0}^{j} C_{\mathrm{T}_n}\right) \left[\mathrm{e}^{i\left(\sum_{n=1}^{j} k_n x_{\mathrm{d}_{n,2\mathrm{D}}} + k_{j+1}\left(x - \sum_{n=1}^{j} x_{\mathrm{d}_{n,2\mathrm{D}}}\right)\right)} \right.$$

$$\left. - \Theta \cdot C_{\mathrm{R}_{j+1}} \mathrm{e}^{i\left(\sum_{n=1}^{j} k_n x_{\mathrm{d}_{n,2\mathrm{D}}} + k_{j+1} 2 x_{\mathrm{d}_{j+1,2\mathrm{D}}} - k_{j+1}\left(x - \sum_{n=1}^{j} x_{\mathrm{d}_{n,2\mathrm{D}}}\right)\right)}\right] \quad . \tag{96}$$

Requiring as in Sect. 4.3 that at the interface between zones j and $j+1$ should hold $[\chi_j = \chi_{j+1}]_{x=\sum_{n=1}^{j} x_{\mathrm{d}_n}}$ and $[\chi_{x,j} = \chi_{x,j+1}]_{x=\sum_{n=1}^{j} x_{\mathrm{d}_n}}$, transmission and reflection coefficients for interface j can be derived as

$$C_{\mathrm{T}_j} = \frac{1 - C_{\mathrm{R}_j}}{1 - \Theta \cdot C_{\mathrm{R}_{j+1}} \mathrm{e}^{i\left(k_{j+1} 2 x_{\mathrm{d}_{j+1,2\mathrm{D}}}\right)}} \quad , \tag{97}$$

$$C_{\mathrm{R}_j} = \frac{k_{j+1}\beta_{j+1} - k_j}{k_{j+1}\beta_{j+1} + k_j} \quad , \tag{98}$$

with

$$\beta_{j+1} = \frac{1 + \Theta \cdot C_{\mathrm{R}_{j+1}} \mathrm{e}^{i\left(k_{j+1} 2 x_{\mathrm{d}_{j+1,2\mathrm{D}}}\right)}}{1 - \Theta \cdot C_{\mathrm{R}_{j+1}} \mathrm{e}^{i\left(k_{j+1} 2 x_{\mathrm{d}_{j+1,2\mathrm{D}}}\right)}} \quad . \tag{99}$$

If the forcing zone starts at zone 1, the ‘global’ reflection coefficient C_{R} for the 2D-case is

$$C_{\mathrm{R}} = |C_{\mathrm{R}_1}| = \sqrt{\mathrm{Re}\{C_{\mathrm{R}_1}\}^2 + \mathrm{Im}\{C_{\mathrm{R}_1}\}^2} \quad , \tag{100}$$

where $\mathrm{Re}\{X\}$ and $\mathrm{Im}\{X\}$ denote the real and the imaginary part of the complex number X.

For free-surface waves, the same results as in Eqs. (97) to (100) are obtained by following the above derivation procedure, when starting from adjacent velocity stream functions

$$\psi_j = \psi_0 \left(\prod_{n=0}^{j-1} C_{\mathrm{T}_n}\right) \left[\mathrm{e}^{i\left(\sum_{n=1}^{j-1} k_n x_{\mathrm{d}_{n,2\mathrm{D}}} + k_j\left(x - \sum_{n=1}^{j-1} x_{\mathrm{d}_{n,2\mathrm{D}}}\right)\right)} \right.$$

$$\left. - C_{\mathrm{R}_j} \mathrm{e}^{i\left(\sum_{n=1}^{j-1} k_n x_{\mathrm{d}_{n,2\mathrm{D}}} + k_j 2 x_{\mathrm{d}_{j,2\mathrm{D}}} - k_j\left(x - \sum_{n=1}^{j-1} x_{\mathrm{d}_{n,2\mathrm{D}}}\right)\right)}\right] \quad , \tag{101}$$

$$\psi_{j+1} = \psi_0 \left(\prod_{n=0}^{j} C_{\mathrm{T}_n}\right) \left[\mathrm{e}^{i\left(\sum_{n=1}^{j} k_n x_{\mathrm{d}_{n,2\mathrm{D}}} + k_{j+1}\left(x - \sum_{n=1}^{j} x_{\mathrm{d}_{n,2\mathrm{D}}}\right)\right)} \right.$$

$$\left. - \Theta \cdot C_{\mathrm{R}_{j+1}} \mathrm{e}^{i\left(\sum_{n=1}^{j} k_n x_{\mathrm{d}_{n,2\mathrm{D}}} + k_{j+1} 2 x_{\mathrm{d}_{j+1,2\mathrm{D}}} - k_{j+1}\left(x - \sum_{n=1}^{j} x_{\mathrm{d}_{n,2\mathrm{D}}}\right)\right)}\right] \quad . \tag{102}$$

and requiring $[\psi_j = \psi_{j+1}]_{x=\sum_{n=1}^{j} x_{\mathrm{d}_n}}$ and $[\psi_{x,j} = \psi_{x,j+1}]_{x=\sum_{n=1}^{j} x_{\mathrm{d}_n}}$.

5 Forcing zones for (hydro-)acoustic waves

Key findings

- The theory from Sect. 4.3 satisfactorily predicts the reflection coefficient C_R and the flow within the forcing zone for linear and highly nonlinear, regular and irregular (hydro-)acoustic waves in 1D-, 2D-, and 3D-flows
- For irregular or highly nonlinear waves, it is recommended to use slightly thicker zones than theoretically necessary to ensure satisfactory reduction of undesired wave reflections
- Depending on the case, tuning towards more efficient narrow-banded or more reliable wide-banded wave absorption characteristics can be more appropriate
- Theory predictions for reflection coefficients apply also when using forcing zones to generate waves

The theory predictions from Sect. 4.3 are compared in Sect. 5.2 to results from finite-volume-based flow simulations with regular and irregular acoustic wave propagation in gases and liquids, based on the setup described in Sect. 5.1, followed by a discussion of the implications of the theory regarding the choice of blending functions and the recommended setup in Sect. 5.3.

In Sect. 5.4, it is found that for many practical 2D- and 3D-wave problems, the 1D-theory from Sect. 4.3 suffices to tune the forcing zone parameters. If greater accuracy is required, Sect. 5.5 demonstrates via 2D-flow simulation results that the 2D-/3D-theory from Sect. 4.5 satisfactorily predicts reflection coefficients for waves entering the forcing zone at oblique incidence angles θ. Practical recommendations are given for setting up forcing zones in 2D- and 3D-flow simulations.

Sections 5.6 and 5.7 demonstrate that the theory is also suitable to tune forcing zones for highly nonlinear waves as well as for simultaneous generation and damping of waves within forcing zones.

When the forcing zone was tuned using the theory, in all simulations from Sect. 5 held $C_{\mathrm{R,sim}} - C_{\mathrm{R,theory}} < 1.7\%$, with reflection coefficients from simulation results $C_{\mathrm{R,sim}}$ and the corresponding theory predictions $C_{\mathrm{R,theory}}$. Thus the theory predictions were considered to be of satisfactory accuracy for engineering practice.

5.1 Simulation setup

In Sect. 5.2, flow simulations of 1D-wave-propagation are performed on a computational domain with dimensions $0 \leq x \leq L_x$ as illustrated in Fig. 15. The coordinate system has its origin at $x = 0\,\mathrm{m}$. At boundary $x = 0\,\mathrm{m}$, a sinusoidal pressure fluctuation is prescribed to produce a continuous regular wave of period $T = 2.\overline{27} \cdot 10^{-3}\,\mathrm{s}$, which corresponds to modern standard concert pitch A 440 Hz. The wave propagates in positive x-direction, is partially reflected, absorbed and transmitted at each cell within the forcing zone, and the remaining wave is fully reflected at the wall boundary $x = L_x$. The simulations are performed quasi-one-dimensional, i.e. they consist of a uniform Cartesian three-dimensional grid, with 1 cell in y- and z-direction and symmetry boundary condition for the y- and z-normal boundaries; thus all gradients in y- and z-direction are zero.

In Sects. 5.4 to 5.6, simulations of 2D- and 3D-wave-propagation are performed on the solution domains shown in Figs. 29, 34, 37, and 40. The wave generation is discussed in the corresponding sections. The 2D-simulations are performed quasi-two-dimensional, i.e. they consist of a uniform Cartesian three-dimensional grid, with 1 cell in y-direction and symmetry boundary condition for the y-normal boundaries.

All simulations are performed using the commercial flow solver STAR-CCM+ (version 8.02.008-R8) by Siemens (formerly CD-adapco) based on the governing equations and the forcing zone formulation given in Sect. 2.5. Unless mentioned otherwise, the reference velocity is set to $u_{i,\mathrm{ref}} = 0$, so the forcing zone damps the waves. The solver is based on the finite volume method (FVM) and the implicit unsteady segregated solver is used. All approximations are of second order in time and space, and under-relaxation is 0.8 for velocities, 0.2 for pressure and 0.9 for energy. The initial conditions are pressure $p = 0$, velocity $u_i = 0$ and density $\rho = \rho_\mathrm{ref}$, the reference density of the fluid. Unless stated otherwise, the wave is discretized by ≥ 30 cells per wavelength and the time step is $\geq T/100$, with 8 outer iterations per time step. Detailed information on finite-volume-based flow simulations can be found e.g. in Ferziger and Perić (2002).

Unless mentioned otherwise in the corresponding sections, simulations are performed for liquid water using the International Association for the Properties of Water and Steam (IAPWS) model as in IAPWS (2007) and solving the energy Eq. (28) for temperature ϑ, with reference temperature $\vartheta_{\mathrm{ref}} = 300\,\mathrm{K}$, or simulations are performed for an ideal gas with speed of sound $c = 291.5\,\frac{\mathrm{m}}{\mathrm{s}}$, which corresponds to air at temperature $\approx -62°C$ or to an appropriate mixture of oxygen and carbon dioxide at room temperature. The gas is considered isothermal, so Eq. (28) is not solved. For simplicity, these fluids will be denoted 'water' and 'ideal gas' in the following. The simulations are performed with different forcing zone parameters, such as forcing strength γ, layer thickness x_{d}, or blending function $b(x)$. For better visualization, several of the following figures (such as e.g. Fig. 16) show the same results in two or three plots: without and with a logarithmic vertical axis, or with close-up views of parts of the plot.

5.2 1D-results

The theory presented in Sect. 4.3 is compared to flow simulation results for 1D regular and irregular pressure waves in an ideal gas and in liquid water. First, results for regular waves are presented. The waves have period $T = 2.\overline{27} \cdot 10^{-3}\,\mathrm{s}$ and the amplitude of the pressure fluctuations at the wave-maker is 10 Pa (ideal gas) or 1000 Pa (water). The setup is described in Sect. 5.1. The computational domain with forcing zone based on Eq. (31) is sketched in Fig. 15.

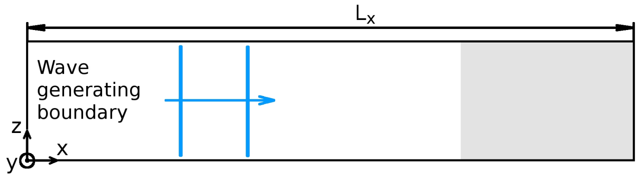

Figure 15: Computational domain with wave-maker at $x = 0\,\mathrm{m}$ and forcing zone (shaded gray) attached to domain boundary at $x = L_x = 9\lambda$

On a single core 2.6 GHz processor, the time to perform a simulation was in the order of 1 min. The reflection coefficient C_{R} is computed via Eq. (36). The theory is evaluated for same wavelength, period and forcing zone parameters in Eq. (31) as in the simulations.

Figures 16 and 17 show reflection coefficients and velocities for sound waves in water. The zone thickness is $x_{\mathrm{d}} = 1\lambda$ and exponential blending according to Eq. (9) is used. Theory and simulation results agree well. The peaks in the partial standing wave in Fig. 17 have different locations depending on forcing strength γ. This shows that, with increasing γ, the effective reflection location shifts from the boundary, to which the zone is attached (here $x/\lambda = 9$), towards the entrance to the forcing zone (here $x/\lambda = 8$); this underlines the importance of including reflections which occur within the zone in the analysis.

In Fig. 16, results are given for the grid and time step from Sect. 5.1, and also for twice and four times refined mesh and time-step size. The difference between the results is small, thus the coarsest discretization is used for the rest of the simulations in this section.

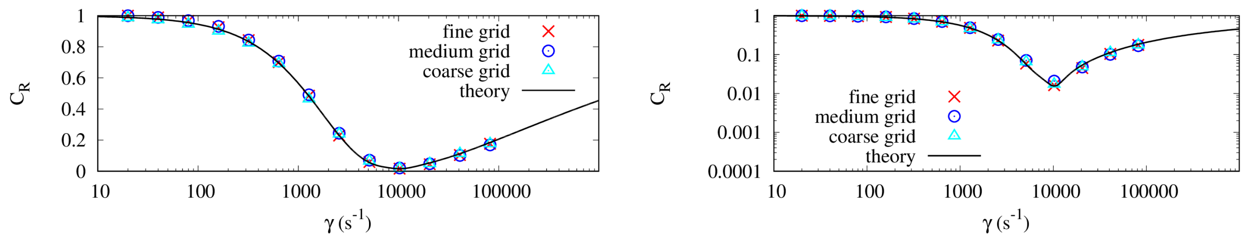

Figure 16: Reflection coefficient C_{R} as a function of forcing strength γ from simulation and theory; for the sound wave from Fig. 17 with period $T = 0.00\overline{227}\,\mathrm{s}$ in water; for forcing of x-momentum via Eq. (31) with exponential blending via Eq. (9) and zone thickness $x_{\mathrm{d}} = 1\lambda$; for coarse (time step $\Delta t = T/100$, cell size $\Delta x = \lambda/30$), medium ($\Delta t = T/200$, $\Delta x = \lambda/60$), and fine ($\Delta t = T/400$, $\Delta x = \lambda/120$) discretization; for all simulation results $C_{\mathrm{R,sim}}$ and corresponding theory predictions $C_{\mathrm{R,theory}}$ holds $C_{\mathrm{R,sim}} - C_{\mathrm{R,theory}} < 1.9\%$ and on average $|C_{\mathrm{R,sim}} - C_{\mathrm{R,theory}}| < 0.7\%$; for the forcing strength $\gamma \geq \gamma_{\mathrm{opt,theory}}$ closest to the theoretical optimum value $\gamma_{\mathrm{opt,theory}}$ holds $C_{\mathrm{R,sim}} - C_{\mathrm{R,theory}} < 0.6\%$

Subsequently, the simulations are repeated with the same setup, except once with linear blending (Fig. 18) and once with constant blending (Fig. 19). Again the results show good agreement between theory and simulation. Compared to

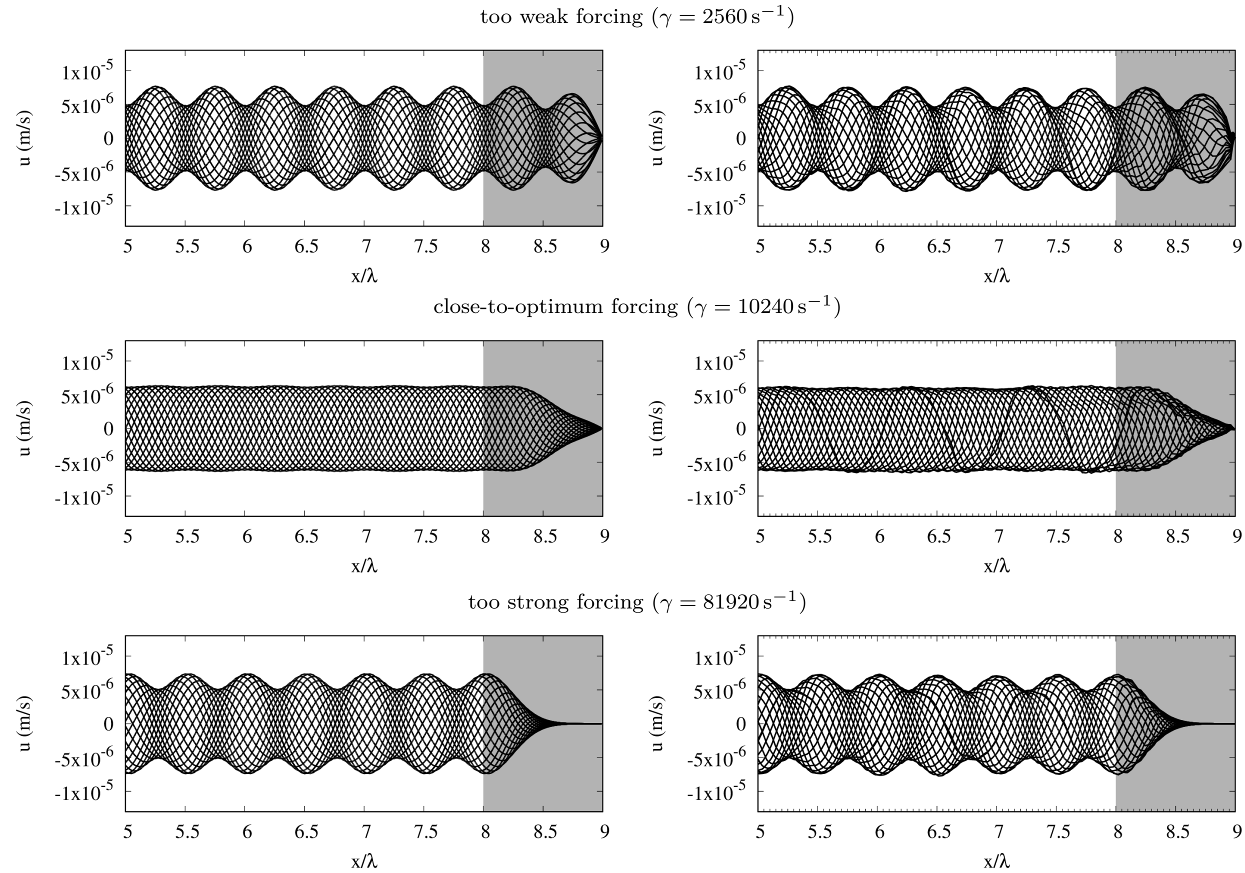

Figure 17: Theory predictions (left) and simulation results (right) for velocity in water as a function of x-coordinate, given at equally spaced time instances during the last simulated period; for a sound wave with period $T = 0.002\overline{27}\,\mathrm{s}$ in water; for forcing of x-momentum via Eq. (31) with exponential blending via Eq. (9), forcing zone (shaded gray) thickness $x_{\mathrm{d}} = 1\lambda$, and different forcing strengths γ

Figs. 16 and 17, the optimum values γ_{opt} of the forcing strength are different. For the investigated blending functions it holds roughly that the smaller the area below the blending function $b(x)$ is, the larger is the value for γ_{opt}.

Simulation results for acoustic waves in an ideal gas are shown in Figs. 20 to 21 for forcing zones with thickness $x_{\mathrm{d}} = 1.18\lambda$ and $x_{\mathrm{d}} = 2.35\lambda$. Theory predictions and simulation results are in good agreement. Figure 20 (at $\gamma = 10240\,\mathrm{s}^{-1}$) demonstrates that, for certain choices of x_{d} and for a very narrow range of wave frequencies, it is possible to achieve reflection coefficients more than one order of magnitude smaller than are possible for slightly smaller or larger x_{d}, which is investigated in more detail in Sect. 5.3. This is expected to be an effect of especially favorable destructive interference between the reflected waves. Figure 21 shows that there may be more than one local optimum for γ.

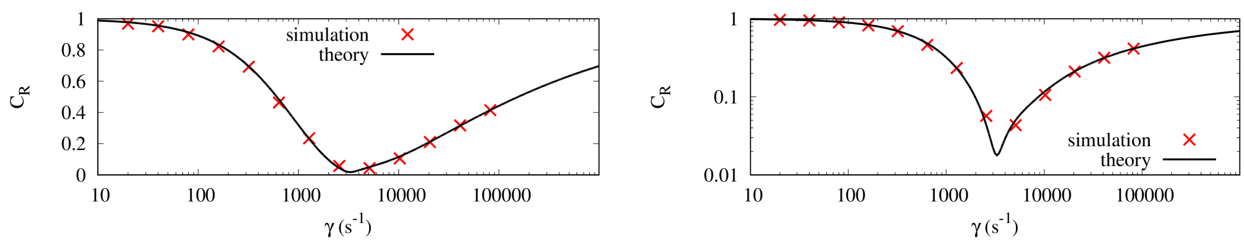

Figure 18: Reflection coefficient C_{R} as a function of forcing strength γ from simulation and theory; for a sound wave with period $T = 0.002\overline{27}\,\mathrm{s}$ in water; for forcing of x-momentum via Eq. (31) with linear blending via Eq. (4) and zone thickness $x_{\mathrm{d}} = 1\lambda$; for all simulation results $C_{\mathrm{R,sim}}$ and corresponding theory predictions $C_{\mathrm{R,theory}}$ holds $C_{\mathrm{R,sim}} - C_{\mathrm{R,theory}} < 1.9\%$ and on average $|C_{\mathrm{R,sim}} - C_{\mathrm{R,theory}}| < 0.4\%$; for the forcing strength $\gamma \geq \gamma_{\mathrm{opt,theory}}$ closest to the theoretical optimum value $\gamma_{\mathrm{opt,theory}}$ holds $C_{\mathrm{R,sim}} - C_{\mathrm{R,theory}} < -0.8\%$

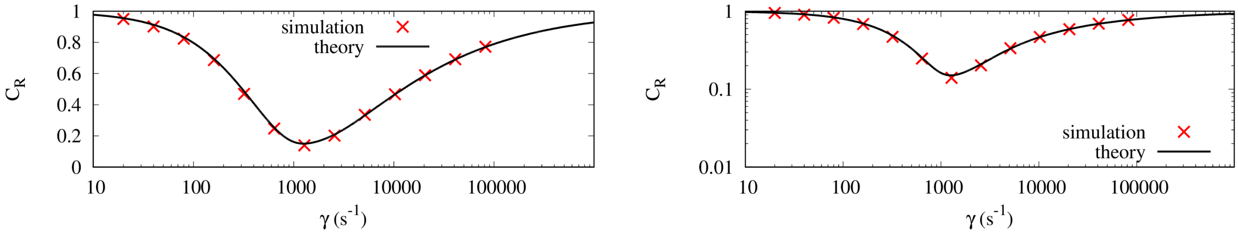

Figure 19: As Fig. 18, except for constant blending via Eq. (3); for all simulation results $C_{\mathrm{R,sim}}$ and corresponding theory predictions $C_{\mathrm{R,theory}}$ holds $C_{\mathrm{R,sim}} - C_{\mathrm{R,theory}} < 2.3\%$ and on average $|C_{\mathrm{R,sim}} - C_{\mathrm{R,theory}}| < 0.4\%$; for the forcing strength $\gamma \geq \gamma_{\mathrm{opt,theory}}$ closest to the theoretical optimum value $\gamma_{\mathrm{opt,theory}}$ holds $C_{\mathrm{R,sim}} - C_{\mathrm{R,theory}} < -1.1\%$

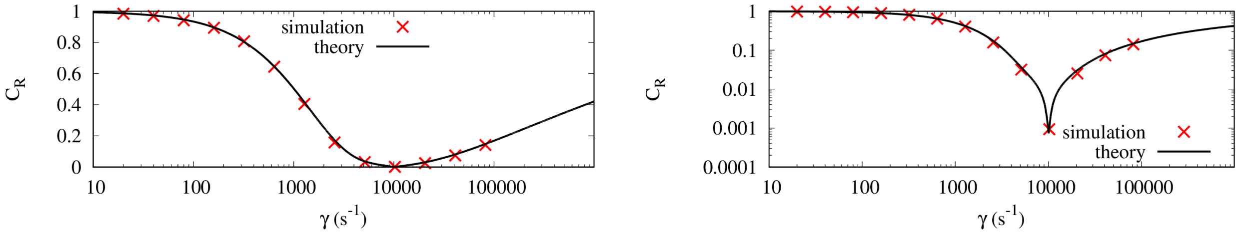

Figure 20: Reflection coefficient C_{R} as a function of forcing strength γ from simulation and theory; for a sound wave with period $T = 0.00\overline{227}\,\mathrm{s}$ in an ideal gas; for forcing of x-momentum via Eq. (31) with exponential blending via Eq. (9) and zone thickness $x_{\mathrm{d}} = 1.18\lambda$; for all simulation results $C_{\mathrm{R,sim}}$ and corresponding theory predictions $C_{\mathrm{R,theory}}$ holds $C_{\mathrm{R,sim}} - C_{\mathrm{R,theory}} < 1.6\%$ and on average $|C_{\mathrm{R,sim}} - C_{\mathrm{R,theory}}| < 0.5\%$; for the forcing strength $\gamma \geq \gamma_{\mathrm{opt,theory}}$ closest to the theoretical optimum value $\gamma_{\mathrm{opt,theory}}$ holds $C_{\mathrm{R,sim}} - C_{\mathrm{R,theory}} < -0.02\%$

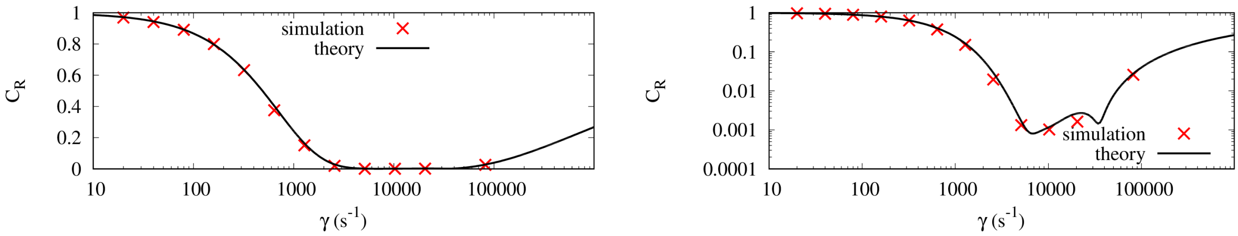

Figure 21: As Fig. 20, except for zone thickness $x_{\mathrm{d}} = 2.35\lambda$; for all simulation results $C_{\mathrm{R,sim}}$ and corresponding theory predictions $C_{\mathrm{R,theory}}$ holds $C_{\mathrm{R,sim}} - C_{\mathrm{R,theory}} < 2.8\%$ and on average $|C_{\mathrm{R,sim}} - C_{\mathrm{R,theory}}| < 0.6\%$; for the forcing strength $\gamma \geq \gamma_{\mathrm{opt,theory}}$ closest to the theoretical optimum value $\gamma_{\mathrm{opt,theory}}$ holds $C_{\mathrm{R,sim}} - C_{\mathrm{R,theory}} < -0.02\%$

The next 1D example is the prediction of reflection coefficients for irregular wave trains. Apart from the following modifications, the setup is the same as in the previous simulations. The fluid is air as ideal gas with speed of sound $c = 347.28\,\frac{\mathrm{m}}{\mathrm{s}}$ and the temperature variation is accounted for via Eq. (28). The domain length is $L_x = 13.36\lambda_{\mathrm{peak}}$, where $\lambda_{\mathrm{peak}} \approx 0.78\,\mathrm{m}$ is the wavelength corresponding to peak wave period T_{peak}. The forcing zone based on Eq. (31) is attached to boundary $x = L_x$, with zone thickness $x_{\mathrm{d}} = 2\lambda_{\mathrm{peak}}$ and exponential blending as in Eq. (9). To generate irregular waves, pressure fluctuations at the inlet are prescribed using the JONSWAP-spectrum by Hasselmann et al. (1973), except that the 'significant wave height' H_{s} was replaced by twice the 'significant pressure amplitude' $2p_{\mathrm{a,s}} = 10\,\mathrm{Pa}$; the parameters are peak wave period $T_{\mathrm{peak}} = 0.00\overline{227}\,\mathrm{s}$, and a peak-shape parameter of 3.3. The spectrum is discretized into 50 wave components.

Figure 22 shows the waves generated by prescribing the pressure at the inlet as $p(t)b'(t)$, where $p(t)$ corresponds to a linear superposition of the pressures of the irregular wave components, and $b'(t)$ is a blending-in and -out during the first $6.6T_{\mathrm{peak}}$ of simulation time:

$$b'(t) = \begin{cases} \cos^2\left(\frac{\pi}{2}(t - 2.2T_{\mathrm{peak}})/(2.2T_{\mathrm{peak}})\right) & \text{if } t < 2.2T_{\mathrm{peak}} \\ 1.0 & \text{if } 2.2T_{\mathrm{peak}} \leq t \leq 4.4T_{\mathrm{peak}} \\ \cos^2\left(\frac{\pi}{2}(t - 4.4T_{\mathrm{peak}})/(2.2T_{\mathrm{peak}})\right) & \text{if } 4.4T_{\mathrm{peak}} < t < 6.6T_{\mathrm{peak}} \\ 0.0 & \text{if } t \geq 6.6T_{\mathrm{peak}} \end{cases} . \tag{103}$$

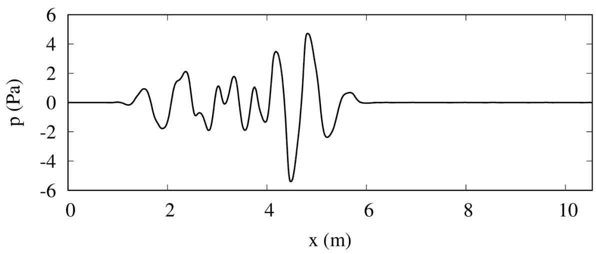

Figure 22: Pressure as a function of x-location at time $t = 21.27T_{\mathrm{peak}}$ with no damping ($\gamma = 0$)

The total simulated time is $t_{\mathrm{end}} = 21.27T_{\mathrm{peak}}$. The waves are discretized by ≈ 62 cells per peak wavelength λ_{peak} and the time step is $\Delta t = T_{\mathrm{peak}}/200$, with 10 iterations per time step. At the end of each simulation, the pressure over space is analyzed using the fast Fourier transform (FFT) algorithm to obtain the pressure amplitude spectrum of the reflected wave. For $\gamma = 0$, the wave is perfectly reflected, so the resulting pressure amplitude spectrum corresponds to the initially generated spectrum; thus for $\gamma \neq 0$, the amount of reflection can be judged by comparing the pressure amplitude spectrum for the reflected wave to the case for no damping ($\gamma = 0$). Thus the global reflection coefficient C_{R} was obtained by Eq. (37).

Figure 23 shows that the resulting pressure amplitude spectrums agree well with the predictions according to the theory from Sect. 4; the theory predictions are based on the assumption that the wave can be treated as a linear superposition of wave components with different frequencies, and that the reflection coefficient for each component equals the reflection coefficient as predicted by the theory from Sect. 4.

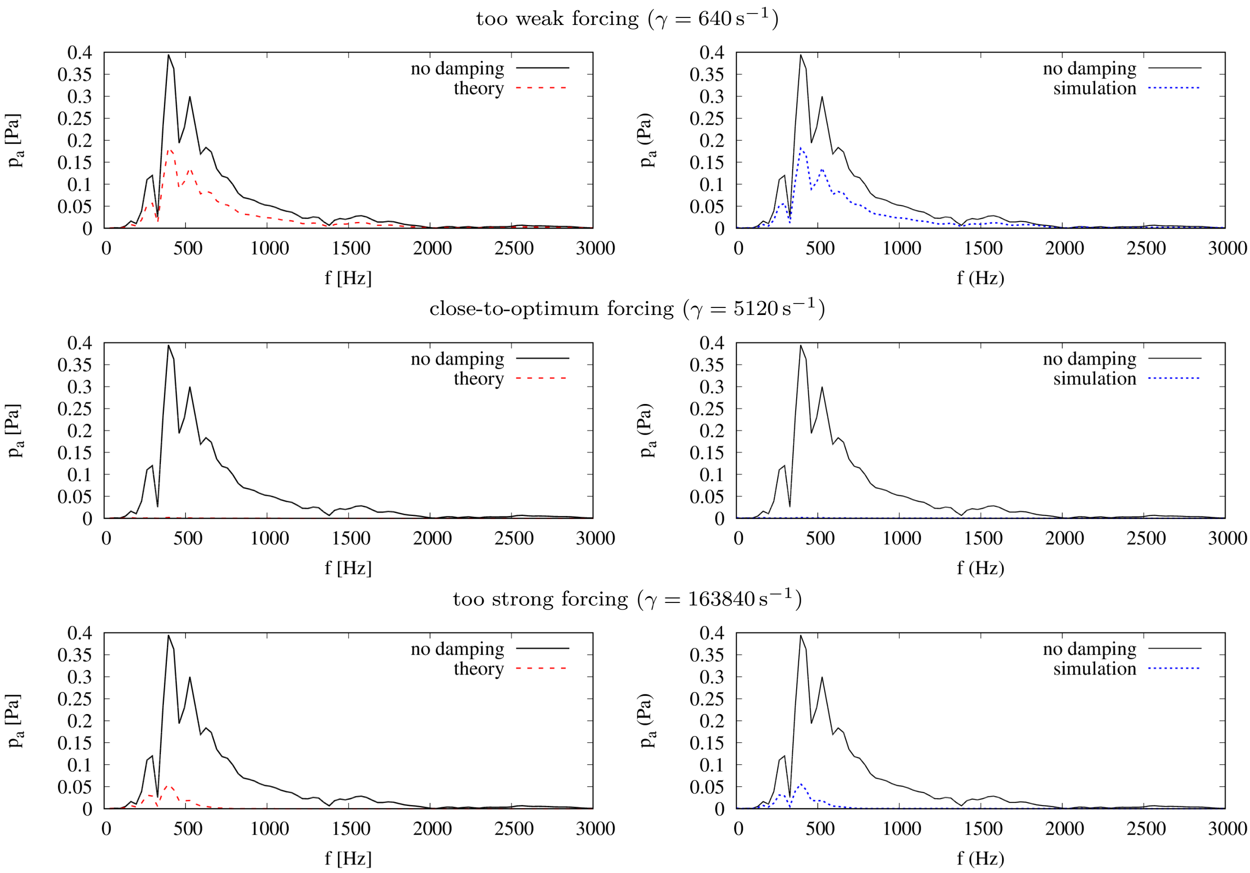

Figure 23: Theory predictions (left) and simulation results (right) for generated and reflected pressure-amplitude spectrum as a function of wave frequency; for an irregular wave train in air with peak period $T_{\mathrm{peak}} = 0.002\overline{27}\,\mathrm{s}$; with forcing of x-momentum via Eq. (31), exponential blending via Eq. (9) and zone thickness $x_{\mathrm{d}} = 2\lambda_{\mathrm{peak}}$

Figure 24 shows that the resulting overall reflection coefficients agree well for simulation and theory; the differences in C_{R} between simulation and theory are $< 1\%$.

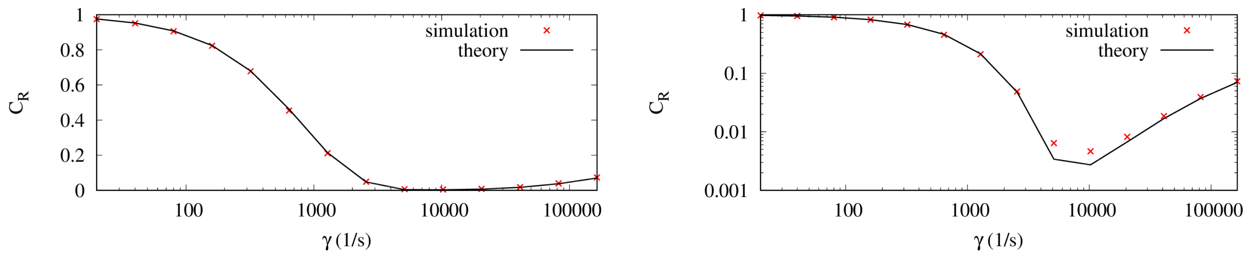

Figure 24: Theory predictions and simulation results for overall reflection coefficient C_{R} according to Eq. (37) as a function of forcing strength γ for the irregular wave train from Fig. 23; for all simulation results $C_{\mathrm{R,sim}}$ and corresponding theory predictions $C_{\mathrm{R,theory}}$ holds $C_{\mathrm{R,sim}} - C_{\mathrm{R,theory}} < 0.9\%$ and on average $|C_{\mathrm{R,sim}} - C_{\mathrm{R,theory}}| < 0.05\%$; for the forcing strength $\gamma \geq \gamma_{\mathrm{opt,theory}}$ closest to the theoretical optimum value $\gamma_{\mathrm{opt,theory}}$ holds $C_{\mathrm{R,sim}} - C_{\mathrm{R,theory}} < 0.2\%$

Figure 25 shows that 1D-theory for a regular wave with period $T = T_{\mathrm{peak}}$ gives a satisfactory prediction of the optimum tuning for the forcing zone, except that close to the optimum settings the reflection coefficients are slightly underpredicted. Thus in practice, 1D-theory can be used to tune the forcing zone, when the zone thickness x_{d} is selected slightly larger than theoretically necessary to ensure reliable wave damping.

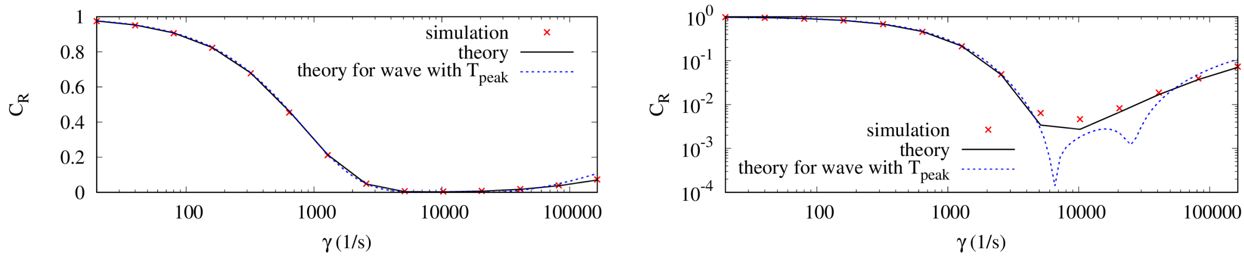

Figure 25: As Fig. 24, except that additionally the theory prediction for a regular monochromatic wave with wave period $T = T_{\mathrm{peak}}$ is shown; T_{peak} is the peak period of the irregular wave; the results show that tuning the forcing zone to the peak period in the wave spectrum can often be sufficiently accurate for practical purposes, at least for comparatively narrow-banded spectrums as are typically found for ocean waves, such as the JONSWAP spectrum used here

5.3 Theory implications for the choice of blending function $b(\mathbf{x})$

Since Sect. 5.2 demonstrated that the theory from Sect. 4 is reliable in its predictions, this section shows theory predictions without backup from simulation results. This is mainly because, to obtain the following results, a very large number of simulations would be required, the combined computational effort being out of the scope of this study.

In Fig. 26, theory predictions are shown for a wave with period $T = 2.\overline{27} \cdot 10^{-3}$ s and forcing zone thicknesses varying between $x_{\mathrm{d}} \in [0.5\lambda, 6\lambda]$. These results can be applied to waves of any other period: If γ and x_{d} are scaled as described in Sect. 2.2, the curves in Fig. 26 need only to be shifted sideways accordingly. The results can guide regarding the choice between the different blending functions $b(\mathbf{x})$ from Sect. 2.1.

As Fig. 26 shows, the quadratic, $\cos^2$ and exponential blending functions $b(\mathbf{x})$ typically produce lower reflection coefficients than linear or even constant blending $b(\mathbf{x})$. Although the curves for quadratic, cosine-squared and exponential blending are substantially different as seen in Fig. 3, their results seem on the whole nearly equally satisfactory, perhaps with a slight preference for the exponential blending function.

For some values of x_{d} in Fig. 26, quadratic or cosine-squared blending produces lower optimum reflection coefficients than exponential blending, e.g. for $x_{\mathrm{d}} = 0.5\lambda$. This can be explained by Fig. 27, which shows that there exist certain values for forcing zone thickness x_{d}, for which especially favorable absorption may occur. This means that the resulting reflection coefficient C_{R} for optimum forcing strength γ can be two orders of magnitude lower than it would be if x_{d} was selected slightly larger or smaller, as illustrated in Fig. 28. This phenomenon may be used to produce satisfactory (say $C_{\mathrm{R}} \lesssim 1\%$) wave damping with very thin (say $x_{\mathrm{d}} \lesssim 0.5\lambda$) forcing zones. The results in Fig. 20 confirm the existence of this phenomenon. It is expected that a combination of grid stretching and forcing zones may produce similar effects.

However, according to the present investigations, these settings, seen as 'negative peaks' in Figs. 27, occur only for a narrow range of wavelengths. This would make the absorption behavior rather sensitive to slight deviations in the wavelength (cf. Fig. 28). For example in finite-volume-based flow solvers, discretization and iteration errors can lead to a change in the wavelength of several percent for coarse discretizations, see e.g. Perić and Abdel-Maksoud (2015b, 2016) or Sect. 7.1. Furthermore, when a superposition of waves of different frequencies is considered, then it is important to have satisfactory minimization of all undesired reflections, not only of those belonging to a specific wave component. Trying to optimize the forcing zone towards one of these negative peaks of C_{R} may therefore lead to false security, and should only be exercised with caution.

In practice, it is desired (especially when the wave may be modified within the domain) to know for a given forcing zone setup the range of forcing strengths γ for which the reflection coefficients will be below a certain threshold. As shown for an example threshold of $C_{\mathrm{R}} < 10\%$ in Fig. 27, this range is larger for the quadratic, $\cos^2$ and exponential blending functions.

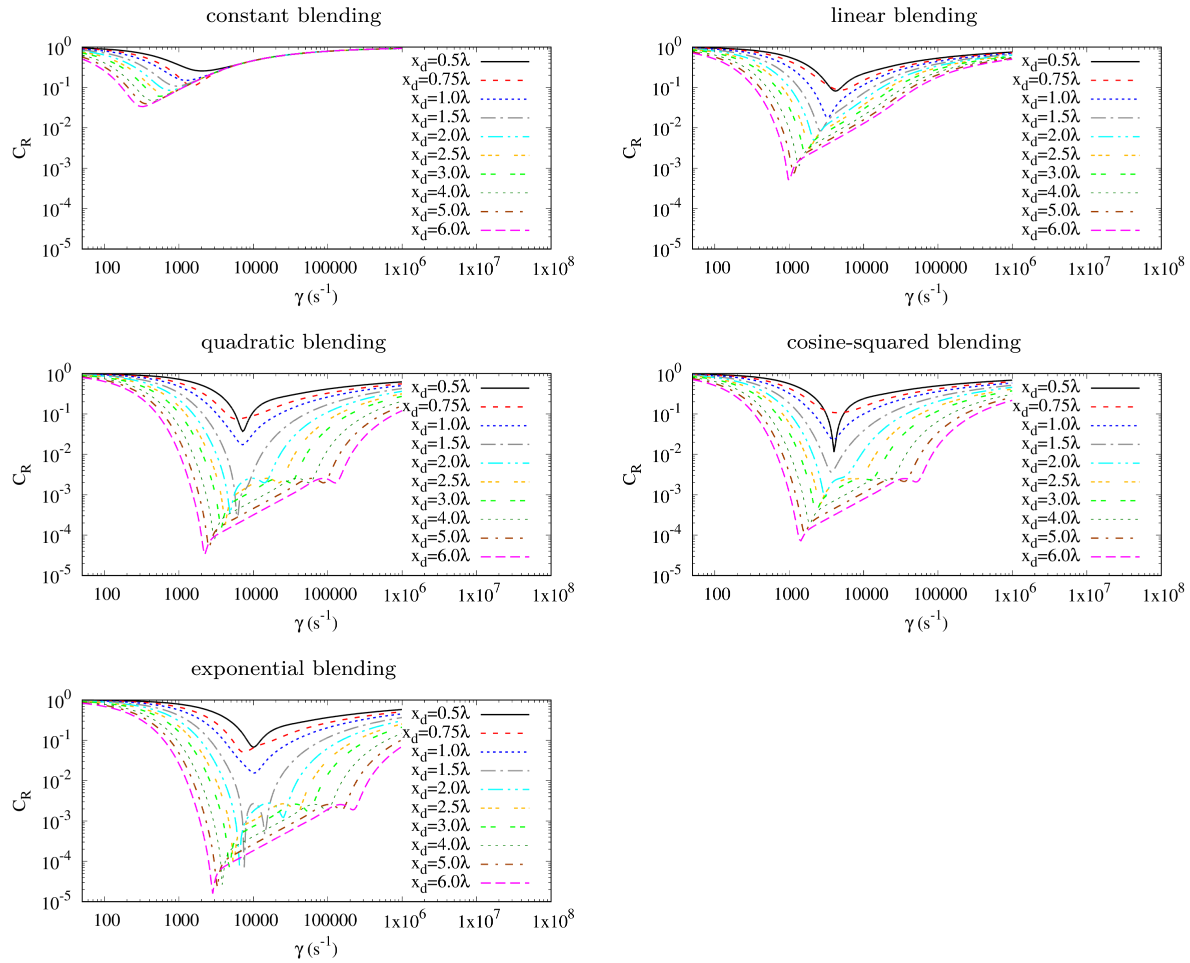

Figure 26: Reflection coefficient C_{R} as a function of forcing strength γ; for a wave with period $T = 0.002\overline{27}\,\mathrm{s}$; for different forcing zone thickness x_{d} and different blending $b(\mathbf{x})$ via Eqs. (3), (4), (5), (7), and (9)

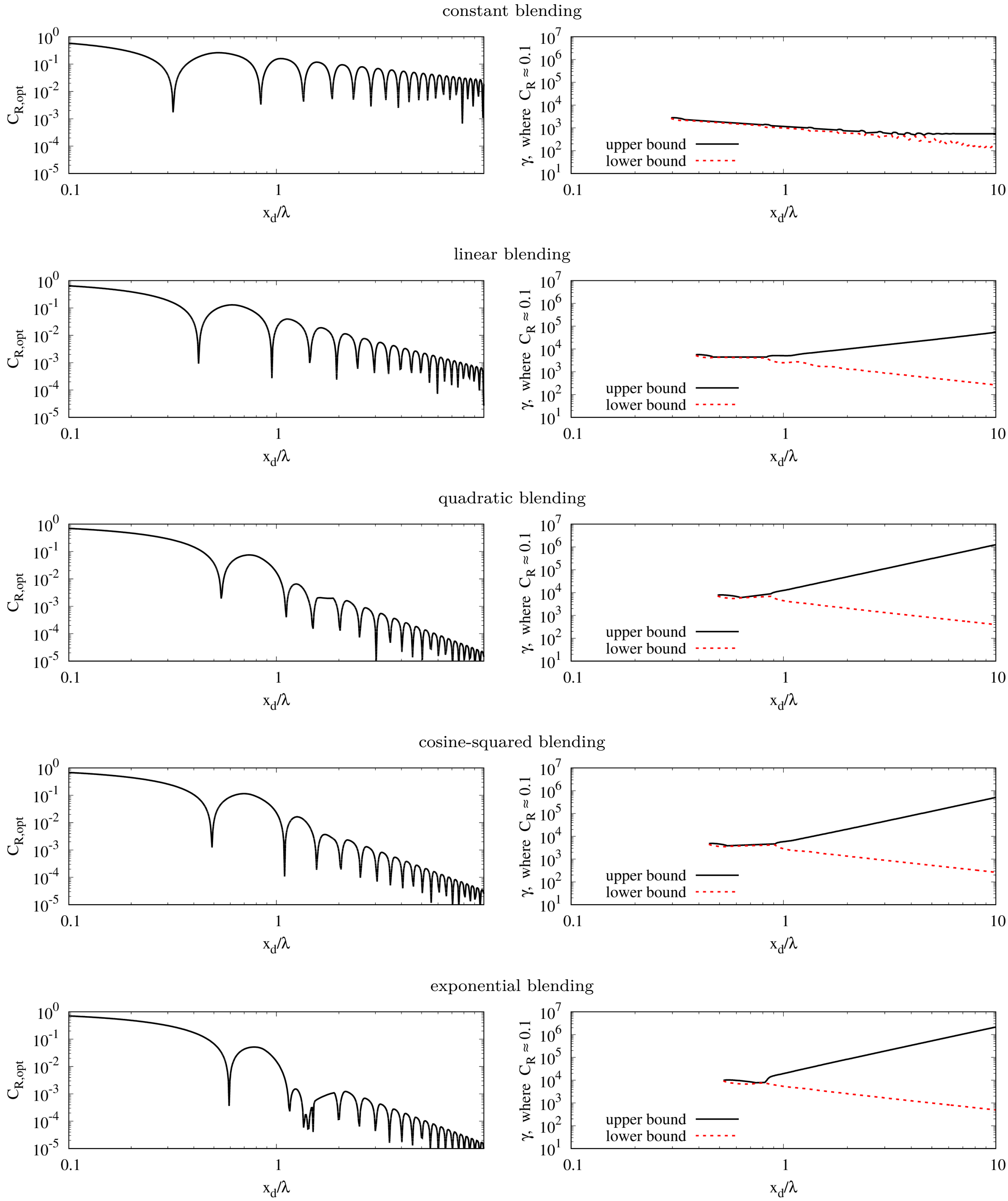

Figure 27: Optimum reflection coefficient $C_{\mathrm{R,opt}}$ (left) and range of γ values for which $C_{\mathrm{R}} < 0.1$ (right) as a function of zone thickness x_{d} per wavelength λ; for a wave with period $T = 0.00\overline{227}\,\mathrm{s}$; for different blending $b(\mathbf{x})$ via Eqs. (3), (4), (5), (7), and (9)

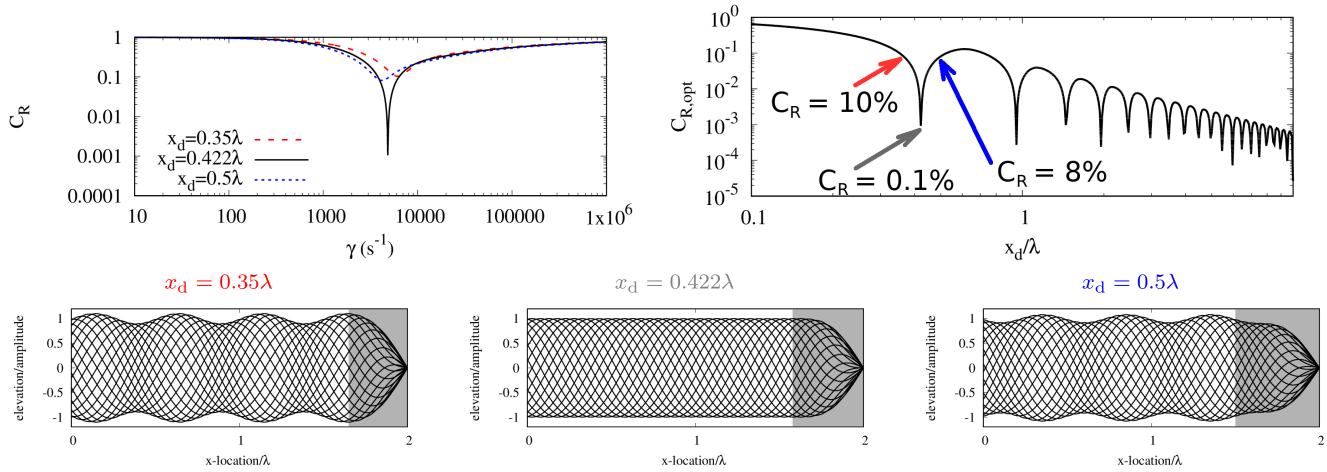

Figure 28: An example of especially favorable absorption for a forcing zone with linear blending $b(\mathbf{x})$ via Eq. (4), different zone thickness x_d and a wave with period $T = 0.00\overline{227}\,\mathrm{s}$; top left: reflection coefficient C_R as a function of forcing strength γ; top right: optimum reflection coefficient $C_{\mathrm{R,opt}}$ (i.e. lowest reflection coefficient that can be obtained for given $b(\mathbf{x})$ and x_d) as a function of zone thickness x_d per wavelength λ; bottom: surface elevation for several time instances per wave period near forcing zone (shaded gray) at optimum reflection coefficient for given zone thickness x_d; although reflection coefficient $C_\mathrm{R} \approx 0.1\%$ can already be obtained for $x_\mathrm{d} = 0.422\lambda$ (cf. first 'negative peak' in top right plot), then increasing or decreasing the zone thickness x_d or the wavelength λ by 8% increases the reflection coefficient C_R by two orders of magnitude

5.4 Application of 1D-theory to 2D- and 3D-flows

This section demonstrates that the wave damping behavior in two or more dimensions can be described using 1D-theory with good approximation in many practical cases. For example, waves are often reflected at or generated by bodies within the domain, and are radiated as more or less circular waves towards the domain boundaries. As a test case for such a behavior, 2D- and 3D-flow simulations are conducted using a point-like wave source. In the 2D-simulations, the source is placed in the center of a quadratic domain filled with water as shown in Fig. 29; the domain dimensions are $0 \le x, z \le 16\lambda$. In the 3D-simulations, the source is placed in the center of a cubic domain with dimensions $0 \le x, y, z \le 16\lambda$ with all domain sides set as symmetry boundary conditions.

Waves are generated for the first $8T$ of simulation time by introducing a mass source term in Eq. (26) for $3.95\,\mathrm{m} \le x, y, z \le 4.05\,\mathrm{m}$ as

$$q_c = \begin{cases} 10 \cdot \sin(-\omega t) \cdot \cos^2(\frac{\pi}{2} + \frac{\pi}{2}\frac{t}{4T})\,\frac{\mathrm{kg}}{\mathrm{s}} & \text{if } t \le 4T \\ 10 \cdot \sin(-\omega t) \cdot \cos^2(\frac{\pi}{2}\frac{t-4T}{4T})\,\frac{\mathrm{kg}}{\mathrm{s}} & \text{if } 4T < t \le 8T \\ 0 & \text{if } t > 8T \end{cases} \quad , \tag{104}$$

with time t and angular wave frequency ω. This produces a wave packet with period $T = 0.00033\,\mathrm{s}$ and wavelength $\lambda \approx 0.5\,\mathrm{m}$.

To each x- and z-normal boundary, a forcing zone according to Eq. (31) is attached to damp the waves via

$$q_x = -\gamma\left(1 - \frac{\tilde{x}}{x_\mathrm{d}}\right)^2 u \quad , \qquad q_z = -\gamma\left(1 - \frac{\tilde{z}}{x_\mathrm{d}}\right)^2 w \quad . \tag{105}$$

In the 3D-simulations, there is further a forcing zone applied to each y-normal boundary with

$$q_y = -\gamma\left(1 - \frac{\tilde{y}}{x_\mathrm{d}}\right)^2 v \quad , \tag{106}$$

with forcing strength γ, Cartesian velocity components u, v, and w, zone thickness $x_\mathrm{d} = 1\lambda$ and quadratic blending, where $\tilde{x}$, $\tilde{y}$, and $\tilde{z}$ give the shortest distance to the nearest x-, y-, and z-normal boundary. Simulations are performed for different values of γ. The reflection coefficient is calculated using Eq. (37).

The time step is $\Delta t = 1.65 \cdot 10^{-6}\,\mathrm{s} = T/200$ and 6 iterations are performed per time step. The simulated time interval is $0 \le t \le 0.00627\,\mathrm{s} = 19T$. The wave is reflected either once, when the incidence angle measured from the boundary normal is $\lesssim 27\,\mathrm{deg}$, or twice for larger angles. In the 2D-simulations, a cell size of $\Delta x = 0.00625\,\mathrm{m} \approx \lambda/80$ in both x- and z-direction is used, which results in a total of $\approx 1.6 \cdot 10^6$ cells. In the 3D-simulations, the grid was chosen substantially coarser to reduce the computational effort. Polyhedral cells with diameter of $\approx 0.02\,\mathrm{m} \approx \lambda/25$ were used, resulting in

$\approx 71.2 \cdot 10^6$ cells; although the resulting 3D-grid is rather coarse, it was considered sufficient for the present purposes, i.e. to demonstrate that 1D-theory has its value also for setting up forcing zone parameters in 2D- and 3D-simulations. The time to perform the parallel simulations was in the order of several hours (2D) or days (3D) with 12 2.6 GHz processors.

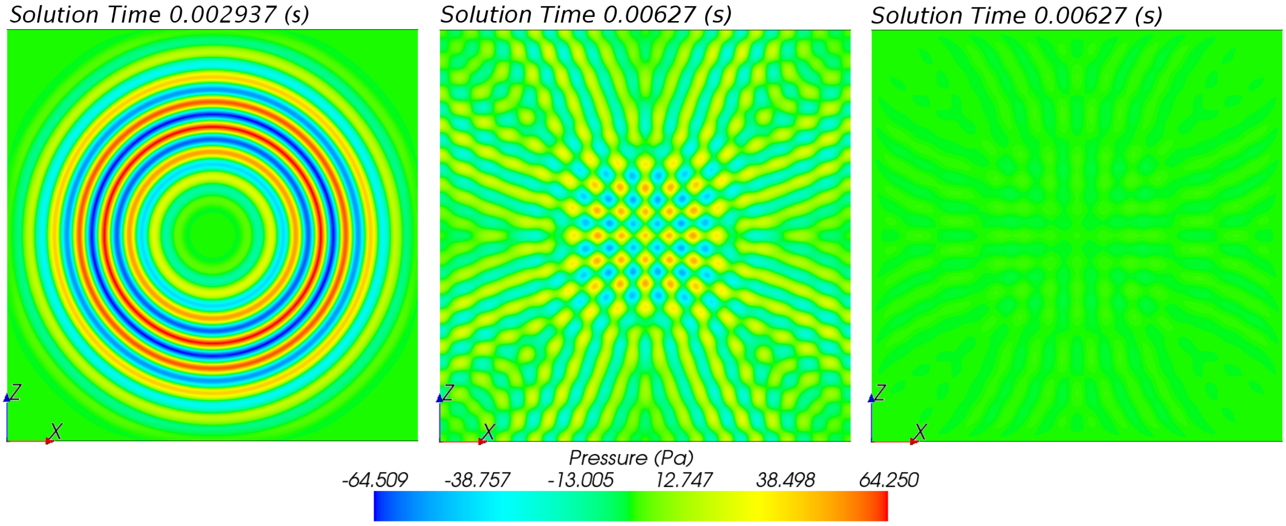

Figure 29: Pressure in 2D-domain at time $t \approx 9T$ (left) and at $t = 19T$ (middle: $\gamma = 5 \cdot 10^3\,\mathrm{s}^{-1}$ (too weak damping); right: $\gamma = 5 \cdot 10^4\,\mathrm{s}^{-1}$ ($\approx$ optimum damping))

Figures 30 and 31 show that the optimum choice for γ and the resulting reflection coefficients agree well with predictions by the 1D-theory from Sect. 4. This indicates that the damping behavior does not change substantially for moderate deviations (say $\lesssim 30$ deg) of the wave incidence angle relative to the boundary normal. Further, for larger incidence angles the waves are reflected twice before propagating back into the domain; this is expected to improve the damping since the waves encounter two forcing zones, and at least one of the two reflections must occur with incidence angle ≤ 45 deg; this explains why most simulation results for C_{R} are slightly lower than 1D-theory predictions. Thus when changing the position of the wave source, or when extending the 2D- or 3D-domains in x-, y-, or z-direction to achieve rectangular or cuboid domain shapes, comparable results can be expected. Tuning the forcing zone parameters according to 1D-theory predictions can therefore be considered sufficiently accurate for many practical 2D- and 3D-flow simulation problems.

However, if the emitted sound intensity would vary substantially with propagation direction, then parameter settings and accuracy of the 1D-theory should be assessed using 2D- and 3D-theory as given in Sects. 4.5 and 5.5.

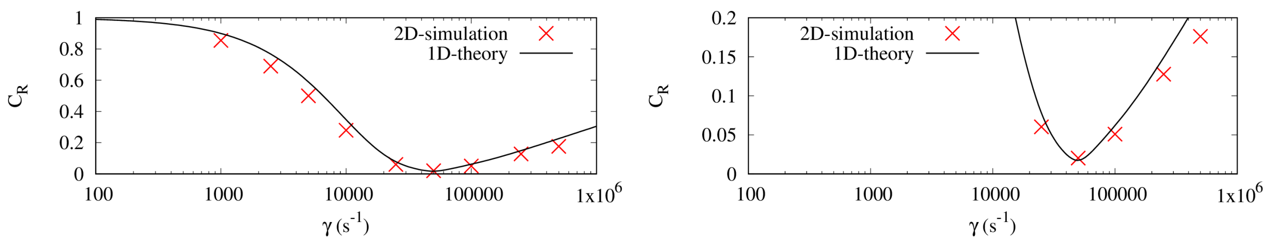

Figure 30: Reflection coefficient C_{R} as a function of forcing strength γ for 2D-simulation and 1D-theory from Sect. 4; for a 2D sound wave with period $T = 0.00033\,\mathrm{s}$ in water; for forcing of x- and z-momentum with quadratic blending via Eq. (105) and zone thickness $x_{\mathrm{d}} = 1\lambda$; for all simulation results $C_{\mathrm{R,sim}}$ and corresponding theory predictions $C_{\mathrm{R,theory}}$ holds $C_{\mathrm{R,sim}} - C_{\mathrm{R,theory}} < 0.4\%$; for the forcing strength $\gamma \geq \gamma_{\mathrm{opt,theory}}$ closest to the theoretical optimum value $\gamma_{\mathrm{opt,theory}}$ holds $C_{\mathrm{R,sim}} - C_{\mathrm{R,theory}} < 0.4\%$

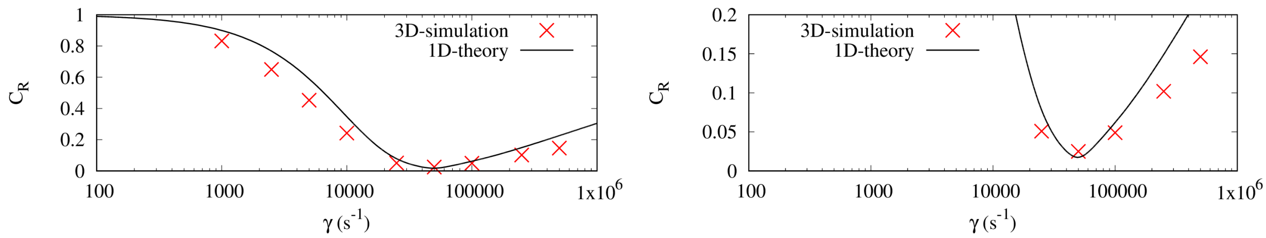

Figure 31: As Fig. 30, except for 3D-simulation and 1D-theory from Sect. 4; for all simulation results $C_{\mathrm{R,sim}}$ and corresponding theory predictions $C_{\mathrm{R,theory}}$ holds $C_{\mathrm{R,sim}} - C_{\mathrm{R,theory}} < 0.8\%$; for the forcing strength $\gamma \geq \gamma_{\mathrm{opt,theory}}$ closest to the theoretical optimum value $\gamma_{\mathrm{opt,theory}}$ holds $C_{\mathrm{R,sim}} - C_{\mathrm{R,theory}} < 0.8\%$

5.5 2D-results

To verify the 2D-theory from Sect. 4.5, 2D-flow simulations are performed based on the setup in Sect. 5.4, except that the domain dimensions are $-43\lambda \approx -21.5\,\mathrm{m} \leq x \leq 0\,\mathrm{m}$ and $0\,\mathrm{m} \leq z \leq 12.9\,\mathrm{m} \approx 26\lambda$, with coordinate system as shown in Fig. 34. The mass source term from Eq. (104) is applied for $-0.05\,\mathrm{m} \leq x \leq 0\,\mathrm{m}$ and $12.85\,\mathrm{m} \leq z \leq 12.9\,\mathrm{m}$ to generate circular waves, and there is a symmetry boundary condition at all walls to reduce the number of cells. This produces a wave packet with period $T = 0.00033\,\mathrm{s}$ and wavelength $\lambda \approx 0.5\,\mathrm{m}$. The waves are reflected at most one time at boundary $z = 0\,\mathrm{m}$, to which a forcing zone is attached according to Eq. (31)

$$q_x = -\gamma b(z) u \quad , \quad q_z = -\gamma b(z) w \quad , \tag{107}$$

with velocities u and w, forcing strength γ and quadratic blending $b(z) = ((x_\mathrm{d} - z)/x_\mathrm{d})^2$. Thus waves are reflected for continuous incidence angles in the range $0 \leq \theta \lesssim 50\,\mathrm{deg}$. Time step and cell sizes are as in Sect. 5.4. The simulated time interval is $0 \leq t \leq 0.016995\,\mathrm{s} = 51.5T$. For volume V_θ of a thin domain slice along the paths of waves reflected at $\theta = 0\,\mathrm{deg}$, $11.25\,\mathrm{deg}$, $22.5\,\mathrm{deg}$, $33.75\,\mathrm{deg}$ and $45\,\mathrm{deg}$ as indicated in Fig. 34, the energy of the reflected waves is integrated. Relating these energies for the damped ($\gamma \neq 0$) and undamped ($\gamma = 0$) case, and evaluating Eq. (37) at $t = 51.5T$ gives the reflection coefficient C_R for each angle θ.

First, flow simulations are performed with zone thickness $x_\mathrm{d} = 1\lambda$ for different forcing strengths γ. Figures 32 to 33 show that the influence of incidence angle θ on reflection coefficient C_R is satisfactorily predicted. Up to optimum forcing strength ($0 \leq \gamma \lesssim \gamma_{\mathrm{opt}}$) the predictions are highly accurate. For too strong damping ($\gamma_{\mathrm{opt}} \lesssim \gamma$) the predictions are slightly conservative. With increasing incidence angle θ, the reflection coefficient C_R decreases or stays roughly the same for most values of γ in the range of $0 \leq \theta \leq 45\,\mathrm{deg}$; only for γ close to its 1D-optimum value a significant increase in C_R occurs, since the 2D-optimum value of γ decreases when increasing θ.

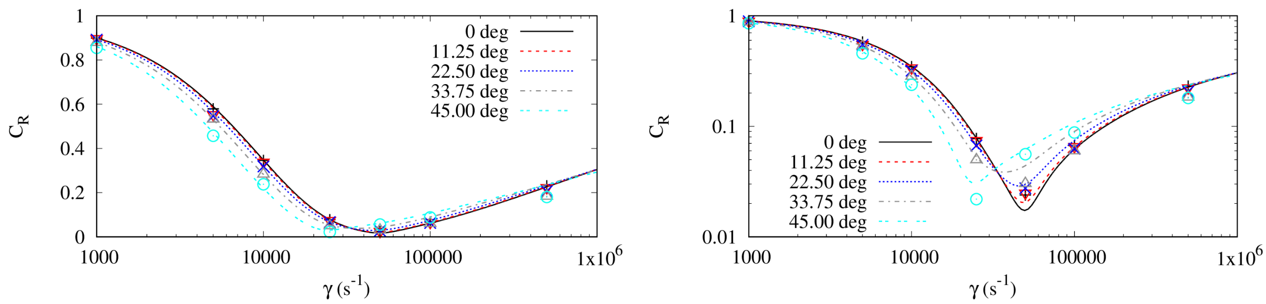

Figure 32: Reflection coefficient as a function of forcing strength γ for different incidence angles θ; for a 2D sound wave with period $T = 0.00033\,\mathrm{s}$ in water; for forcing of x- and z-momentum with quadratic blending via Eq. (107) and zone thickness $x_\mathrm{d} = 1\lambda$; for incidence angles 0 deg (+), 11.25 deg ($\bigtriangledown$), 22.5 deg ($\times$), 33.75 deg ($\triangle$), 45 deg ($\bigcirc$), and for 2D-theory (dashed lines); for all simulation results $C_{\mathrm{R,sim}}$ and corresponding theory predictions $C_{\mathrm{R,theory}}$ holds $C_{\mathrm{R,sim}} - C_{\mathrm{R,theory}} < 1.9\%$ and on average $|C_{\mathrm{R,sim}} - C_{\mathrm{R,theory}}| < 1.5\%$; for the forcing strength $\gamma \geq \gamma_{\mathrm{opt,theory}}$ closest to the theoretical optimum value $\gamma_{\mathrm{opt,theory}}$ holds $C_{\mathrm{R,sim}} - C_{\mathrm{R,theory}} < 0.7\%$

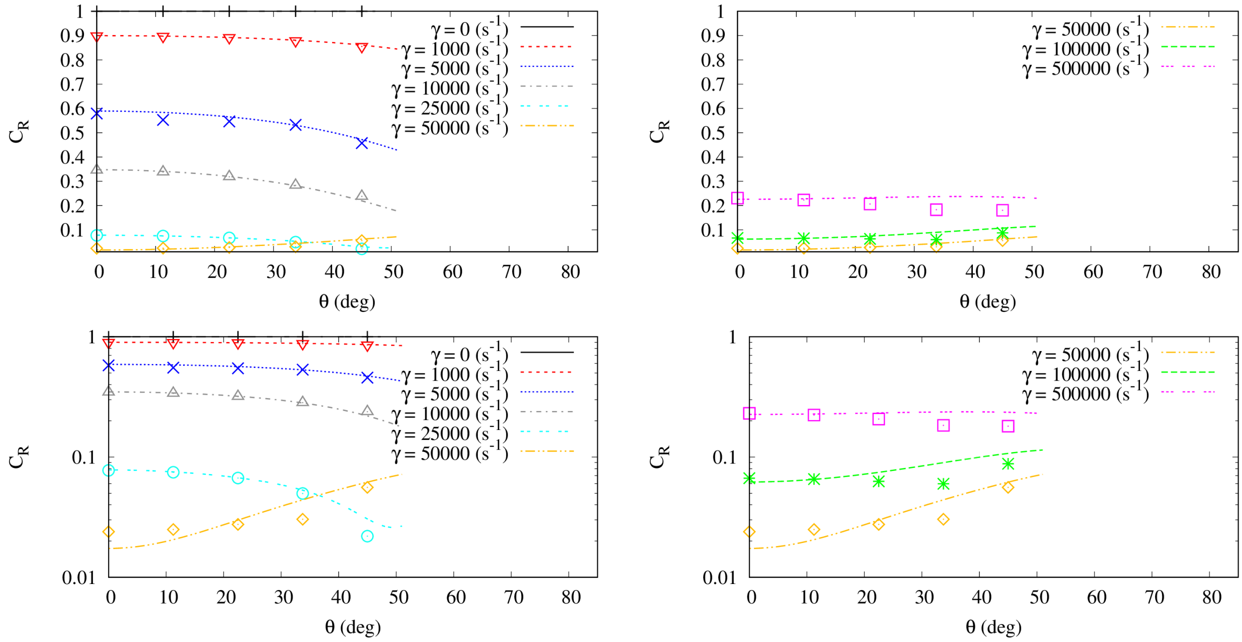

Figure 33: Reflection coefficient C_R as a function of incidence angle θ; for a 2D sound wave with period $T = 0.00033\,\mathrm{s}$ in water; for forcing of x- and z-momentum with quadratic blending via Eq. (107) and zone thickness $x_\mathrm{d} = 1\lambda$; for $\gamma \lesssim \gamma_\mathrm{opt,1D}$ (left) and for $\gamma \gtrsim \gamma_\mathrm{opt,1D}$ (right), where $\gamma_\mathrm{opt,1D} \approx 50000\,\frac{1}{\mathrm{s}}$ is the optimum forcing strength for incidence angle $\theta = 0$; for forcing strengths $\gamma = 0\,\frac{1}{\mathrm{s}}$ (+), $\gamma = 1000\,\frac{1}{\mathrm{s}}$ ($\bigtriangledown$), $\gamma = 5000\,\frac{1}{\mathrm{s}}$ ($\times$), $\gamma = 10000\,\frac{1}{\mathrm{s}}$ ($\triangle$), $\gamma = 25000\,\frac{1}{\mathrm{s}}$ ($\bigcirc$), $\gamma = 50000\,\frac{1}{\mathrm{s}}$ ($\diamond$), $\gamma = 100000\,\frac{1}{\mathrm{s}}$ ($\circledast$), $\gamma = 500000\,\frac{1}{\mathrm{s}}$ ($\square$), and for 2D-theory (dashed lines)

Further, Fig. 34 shows that for γ slightly below 1D optimum (here: $\gamma = 25000\,\mathrm{s}^{-1}$), the reflection coefficient may first decrease ($0^\circ \leq \theta \lesssim 45^\circ$), and then increase again ($\theta \gtrsim 45^\circ$); this is also predicted by 2D-theory in Fig. 33.

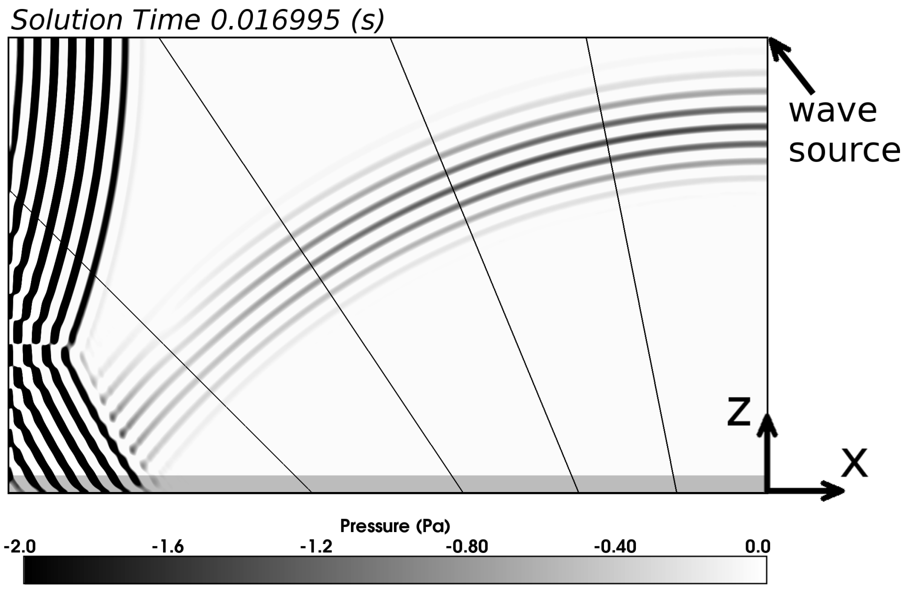

Figure 34: Pressure in domain at time $t = 51.5T$ for $\gamma = 25000\,\mathrm{s}^{-1}$; straight lines within domain denote the paths of waves reflected at incidence angles $\theta = 11.25\,\mathrm{deg}, 22.5\,\mathrm{deg}, 33.75\,\mathrm{deg}, 45\,\mathrm{deg}$ relative to boundary normal; the forcing zone (shaded gray, thickness $x_\mathrm{d} = 1\lambda$) is attached to boundary $z = 0$; the reflection coefficient decreases from 0 deg until $\approx 45\,\mathrm{deg}$, and increases for larger incidence angles, as predicted by 2D-theory (see Fig. 33)

Second, the flow simulations are repeated with zone thickness $x_\mathrm{d} = 2\lambda$. Figures 35 to 36 show that, as before, the 2D-theory from Sect. 4.5 satisfactorily predicts the reflection coefficients for incidence angles in the range of practical interest. Apart from improved damping due to the increased zone thickness, the trends of the curves are similar as before; again, for γ slightly below 1D optimum (here: $\gamma = 25000\,\mathrm{s}^{-1}$) the decrease ($0^\circ \leq \theta \lesssim 40^\circ$) and subsequent increase ($\theta \gtrsim 40^\circ$) of C_R for increasing θ is captured by 2D-theory as Figs. 36 and 37 show.

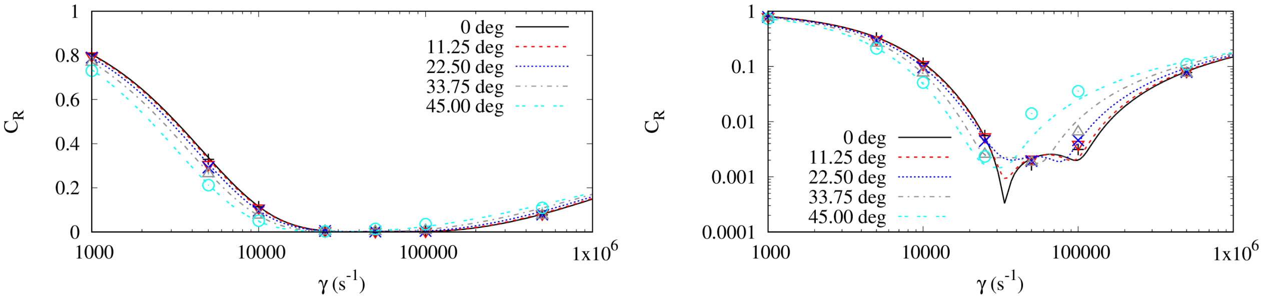

Figure 35: Reflection coefficient as a function of forcing strength γ for different incidence angles θ; for a 2D sound wave with period $T = 0.00033\,\mathrm{s}$ in water; for forcing of x- and z-momentum with quadratic blending via Eq. (107) and zone thickness $x_\mathrm{d} = 2\lambda$; for incidence angles 0 deg (+), 11.25 deg ($\bigtriangledown$), 22.5 deg ($\times$), 33.75 deg ($\bigtriangleup$), 45 deg ($\bigcirc$), and for 2D-theory (dashed lines); for all simulation results $C_{\mathrm{R,sim}}$ and corresponding theory predictions $C_{\mathrm{R,theory}}$ holds $C_{\mathrm{R,sim}} - C_{\mathrm{R,theory}} < 1.1\%$ and on average $|C_{\mathrm{R,sim}} - C_{\mathrm{R,theory}}| < 0.7\%$; for the forcing strength $\gamma \geq \gamma_{\mathrm{opt,theory}}$ closest to the theoretical optimum value $\gamma_{\mathrm{opt,theory}}$ holds $C_{\mathrm{R,sim}} - C_{\mathrm{R,theory}} < 0.07\%$

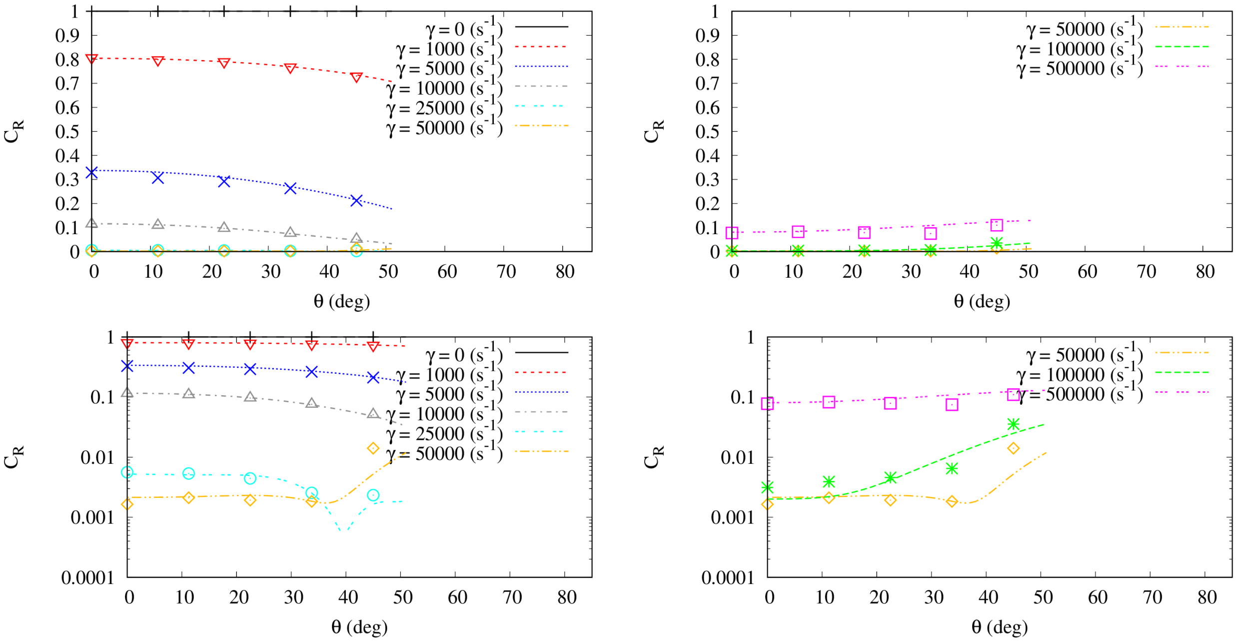

Figure 36: Reflection coefficient C_R as a function of incidence angle θ; for a 2D sound wave with period $T = 0.00033\,\mathrm{s}$ in water; for forcing of x- and z-momentum with quadratic blending via Eq. (107) and zone thickness $x_\mathrm{d} = 2\lambda$; for $\gamma \lesssim \gamma_{\mathrm{opt,1D}}$ (left) and for $\gamma \gtrsim \gamma_{\mathrm{opt,1D}}$ (right), where $\gamma_{\mathrm{opt,1D}} \approx 50000\,\frac{1}{\mathrm{s}}$ is the optimum forcing strength for incidence angle $\theta = 0$; for forcing strengths $\gamma = 0\,\frac{1}{\mathrm{s}}$ (+), $\gamma = 1000\,\frac{1}{\mathrm{s}}$ ($\bigtriangledown$), $\gamma = 5000\,\frac{1}{\mathrm{s}}$ ($\times$), $\gamma = 10000\,\frac{1}{\mathrm{s}}$ ($\bigtriangleup$), $\gamma = 25000\,\frac{1}{\mathrm{s}}$ ($\bigcirc$), $\gamma = 50000\,\frac{1}{\mathrm{s}}$ ($\diamond$), $\gamma = 100000\,\frac{1}{\mathrm{s}}$ ($\circledast$), $\gamma = 500000\,\frac{1}{\mathrm{s}}$ ($\square$), and for 2D-theory (dashed lines)

Based on the results in this section, the following procedure is recommended for practice: When using forcing zones that can be described in terms of the generic formulation given in Sect. 2.1, then 1D-theory from Sect. 4 can be used to tune the forcing zone parameters (forcing strength γ, blending function $b(x)$, zone thickness x_d) to the specific problem; in most 2D- and 3D-flow problems, the prediction for optimum forcing strength and corresponding reflection coefficient will already be sufficiently accurate for practical purposes.

If higher accuracy is needed, or if the problem is such that strong wave incidence at larger angles θ may occur, then the 2D-theory from Sect. 4.5 should be used, and with the following procedure it is possible to obtain a theory prediction for the upper bound for the overall reflection coefficient C_R. The results show that, for rectangular domains with forcing zones at all boundaries, waves that are reflected twice before traveling back into the solution domain encounter a forcing zone at least once with an angle $|\theta| \leq 45\,\mathrm{deg}$; thus then reflection coefficient C_R can be considered with good approximation to be lower or equal to the 1D-theory prediction based on the findings from Sects. 4.5, 5.4 and 5.5; if higher accuracy were required, the desired reflection coefficients could also be obtained from 2D-theory[15].

[15] For a square domain with forcing zones at all sides as in Fig. 29, if a wave segment originating from a domain part close to the center is reflected twice at a domain boundary before traveling back towards the solution domain center, then the first reflection occurs for

Therefore it suffices to look at the range for θ in which reflection occurs only once, which in most cases can be determined easily; for example for the problem in Sect. 5.4, where single reflection occurs for $|\theta| < 30\,\mathrm{deg}$, the upper bound for the overall reflection coefficient C_R for a given forcing strength γ corresponds to the maximum $C_\mathrm{R}(\theta)$ for 2D-theory in the range $|\theta| < 30\,\mathrm{deg}$. Since a 2D-theory prediction for one angle requires roughly the same computational effort as a 1D-theory prediction, a plot like Fig. 36 can be generated within a few seconds on a single core 2.6GHz processor. Problems in 3D can be reduced to 2D by considering the plane spanned by wave propagation direction and forcing zone normal vector.

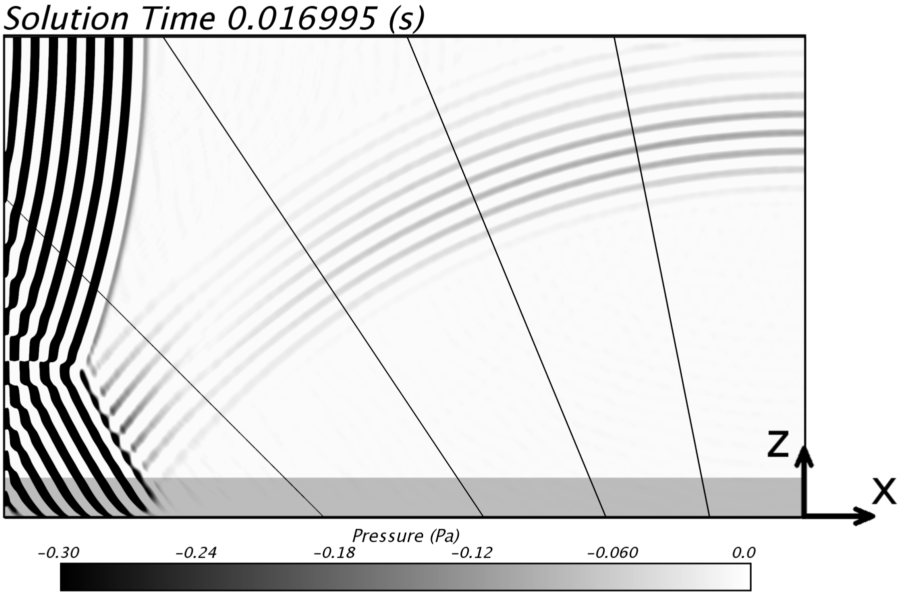

Figure 37: Pressure in domain at time $t = 51.5T$ for $\gamma = 25000\,\mathrm{s}^{-1}$; straight lines within domain denote paths of waves reflected at incidence angles $\theta = 11.25\,\mathrm{deg}, 22.5\,\mathrm{deg}, 33.75\,\mathrm{deg}, 45\,\mathrm{deg}$, measured between wave propagation direction and boundary normal; the forcing zone (shaded gray, thickness $x_\mathrm{d} = 2\lambda$) is attached to boundary $z = 0$; the reflection coefficient decreases from 0 deg until $\approx 40\,\mathrm{deg}$, and increases for larger incidence angles, as predicted by 2D-theory (see Fig. 36)

5.6 Damping of highly nonlinear (hydro-)acoustic waves in 1D- and 2D-flows

This section investigates the capability of forcing zones for damping of highly nonlinear 1D and 2D (hydro-)acoustic waves. Nonlinear sound waves occur in a variety of applications, such as biomedical imaging (Spadoni and Daraio, 2010), sound generation of musical instruments (Myers et al., 2012), or medical use of ultrasound (Lerch et al., 2009). Nonlinear sound waves can change their shape the further they travel. For example, they tend to take a saw-toothed shape as seen in Fig. 38 when they travel a sufficient distance, see e.g. Lerch et al. (2009) for a detailed discussion.

For the 1D-flow simulations, the setup from Sect. 5.1 is used with the following modifications. The domain has dimensions $0 \le x \le 23.87\,\mathrm{m} \approx 30.2\lambda$. At boundary $x = L_x \approx 30.2\lambda$, pressure $p(t)$ is prescribed to generate waves traveling in negative x-direction. The opposite boundary $x = 0$ is a fully reflective wall, to which a forcing zone with exponential blending according to Eq. (9) and forcing according to Eq. (31) with reference solution $u_\mathrm{ref} = 0$ is attached to damp the waves. The simulations are performed for air as ideal gas with temperature variations accounted for via Eq. (28) and speed of sound $c \approx 347.28\,\frac{\mathrm{m}}{\mathrm{s}}$. The mesh size is $\Delta x = 0.0062504\,\mathrm{m} \approx \lambda/125$ and 10 iterations are performed per time-step $\Delta t = 1.1\overline{36}\,\mathrm{s} \approx T/200$.

At the inlet, pressure $p(t)$ is prescribed to generate the saw-tooth wave packet shown in Fig. 38 via

$$p(t) = \begin{cases} 10 \cdot \left(\frac{t \mod T}{T} - 5.0\right) \cdot \cos^2\!\left(\frac{\pi}{2} + \frac{\pi}{2}\frac{t}{4T}\right)\mathrm{Pa} & \text{if } t \le 4T \\ 10 \cdot \left(\frac{t \mod T}{T} - 5.0\right)\mathrm{Pa} & \text{if } 4T < t < 6T \\ 10 \cdot \left(\frac{t \mod T}{T} - 5.0\right) \cdot \cos^2\!\left(\frac{\pi}{2}\frac{t-6T}{4T}\right)\mathrm{Pa} & \text{if } 6T < t \le 10T \\ 0 & \text{if } t > 10T \end{cases}, \tag{108}$$

with time t, modulo operator '$\mod$', and angular wave frequency $\omega = 2\pi/T$, and wave period $T = 0.00\overline{227}\,\mathrm{s}$.

incidence angle $0\,\mathrm{deg} \le \theta_1 \le 90\,\mathrm{deg}$ with reflection coefficient $C_{\mathrm{R}_{\theta_1}}$, and the second reflection occurs at incidence angle $\theta_2 = 90\,\mathrm{deg} - \theta_1$ with reflection coefficient $C_{\mathrm{R}_{\theta_2}}$. The overall reflection coefficient C_R for this wave segment is then $C_\mathrm{R} = C_{\mathrm{R}_{\theta_1}} \cdot C_{\mathrm{R}_{\theta_2}}$.

The simulations start at $t = 0$ and end at $t = 0.11\overline{36}\,\mathrm{s}$, when the whole wave packet has encountered the forcing zone once. Flow simulations are performed for different values of forcing strength γ and zone thickness x_{d}. The reflection coefficient is calculated according to Eq. (37).

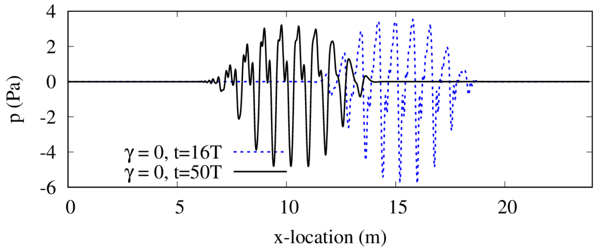

Figure 38: Pressure as a function of x-location from simulations without forcing (i.e. $\gamma = 0$), before ($t \approx 16T$) and after ($t \approx 50T$) reflection at boundary $x = 0$

Figure 39 shows that the theory satisfactorily predicts the optimum setting of γ and the corresponding reflection coefficients C_{R}.

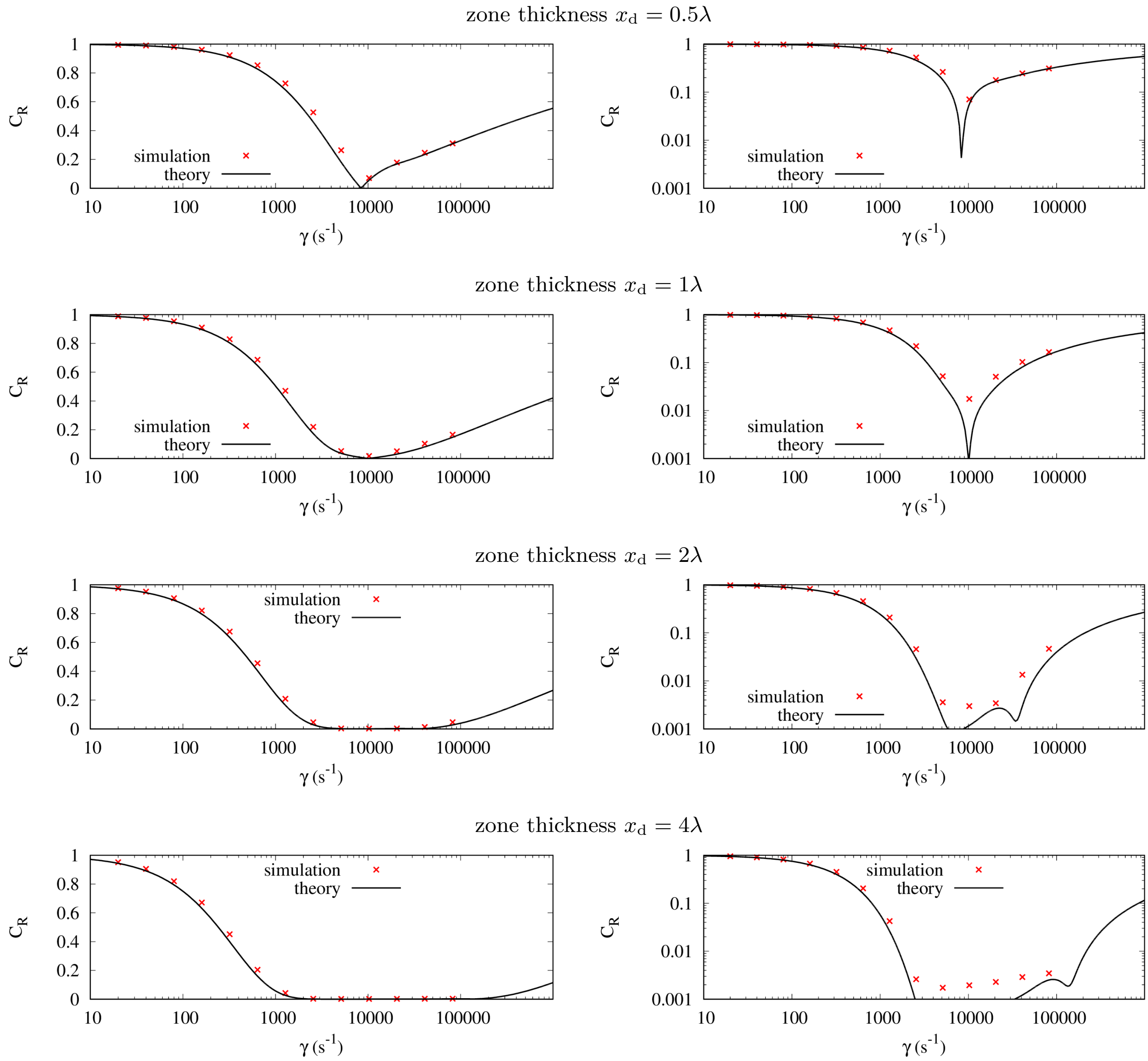

Figure 39: Reflection coefficient C_{R} as a function of forcing strength γ from simulations and 1D-theory; for a highly nonlinear wave train with period $T = 0.00\overline{227}\,\mathrm{s}$ in an ideal gas; for forcing of x-momentum via Eq. (31) with exponential blending via Eq. (9); for all simulation results $C_{\mathrm{R,sim}}$ and corresponding theory predictions $C_{\mathrm{R,theory}}$ holds $C_{\mathrm{R,sim}} - C_{\mathrm{R,theory}} < 8.3\%$ and on average $|C_{\mathrm{R,sim}} - C_{\mathrm{R,theory}}| < 2.1\%$; for the forcing strength $\gamma \geq \gamma_{\mathrm{opt,theory}}$ closest to the theoretical optimum value $\gamma_{\mathrm{opt,theory}}$ holds $C_{\mathrm{R,sim}} - C_{\mathrm{R,theory}} < 1.7\%$ ($x_{\mathrm{d}} \leq 1\lambda$) and $< 0.2\%$ ($x_{\mathrm{d}} \geq 2\lambda$)

Compared to the results for nearly linear sound waves in Sects. 5.2, the reflection coefficients for close-to-optimum tuning in Fig. 39 are slightly under-predicted though; thus for highly nonlinear waves, it is recommended to select the zone thickness slightly thicker than theoretically necessary, so that the desired reflection coefficient is obtained.

In the following, the capability of forcing zones for damping of highly nonlinear pressure waves for 2D-wave-propagation in water is investigated. For this, flow simulations are performed with the same setup as in Sect. 5.4, except that instead of a sine wave a saw-tooth wave is generated. The saw-tooth wave has a $\cos^2$-type blending-in/-out and is generated by introducing the following mass source term in Eq. (26) within the domain part $3.95\,\mathrm{m} \le x, y, z \le 4.05\,\mathrm{m}$ as

$$q_\mathrm{c} = \begin{cases} 10 \cdot \left(\frac{t \mod T}{T} - 5.0\right) \cdot \cos^2\!\left(\frac{\pi}{2} + \frac{\pi}{2}\frac{t}{4T}\right) \frac{\mathrm{kg}}{\mathrm{s}} & \text{if } t \le 4T \\ 10 \cdot \left(\frac{t \mod T}{T} - 5.0\right) \cdot \cos^2\!\left(\frac{\pi}{2}\frac{t-4T}{4T}\right) \frac{\mathrm{kg}}{\mathrm{s}} & \text{if } 4T < t \le 8T \\ 0 & \text{if } t > 8T \end{cases} , \tag{109}$$

with time t, modulo operator ' mod ', and angular wave frequency ω. This produces a highly nonlinear wave packet with period $T = 0.00033\,\mathrm{s}$ and wavelength $\lambda \approx 0.5\,\mathrm{m}$.

Figures 40 and 41 demonstrate that the 1D-theory satisfactorily predicts the optimum values for the case-dependent parameters of the forcing zones. Further, theory predictions and simulation results for the corresponding reflection coefficients agree well, with simulation results being slightly lower than theory predictions. Therefore, the theory is recommended for tuning forcing zones in flow simulations with highly nonlinear (hydro-)acoustic waves. Since the results for liquid water and air as an ideal gas agree well, the findings are expected to apply also to other mediums for sound wave propagation.

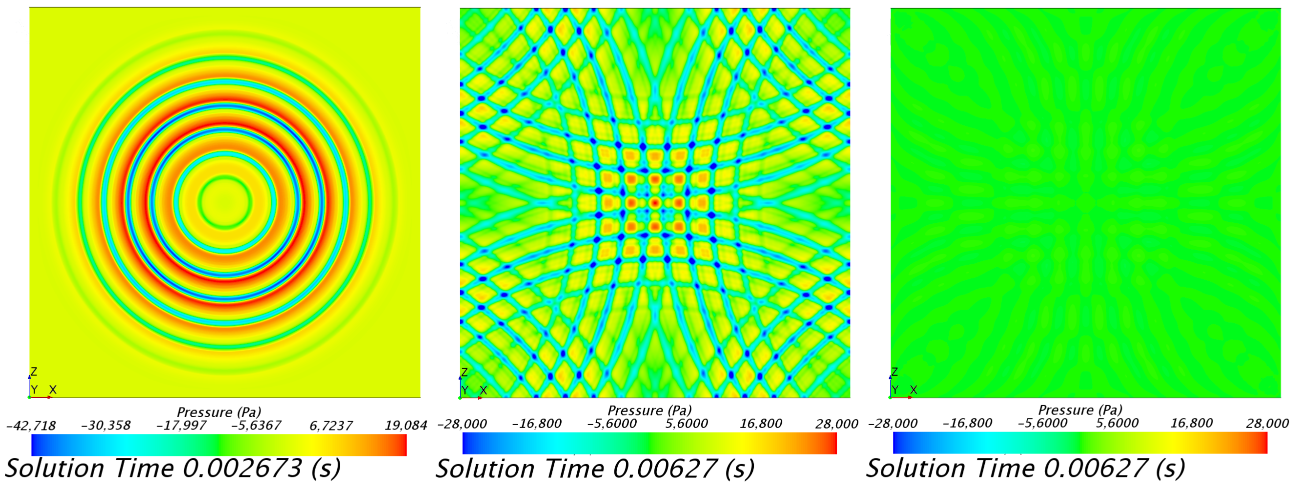

Figure 40: Pressure in 2D-domain for nonlinear sound wave in water at time $t \approx 8T$ (left) and at $t = 19T$ (middle: no damping ($\gamma = 0\,\mathrm{s}^{-1}$); right: close-to-optimum damping ($\gamma = 5 \cdot 10^4\,\mathrm{s}^{-1}$)); for forcing of all fluid velocities towards $u_{i,\mathrm{ref}} = 0$ with quadratic blending according to Eq. (105) and zone thickness $x_\mathrm{d} = 1\lambda$

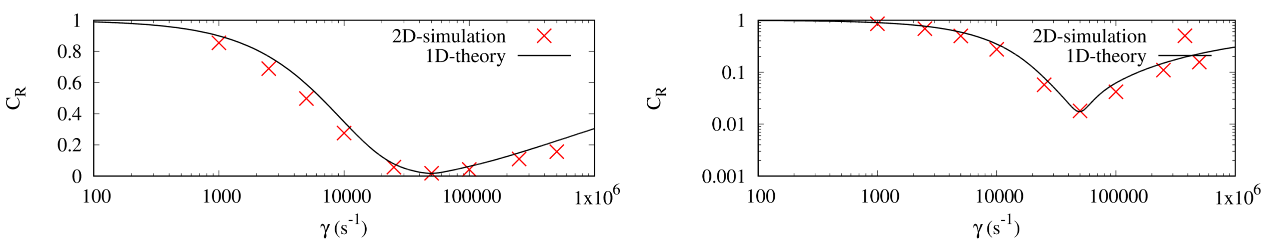

Figure 41: Reflection coefficient C_R as a function of forcing strength γ for 2D-simulations with nonlinear sound waves in water and 1D-theory from Sect. 4.3; for forcing according to Eq. (105) with zone thickness $x_\mathrm{d} = 1\lambda$ and forcing of all fluid velocities towards zero; for all simulation results $C_{\mathrm{R,sim}}$ and corresponding theory predictions $C_{\mathrm{R,theory}}$ holds $C_{\mathrm{R,sim}} - C_{\mathrm{R,theory}} < 0.06\%$; for the forcing strength $\gamma \ge \gamma_{\mathrm{opt,theory}}$ closest to the theoretical optimum value $\gamma_{\mathrm{opt,theory}}$ holds $C_{\mathrm{R,sim}} - C_{\mathrm{R,theory}} < 0.06\%$

5.7 Simultaneous generation and damping of (hydro-)acoustic waves

This section investigates to which extent the theory predicts reflection coefficients C_R for forcing zones which simultaneously generate waves and reduce undesired wave reflections. For this, a standing pressure wave is simulated based on the setup from Sect. 5.1, with the following modifications.

Figure 42 shows the simulation domain with dimensions $0 \leq x \leq L_x$ with $L_x \approx 3.5448\,\mathrm{m} \approx 4.49\lambda$. The fluid is air as ideal gas with temperature variations accounted for via Eq. (28). At the inlet boundary $x = 0$, a monochromatic wave is generated by prescribing velocity as

$$u_\mathrm{ref} = u_\mathrm{a} \sin(-\omega t + kx) \quad , \tag{110}$$

with reference velocity amplitude $u_\mathrm{a} = 0.4331\,\mathrm{m/s}$, angular wave frequency $\omega = 2\pi/T$, wave period $T = 0.002\overline{27}\,\mathrm{s}$, wave number $k = 2\pi/\lambda$, wavelength $\lambda \approx 0.789\,\mathrm{m}$, location x in wave propagation direction, and time t.

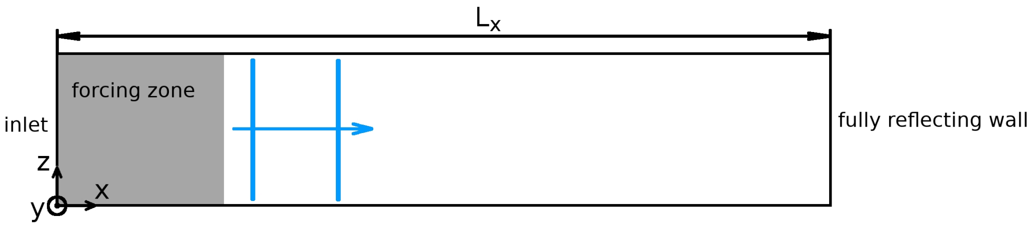

Figure 42: Solution domain with wave-generating forcing zone (shaded gray) opposite to a fully reflecting wall boundary

Attached to the inlet is a forcing zone for x-momentum according to Eq. (31) with source term

$$q_x = \gamma b(x)(u_\mathrm{ref} - u) \quad , \tag{111}$$

with forcing strength γ, quadratic blending function $b(x)$ according to Eq. (5), velocity u, reference velocity u_ref according to Eq. (110), and forcing zone thickness $x_\mathrm{d} = 2\lambda$. Thus the solution is forced towards the desired, monochromatic wave traveling in positive x-direction.

The wave travels through the domain, is perfectly reflected at the no-slip wall boundary $x = L_x$, and then travels back towards the inlet, so that the superposition of generated and reflected wave forms a perfect standing wave. This is the intended solution for the present simulations, corresponding to a reflection coefficient of $C_\mathrm{R} = 1$ within the domain.

Without the forcing zone, the reflected wave would reach the inlet again after traveling a distance of $2L_x \approx 8.98\lambda$. The following re-reflection at the inlet would then produce nearly perfect constructive interference due to the negligible phase difference, resulting in a standing wave of roughly twice the amplitude as before ($C_\mathrm{R} \approx 2$). To avoid this worst-case solution, the forcing zone is tuned using the theory from Sect. 4 to minimize undesired re-reflections and obtain the target solution with $C_\mathrm{R} = 1$.

The mesh size is $\Delta x \approx 0.00438\,\mathrm{m} = \lambda/180$ and the time-step size is $\Delta t \approx 5.682 \cdot 10^{-6}\,\mathrm{s} \approx T/400$. Per time-step, 5 iterations are performed with under-relaxation of 0.8 for velocities, 0.2 for pressure, and 0.9 for energy. The simulated time interval is $0 \leq t \leq 0.046\,\mathrm{s} \approx 20.24T$.

The potential and kinetic energies on interval $2.0\,\mathrm{m} \leq x \leq 3.544\,\mathrm{m}$ are recorded as a function of time according to Eq. (38). Note that energy $E \propto C_R^2 \propto u_\mathrm{a}^2$, so the superposition of two standing waves with same amplitude u_a results in four times larger peaks in energies E_pot and E_kin compared to a single standing wave with amplitude u_a, as shown in Fig. 44.

The reflection coefficient is obtained from the maximum kinetic and potential energies during the time interval $0.043\,\mathrm{s} \leq t \leq 0.046\,\mathrm{s}$, i.e. when re-reflections have fully developed, compared to the time interval $0.018\,\mathrm{s} \leq t \leq 0.022\,\mathrm{s}$, i.e. when the desired standing wave is fully developed but no re-reflections are present yet, via

$$C_\mathrm{R} = \sqrt{\frac{\max\left(E_\mathrm{kin} + E_\mathrm{pot}|_{\gamma,\, 0.043\,\mathrm{s} \leq t \leq 0.046\,\mathrm{s}}\right)}{\max\left(E_\mathrm{kin} + E_\mathrm{pot}|_{\gamma = 0\,\mathrm{s}^{-1},\, 0.018\,\mathrm{s} \leq t \leq 0.022\,\mathrm{s}}\right)}} \quad , \tag{112}$$

Figures 43 to 46 demonstrate that the theory from Sect. 4 is suitable also for forcing zones where the reference solution is unsteady. For too weak forcing, wave reflections accumulate so that a standing wave with a larger than desired amplitude occurs ($C_{\mathrm{R}} \approx 2$ without forcing (i.e. $\gamma = 0$)). For too strong forcing, most undesired reflections occur close to the entrance of the forcing zone; since the effective location of reflection changes with forcing strength γ, undesired wave reflections will interfere destructively or constructively with the reference wave depending on their phase difference. Thus recorded reflection coefficients may be larger or smaller than the target value of $C_{\mathrm{R}} = 1$; the corresponding deviation margins are satisfactorily predicted by theory as Fig. 46 shows. For close-to-optimum forcing, the desired standing wave with amplitude $2u_{\mathrm{a}}$ is obtained, which corresponds to a reflection coefficient of $C_{\mathrm{R}} = 1$; the solution is periodic and shows no noticeable accumulation of undesired reflections.

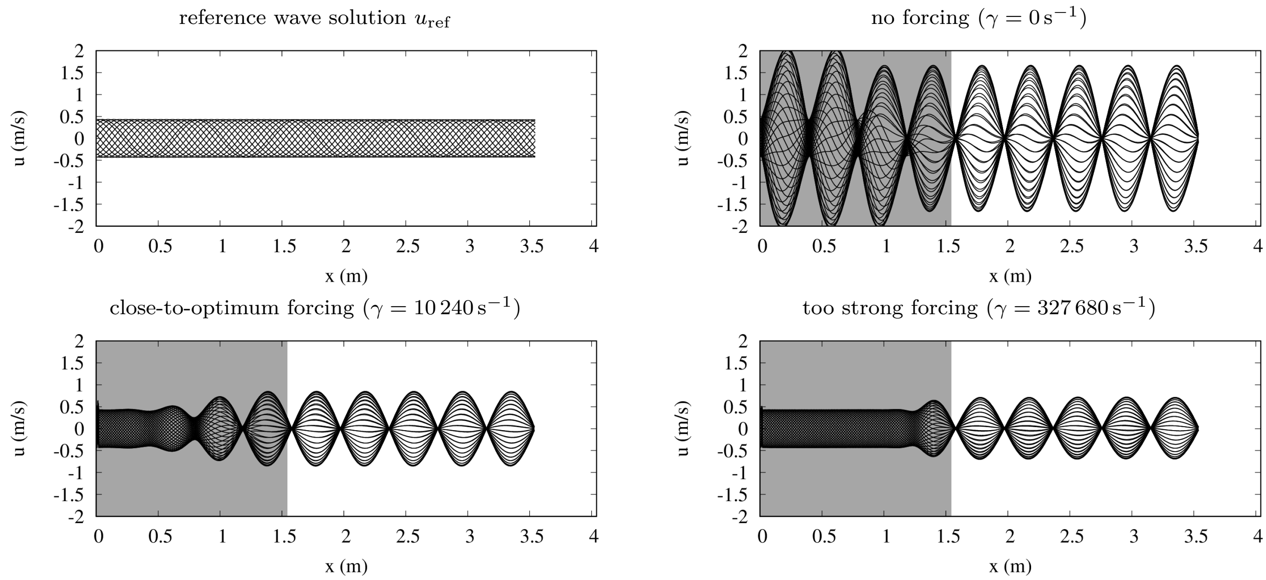

Figure 43: Velocity u as a function of x-location for several equally spaced time-instances during the last simulated wave period; for close-to-optimum tuning of the forcing zone (shaded gray), the desired periodic standing-wave solution is obtained

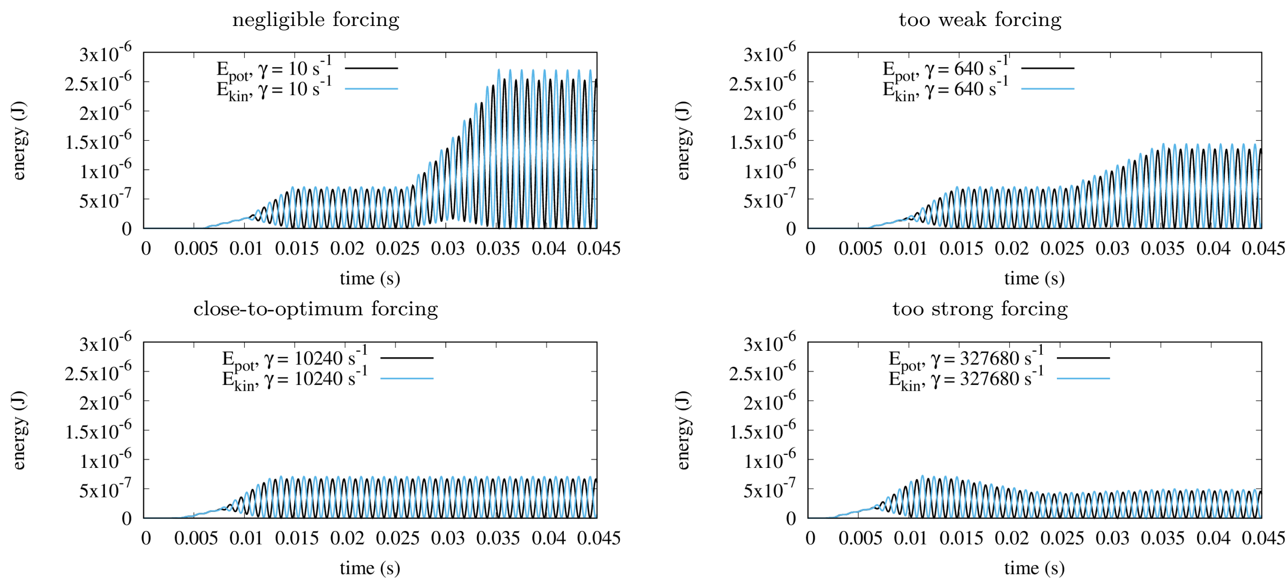

Figure 44: Potential and kinetic energy as a function of time in domain part $2.0\,\mathrm{m} \leq x \leq 3.544\,\mathrm{m}$; since this interval ($\approx 1.95\lambda$) is no perfect multiple of the wavelength, the peaks of E_{kin} are roughly 8% higher than peaks of E_{pot}, which was verified to have no significant influence on the results; a perfect standing wave occurs ca. during 0.015 s to 0.025 s; the additional superposition of the wave re-reflected at the inlet occurs ca. from 0.036 s to 0.045 s

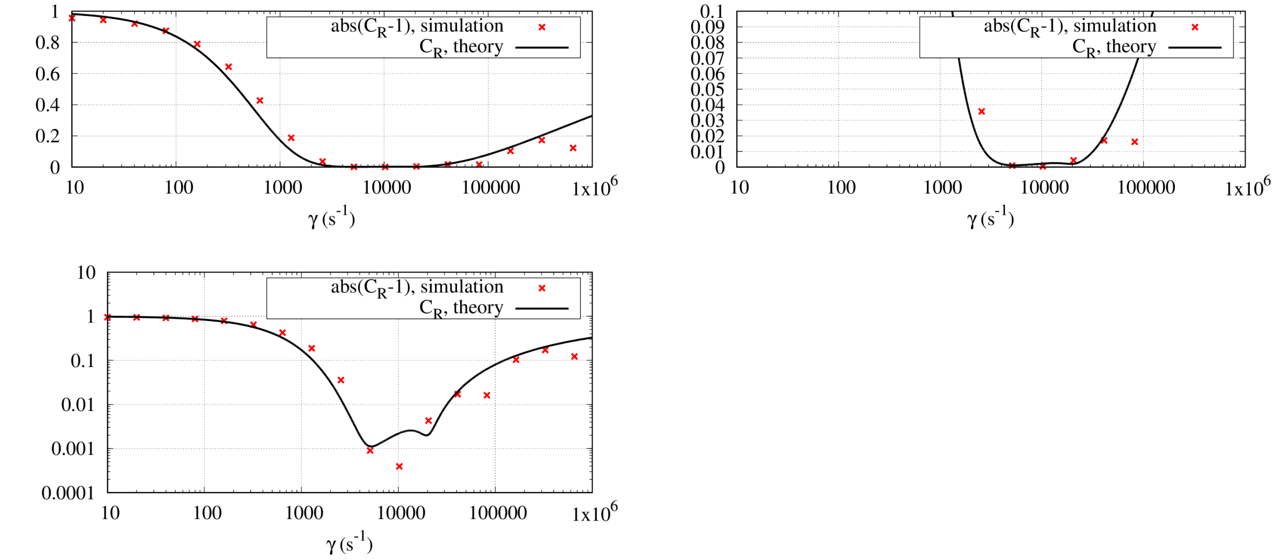

Figure 45: Simulation results for the absolute deviation of the reflection coefficient C_{R} from its target value $C_{\mathrm{R}} = 1$ as a function of forcing strength γ; for a standing wave with period $T = 0.002\overline{27}\,\mathrm{s}$, forcing of x-momentum via Eq. (111) with quadratic blending via Eq. (5), zone thickness $x_{\mathrm{d}} = 2\lambda$, and reference solution u_{ref} according to Eq. (110); for all simulation results $C_{\mathrm{R,sim}}$ and corresponding theory predictions $C_{\mathrm{R,theory}}$ holds $|C_{\mathrm{R,sim}} - 1| - C_{\mathrm{R,theory}} < 10.5\%$; for the forcing strength $\gamma \geq \gamma_{\mathrm{opt,theory}}$ closest to the theoretical optimum value $\gamma_{\mathrm{opt,theory}}$ holds $|C_{\mathrm{R,sim}} - 1| - C_{\mathrm{R,theory}} < -0.2\%$

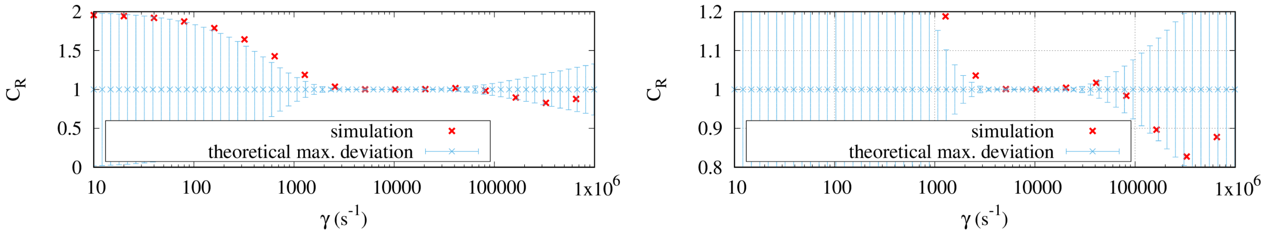

Figure 46: Simulation results for reflection coefficient C_{R} as a function of forcing strength γ for the case in Fig. 45, and theoretical deviation margins from target solution $C_{\mathrm{R}} = 1$

To raise awareness that the presence of undesired wave reflections can sometimes be difficult to detect, the simulations are repeated with a larger domain size of $L_x \approx 4.0467\,\mathrm{m}$ and an accordingly increased simulated time interval of $0 \leq t \leq 0.05\,\mathrm{s}$.

In this case, the distance a wave travels from the inlet ($x = 0$) to the reflecting wall ($x = L_x$) and back to the inlet is $2L_x \approx 10.25\lambda$. Thus for no or too weak forcing, the resulting phase difference relative to the generated wave leads to partial destructive interference, so the superposition of reference and re-reflected wave produces a standing wave with an amplitude of significantly less than the $4u_\mathrm{a}$ obtained in the previous simulations.

Therefore, although for the smallest γ-values in Figs. 47 and 48 there is nearly complete reflection at the inlet boundary, this does not show in the values for reflection coefficient C_R, since depending on the phase difference the values may lie anywhere within the range given by theory. However, for close to optimum forcing, results agree well as before and a periodic solution is obtained.

The findings demonstrate that the theory is suitable for tuning forcing zones with unsteady reference solutions, regardless of the phase difference between the reference wave and the wave entering the forcing zone.

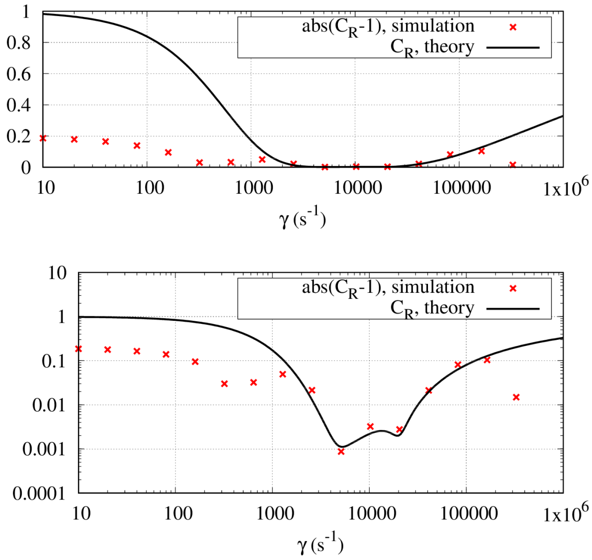

Figure 47: As Fig. 45, except for different domain size $L_x \approx 4.047\,\mathrm{m}$ and thus a different phase between generated and re-reflected wave, which results in different destructive interference and thus reflection coefficients C_R can be lower than theoretically predicted; for all simulation results $C_\mathrm{R,sim}$ and corresponding theory predictions $C_\mathrm{R,theory}$ holds $|C_\mathrm{R,sim} - 1| - C_\mathrm{R,theory} < 1.8\%$; for the forcing strength $\gamma \geq \gamma_\mathrm{opt,theory}$ closest to the theoretical optimum value $\gamma_\mathrm{opt,theory}$ holds $|C_\mathrm{R,sim} - 1| - C_\mathrm{R,theory} < 0.1\%$

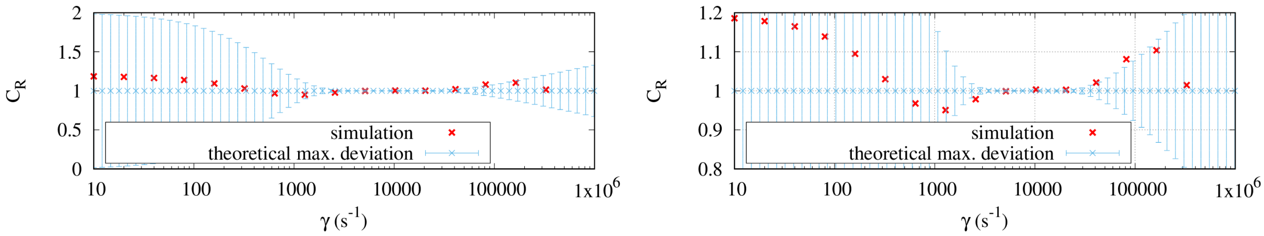

Figure 48: As Fig. 46, except for different domain size $L_x \approx 4.047\,\mathrm{m}$; as before, the C_R-values stay roughly within the theoretically expected deviation margins

6 Forcing zones for free-surface waves in 2D-flow simulations

Key findings

- Theory predictions for reflection coefficient C_R and flow inside the forcing zone agree closely for forcing of horizontal fluid momentum
- If forcing is applied to the vertical fluid momentum (as well), then the flow becomes more complex and simulation results for C_R can be significantly lower than theory predictions; however, the theory still captures the relevant flow features, so predictions for optimum forcing parameters and corresponding reflection coefficients are satisfactory
- When correctly tuned, there appears to be no preference for introducing source terms to one governing equation over the other, so similar reflection coefficients C_R can be expected
- The theory gives satisfactory results for a wide range of wave steepnesses, regular and irregular waves, under shallow-water and deep-water conditions

In this section, the theory from Sect. 4.1 is validated via results from finite-volume-based 2D-flow simulations with long-crested waves. The simulation setup is given in Sect. 6.1.

For forcing of horizontal fluid momentum in Sect. 6.2, theory predictions and simulation results agreed closely, both for the flow within the forcing zone and for the reflection coefficients C_R (average difference of $< 0.9\%$).

In contrast, for forcing of (also) the vertical fluid momentum in Sects. 6.3 to 6.5, not all flow features were captured by the theory, and for some forcing strengths γ (especially for γ-values larger than optimum) reflection coefficients C_R were significantly lower than theory predictions. However, since the optimum values of the forcing zone parameters and the corresponding reflection coefficients C_R were satisfactorily predicted, it was argued that the relevant flow features were captured by the theory regardless of which governing equations the forcing source terms are applied to.

Section 6.6 demonstrates that the wave's nonlinearity has a negligible influence on the forcing zone behavior.

Section 6.7 shows that the reflection coefficient for irregular waves can be predicted using two approaches. The more accurate approach is to compute the reflection coefficient for each wave component of the spectrum. The more practical approach is to evaluate the theory for a regular wave with the same period as the irregular wave's peak period, i.e. the period for which the wave energy spectrum takes its largest value; this approach satisfactorily predicted the optimum tuning of the forcing zone; however, since it slightly under-predicted the corresponding reflection coefficients, it is suggested to choose the zone thickness slightly larger than theoretically necessary to reliably obtain the intended reduction of undesired wave reflections.

Section 6.8 shows that the theory predictions hold in shallow water as well, demonstrating that the theory applies in all water depths of practical engineering interest.

Section 6.9 discusses two widely-used implementations of forcing zones, followed by a discussion of theory implications regarding the tuning of forcing zones with special focus on the choice of blending functions in Sect. 6.10.

When the forcing zone was tuned using the theory, in all simulations from Sect. 6 held $C_\mathrm{R,sim} - C_\mathrm{R,theory} < 2.4\%$, with reflection coefficients from simulation results $C_\mathrm{R,sim}$ and the corresponding theory predictions $C_\mathrm{R,theory}$. Thus the theory predictions were considered to be of satisfactory accuracy for engineering practice.

6.1 Simulation setup

In the following, the setup for the flow simulations in Sect. 6.2 to 6.5 is given. Unless mentioned otherwise, as e.g. for the setup modifications given in Sects. 6.6 to 6.9, the setup applies for the simulations in Sect. 6.

The commercial flow solver STAR-CCM+ version 11.06.010-R8 from Siemens (formerly CD-adapco) is used for the simulations. The governing Eqs. are (17) to (19). The volume of fluid (VOF) method is used to account for the two fluid phases, liquid water and gaseous air, using the high resolution interface capturing scheme (HRIC) as given in Muzaferija and Perić (1999). The governing equations are applied to each cell and discretized according to the finite volume method. All integrals are approximated by the midpoint rule. The interpolation of variables from cell center to face center and the numerical differentiation are performed using linear shape functions, leading to approximations of second order. The integration in time is based on assumed quadratic variation of variables in time, which is also a second-order approximation. Each algebraic equation contains the unknown value from the cell center and the centers of all neighboring cells with which it shares common faces. The resulting coupled equation system is then linearized and solved by the iterative STAR-CCM+ implicit unsteady segregated solver, using an algebraic multigrid method with Gauss-Seidel relaxation scheme, V-cycles for pressure and volume fraction of water, and flexible cycles for velocity calculation. The under-relaxation factor is 0.9 for velocities and volume fraction and 0.4 for pressure. For each time step, eight iterations are performed; one iteration consists of solving the governing equations for the velocity components, the pressure-correction equation (using the SIMPLE method for collocated grids to obtain the pressure values and to correct the velocities) and the transport equation for the volume fraction of water. Further information on the discretization of and solvers for the governing equations can be found in Ferziger and Perić (2002) or the STAR-CCM+ software manual.

Regular long-crested free-surface waves are created and propagate in positive x-direction towards a forcing zone as sketched in Fig. 7, where they are partly reflected and partly absorbed. The waves have height $H = 0.16\,\mathrm{m}$, period $T = 1.6\,\mathrm{s}$, wavelength $\lambda \approx 4\,\mathrm{m}$ and are moderately nonlinear (steepness H/λ is $\approx 29\%$ of the maximum steepness). Deep-water conditions apply ($h/\lambda \geq 0.5$ with water depth h).

The forcing approaches from Sect. 2.3 are used to minimize wave reflections. Simulations are either performed with forcing of x-momentum (q_x), of z-momentum (q_z), of both x- and z-momentum (q_x, q_z), or of volume fraction α and x- and z-momentum (q_α, q_x, q_z). The forcing zone has exponential blending according to Eq. (9) and the solution is forced towards the calm-surface solution. Forcing zone thicknesses x_d in the range between 0.25λ and 2λ are investigated.

The simulations are performed quasi-2D, i.e. with only one layer of cells in y-direction and symmetry boundary conditions applied to the y-normal boundaries. The domain has dimensions $0 \leq x \leq L_x$ and $-h \leq z \leq 0.5\lambda$, with domain length $L_x = 6\lambda$ and water depth $h = 4.5\lambda$.

The volume fraction and velocities in the solution domain are initialized according to Fenton's (1985) 5^{th}-order Stokes wave theory to reduce the simulation time. The wave is generated by prescribing the volume fraction and velocities according to Fenton's (1985) 5^{th}-order Stokes wave theory at the inlet boundary ($x = 0$).

Due to the Stokes drift of the fluid particles in the wave, the inlet produces a net mass flux into the domain, which acts to raise the mean water level; by prescribing the hydrostatic pressure at either the vertical boundary to which the forcing zone is attached ($x = L_x$) or the bottom boundary ($z = -h$), such an undesired accumulation of mass can be avoided. Perić and Abdel-Maksoud (2015) found that the first option can lead to low-frequency fluctuations in the amount of mass within the domain, since the forcing zone can delay how the pressure boundary regulates the amount of mass within the domain; prescribing the pressure at the domain bottom resolved this problem. In practice however, it is far more common to prescribe the pressure at the boundary to which the forcing zone is attached. For this reason, all cases investigated in this work were simulated with pressure prescribed at boundary $x = L_x$.

Additionally, the simulations with $x_\mathrm{d} = 2\lambda$ from Figs. 51 and 58 were repeated with pressure prescribed at the bottom boundary $z = -h$ and vertical boundary $x = L_x$ set to no-slip wall. The results confirmed that the choice for the pressure boundary does not significantly influence the reflection coefficients (on average $< 1\%$ difference).

Therefore in practice, the theory presented in this work can be used for both boundary choices. Yet from an academical point of view, there is a difference: as illustrated in Fig. 49, prescribing the pressure at the vertical boundary $x = L_x$ produces a node in the surface elevation at that boundary; when the boundary condition for $x = L_x$ is set to wall instead, there occurs a maximum amplification point. The theory in Sect. 4.1 is derived for the latter case. Thus in Sect. 6, comparisons of surface elevation with theory (Figs. 52 and 59) are given for the simulations with pressure prescribed at the domain bottom for better comparison; all other results are given for pressure prescribed at $x = L_x$, because this approach is primarily used in practice and the observed difference in results for the reflection coefficient between the two approaches were insignificant.

All remaining boundaries are no-slip walls. For further details on boundary conditions, see Ferziger and Perić (2002).

The domain is discretized using a rectilinear grid with local mesh refinement around the free surface. The free surface stays at all times within the region of the finest mesh with 100 cells per wavelength and 16 cells per wave height. The computational grid, which consists of $\approx 43\,000$ cells, is shown in Fig. 50. The total simulated time is $18\,\mathrm{s} \approx 11.3T$ with a time step of $\Delta t = T/1000$. The reflection coefficient C_R is calculated via Eq. (34).

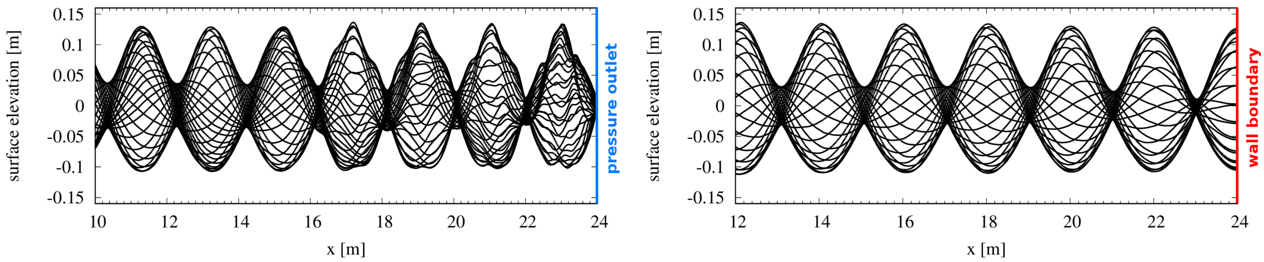

Figure 49: Simulated free-surface elevation for equally spaced time instances during the last simulated wave period, with vertical boundary $x = L_x = 24\,\mathrm{m}$ set as prescribed pressure (left image, node at $x = 24\,\mathrm{m}$) or wall boundary (right image, maximum amplification at $x = 24\,\mathrm{m}$); results from Sect. 6.2 for $x_\mathrm{d} = 2\lambda$ and weak damping ($\gamma = 0.625\,\mathrm{rad/s}$)

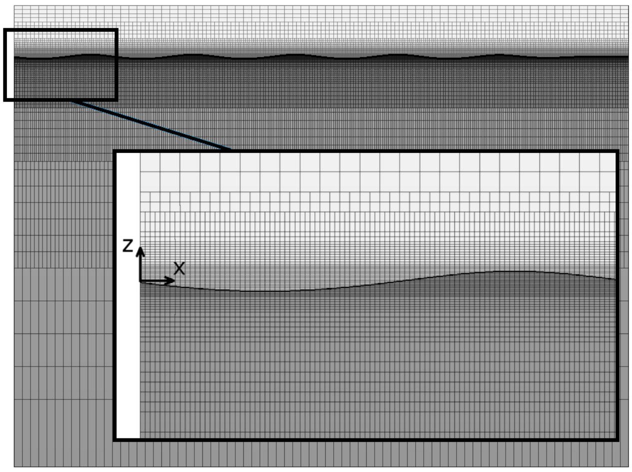

Figure 50: Computational grid with close-up, showing the initialized location of the free surface (thick black curve) and of the liquid phase (shaded dark gray)

6.2 Results for forcing of x-momentum

Flow simulations are carried out with the setup from Sect. 6.1 and compared to the theory presented in Sect. 4.1. Forcing of x-momentum according to Eq. (20) with exponential blending from Eq. (9) is used to damp waves with period $T = 1.6\,\mathrm{s}$ and height $H = 0.16\,\mathrm{m}$. Simulations are performed for different values of forcing strength γ and zone thickness x_d.

Comparing simulation results and theory in Figs. 51 and 52 shows that the theory predicts reflection coefficient C_R with high accuracy. Although the waves are moderately nonlinear ($\approx 29\%$ of maximum steepness), the differences between theory predictions and simulation results are small.

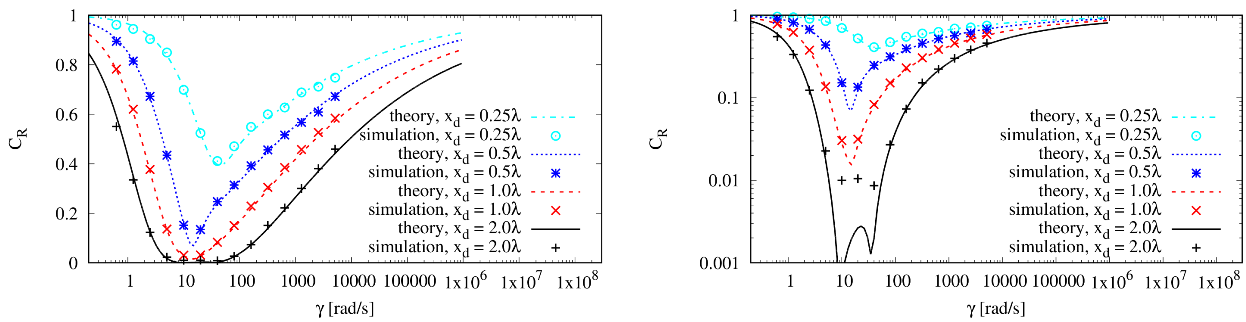

Figure 51: Theory predictions and simulation results for reflection coefficient C_R as a function of forcing strength γ; for deep-water waves with period $T = 1.6\,\mathrm{s}$; for forcing of x-momentum with exponential blending via Eq. (9) and different values of zone thickness x_d; the theory predicts reflection coefficient C_R with high accuracy; for all simulation results $C_\mathrm{R,sim}$ and corresponding theory predictions $C_\mathrm{R,theory}$ holds $C_\mathrm{R,sim} - C_\mathrm{R,theory} < 2.4\%$ and on average $|C_\mathrm{R,sim} - C_\mathrm{R,theory}| < 0.9\%$; for the forcing strength $\gamma \geq \gamma_\mathrm{opt,theory}$ closest to the theoretical optimum value $\gamma_\mathrm{opt,theory}$ holds $C_\mathrm{R,sim} - C_\mathrm{R,theory} < 2.4\%$ ($x_\mathrm{d} = 0.25\lambda$) and $< 1.1\%$ ($x_\mathrm{d} \geq 0.5\lambda$)

The close-up in Fig. 51 right shows that simulation results were not able to reproduce reflection coefficients below $\approx 1\%$, see e.g. the curve for $x_\mathrm{d} = 2\lambda$ at $\gamma \approx 20\,\mathrm{rad/s}$ in the right plot in Fig. 51; this was attributed to a background noise in the approach for calculating C_R possibly due to the interface-capturing and -sharpening schemes.

Further, while for the thinner zones ($x_\mathrm{d} < 1.5\lambda$) in Fig. 51 there is a single optimum for forcing strength γ, for thicker zones ($x_\mathrm{d} = 2\lambda$) there is more than one local optimum.

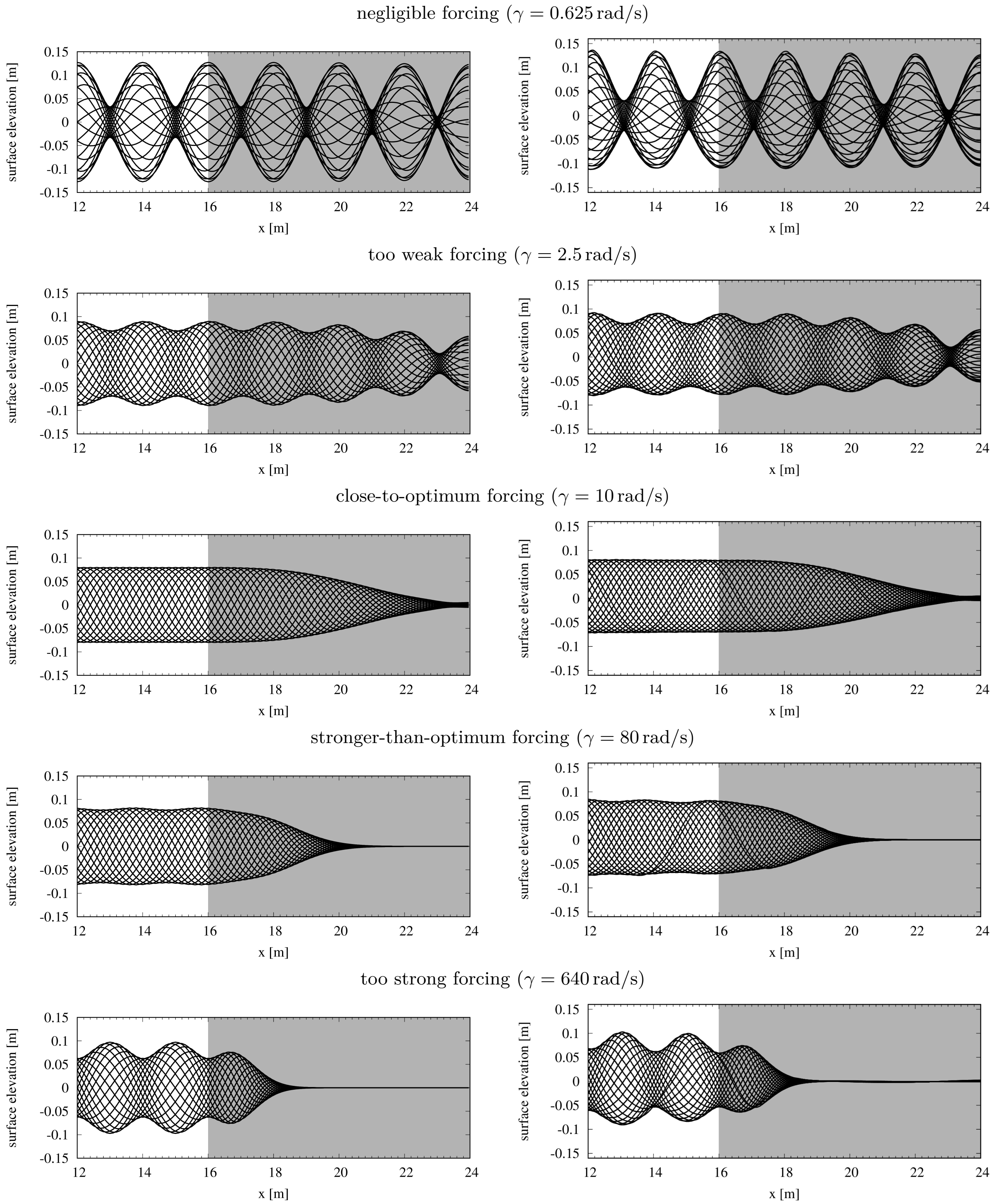

Figure 52: Theory predictions (left) and simulation results (right) for surface elevation as a function of x-coordinate, evaluated for equally spaced time intervals during the last simulated period; with a forcing zone (shaded gray) with forcing of x-momentum, exponential blending via Eq. (9) and zone thickness $x_\mathrm{d} = 2\lambda$, for different values of forcing strength γ; the theory predicts the surface elevation with high accuracy

Figure 52 explains why in Fig. 51 the reflection coefficient C_R increases for stronger than optimum forcing, i.e. for $\gamma > \gamma_\mathrm{opt}$ with γ_opt being the forcing strength at which the lowest value for C_R occurs.

For too weak forcing (i.e. forcing strength $\gamma < \gamma_\mathrm{opt}$), the wave is mainly reflected at the domain boundary to which the forcing zone is attached (here $x = 24\,\mathrm{m}$), as seen in the upper two images in Fig. 52. Since the main reflection location is the same, the peaks in the wave height envelope stay at the same positions.

For close-to-optimum forcing (i.e. forcing strength $\gamma \approx \gamma_\mathrm{opt}$), the wave is partially reflected throughout the forcing zone and the wave heights of these partially reflected waves are small compared to the original wave's height, so that destructive interference of these partial reflections improves the wave absorption and the forcing zone's reflection coefficient C_R is minimized.

For too strong forcing (i.e. forcing strength $\gamma > \gamma_\mathrm{opt}$), the wave is mainly reflected close to the entrance of the forcing zone (here $x = 16\,\mathrm{m}$), as seen in the lower two images in Fig. 52. The remaining part of the forcing zone does not contribute significantly to the wave damping, since there the surface elevations and velocities are negligible; thus essentially the same solution could be obtained if these domain parts were not there at all, i.e. if a smaller computational domain were used. With increasing forcing strength γ the effective reflection location moves closer towards the entrance of the forcing zone, which can be seen from the different locations of the peaks in the wave height envelope. This underlines the importance of including reflections which occur within the zone in the analysis.

The simulated and theoretical surface elevations agree well as shown in Fig. 52. Just as the surface elevations, the theory predictions for horizontal and vertical velocities agree well with simulation results; since there are no significant differences, these are not plotted here.

Figure 53 shows that the forcing produces vorticity (here: $\frac{\partial w}{\partial x} - \frac{\partial u}{\partial z}$) in the flow field within the forcing zone. Although the generated amount of vorticity is comparatively small, it is clearly visible. Further, small amounts of vorticity are also generated at the free surface and at locations where the mesh size changes, as artifacts of the interface capturing scheme and the discretization; however, such a vorticity generation is discretization dependent, i.e. it disappears on infinitely fine grids, whereas the forcing-generated vorticity turned out to be grid-independent.

Figure 54 shows that the theory predicts the forcing-based vorticity generation remarkably well.

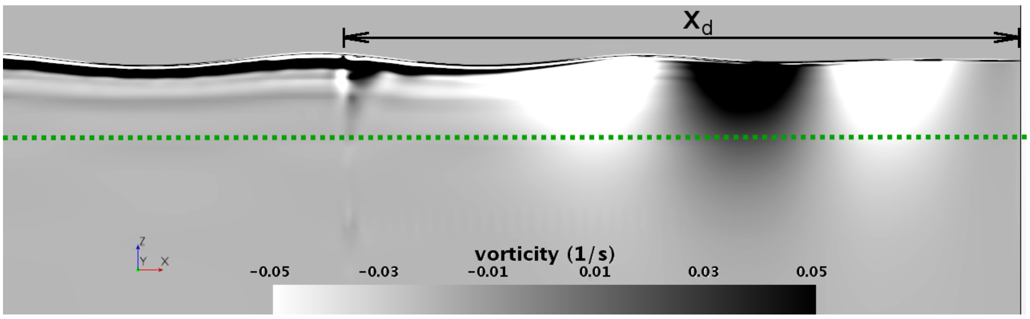

Figure 53: Simulation results at time $t = 18\,\mathrm{s}$ for vorticity in a domain section including the forcing zone with zone thickness $x_\mathrm{d} = 2\lambda$; for forcing of x-momentum with exponential blending via Eq. (9) and forcing strength $\gamma = 10\,\mathrm{rad/s}$; the dotted green line denotes depth $z = -1.2\,\mathrm{m}$ where vorticity is evaluated in Fig. 54

While the velocities and particle displacements are continuous everywhere within the domain according to the theory given in Sect. 4.1, evaluating vorticity $\frac{\partial w}{\partial x} - \frac{\partial u}{\partial z}$ for the theory shows that the vorticity is continuous within each zone, as well as at each interface between two zones where the blending function $b(x)$ has the same value. When $b(x)$ changes between two adjacent zones, then the vorticity must be discontinuous at the interface between these zones.

To show that this is realistic and occurs in the flow simulations as well, the simulations are repeated using a strongly discontinuous blending function $b(x)$ as depicted in Fig. 55

$$b(x) = \begin{cases} 0.25 & \text{if } 16\,\mathrm{m} \le x < 18\,\mathrm{m} \quad , \\ 0.5 & \text{if } 18\,\mathrm{m} \le x < 20\,\mathrm{m} \quad , \\ 0.75 & \text{if } 20\,\mathrm{m} \le x < 22\,\mathrm{m} \quad , \\ 1.0 & \text{if } 22\,\mathrm{m} \le x \le 24\,\mathrm{m} \quad , \\ 0 & \text{else} \quad , \end{cases} \tag{113}$$

with forcing zone thickness $x_{\mathrm{d}} = 24\,\mathrm{m} - 16\,\mathrm{m} = 8\,\mathrm{m} \approx 2\lambda$.

Figures 56 and 57 show that, as predicted by theory, also in the flow simulations the vorticity is discontinuous between cells where $b(x)$ changes, and is continuous otherwise; the agreement between theory and simulation was again satisfactory, as is exemplarily shown for $\gamma = 10\,\mathrm{rad/s}$ in Fig. 57.

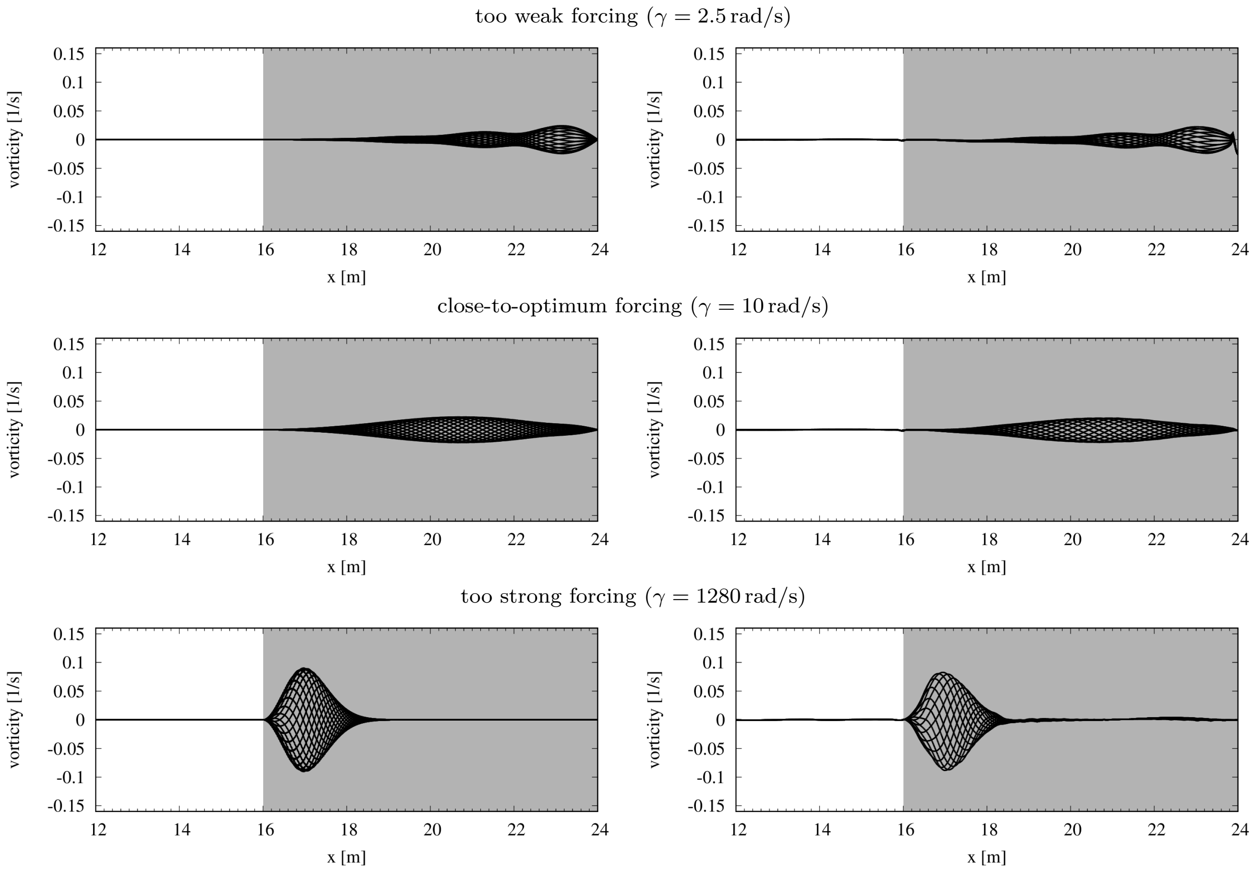

Figure 54: Vorticity as a function of x-coordinate for theory (left) and simulation (right); evaluated at $z = -1.2\,\mathrm{m}$ below the free-surface for equally spaced time intervals during the last simulated period; for forcing of x-momentum with exponential blending via Eq. (9) and zone thickness $x_{\mathrm{d}} = 2\lambda$; theory predictions for vorticity in forcing zone (shaded gray) are highly accurate

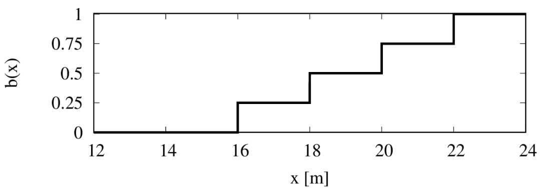

Figure 55: Discontinuous blending function $b(x)$ according to Eq. (113) as a function of x-coordinate

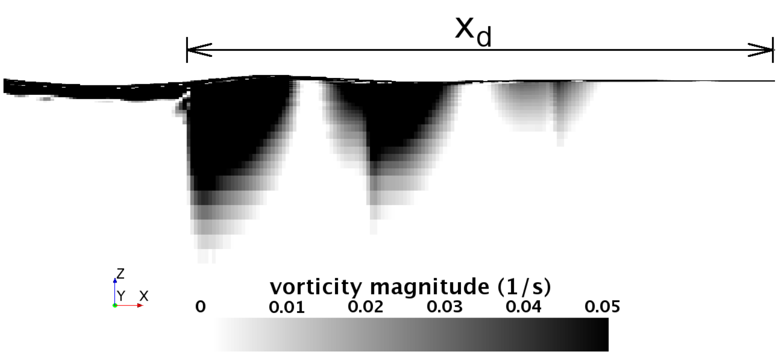

Figure 56: Simulation results at time $t \approx 17.06\,\mathrm{s}$ for vorticity magnitude in domain section including the forcing zone, for forcing of x-momentum with forcing strength $\gamma = 10\,\mathrm{rad/s}$, zone thickness $x_{\mathrm{d}} = 8\,\mathrm{m}$, and step-like blending according to Eq. (113)

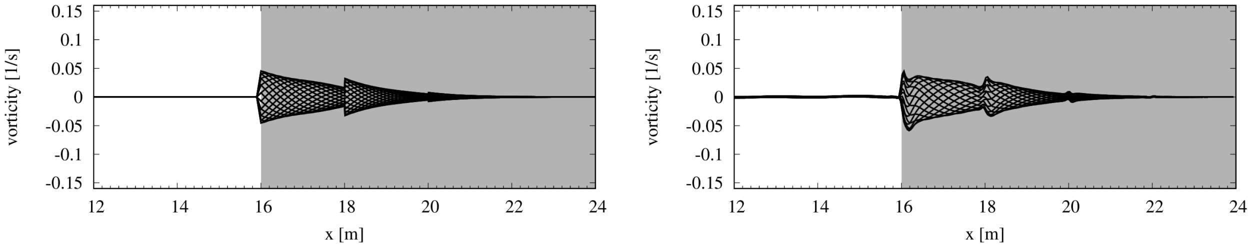

Figure 57: Vorticity as a function of x-coordinate for theory (left) and simulation (right); evaluated at depth $z = -1.2$ m below the free-surface for equally spaced time intervals during the last simulated period; for forcing of x-momentum with forcing strength $\gamma = 10$ rad/s, zone thickness $x_{\mathrm{d}} = 8$ m and step-like blending according to Eq. (113)

Thus the theory from Sect. 4.1 predicts reflection coefficient C_{R} and the whole flow inside the forcing zone with high accuracy.

6.3 Results for forcing of z-momentum

The simulations from Sect. 6.2 are repeated with forcing of z-momentum instead of x-momentum. Comparing Figs. 58 and 59 with Figs. 51 to 52 shows that, when the source term strength increases comparatively slowly, for example for zone thickness $x_{\mathrm{d}} \geq 1\lambda$ and close-to-optimum or lower values ($\gamma \lesssim 40$ rad/s) of forcing strength γ, the results for forcing of x- and z-momentum both agree well with theory predictions.

When the source term strength increases comparatively rapidly, though, simulation results for C_{R} are lower than theory predictions, as for example for zone thickness $x_{\mathrm{d}} = 0.5\lambda$, or for too strong forcing ($\gamma \gtrsim 40$ rad/s), where most wave reflections occur over a comparatively short interval close to the entrance of the forcing zone as shown in the bottom images in Fig. 59. For such cases, the flow becomes more complex than for forcing of horizontal momentum. For example, Fig. 59 shows that for such γ-values the mean surface elevation can increase within the forcing zone, which becomes more pronounced with increasing forcing strength γ. Thus stronger-than-optimum forcing of z-momentum leads to a noticeable net mass flux into the forcing zone in the simulation. In the present case, this mass flux resulted in a lower reflection coefficient C_{R} compared to x-momentum forcing for the same γ.

However, the relevant flow behavior was satisfactorily predicted, since the theory predictions for the optimum forcing strength γ and the corresponding reflection coefficients C_{R} agree well with the simulation results.

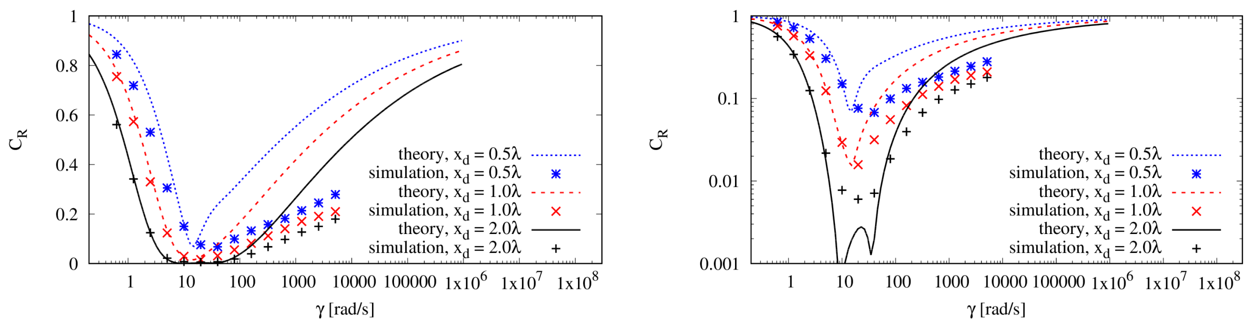

Figure 58: Theory predictions and simulation results for reflection coefficient C_{R} as a function of forcing strength γ; for deep-water waves with period $T = 1.6$ s; for forcing of z-momentum with exponential blending via Eq. (9) and different values of zone thickness x_{d}; the theory satisfactorily predicts optimum forcing strength γ and corresponding reflection coefficient C_{R}; for all simulation results $C_{\mathrm{R,sim}}$ and corresponding theory predictions $C_{\mathrm{R,theory}}$ holds $C_{\mathrm{R,sim}} - C_{\mathrm{R,theory}} < 0.8\%$; for the forcing strength $\gamma \geq \gamma_{\mathrm{opt,theory}}$ closest to the theoretical optimum value $\gamma_{\mathrm{opt,theory}}$ holds $C_{\mathrm{R,sim}} - C_{\mathrm{R,theory}} < 0.8\%$

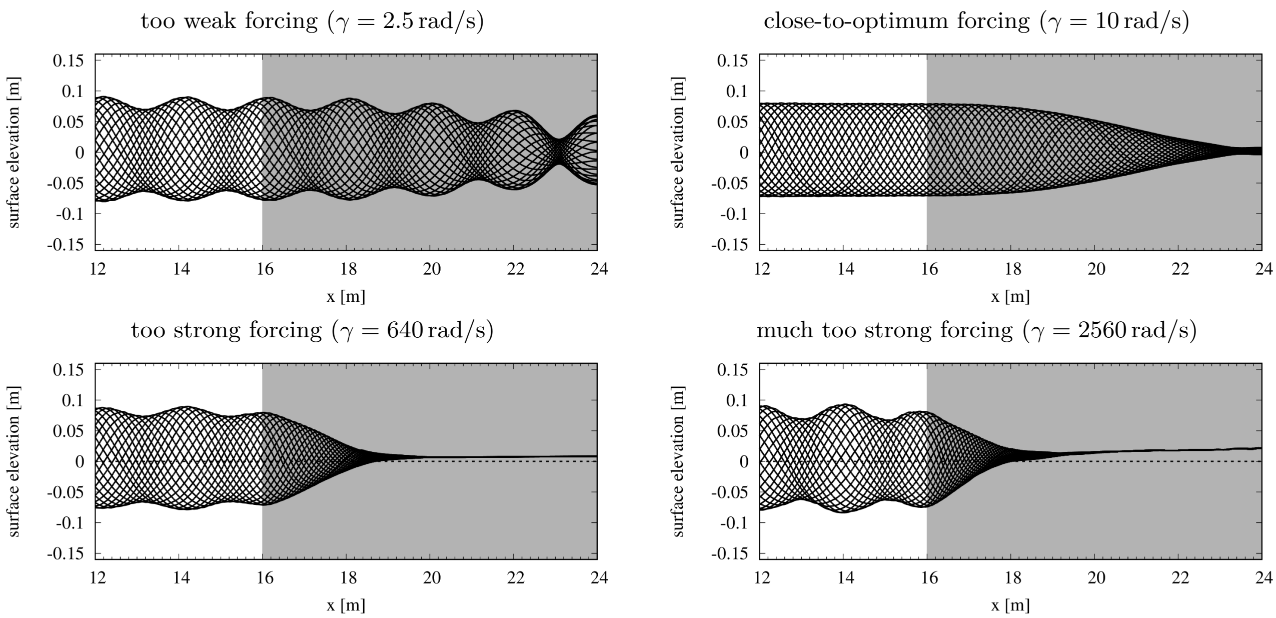

Figure 59: Simulation results for surface elevation as a function of x-coordinate for forcing of z-momentum, exponential blending via Eq. (9) and forcing zone (shaded gray) thickness $x_\mathrm{d} = 2\lambda$; evaluated for equally spaced time intervals during the last simulated period; for $\gamma \lesssim$ than optimum (upper two plots) there are no noticeable differences to x-momentum forcing (compare Fig. 52); for stronger than optimum damping (lower two plots) a rise in water level (the dashed line indicates the undisturbed free surface) occurs close to the domain boundary at $x = 24\,\mathrm{m}$, which indicates a net mass flux into the forcing zone that does not occur for x-momentum forcing

6.4 Results for forcing of x- and z-momentum

Repeating the simulations from Sect. 6.2 with forcing of both x- and z-momentum shows that the theory, with the extension given in Sect. 4.1.2, reliably predicts the optimum forcing strength γ and the corresponding reflection coefficient C_R. As expected from the results in Sects. 6.2 and 6.3, Fig. 60 shows that for stronger than optimum forcing the theory overpredicts the reflection coefficients.

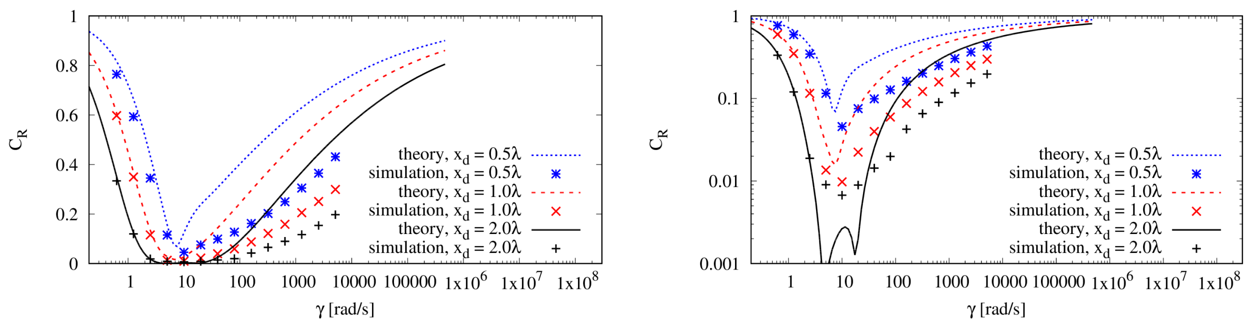

Figure 60: Theory predictions and simulation results for reflection coefficient C_R as a function of forcing strength γ; for deep-water waves with period $T = 1.6\,\mathrm{s}$; for forcing of x- and z-momentum with exponential blending via Eq. (9) and different values of zone thickness x_d; for all simulation results $C_\mathrm{R,sim}$ and corresponding theory predictions $C_\mathrm{R,theory}$ holds $C_\mathrm{R,sim} - C_\mathrm{R,theory} < 0.9\%$; for the forcing strength $\gamma \geq \gamma_\mathrm{opt,theory}$ closest to the theoretical optimum value $\gamma_\mathrm{opt,theory}$ holds $C_\mathrm{R,sim} - C_\mathrm{R,theory} < 0.9\%$

6.5 Results for forcing of volume fraction α and x- and z-momentum

Repeating the simulations from Sect. 6.2 with forcing of volume fraction α and both x- and z-momentum shows that the theory, with the extension given in Sect. 4.1.2, satisfactorily predicts the optimum forcing strength and the corresponding reflection coefficient. Figure 61 shows that for stronger than optimum damping the theory overpredicts the reflection coefficients, otherwise the results agree well.

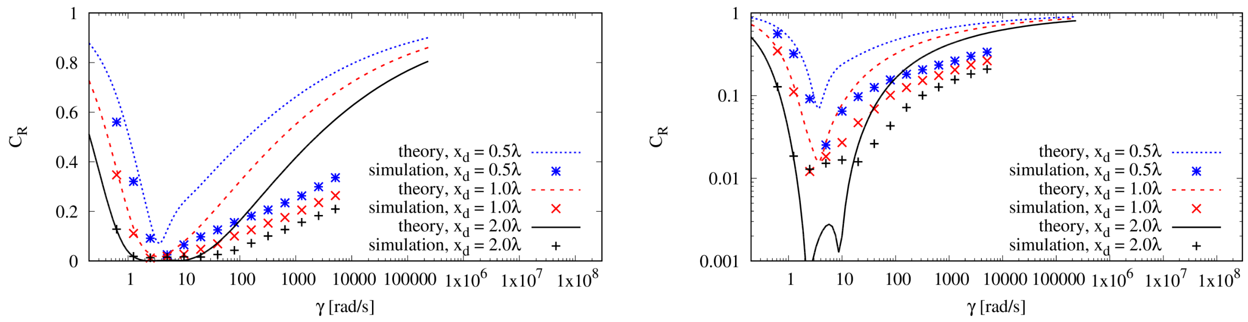

Figure 61: Theory predictions and simulation results for reflection coefficient C_{R} as a function of forcing strength γ; for deep-water waves with period $T = 1.6\,\mathrm{s}$; for forcing of x- and z-momentum and volume fraction α, with exponential blending via Eq. (9) and different values of zone thickness x_{d}; for all simulation results $C_{\mathrm{R,sim}}$ and corresponding theory predictions $C_{\mathrm{R,theory}}$ holds $C_{\mathrm{R,sim}} - C_{\mathrm{R,theory}} < 1.5\%$; for the forcing strength $\gamma \geq \gamma_{\mathrm{opt,theory}}$ closest to the theoretical optimum value $\gamma_{\mathrm{opt,theory}}$ holds $C_{\mathrm{R,sim}} - C_{\mathrm{R,theory}} < 1.3\%$

6.6 Results for forcing of steep free-surface waves

This section investigates the applicability of the theory from Sect. 4.1 to forcing of nonlinear free-surface waves in deep water. For this, flow simulations are performed using the setup from Sect. 6.1 with the following exceptions: The local mesh refinement was extended further away from the calm-surface level, so that the same grid could be used for all simulations. The free-surface was discretized by > 100 cells per wavelength and > 14 cells per wave height. The time-step was $\Delta t > T/500$ in terms of wave period T and 8 iterations were performed per time-step.

Simulations were performed with different wave height H ranging from 50% to 85% of the breaking wave height H_{break} according to Michell (1893). For better comparability, the following approximation will be used $H_{\mathrm{break}} = 0.142\lambda_0 = 0.589\,\mathrm{m}$, where λ_0 is the wavelength according to linear wave theory. Steeper waves were not generated since 5$^{\mathrm{th}}$-order Stokes wave theory was used to initialize and generate the waves; close to breaking steepness, the theory becomes inaccurate and thus introduces disturbances that can trigger wave breaking, after which a calculation of reflection coefficient C_{R} was not considered feasible[16]. As in previous sections, reflection coefficients below $1\% \lesssim C_{\mathrm{R}}$ could not be detected due to the background-noise of the approach to calculate C_{R} as discussed in Sect. 6.2 .

Figures 62 and 63 show that the influence of the wave steepness – and thus also the wave's nonlinearity – can be considered negligible for practical purposes.

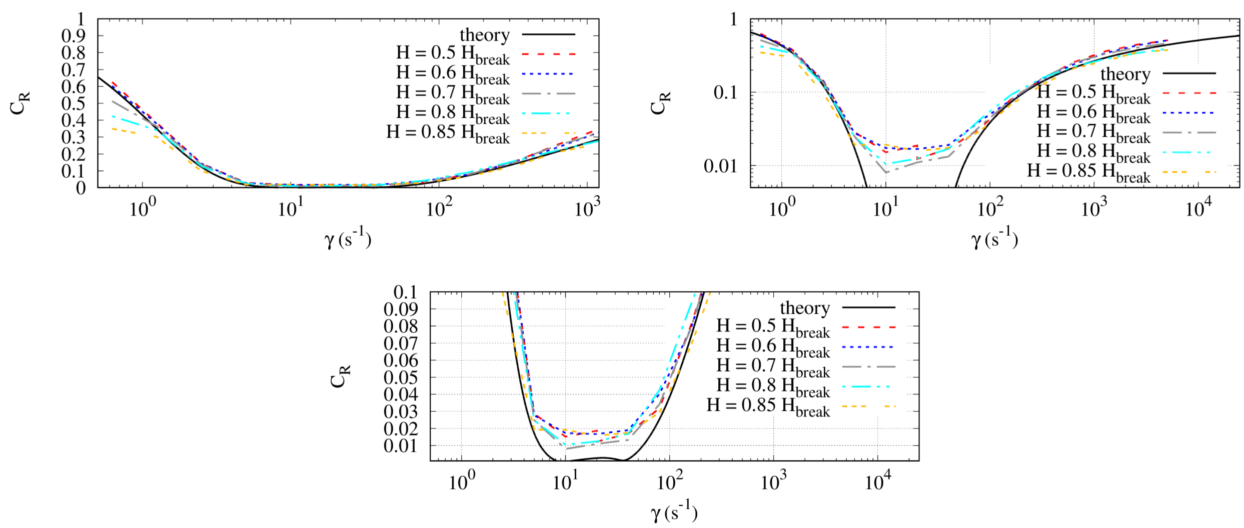

Figure 62: Reflection coefficient C_{R} as a function of forcing strength γ for different wave heights H relative to wave breaking height H_{break}, according to simulation results and theory prediction; for deep-water waves with period $T = 1.6\,\mathrm{s}$; for blending according to Eq. (9), zone thickness $x_{\mathrm{d}} = 2\lambda_0$, and forcing of x-momentum towards $u_{\mathrm{ref}} = 0$; for all simulation results $C_{\mathrm{R,sim}}$ and corresponding theory predictions $C_{\mathrm{R,theory}}$ holds $C_{\mathrm{R,sim}} - C_{\mathrm{R,theory}} < 7.4\%$ and on average $|C_{\mathrm{R,sim}} - C_{\mathrm{R,theory}}| < 3.1\%$; for the forcing strength $\gamma \geq \gamma_{\mathrm{opt,theory}}$ closest to the theoretical optimum value $\gamma_{\mathrm{opt,theory}}$ holds $C_{\mathrm{R,sim}} - C_{\mathrm{R,theory}} < 1.9\%$

[16] In the simulations presented in this section, slight wave breaking occurred only in a few simulations for $H \geq 0.8 H_{\mathrm{break}}$ and for γ-values significantly smaller ($\gamma \lesssim \mathcal{O}(1\,\mathrm{s}^{-1})$) or larger ($\gamma \gtrsim \mathcal{O}(10^3\,\mathrm{s}^{-1})$) than optimum; these values can differ noticeably in reflection coefficient compared to the other simulation results.

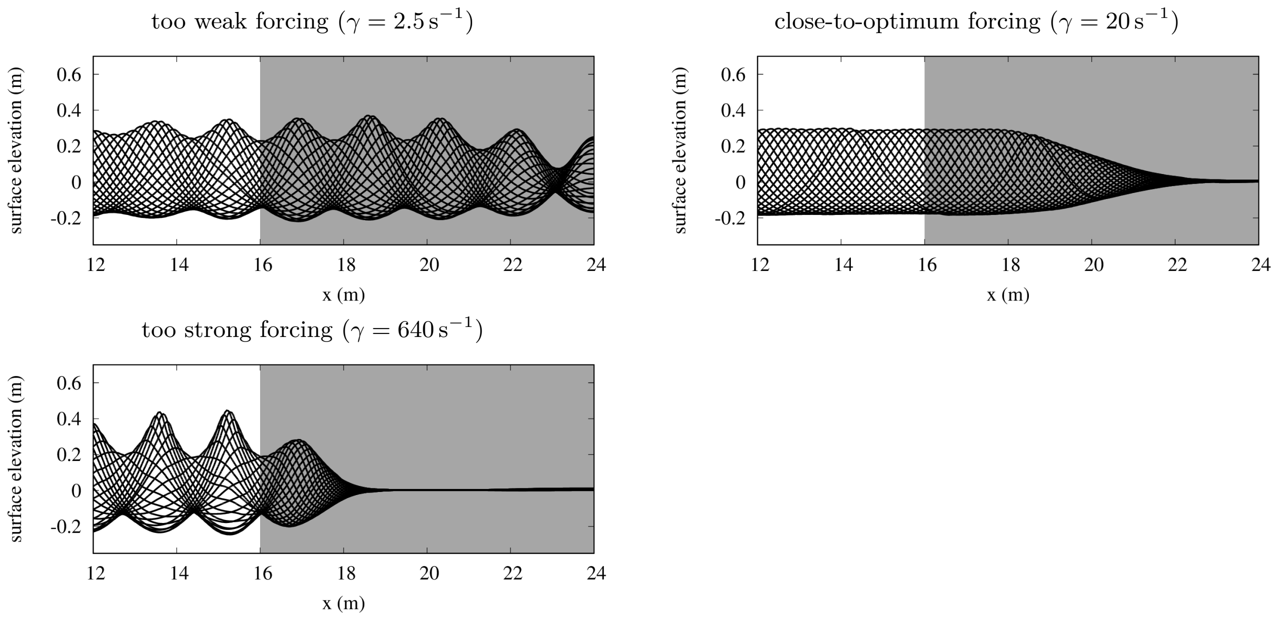

Figure 63: Simulation results for surface elevation as a function of x-coordinate in the vicinity of the forcing zone (shaded gray), evaluated for equally spaced time intervals during the last simulated period; for the waves from Fig. 62 with height $H \approx 0.85 H_{\mathrm{break}}$ relative to breaking wave height H_{break}

Figure 64 shows that the theory also applies to forcing of all velocities u_i and volume fraction α. Although for too strong forcing the theory over-predicts C_{R}, the optimum values for the case-dependent parameters of the forcing zone are predicted reasonably well as before.

Therefore the theory is also recommended for tuning forcing zones in the presence of nonlinear free-surface waves.

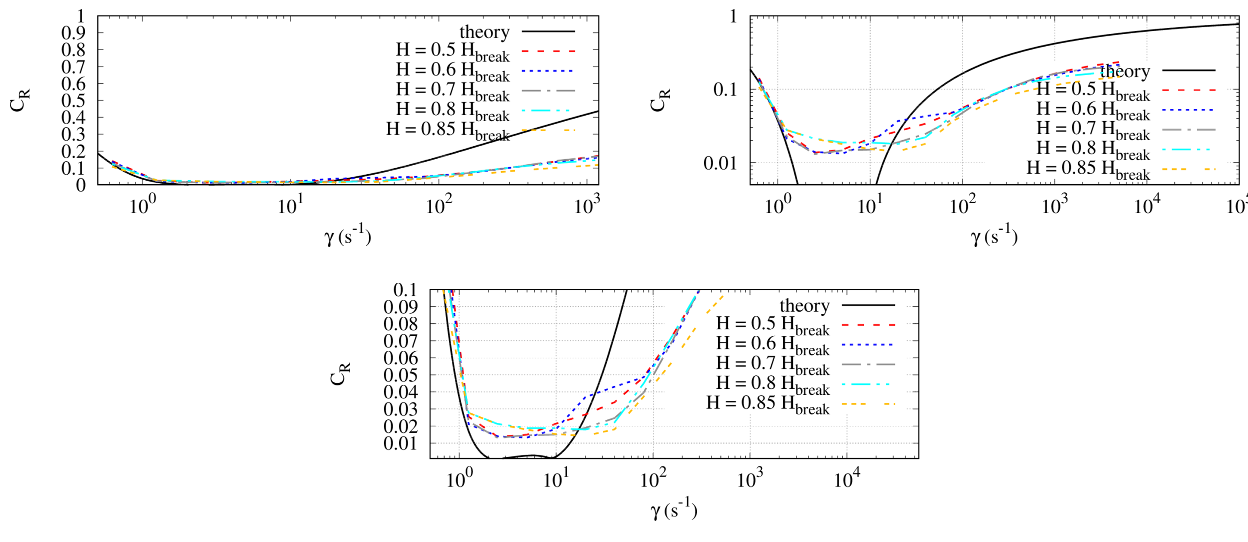

Figure 64: As Fig. 62, except for forcing of x- and z-momentum as well as volume fraction α towards the calm-surface solution; for all simulation results $C_{\mathrm{R,sim}}$ and corresponding theory predictions $C_{\mathrm{R,theory}}$ holds $C_{\mathrm{R,sim}} - C_{\mathrm{R,theory}} < 2.1\%$; for the forcing strength $\gamma \geq \gamma_{\mathrm{opt,theory}}$ closest to the theoretical optimum value $\gamma_{\mathrm{opt,theory}}$ holds $C_{\mathrm{R,sim}} - C_{\mathrm{R,theory}} < 2.1\%$

6.7 Results for forcing of irregular free-surface waves

This section investigates to which extent the theory from Sect. 4.1 is suitable for predicting reflection coefficients for forcing zones with irregular free-surface waves. For this, simulations are performed based on the setup from Sect. 6.1, with the following exceptions: The solution domain from Fig. 7 is used with dimensions $0 \leq x \leq L_x = 400\,\mathrm{m}$ and $-h \leq z \leq 0.5\,\mathrm{m}$. It is filled with water to a depth of $h = 1\,\mathrm{m}$, the rest is filled with air. Initially velocities u_i and volume fraction α are prescribed according to the solution for the calm free-surface. At the top boundary ($z = 0.5\,\mathrm{m}$) atmospheric pressure is prescribed. All other boundaries are no-slip walls, except the inlet ($x = 0$), where velocities u_i

and volume fraction α are prescribed to generate an irregular wave train traveling in positive x-direction. The wave train is generated during the first 60 s of simulated time, using the analytical solution for a JONSWAP wave energy spectrum (see e.g. DNV, 2014; Hasselmann et al., 1973) discretized into 300 wave components, to obtain a peak period $T_{\text{peak}} = 12.82\,\text{s}$, significant wave height $H_{\text{s}} \approx 0.056\,\text{m}$, peak wavelength λ_{peak} and peak-shape parameter 3.3. The peak wave period is the period for which the wave energy spectrum takes its maximum value. The wave travels in positive x-direction until it encounters the forcing zone attached to the opposite boundary ($x = L_x$), where it is partially absorbed, depending on the settings of the forcing zone. The reflected part of the wave travels back into the domain. When the simulation ends at $t_{\text{end}} = 220\,\text{s}$, the whole wave train has encountered the forcing zone once.

After each simulation, the surface elevation in the whole domain is written to a file and a fast Fourier transform (FFT) is performed on the recording to obtain the amplitudes and frequencies of the wave components. For the simulation results, the overall reflection coefficient C_{R} is then computed from the FFT results for the given forcing strength γ in relation to the FFT results for the case of $\gamma = 0$ via Eq. (35).

The theory prediction of the overall reflection coefficient C_{R} is obtained via Eq. (35) by inserting $a_n|_{\gamma} \approx C_{\text{R},n} a_n|_{\gamma=0}$, with amplitude $a_n|_{\gamma=0}$ obtained for the simulation results for the case without forcing, and the corresponding reflection coefficient $C_{\text{R},n}$ for each wave component n is obtained from the 1D-theory from Sect. 4.1. The underlying assumption is that the FFT-results can be treated as a linear superposition of waves so that the theory from Sect. 4 can be applied to each wave component separately.

The forcing zone is based on Eqs. (20) and (21) with exponential blending via Eq. (9). Simulations are performed for different forcing zone thickness x_{d}, different forcing strength γ, and with source terms applied in different governing equations. The free-surface is discretized with cell sizes $\Delta x = 0.625\,\text{m} \approx \lambda_{\text{peak}}/64$ and $\Delta z = 0.0098\,\text{m} \approx H_{\text{s}}/6$. The grid consists of $\approx 40\,000$ cells. The time-step is $\Delta t = 0.012823\,\text{s} \approx T_{\text{peak}}/1000$. Per time-step, 10 iterations are performed with under-relaxation of 0.9 for velocities and volume fraction, as well as 0.4 for pressure.

For most wave components hold shallow-water conditions ($h \leq 0.05\lambda$), or else intermediate-water conditions ($0.05\lambda < h < 0.5\lambda$) which are sufficiently close to shallow water, so that the wave propagation shows comparatively small dispersion; for example, for wavelengths between $0.25\lambda_{\text{peak}}$ and $4\lambda_{\text{peak}}$, phase velocity c varies by $\lesssim 6\%$ according to linear wave theory. Therefore, although the wave train will change its shape during propagation, it will remain relatively compact, so that Eq. (35) is suitable for computing the reflection coefficient.

Figures 65 to 67 show that, for a zone thickness of $x_{\text{d}} \approx 1\lambda_{\text{peak}} \approx 40\,\text{m}$ and forcing of velocity u towards $u_{\text{ref}} = 0$, theory predictions and simulation results for reflection coefficient C_{R} show satisfactory agreement. Further, Fig. 67 shows that 1D-theory for a regular wave with period $T = T_{\text{peak}}$ can be used to tune the forcing zone: the optimum value for γ is reasonably well predicted, although the reflection coefficient is under-predicted; thus when tuning only according to the peak period, thicker forcing zones should be used to ensure that the desired reflection coefficient is obtained.

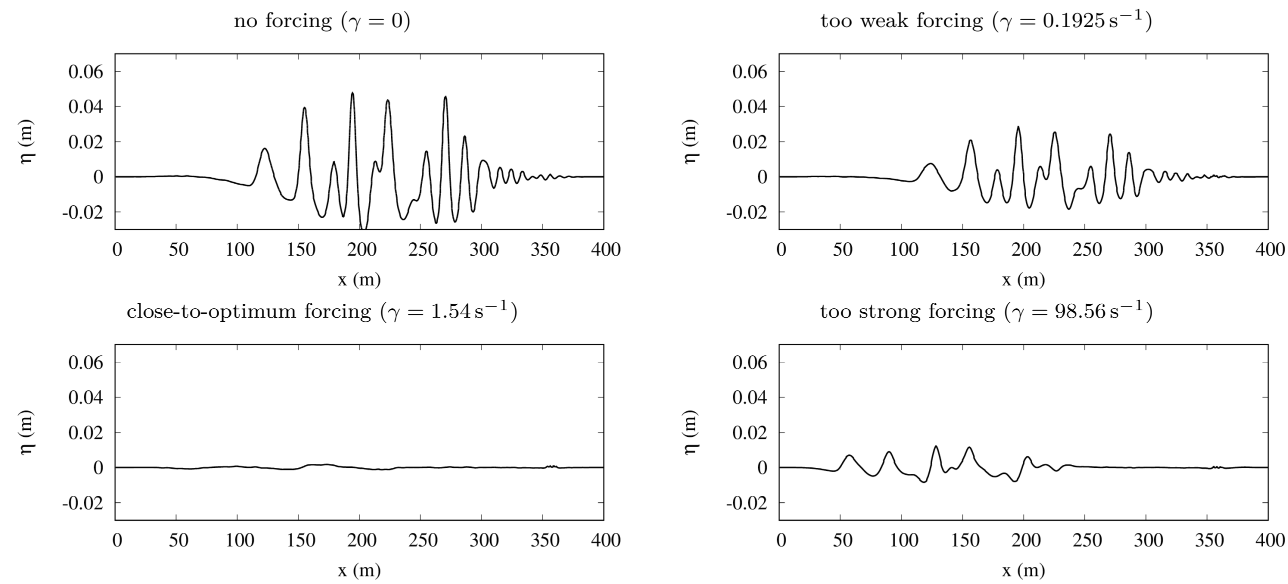

Figure 65: Surface elevation as a function of x-location at time $t = 220\,\text{s}$; for irregular waves with peak period $T_{\text{peak}} = 12.82\,\text{s}$ in intermediate to shallow water; for forcing of x-momentum with blending via Eq. (9) and zone thickness $x_{\text{d}} \approx 1\lambda_{\text{peak}}$

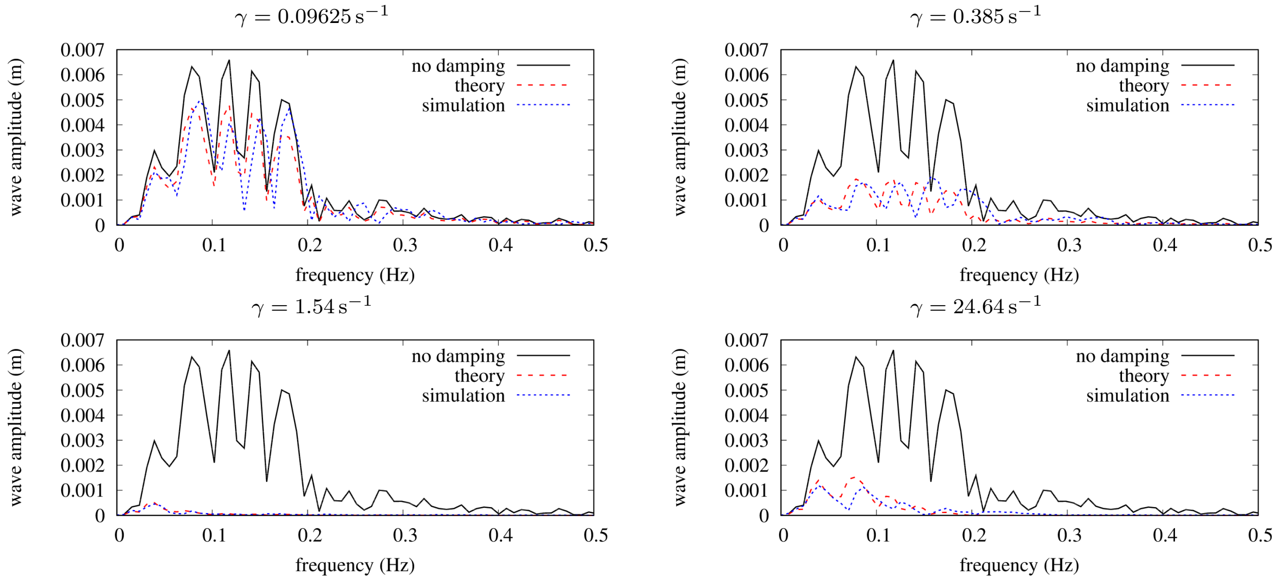

Figure 66: Simulation results and theory predictions for wave amplitude a_n as a function of frequency f_n, obtained from FFT of the surface elevation at time $t = 220\,\mathrm{s}$ as in Fig. 65; for irregular waves with peak period $T_{\mathrm{peak}} = 12.82\,\mathrm{s}$ in intermediate to shallow water; for forcing of x-momentum with exponential blending via Eq. (9) and zone thickness $x_{\mathrm{d}} \approx 1\lambda_{\mathrm{peak}}$

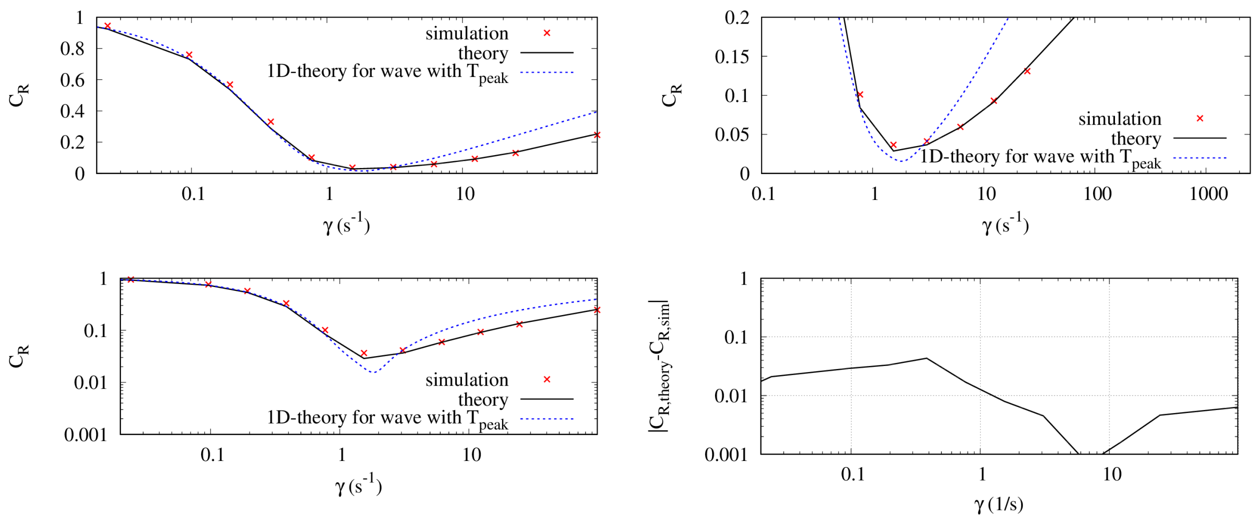

Figure 67: Top left, top right, bottom left: Overall reflection coefficient C_{R} for damping of the irregular wave train from Fig. 66 as a function of forcing strength γ, from theory prediction and simulation results; for forcing of x-momentum with exponential blending via Eq. (9) and zone thickness $x_{\mathrm{d}} \approx 1\lambda_{\mathrm{peak}}$; for all simulation results $C_{\mathrm{R,sim}}$ and corresponding theory predictions $C_{\mathrm{R,theory}}$ holds $C_{\mathrm{R,sim}} - C_{\mathrm{R,theory}} < 4.4\%$ and on average $|C_{\mathrm{R,sim}} - C_{\mathrm{R,theory}}| < 1.3\%$; for the forcing strength $\gamma \geq \gamma_{\mathrm{opt,theory}}$ closest to the theoretical optimum value $\gamma_{\mathrm{opt,theory}}$ holds $C_{\mathrm{R,sim}} - C_{\mathrm{R,theory}} < 0.8\%$; the curve for 1D-theory for a monochromatic wave with T_{peak} shows that tuning the forcing zone for the peak period gives a satisfactory guess at the optimum choice of γ; bottom right: absolute difference between theory prediction and simulation results for C_{R} as a function of γ

Repeating the simulations from Figs. 65 to 67 with only forcing of volume fraction α, the results in Figs. 68 to 70 are remarkably similar to those obtained for forcing of x-momentum.

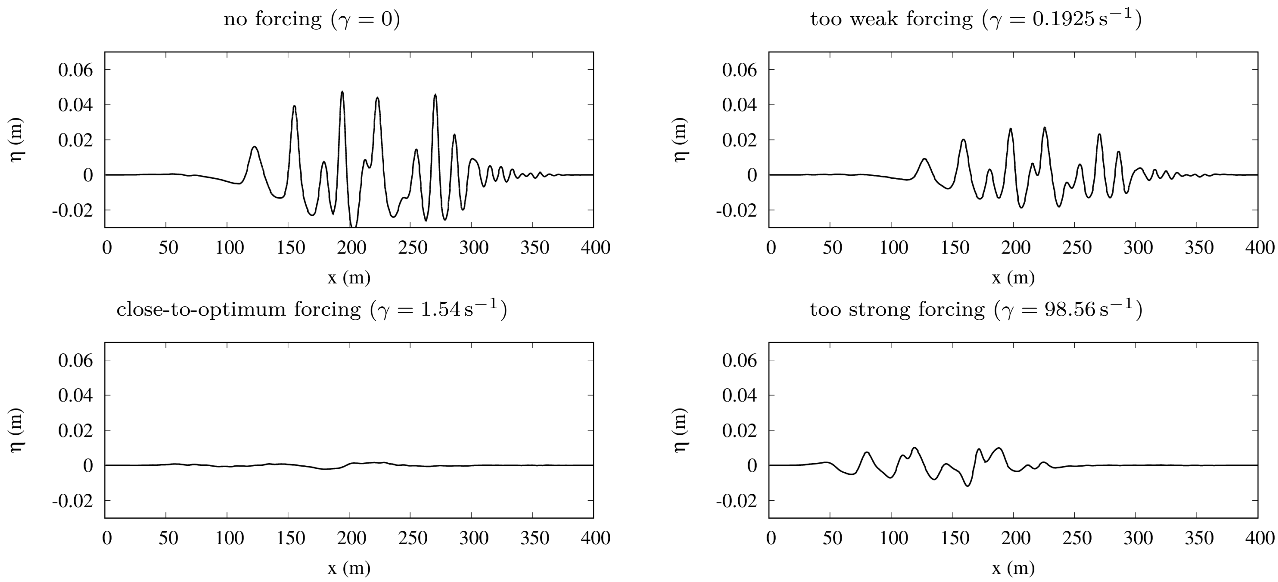

Figure 68: As Fig. 65, except for forcing of volume fraction α; note that for too strong forcing ($\gamma = 98.56\,\mathrm{s}^{-1}$), the surface elevation looks like the inverted corresponding plot from Fig. 65, meaning that all wave troughs from Fig. 65 are peaks in Fig. 68 and all peaks are troughs; this explains why forcing of both x-momentum and volume fraction α in Fig. 72 produces low reflection coefficients even for substantially stronger than optimum forcing, since the wave components reflected due to forcing of x-momentum and volume fraction α cancel

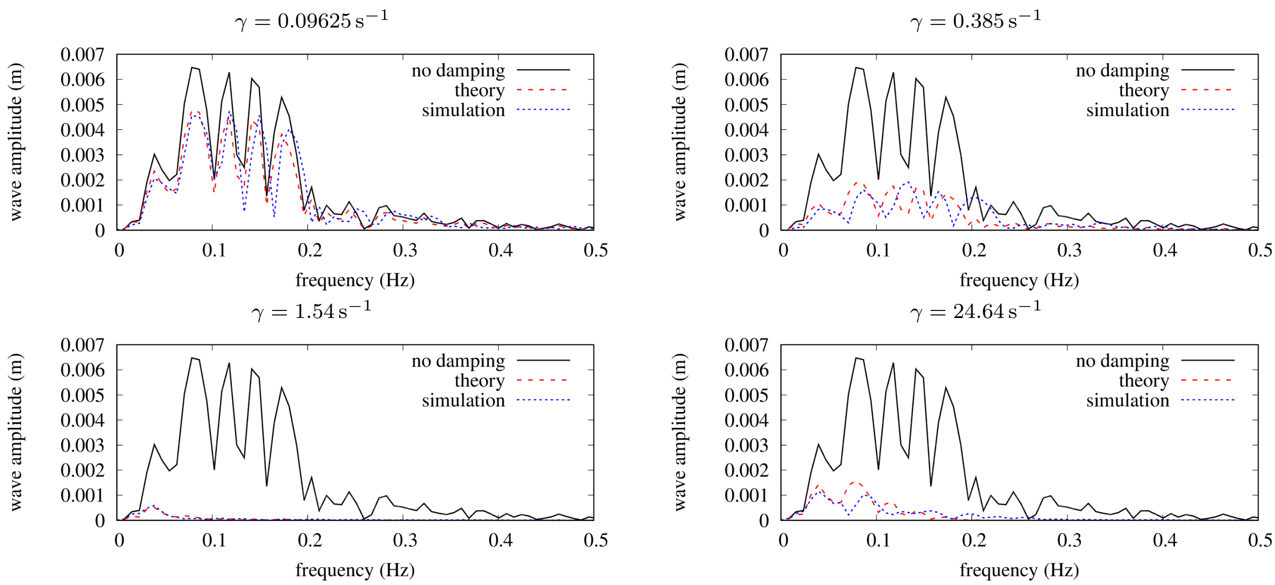

Figure 69: As Fig. 66, except for forcing of volume fraction α

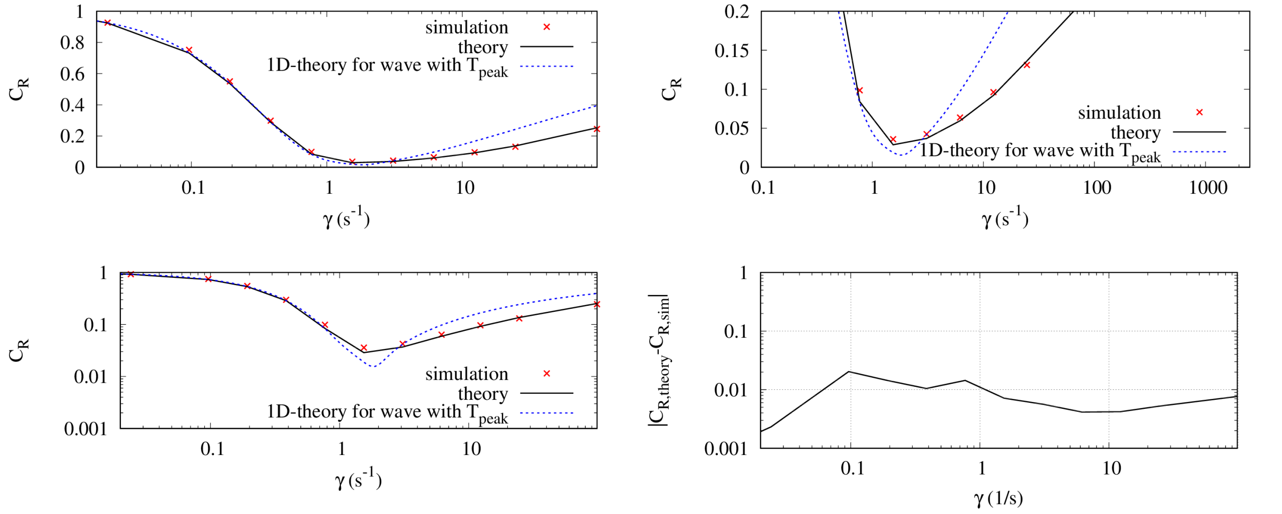

Figure 70: As Fig. 67, except for forcing of volume fraction α; for all simulation results $C_{\mathrm{R,sim}}$ and corresponding theory predictions $C_{\mathrm{R,theory}}$ holds $C_{\mathrm{R,sim}} - C_{\mathrm{R,theory}} < 2.1\%$ and on average $|C_{\mathrm{R,sim}} - C_{\mathrm{R,theory}}| < 0.6\%$; for the forcing strength $\gamma \geq \gamma_{\mathrm{opt,theory}}$ closest to the theoretical optimum value $\gamma_{\mathrm{opt,theory}}$ holds $C_{\mathrm{R,sim}} - C_{\mathrm{R,theory}} < 0.8\%$

Repeating the simulations from Figs. 65 to 67 with only forcing of z-momentum, the results in Fig. 71 differ considerably from those obtained for forcing of x-momentum: The optimum value for γ is two orders of magnitude larger. This was expected, since linear wave theory shows that the vertical component of the kinetic energy is two orders of magnitude smaller than the horizontal kinetic energy due to the limited water depth. Since the forcing acts on the vertical kinetic energy, a significantly larger forcing strength is therefore required as outlined in Sect. 4.1.2.

Figure 71 further shows that for too weak forcing the theory overpredicts reflection coefficient C_{R}. In the extension of the theory for applying forcing source terms in different governing equations in Sect. 4.1.2, it was assumed that it does not matter to which governing equations forcing is applied, as long as the forcing occurs gradually over a thick enough zone. The present findings implicate though, that predictions may be less accurate when applying forcing to a governing equation which has a negligible contribution to the overall wave energy (for a wave with period $T = T_{\mathrm{peak}}$, the vertical kinetic energy is only $E_{\mathrm{kin},z} \approx 0.006 E_{\mathrm{kin},x}$, i.e. roughly 0.3% of the total wave energy). In spite of the slight decrease in accuracy for parameter settings far from the optimum values, for close-to-optimum forcing the theory predictions and simulation results agree reasonably well as before.

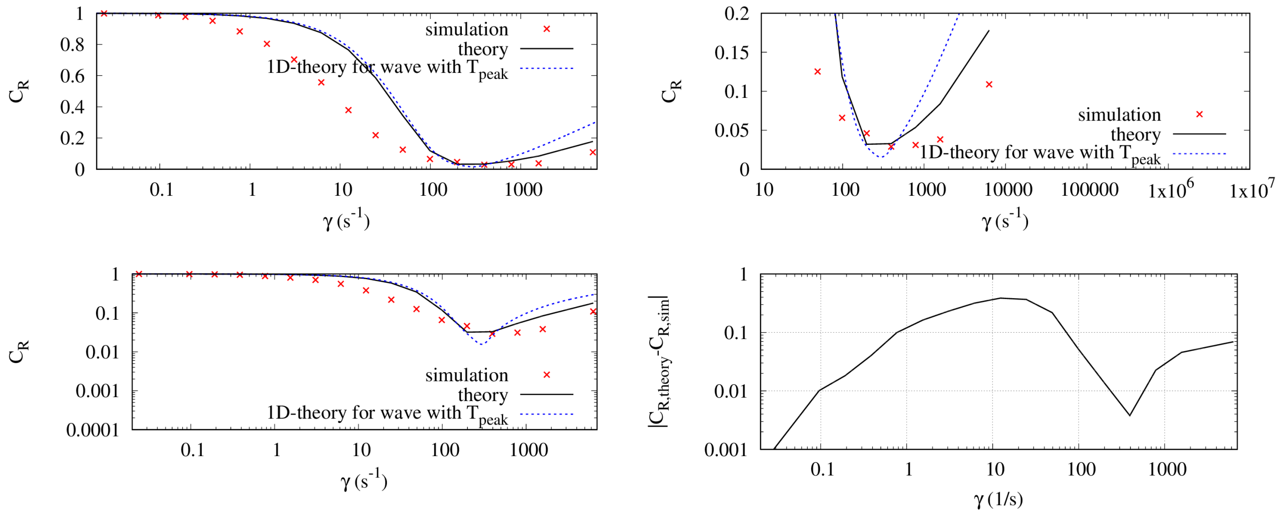

Figure 71: As Fig. 67, except for forcing of z-momentum; for all simulation results $C_{\mathrm{R,sim}}$ and corresponding theory predictions $C_{\mathrm{R,theory}}$ holds $C_{\mathrm{R,sim}} - C_{\mathrm{R,theory}} < 1.5\%$; for the forcing strength $\gamma \geq \gamma_{\mathrm{opt,theory}}$ closest to the theoretical optimum value $\gamma_{\mathrm{opt,theory}}$ holds $C_{\mathrm{R,sim}} - C_{\mathrm{R,theory}} < 1.5\%$

Additionally, the simulations from Figs. 65 to 67 were repeated with forcing of velocities u and w as well as volume fraction α towards the calm-surface solution. The theory predictions for optimum γ-values provide satisfactory reduction of undesired wave reflections, and tuning the forcing zone to the peak wave period T_{peak} again predicts these settings reasonably well.

As with regular waves, Figs. 72 to 74 show that reflection is over-predicted by theory for larger-than-optimum values of γ. In contrast to deep-water conditions, the range for satisfactory reduction of undesired reflections (say $C_{\text{R}} < 5\%$) is significantly wider and extends onto several orders of magnitude larger values of forcing strength γ than theoretically expected.

Comparison of Figs. 65 and 68 (bottom, right) shows that for too strong forcing in shallow water, forcing of volume fraction α reflects the waves with similar reflection coefficients but with *inverted surface elevation* compared to forcing of x-momentum as explained in the caption of Fig. 68. The reason for the low reflection coefficients for theoretically too-strong forcing in Figs. 72 to 74 is therefore destructive interference due to the cancellation of the waves reflected due to the forcing of x-momentum and due to the forcing of volume fraction α.

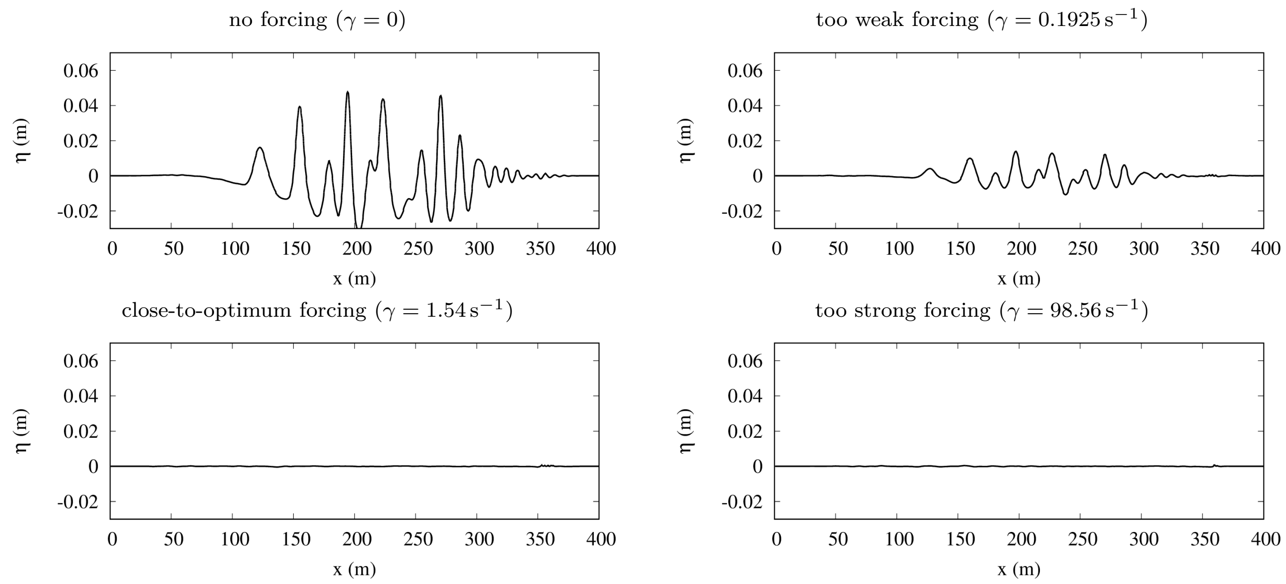

Figure 72: As Fig. 65, except for forcing of x- and z-momentum and volume fraction α

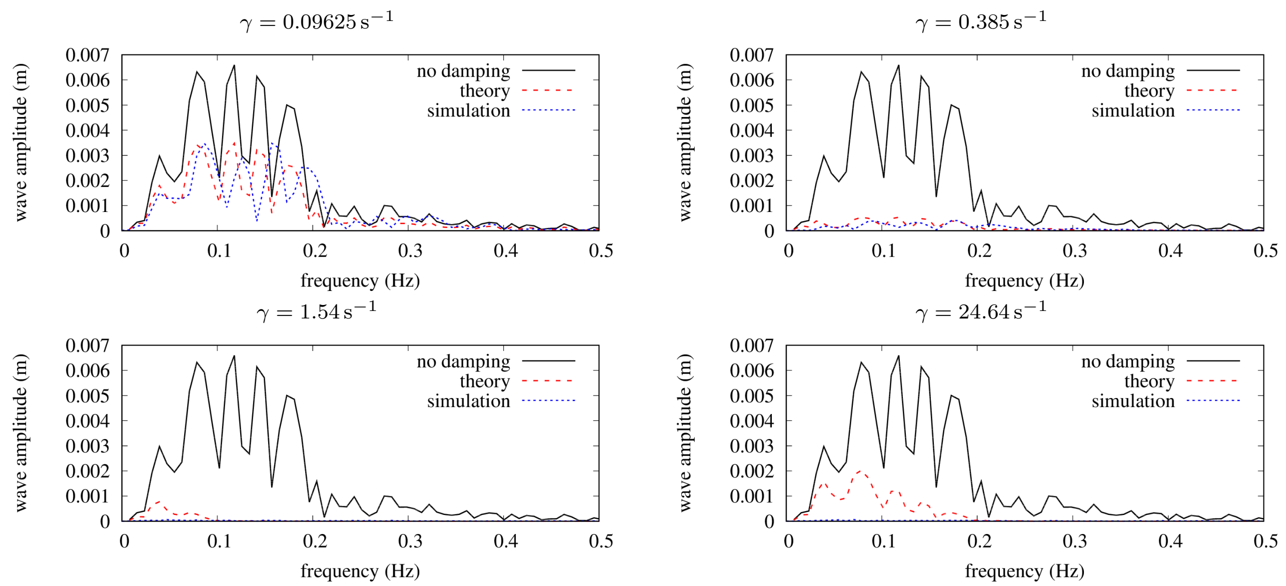

Figure 73: As Fig. 66, except for forcing of x- and z-momentum and volume fraction α

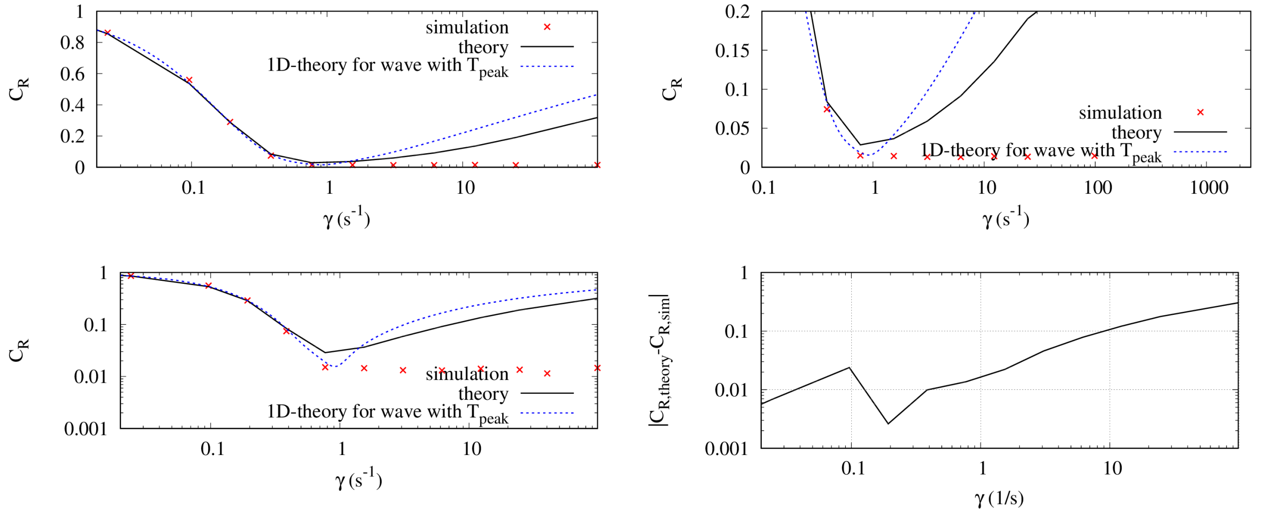

Figure 74: As Fig. 67, except for forcing of x- and z-momentum and volume fraction α; for all simulation results $C_{\mathrm{R,sim}}$ and corresponding theory predictions $C_{\mathrm{R,theory}}$ holds $C_{\mathrm{R,sim}} - C_{\mathrm{R,theory}} < 2.4\%$; for the forcing strength $\gamma \geq \gamma_{\mathrm{opt,theory}}$ closest to the theoretical optimum value $\gamma_{\mathrm{opt,theory}}$ holds $C_{\mathrm{R,sim}} - C_{\mathrm{R,theory}} < -1.3\%$

Finally, repeating the simulations with x-momentum forcing with a thicker forcing zone ($x_{\mathrm{d}} = 2\lambda_{\mathrm{peak}}$) in Figs. 75 to 77 shows that the range of γ-values which provide satisfactory reduction of undesired wave reflections widens and the reflection coefficient C_{R} at optimum tuning decreases. The theory predicts the simulation results reasonably well, though reflection coefficients at close-to-optimum setting are slightly under-predicted. Thus it is recommended to use slightly thicker forcing zones than theory may suggest to ensure reliable damping.

As before, tuning the forcing zone to the peak period detects the optimum choice of forcing strength γ reasonably well, although it underpredicts the corresponding reflection coefficients C_{R} more strongly than the theory for the overall reflection coefficient.

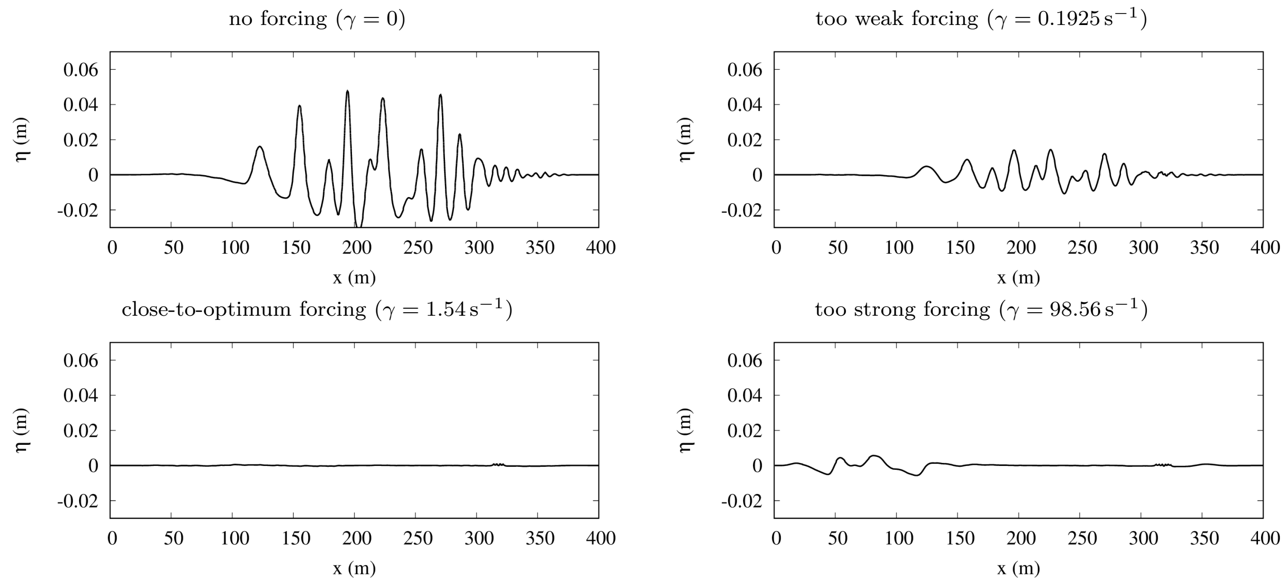

Figure 75: As Fig. 65, except for zone thickness $x_{\mathrm{d}} = 2\lambda_{\mathrm{peak}}$

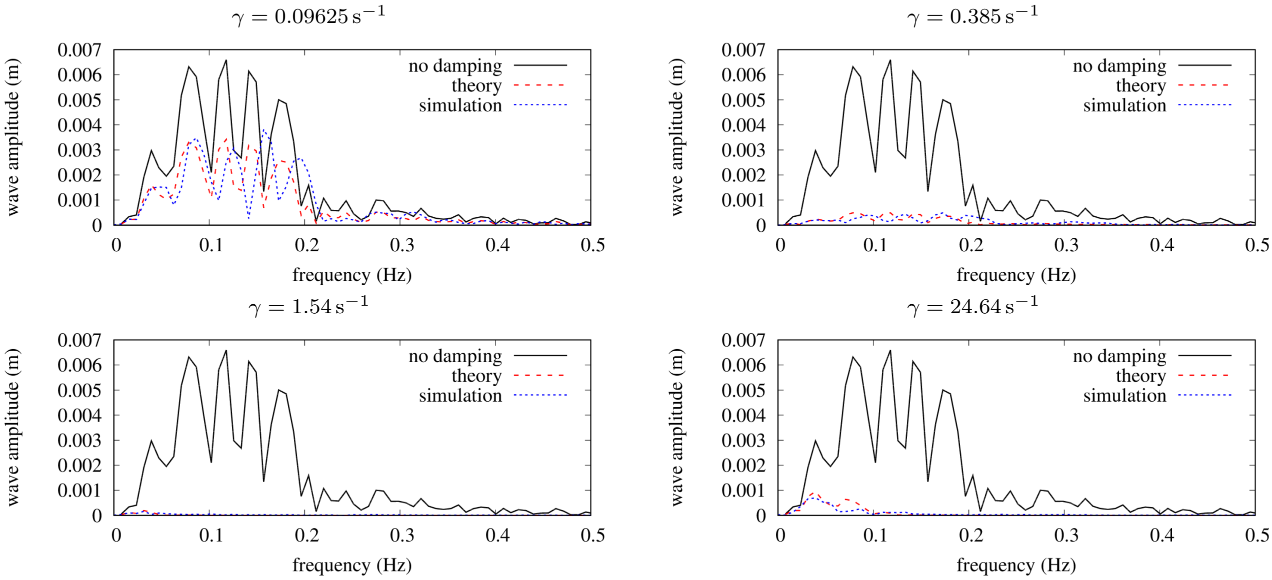

Figure 76: As Fig. 66, except for zone thickness $x_{\mathrm{d}} = 2\lambda_{\mathrm{peak}}$

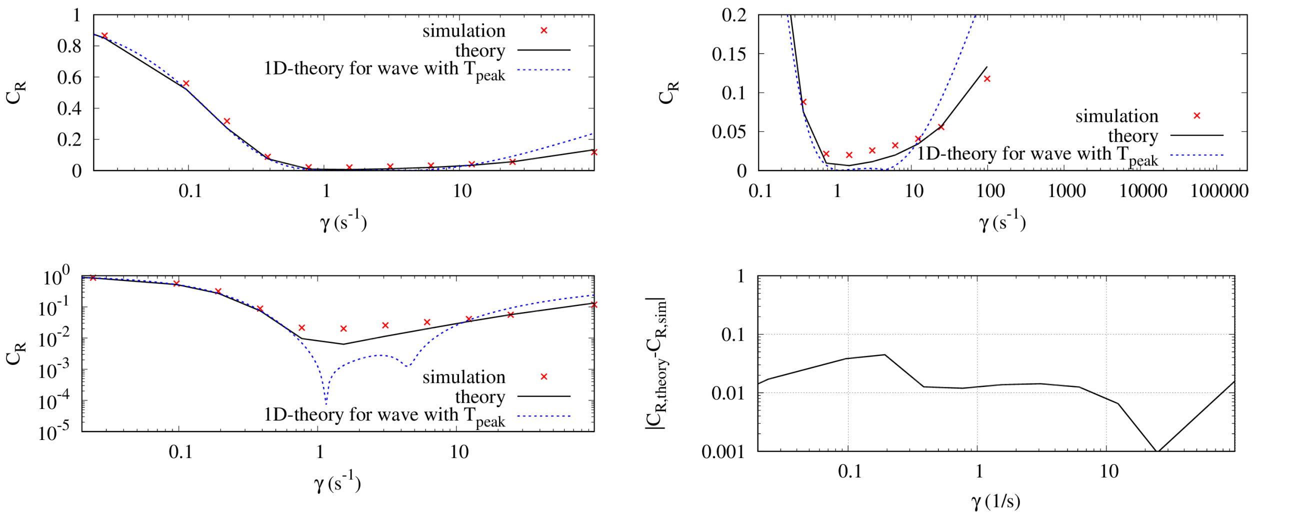

Figure 77: As Fig. 67, except for zone thickness $x_{\mathrm{d}} = 2\lambda_{\mathrm{peak}}$; for all simulation results $C_{\mathrm{R,sim}}$ and corresponding theory predictions $C_{\mathrm{R,theory}}$ holds $C_{\mathrm{R,sim}} - C_{\mathrm{R,theory}} < 4.5\%$ and on average $|C_{\mathrm{R,sim}} - C_{\mathrm{R,theory}}| < 1.3\%$; for the forcing strength $\gamma \geq \gamma_{\mathrm{opt,theory}}$ closest to the theoretical optimum value $\gamma_{\mathrm{opt,theory}}$ holds $C_{\mathrm{R,sim}} - C_{\mathrm{R,theory}} < 1.4\%$

6.8 Forcing of regular free-surface waves in shallow water

To verify that the theory from Sect. 4.1 holds in shallow water as well, flow simulations were performed using the setup from Sect. 6.1, with the following exceptions: The computational domain has dimensions $0 \leq x \leq L_x$ with $L_x = 6\,\mathrm{m}$ and $-h \leq z \leq h$ with water depth $h = 0.04\,\mathrm{m}$, which corresponds to shallow-water conditions ($h \leq 0.05\lambda$). The regular free-surface waves have the period $T = 1.6\,\mathrm{s}$, wavelength $\lambda \approx 1\,\mathrm{m}$, and wave height $= H = 0.0001\,\mathrm{m}$.

A forcing zone based on Eqs. (20) and (21) with exponential blending via Eq. (9) is attached to boundary $x = L_x$. Inside the forcing zone, the flow is forced towards the calm surface solution. Simulations are performed for different forcing zone thickness x_{d} and forcing strength γ.

Simulations start at time $t = 0$ with volume fraction and velocities initialized in the whole domain according to linear wave theory and end at $t = 12.8\,\mathrm{s} = 8T$. Per time-step $\Delta t = 0.0004\,\mathrm{s}$ there are 8 iterations with under-relaxation factors of 0.9 for velocity and volume fraction, and 0.4 for pressure. The mesh sizes within the zone of finest local mesh refinement are $\Delta x \approx 0.0061\,\mathrm{m} \approx \lambda/164$ and $\Delta z \approx 5.4 \cdot 10^{-6}\,\mathrm{m} \approx H/18$. The total number of cells is $1.35 \cdot 10^5$.

Figure 78 shows that, for forcing of x-momentum, the theory predicts the simulation results for reflection coefficients C_{R} with high accuracy.

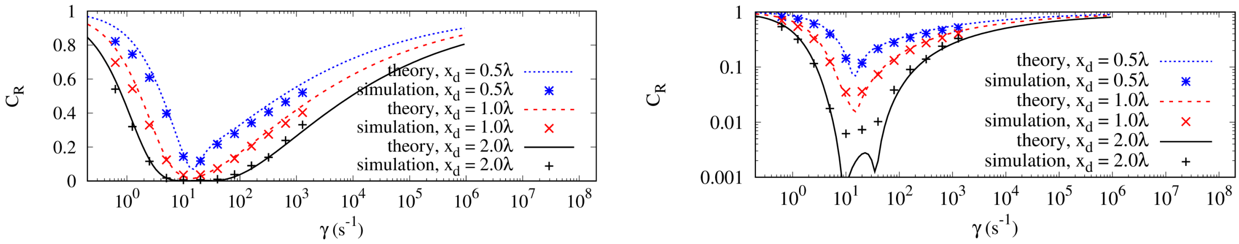

Figure 78: Simulation results and theory predictions for reflection coefficient C_R as a function of forcing strength γ; for shallow-water waves with period $T = 1.6\,\mathrm{s}$, wavelength $\lambda \approx 1\,\mathrm{m}$, and water depth $h = 0.04\,\mathrm{m}$; for different zone thickness x_d with exponential blending via Eq. (9) and forcing of x-momentum; for all simulation results $C_{\mathrm{R,sim}}$ and corresponding theory predictions $C_{\mathrm{R,theory}}$ holds $C_{\mathrm{R,sim}} - C_{\mathrm{R,theory}} < 3.9\%$ and on average $|C_{\mathrm{R,sim}} - C_{\mathrm{R,theory}}| < 4.2\%$; for the forcing strength $\gamma \geq \gamma_{\mathrm{opt,theory}}$ closest to the theoretical optimum value $\gamma_{\mathrm{opt,theory}}$ holds $C_{\mathrm{R,sim}} - C_{\mathrm{R,theory}} < 0.9\%$

For forcing of volume fraction α as well as x- and z-momentum in Fig. 79, reflection coefficients are lower than theory predictions when forcing strength γ is chosen larger than the theoretical optimum; however, the optimum choice of γ is again reasonably well predicted by theory. So far, the results agree with those from the deep-water case from Sects. 6.2 to 6.5.

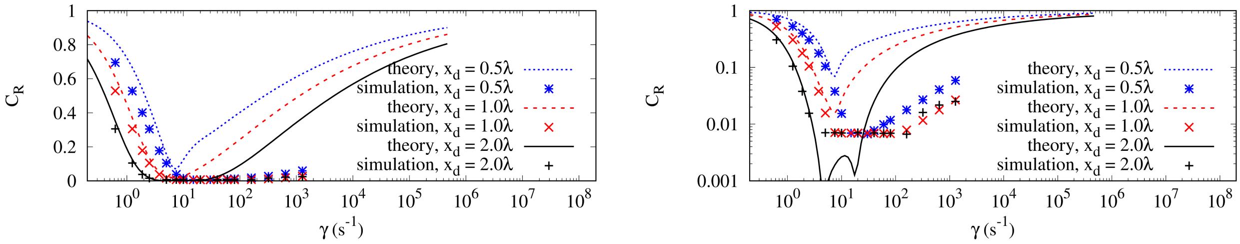

Figure 79: As Fig. 78, except for forcing of x- and z-momentum as well as volume fraction α; for all simulation results $C_{\mathrm{R,sim}}$ and corresponding theory predictions $C_{\mathrm{R,theory}}$ holds $C_{\mathrm{R,sim}} - C_{\mathrm{R,theory}} < 3.3\%$; for the forcing strength $\gamma \geq \gamma_{\mathrm{opt,theory}}$ closest to the theoretical optimum value $\gamma_{\mathrm{opt,theory}}$ holds $C_{\mathrm{R,sim}} - C_{\mathrm{R,theory}} < 0.5\%$

In contrast to the deep-water case, the results for forcing of both x- and z-momentum in Fig. 80 are nearly identical to those for forcing of x-momentum in Fig. 78. This was expected, since in shallow-water waves, the vertical velocity amplitudes are negligible compared to the horizontal velocity amplitudes, so the forcing source terms in x-direction dominate as discussed in Sect. 4.1.2.

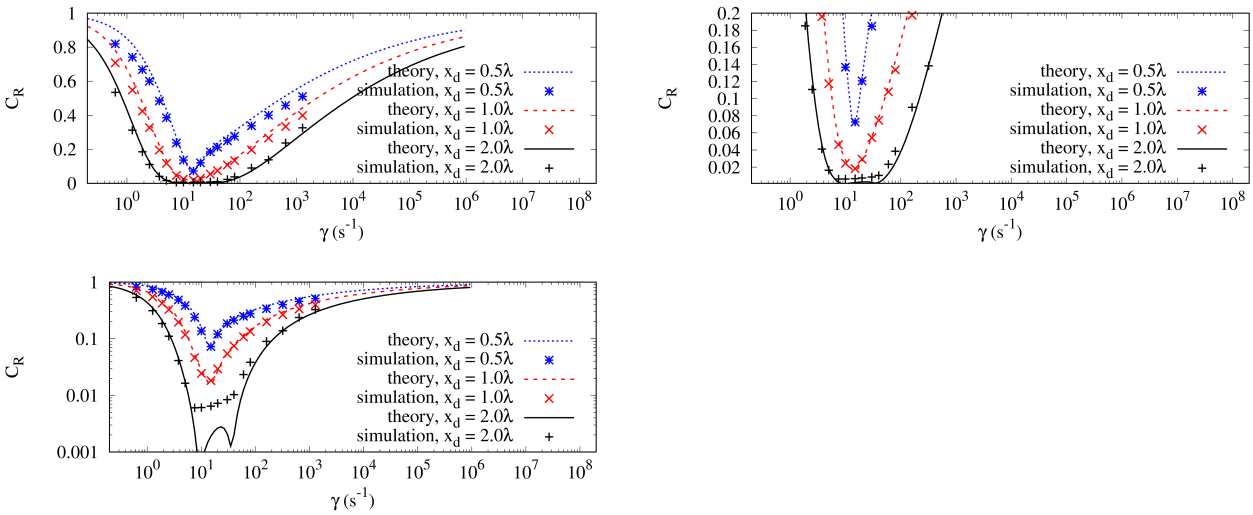

Figure 80: As Fig. 78, except for forcing of x- and z-momentum

The good agreement between theory predictions and simulation results for the shallow-water to deep-water conditions investigated in this work demonstrates that the theory from Sect. 4 applies to all water depths of practical engineering interest.

6.9 Forcing proportional to the velocity squared

Examples of widely used wave damping implementations are the approaches by Choi and Yoon (2009, implemented in STAR-CCM+ by Siemens) and by Park et al. (1999, implemented in ANSYS Fluent), which are

$$q_{z_{\mathrm{CCM+}}} = \underbrace{\gamma b(x)(-w)}_{\text{forcing } \propto\, w} + \underbrace{\tilde{\gamma} b(x)(-w)|w|}_{\text{forcing } \propto\, w|w|} \quad , \tag{114}$$

$$q_{z_{\mathrm{ANSYS}}} = \underbrace{0.5\left(1 - \frac{z - z_{\mathrm{fs}}}{z_{\mathrm{b}} - z_{\mathrm{fs}}}\right)}_{\text{additional factor}} \underbrace{\tilde{\gamma} b(x)(-w)|w|}_{\text{forcing } \propto\, w|w|} \quad , \tag{115}$$

with vertical velocity w, forcing strengths γ and $\tilde{\gamma}$, vertical coordinate z with domain bottom at z_{b}, and vertical location z_{fs} of the free surface. Blending $b(x)$ is exponential (Eq. (9)) in Eq. (114) and quadratic (Eq. (5)) in Eq. (115). In Eq. (114), the first term corresponds to Eq. (20) and is therefore directly proportional to the vertical velocity, while the second term contains an additional factor $|w|$, which renders this forcing term directly proportional to $w|w|$, and thus the corresponding forcing strength scales as $\tilde{\gamma} \propto \lambda^{-1}$. Equation (115) corresponds to the second term in Eq. (114), except for a factor 0.5, an additional vertical blending $\left(1 - \frac{z - z_{\mathrm{fs}}}{z_{\mathrm{b}} - z_{\mathrm{fs}}}\right)$ and a slightly different $b(x)$ (see Fig. 3).

At the time this work was conducted, the default values in the commercial codes for forcing strengths in Eqs. (114) and (115) are $\gamma = 10.0\,\mathrm{rad/s}$ and $\tilde{\gamma} = 10.0\,\mathrm{m}^{-1}$. Perić and Abdel-Maksoud (2016) found that for a $w|w|$-proportional forcing, as in the second term in Eq. (114) and in Eq. (115), the optimum value for $\tilde{\gamma}$ is more than one order of magnitude larger than the optimum value for γ. Thus with default settings in STAR-CCM+, the second term in Eq. (114) has a negligible effect compared to the first term.

Both w-proportional and $w|w|$-proportional forcing produced reflection coefficients with $\approx 1\%$ difference at optimum settings, so both approaches can be used to damp waves successfully. However, for a fixed forcing strength, directly-proportional forcing as in Eq. (20) has a wider range of wave frequencies which are damped satisfactorily, as illustrated in Fig. 81. Historically, $w|w|$-proportional forcing terms may have been introduced as analogy to porous media flows, where for larger flow rates effects like turbulence lead to nonlinearities which can be expressed as quadratically dependent on the flow velocity, such as the Forchheimer or Brinkman extension to Darcy's law, see Straughan (2008). However, this analogy is not entirely valid. Even in steep nonlinear ocean waves, turbulence effects are insignificant unless there is wave breaking. Moreover, Fourier approximation methods allow to split nonlinear waves into different regular harmonics, so applying a forcing directly proportional to the velocity according to Eq. (20) acts on the higher harmonics as well, so the damping of the higher harmonics is already accounted for in w-proportional forcing.

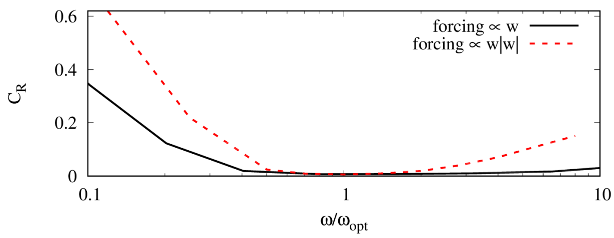

Figure 81: Reflection coefficient C_{R} as a function of angular wave frequency ω scaled by optimum angular wave frequency ω_{opt}, given for simulation results from Perić and Abdel-Maksoud (2016); for forcing zone thickness $x_{\mathrm{d}} = 2\lambda$ and blending $b(x)$ according to Eq. (9); for forcing using only the first term in Eq. (114) (continuous line) with fixed forcing strength γ, versus using only the second term in Eq. (114) (dotted line) with fixed forcing strength $\tilde{\gamma}$

6.10 Theory implications for tuning forcing strength γ and for the choice of blending function $b(x)$

Since the theory from Sect. 4 was validated in the previous sections and can be considered sufficiently accurate for practical purposes, this section shows theoretical predictions without backup from simulation results.

For a typical forcing zone setup, Fig. 82 illustrates the necessity of adjusting the forcing strength γ for different waves.

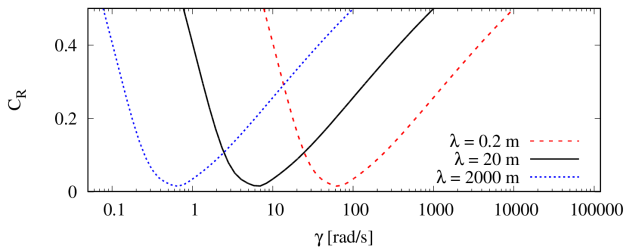

Figure 82: Theory prediction for reflection coefficient C_R as a function of forcing strength γ; for forcing of x-momentum with zone thickness $x_\mathrm{d} = 1\lambda$, blending $b(x)$ via Eq. (9) and deep-water waves; for three different wavelengths $\lambda = 0.2\,\mathrm{m}, 20\,\mathrm{m}, 2000\,\mathrm{m}$; it is evident that forcing strength γ must be adjusted for each wave

Figure 83 shows that common choices for blending functions such as quadratic blending (Eq. (5)), cosine-square blending (Eq. (7)) and exponential blending according to Eq. (9) perform similarly well, with perhaps a slight preference towards the exponential blending. Constant blending (Eq. (3)) and linear blending (Eq. (4)) are not recommended, since they typically lead to considerably higher reflection coefficients, which agrees with literature findings (Israeli and Orszag, 1981; Kim et al., 2014).

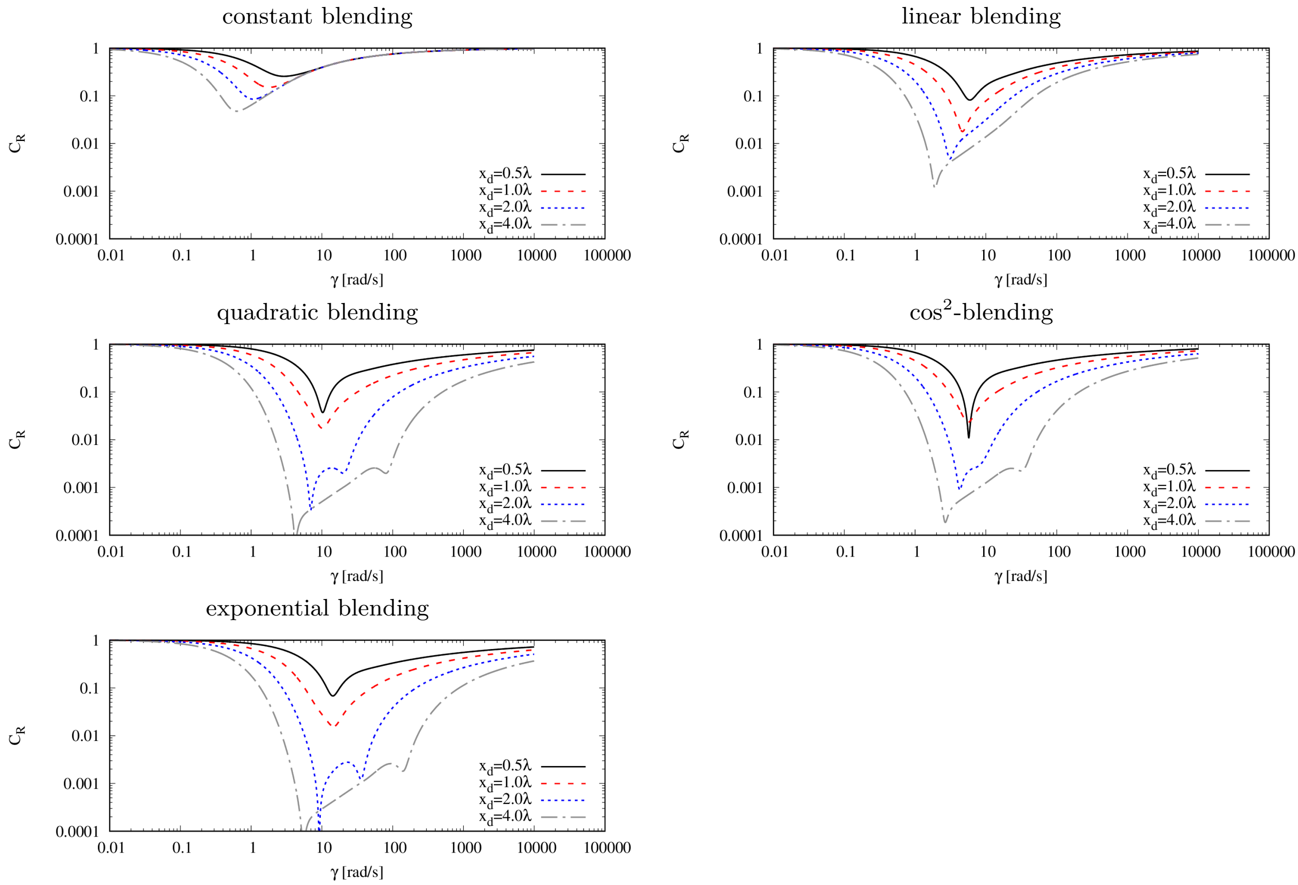

Figure 83: Theory prediction for reflection coefficient C_R as a function of forcing strength γ; for forcing of x-momentum with different forcing zone thickness $0.5\lambda \leq x_\mathrm{d} \leq 4\lambda$ and free-surface waves with period $T = 1.6\,\mathrm{s}$; for constant (Eq. (3)), linear (Eq. (4)), quadratic (Eq. (5)), cosine-square (Eq. (7)) and exponential (Eq. (9)) blending; the results agree with the findings from Sect. 5.3

7 Forcing zones for free-surface waves in 3D-flow simulations

Key findings

- The theory from Sect. 4 satisfactorily predicts optimum forcing zone parameters for 3D-flow simulations with strongly reflecting bodies in free-surface waves
- Forcing zone arrangements in 3D-flow simulations can differ in the choice of
  - governing equations, to which source terms are applied
  - reference solutions, towards which the flow is forced
  - domain boundaries, to which forcing is applied
- If waves travel tangential to a forcing zone, discrepancies between the simulated flow and the reference solution can create flow disturbances for some forcing zone arrangements
- A forcing zone arrangements is proposed which is free of the aforementioned discrepancies and disturbances
- Correct tuning of the forcing zones enables the use of smaller domains and thus reduces the computational effort

This section demonstrates, as Sects. 4.5, 5.4, and 5.5 suggest, that the theory from Sect. 4 predicts optimum forcing zone parameters for 3D-flow simulations with strongly reflecting floating bodies in free-surface waves, so that it can be recommended for use in engineering practice.

In practice, different 'forcing zone arrangements' are used in 3D-flow simulations, which can differ in the choice of the governing equations to which forcing source terms are applied, the reference solution towards which the flow is forced, and the domain boundaries to which forcing zones are attached.

Common choices range from forcing velocities towards zero in the vicinity of the domain outlet (e.g. Choi and Yoon, 2009; Park et al., 2001) as in the left image of Fig. 84, to forcing of volume fraction and all velocities towards the incidence wave field at all vertical domain boundaries (e.g. Chen et al., 2006; Kim et al., 2012; Vukčević et al., 2016, 2016b) as in the right image of Fig. 84.

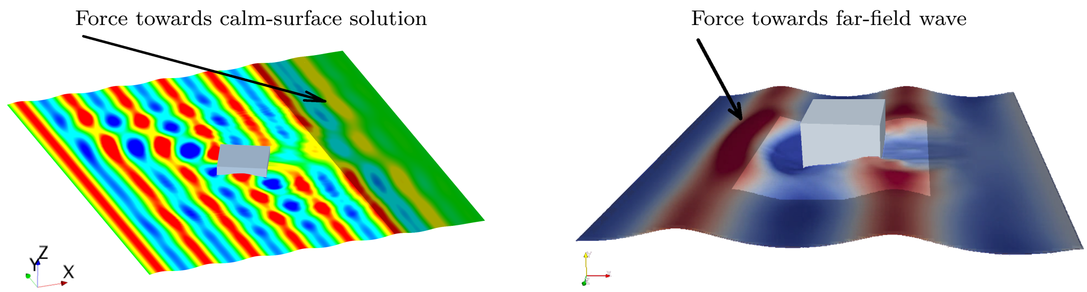

Figure 84: Examples of different forcing zone arrangements used in practice; forcing zones (shaded gray) may be attached to one or several domain boundaries, source terms can be applied in different governing equations and the flow can be forced towards different reference solutions

Section 7.1 gives an overview of common forcing zone arrangements, compares their benefits and limitations based on the literature and theoretical considerations, and discusses which of these arrangements are recommended for 3D-flow simulations with strongly reflecting bodies in waves. Theoretical considerations suggest, for forcing of velocities and volume fraction towards the far-field wave, that if waves travel tangential to such forcing zones, then discrepancies between simulated flow and reference solution can create flow disturbances, which is verified in the following Sect. 7.2. In Sects. 7.1 and 7.3, a forcing zone arrangement is proposed for which no such discrepancies or disturbances occur.

Section 7.4 investigates the proposed forcing zone arrangement via 3D-flow simulations with a strongly reflecting body subjected to regular waves, based on the setup in Sect. 7.3. The results demonstrate that the theory from Sect. 4.1 can be recommended for tuning forcing zones in 3D-flow simulations. Further, tuning the forcing zones via the theory enables the use of smaller computational domains and can thus decrease the computational effort substantially.

In Sect. 7.5, flow simulations are performed with other forcing zone arrangements, regular and irregular waves, and also with a different wave-reflecting body within the domain. The results indicate that forcing zones should be applied near all vertical domain boundaries. If forcing was applied only near the outlet boundary, significant errors occurred. If undesired wave reflections occurred only at the inlet boundary, it was shown that whether acceptable results can be obtained depends on the directionality of the wave reflections that occur at the body placed within the domain. From the results follow recommendations for using forcing zones in 3D-flow simulations.

7.1 Discussion of choice of forcing zones for different domain boundaries

As illustrated in Fig. 84, different 'forcing zone arrangements' are commonly used in 3D-flow simulations. This indicates that perhaps there is not one arrangement that suits all needs, but depending on the problem different arrangements may be more efficient or accurate. In the following, a few common arrangements are discussed, with focus on long-crested incidence waves.

A natural approach would be to apply forcing zones at all vertical domain boundaries and in all governing equations (except the pressure-correction equation) as in the right image of Fig. 84. The solution is forced towards the incidence wave field, as it would develop when no reflecting structures were present; this reference solution could be taken from some wave theory or e.g. from coupling to another flow solver, as used with success e.g. in Gatin et al. (2017) or Vukčević et al. (2016). With such approaches, comparatively small simulation domains can be used, which can reduce the computational effort. However, this approach can be problematic if the wave in the simulation domain propagates differently than the reference solution, for the following reason.

In finite-volume-based flow simulations, discretization and iteration errors lead to numerical diffusion and dispersion. Thus the wave's height and phase change the further it travels within the solution domain (Mayer et al., 1998; Perić and Abdel-Maksoud, 2015 and 2015b). Even when the forcing zone is correctly tuned, if the wave in the simulation does not fit with the reference solution as illustrated in Fig. 85, disturbances can occur. For example, this becomes problematic if the domain size is large compared to the wavelength or when irregular waves are simulated: since each wave component is discretized by a different number of cells per wavelength, discretization errors will be different for each wave component; therefore, the wave will develop differently than in the reference solution. Although the disturbances may vanish for an infinitely fine discretization (given that the reference solution is exact), for practical discretizations further research is necessary to better assess the conditions of validity of such a forcing approach.

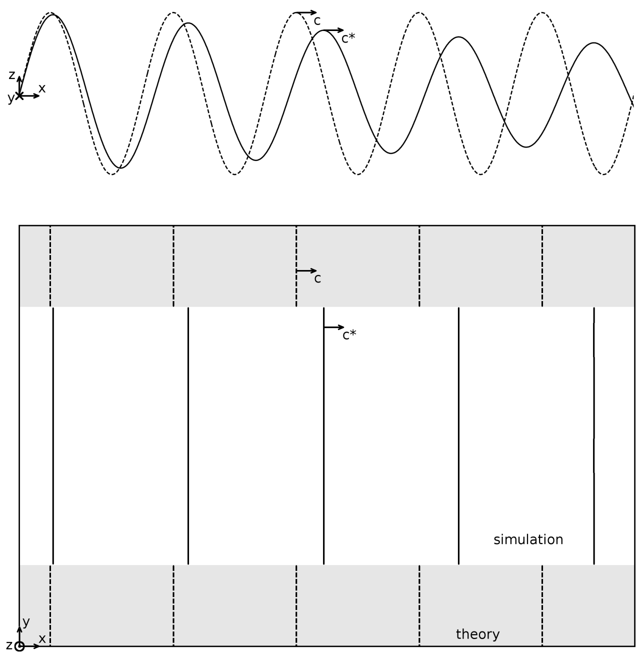

Figure 85: Wave propagation for flow simulation with discretization and iteration errors (full line) and theory (dotted line); surface elevation (top) and location of wave crests (bottom): if the zones with theory and simulation results were coupled using forcing zones, the discrepancy between wave crest locations could produce disturbances, which would be radiated into the solution domain in the form of undesired waves

Chen et al. (2006) presented an approach to avoid such flow disturbances due to discrepancies between computed and reference solution. As shown in Fig. 86, they suggest to compute the flow twice, first without and then with the wave-disturbing body. By using the same discretization for both simulations and taking the solution of the simulation without wave-disturbing body as the reference solution for the forcing in the simulation with the wave-disturbing body, the numerical diffusion and dispersion in both simulations is similar. Thus discrepancies between simulated and reference wave propagation are avoided and no disturbances will occur. However, since two instead of one simulations have to be performed, the computational effort increases[17].

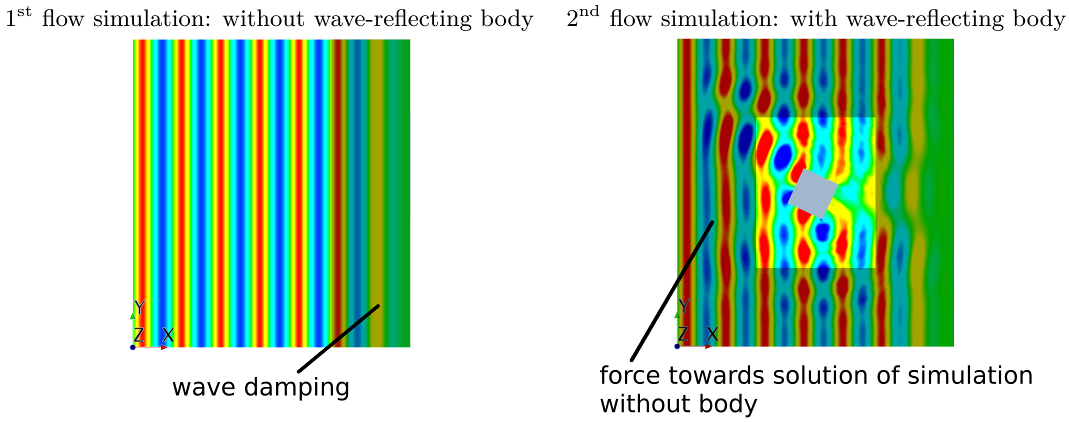

Figure 86: Illustration of the approach by Chen et al. (2006); flow disturbances due to discrepancies between computed flow and reference solution are avoided by first performing the flow simulation without reflecting bodies using only a wave damping zone (shaded gray) at the outlet boundary, and then performing a second simulation with similar discretization with forcing zones (shaded gray) at all vertical domain boundaries and forcing velocities and volume fraction towards the solution from the first simulation

The present work proposes to use a combination of damping and forcing as illustrated in Fig. 87.

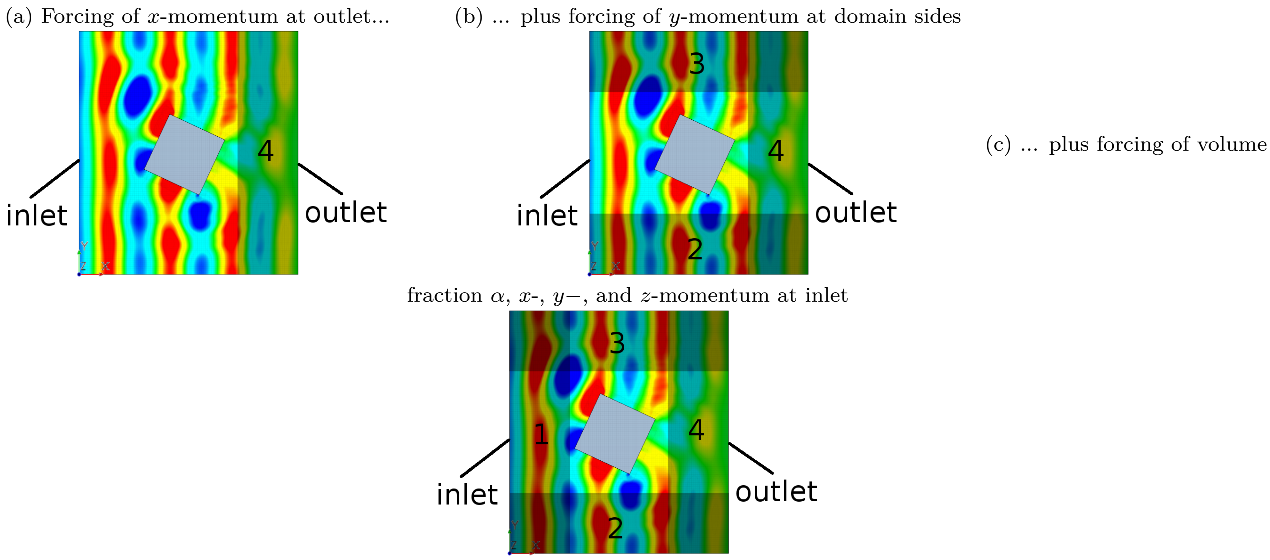

Figure 87: Forcing zone arrangements investigated in this work; forcing via Eq. (116) with $u_{\text{ref}} = 0$ to damp waves at the outlet boundary (zone 4), forcing via Eq. (117) with $v_{\text{ref}} = 0$ to damp waves at the domain sides but let waves traveling in x-direction pass through undisturbed (zones 2 and 3), and forcing via Eqs. (118) and (119) with u_{ref} and α_{ref} according to the far-field wave solution, to simultaneously generate the desired wave traveling in x-direction and minimize undesired wave reflections at the inlet boundary (zone 1)

This approach (i.e. forcing zone arrangement (c) from Fig. 87) combines forcing of all governing equations (except the pressure-correction equation) towards the incidence wave field at the inlet boundary (to simultaneously generate waves and reduce reflections) with damping (i.e. forcing towards the solution for the calm free surface) *of the boundary-normal velocity component* at the outlet[18] and side boundaries. Thus the far-field wave passes through zones 2 and 3 undisturbed, since it has no velocity component in y-direction (i.e. in boundary-normal direction), while waves which were reflected

[17] For long-crested far-field waves, the efficiency of this approach could be improved by performing the flow simulation without the wave-disturbing body as 2D simulation; to the best knowledge of the author, this has not yet been investigated.

[18] The proposed forcing zone arrangement works equivalently when in zone 4 the velocities u_i and/or volume fraction α are forced towards the solution for the calm surface. Thus if there is a current with velocity $\mathbf{u}_\infty$ superposed on the generated wave $\mathbf{u}_{\text{ref,wave}}$, then the velocities in zone 4 should be forced towards $\mathbf{u}_{\text{ref,zone 4}} = \mathbf{u}_\infty$, whereas the velocities in zone 1 should be forced towards $\mathbf{u}_{\text{ref,zone 1}} = \mathbf{u}_\infty + \mathbf{u}_{\text{ref,wave}}$.

at the floating body and travel towards domain sides 2 and 3 are damped. Thus the same reduction of undesired wave reflections can be obtained as in the approach by Chen et al. (2006), but with half the computational effort.

In some flow solvers, forcing towards an incidence wave field at all vertical domain boundaries as in Chen at al. (2006) or Vukčević et al. (2016) is not trivial to implement. However, simple forcing zones for wave damping as in the upper two images in Fig. 87 are comparatively easy to implement. Although less efficient, this approach (forcing zone arrangement (b) from Fig. 87) can also produce satisfactory results. Consider Fig. 88, where a structure within the domain reflects waves evenly in all directions. The crests of the reflected waves form a circle. The further the reflections travel, the larger becomes the circle's circumference and the smaller becomes the wave power per meter wave crest, since its integral over the circumference remains constant. Assume that waves are fully damped at all boundaries except at the inlet, where they are reflected again. If the distance r between the structure and the inlet is sufficiently large, then only a small part of these re-reflected waves reaches the structure again, as indicated in Fig. 88. For example, require that less than 5% of the waves reflected at the structure should reach the structure again. Then by relating the structure diameter D to the wave crest circumference $2\pi r$ one obtains $D/(2\pi r) \leq 0.05$, and thus $r \geq 10D/\pi \approx 3.2D$, so the structure should be positioned $3.2D$ away from the inlet. Note though that different body shapes and orientations can produce uneven wave reflection, which may increase/decrease this distance as discussed in Fig. 126.

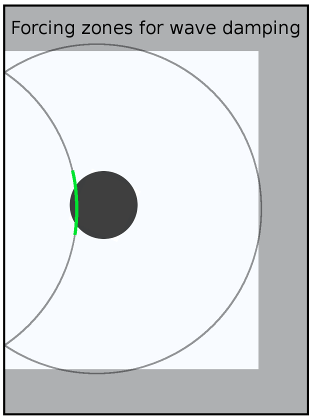

Figure 88: Domain with forcing zones (shaded gray) for wave damping at all domain boundaries except for the inlet (left boundary); reflections at a structure (dark circle) within the domain lead to roughly circular waves (gray lines); most of these will be damped by the forcing zones, and even of those wave components that are re-reflected at the inlet only a comparatively small part (marked green) reaches the structure again, given that the distance between structure and inlet is sufficiently large

Further, for some applications forcing at the outlet may suffice. Especially when the body can be considered transparent (diameter $D < 0.1\lambda$), or at least not strongly reflecting, then the influence of undesired wave reflections on the results will be lower than for the strongly reflecting bodies investigated in the rest of Sect. 7.

In the following, the approaches in Fig. 87 will be investigated to assess the influence of undesired wave reflections for different forcing zone arrangements.

7.2 Investigation of flow disturbances due to discrepancies between computed flow and reference solution in 3D-flow simulations with free-surface waves

To investigate the influence of discrepancies between computed flow and reference solution discussed in Sect. 7.1, 3D-flow simulations are performed of long-crested free-surface wave propagation. Inside the domain there are no wave-disturbing bodies, so that all flow disturbances that occur can be traced back to the forcing zone arrangement used.

In this section, the simulation domain has dimensions $-80\,\text{m} < x < 140\,\text{m}$, $0 < y < 156\,\text{m}$, $-13.104\,\text{m} < z < 14.976\,\text{m}$. The coordinate system lies at the calm free surface level $(0,0,0)^\text{T}$, with x pointing in wave propagation direction and z pointing upwards as shown in Fig. 89.

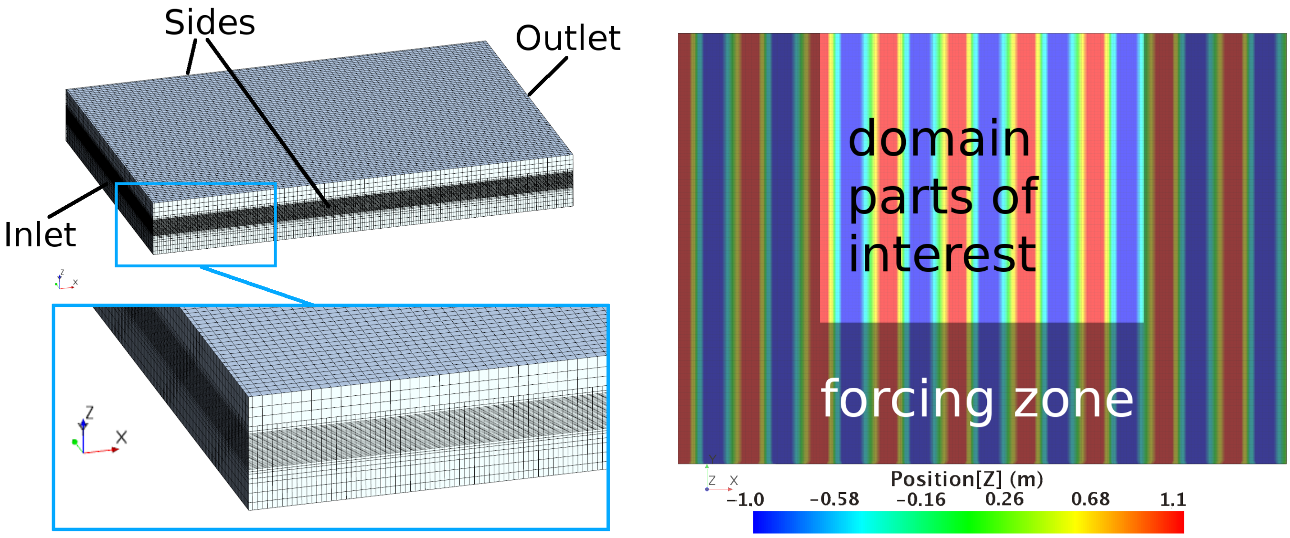

Figure 89: Computational grid with local mesh refinement near the free surface (left), and top view on solution domain (right) with forcing zones (shaded gray) attached to inlet, outlet, and one side boundary, and forcing of velocities and volume fraction towards the far-field waves

The wave is generated by forcing velocities and volume fraction towards the far-field wave solution as given in Sect. 2.3 in combination with accordingly prescribing volume fraction and velocities at all vertical domain boundaries, except for side boundary $y = 156\,\mathrm{m}$ which is set to a symmetry boundary condition to reduce the total number of cells. At the top boundary $z = 14.976\,\mathrm{m}$ atmospheric pressure is prescribed and the bottom boundary $z = -13.104\,\mathrm{m}$ is set to a slip wall. The forcing zone thickness is $x_\mathrm{d} = 50\,\mathrm{m} \approx 2\lambda$, so that with correct tuning no significant wave reflections are expected from the theory predictions shown in Fig. 90. As initial condition, volume fraction and velocities in the whole domain are initialized according to the far-field wave. The wave parameters are (peak) wave period $T = 4\,\mathrm{s}$, wave height $H = 3\,\mathrm{m}$, (peak) wavelength $\lambda \approx 25\,\mathrm{m}$, and thus steepness $H/\lambda \approx 85\%$ of the maximum steepness. Deep water conditions apply.

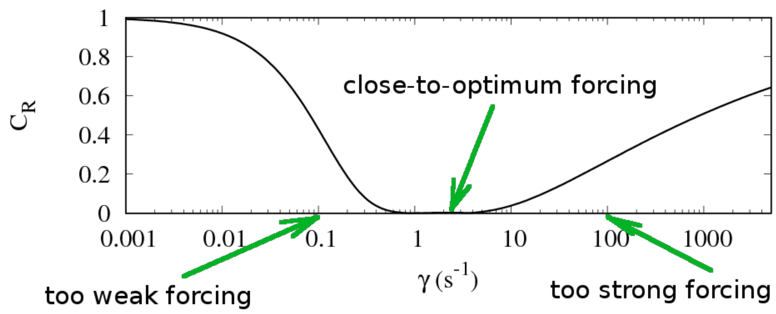

Figure 90: Reflection coefficient C_R as a function of forcing strength γ for the wave with period $T = 4\,\mathrm{s}$ used in this section according to the theory from Sect. 4.1; at close-to-optimum forcing ($\gamma = 2.5\,\mathrm{s}^{-1}$), wave reflections at the forcing zone should be negligible

The finite-volume-based commercial flow solver STAR-CCM+ version 11.06.010-R8 from Siemens (formerly CD-adapco) is used, with settings as in Sect. 7.3. The under-relaxation factor is 0.9 for velocities and volume fraction and 0.4 for pressure. The domain is discretized using a rectilinear grid with local mesh refinement around the free surface as shown in Fig. 89. The free surface stays at all times within the region of the finest mesh with ≈ 23 (coarser grid) or 47 (finer grid) cells per (peak) wavelength and ≈ 10 cells per (significant) wave height. The computational grid, which consists of $\approx 1 \cdot 10^6$ (coarser grid) or $\approx 4 \cdot 10^6$ (finer grid) cells, is shown in Fig. 89. The total simulated time is $60\,\mathrm{s} \approx 15T$ with a time step of $\Delta t = T/500$. Six iterations are performed per time-step.

First, the reference solution for the forcing will be the linear wave theory solution for the steep wave. Since no flow-disturbing body is present within the domain, and since the mesh size does not change in horizontal directions, the correct solution would be a long-crested wave traveling through the domain undisturbed. The linear wave theory was deliberately chosen as an example for a reference solution that does not fit the flow solution within the domain, since the flow within the domain will take on a realistic wave shape, which for the given steepness would have a slightly different shape and a ca. 11.8% larger wavelength and phase velocity than the linear reference solution. Figure 91 shows that even for close-to-optimum tuning of the forcing zone parameters, the mismatch between the reference solution and the computed flow solution produces disturbances within the whole domain. These disturbances were generated by the forcing zone parallel to the wave propagation direction and seem unaffected by the discretization, or perhaps even more pronounced on the finer grid. As expected, on the coarse grid an additional loss in wave height is observed. On the finer grid, this loss is reduced in most domain parts, but remains in the vicinity of the forcing zone due to the cancellation between reference and computed flow solution. This example highlights that if there is a discrepancy between the reference solution for the forcing and the actually computed flow within the domain (including effects of discretization and iteration errors), then the forcing zone at the domain sides can produce significant disturbances, which are radiated as undesired waves into the solution domain.

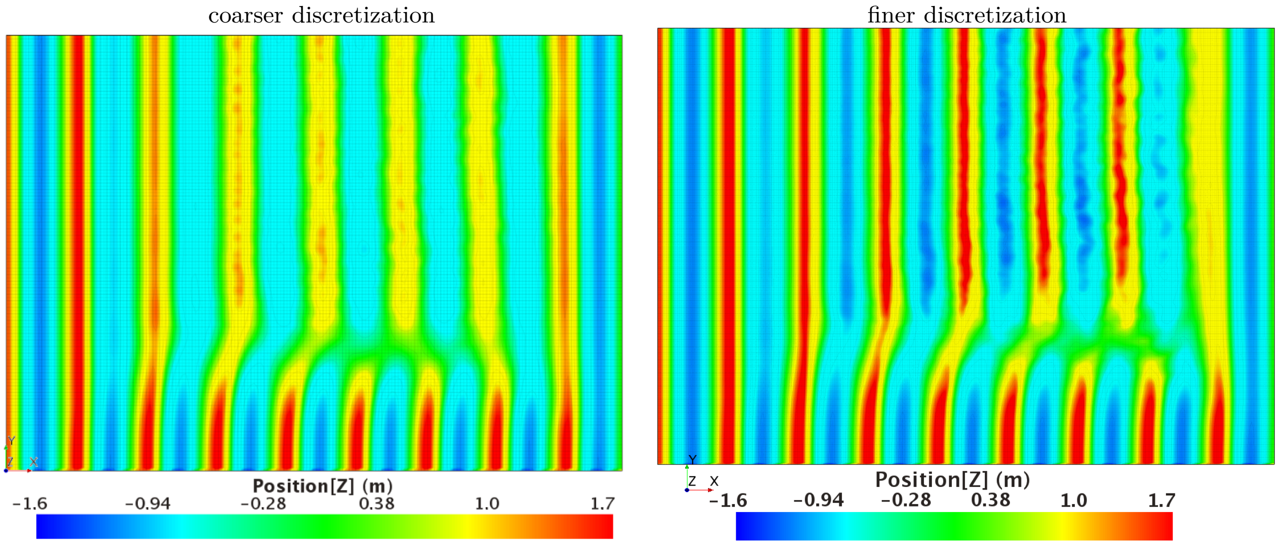

Figure 91: Free-surface elevation in solution domain at time $t = 60\,\mathrm{s}$ for forcing towards *linear wave theory* with close-to-optimum forcing strength γ; for coarser ($\approx 1 \cdot 10^6$ cells) and finer discretization ($\approx 4 \cdot 10^6$ cells)

Figure 92 shows that if the forcing zone parameters are set to theoretically ineffective values, these also produce unsatisfactory forcing in the flow simulations. If the source terms are too weak, then even close to the domain boundaries the reference solution is not maintained (Fig. 92 top left), and reflections at the outlet boundary produce a partial standing wave. For too large source terms, the reference solution is enforced nearly up to the entrance to the forcing zone, so reflections occur at the entrance to the forcing zone and disturbances reach even further into the solution domain (Fig. 92 bottom).

To investigate to which extent these disturbances will be present if a more accurate reference solution is used, the simulations were repeated using Fenton's (1985) 5$^{\text{th}}$-order Stokes wave theory to obtain a highly accurate prediction of the wave propagation for the case that no discretization or iteration errors are present. Figure 93 shows that with this setup, the discrepancy between reference and computed flow solution is smaller; yet even for the fine discretization, flow disturbances are clearly visible (cf. the 'zig-zag' shape of the wave crests), although especially on the finer grid the discrepancy between theoretical and computed wave phases is rather small. This error is expected to reduce when refining the mesh. To investigate this, the simulation is repeated on a further refined discretization, with 95 cells per wavelength λ, and 20 cells per wave height H, and 666 time-steps per period T. The resulting mesh contains $14.6 \cdot 10^6$ cells and is shown in Fig. 94. Due to the comparatively fine discretization, the parallel computation took several weeks to complete on 24 intel E5-2680V3 processors. Figure 95 shows that further refining the discretization decreases the flow disturbances which were clearly visible on the coarser discretizations (cf. Fig. 93). However, Fig. 96 illustrates that flow disturbances are still present in the results, although their magnitude has been reduced so far that their influence would be considered negligible for typical flow simulations with bodies in waves. These findings demonstrate that when the waves travel tangential to a forcing zone with forcing of all velocities u_i and volume fraction α towards the far-field wave solution, then finer discretizations than commonly used can be required to reduce the flow disturbances which occur due to the mismatch between computed flow and reference solution.

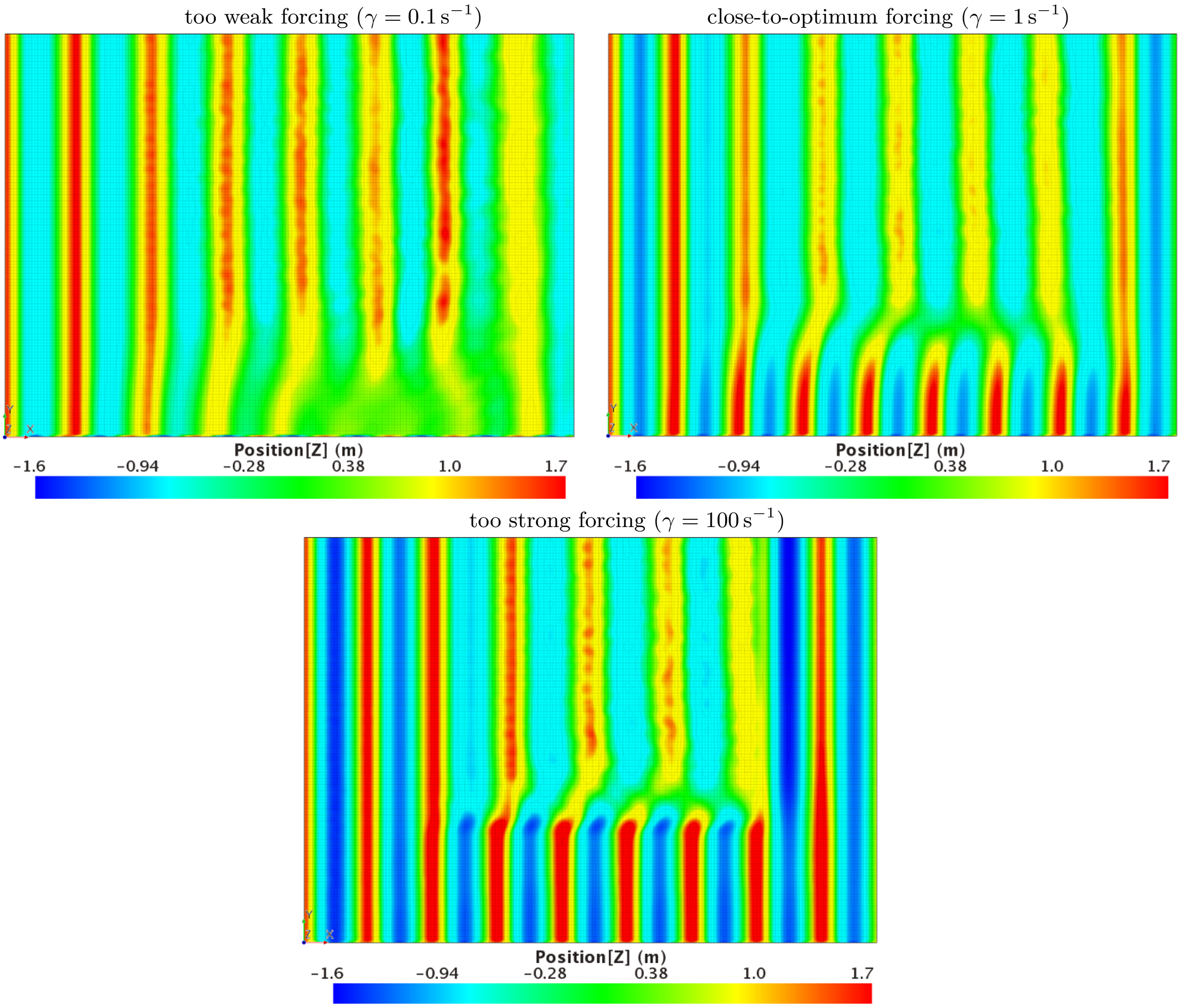

Figure 92: Free-surface elevation in solution domain at time $t = 60\,\mathrm{s}$ for forcing towards *linear wave theory* solution at all domain boundaries for different values of forcing strength γ

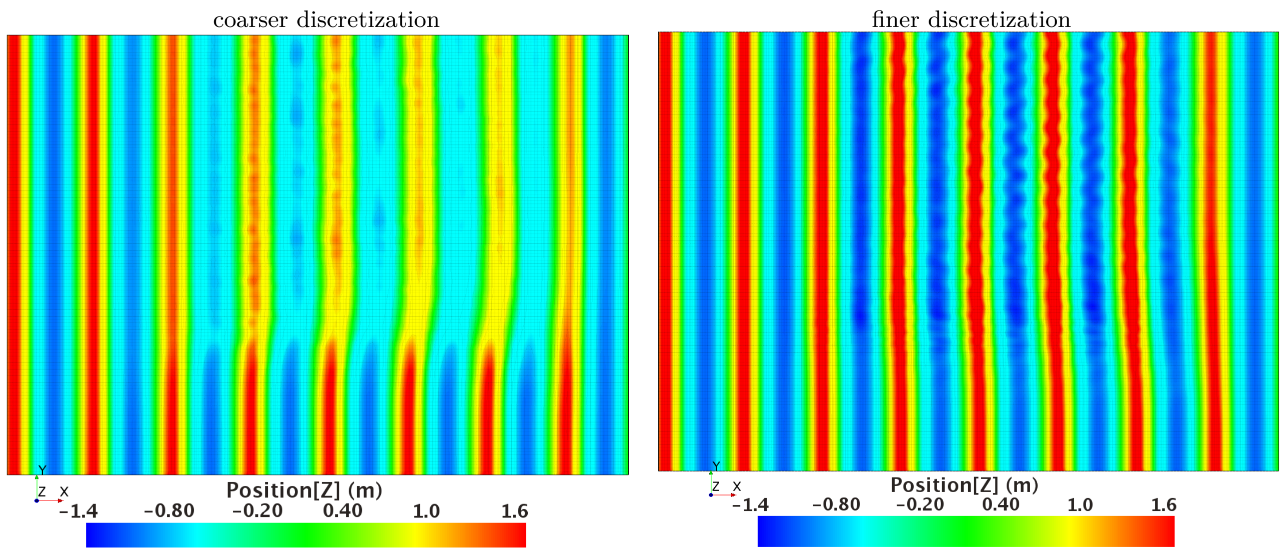

Figure 93: Free-surface elevation in solution domain at time $t = 60\,\mathrm{s}$ for forcing towards 5^{th}-*order Stokes wave theory* with close-to-optimum forcing strength γ; for coarser ($1 \cdot 10^6$ cells) and finer discretization ($4 \cdot 10^6$ cells)

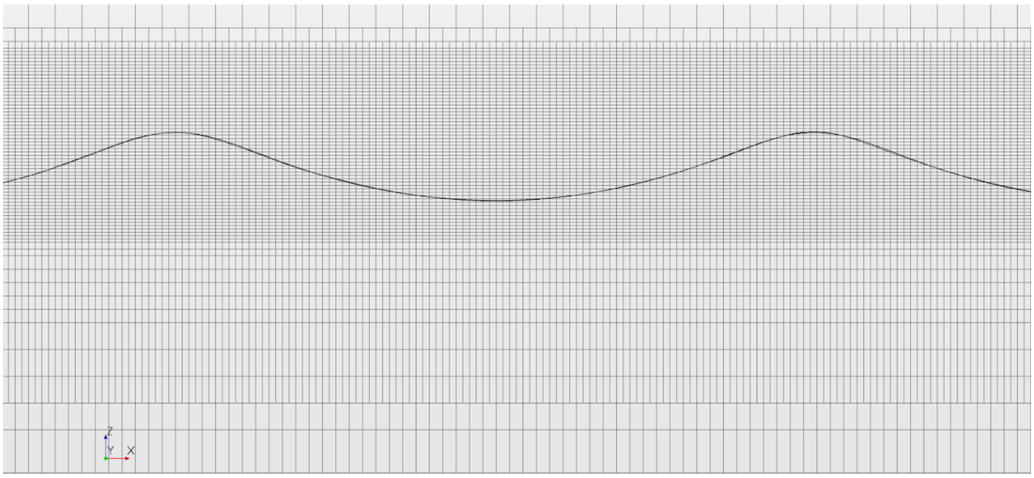

Figure 94: Mesh section in the vicinity of the free surface (black line) for further refined discretization ($14.6 \cdot 10^6$ cells)

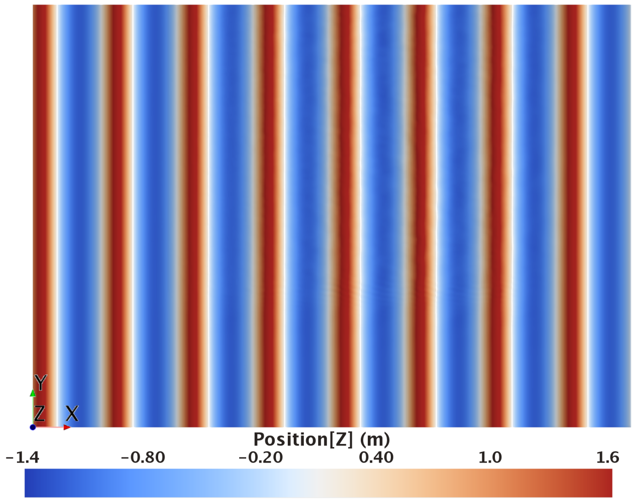

Figure 95: Free-surface elevation in solution domain at time $t = 60\,\mathrm{s}$ for forcing towards 5^{th}-*order Stokes wave theory* with close-to-optimum forcing strength γ and further refined discretization ($14.6 \cdot 10^6$ cells)

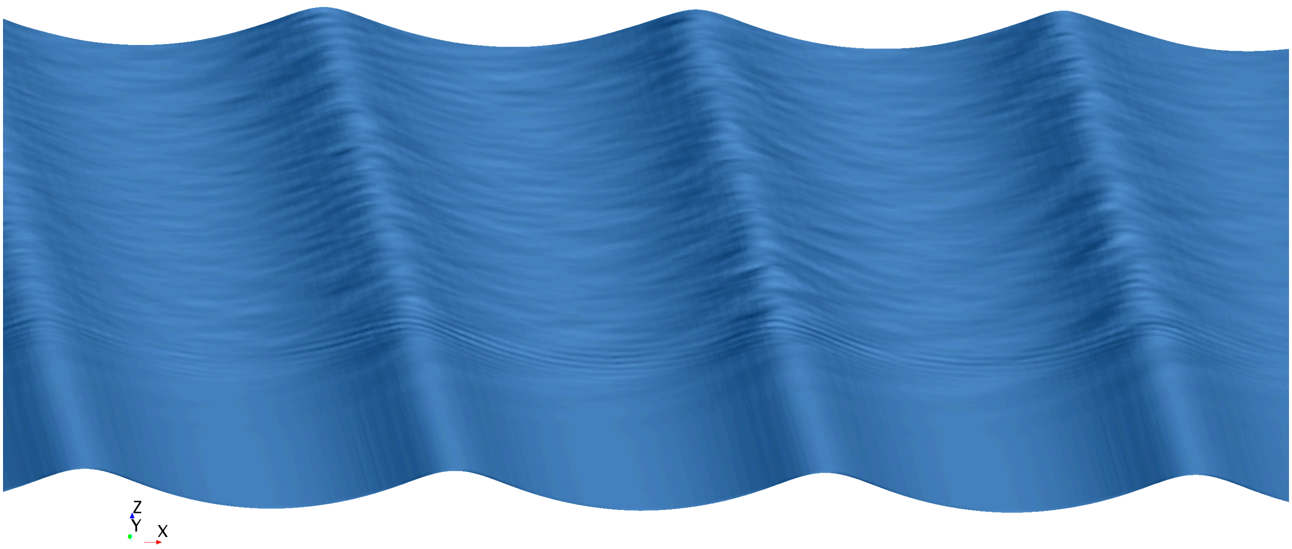

Figure 96: As Fig. 95, except for side view and uniformly colored free surface, to illustrate that flow disturbances are still present even with the further refined discretization ($14.6 \cdot 10^6$ cells)

Another case when theoretical and computed solutions are expected to show considerable discrepancies is when simulating irregular waves as shown in Fig. 97 left.

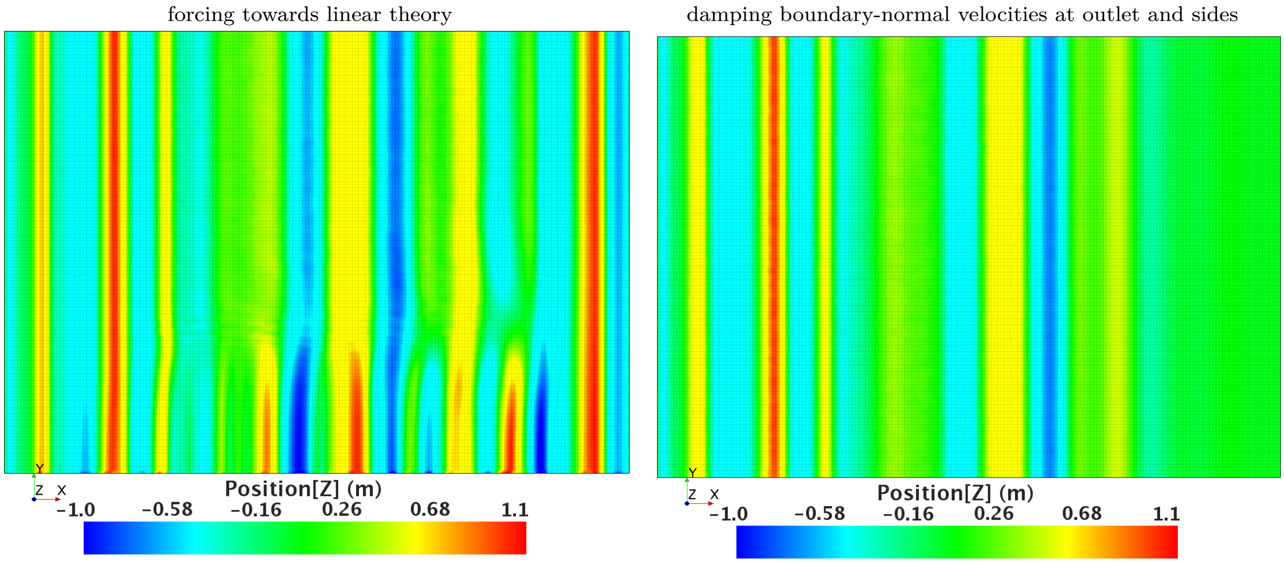

Figure 97: Free-surface elevation in solution domain at time $t = 40\,\mathrm{s}$ for forcing towards linear wave theory solution for an irregular wave as a *superposition of linear wave components* (left) compared to employing forcing zone arrangement (b) from Fig. 87, i.e. forcing only boundary-normal velocities towards zero at the outlet and domain sides (right); despite the comparatively coarse discretization, forcing zone arrangement (b) from Sect. 7.1 (right) does not create flow disturbances

For the proposed forcing zone arrangement (c) from Fig. 87 in Sect. 7.1, such errors due to discrepancies between computed flow and reference solution do not occur as demonstrated in Sect. 7.4.

7.3 Simulation setup

In the flow simulations in Sects. 7.4 and 7.5, long-crested free-surface waves are created and propagate in positive x-direction. The waves have height $H = 2\,\mathrm{m}$, period $T = 5\,\mathrm{s}$, wavelength $\lambda \approx 39.6\,\mathrm{m}$, and are moderately nonlinear (steepness H/λ is $\approx 36\%$ of maximum steepness). The water depth is $h \approx 0.41\lambda$ (intermediate-water conditions), which is close to deep-water conditions, i.e. the difference in wavelength to the deep-water ($h > 0.5\lambda$) case is only $\approx 1\%$.

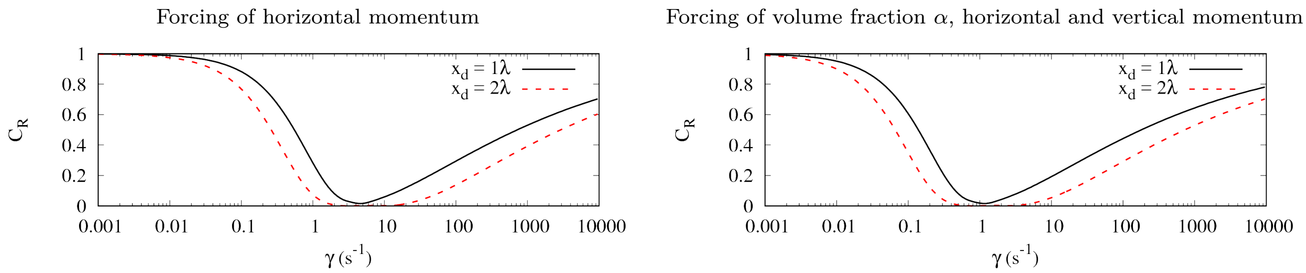

Figure 98: Theory prediction for reflection coefficient C_R as a function of forcing strength γ for the considered wave (period $T = 5\,\mathrm{s}$, wavelength $\lambda \approx 39.6\,\mathrm{m}$) for zone thickness $x_\mathrm{d} = 1\lambda, 2\lambda$ based on Sect. 4; the optimum value of γ depends on to which governing equations forcing source terms are introduced

The solution domain is box-shaped with dimensions $0 \leq x \leq L_x$, $0 \leq y \leq L_y$, and $-0.41\lambda \leq z \leq 0.46\lambda$ as shown in Fig. 99. Unless mentioned otherwise simulations are performed in a small domain ($L_x = 3.55\lambda$, $L_y = 3.94\lambda$). To investigate the influence of the domain size, some simulations are performed in a larger domain ($L_x = 7.09\lambda$, $L_y = 7.88\lambda$). The origin of the coordinate system lies on the calm free-surface level at the inlet boundary as shown in Figs. 99 and 100. At the inlet boundary $x = 0$, velocities and volume fraction according to Fenton's (1985) 5^{th}-order Stokes wave theory are prescribed to generate the wave. At the outlet boundary $x = L_x$, the hydrostatic pressure and volume fraction for the calm water-surface solution is prescribed. All remaining boundaries are no-slip walls. As initial condition, the volume fraction and velocities in the solution domain are prescribed according to Fenton's (1985) 5^{th}-order Stokes wave theory to reduce the simulation time, as shown in Fig. 99 middle.

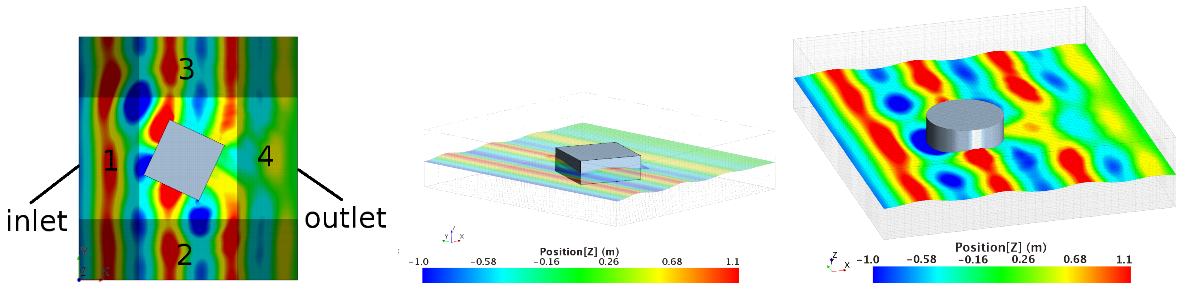

Figure 99: Top (left) and side view (middle, right) on simulation domain with floating pontoon (left, middle) or cylinder (right) in waves and forcing zones 1 to 4 (shaded gray), with forcing of x-momentum (zone 4), y-momentum (zones 2 and 3) and all momentum plus volume fraction (zone 1)

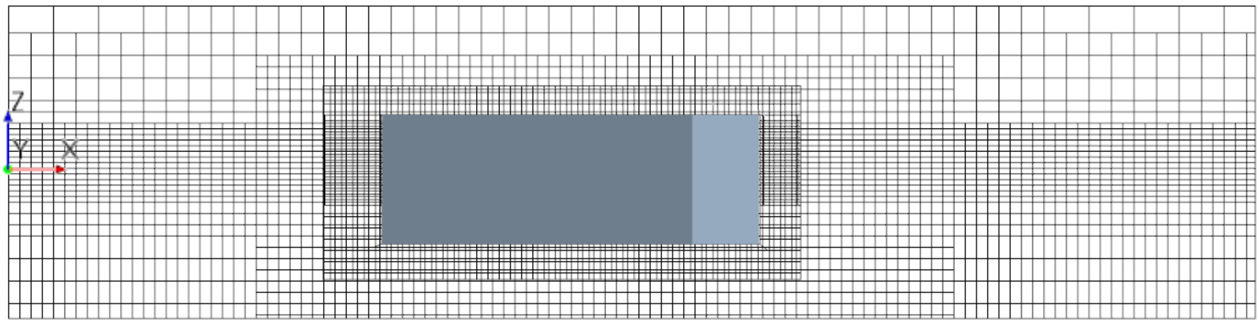

Figure 100: Slice through the computational grid at $y \approx 1.7\lambda$ with pontoon (gray)

Positioned within the domain is either a box-shaped semi-submerged pontoon or a vertical cylinder, as depicted in Fig. 99. The structures are placed slightly off-center so that undesired wave reflections at the domain sides will be asymmetrical.

The pontoon is a rectangular cuboid with side lengths $l_x = l_y = 0.985\lambda$ in horizontal direction, and $l_z = 0.364\lambda$ in vertical direction. Initially, its center is located at $x \approx 1.71\lambda$, $y \approx 1.94\lambda$, $z = 0$ (small domain) or $x \approx 3.48\lambda$, $y \approx 3.91\lambda$, $z = 0$ (large domain). The angle between the normal vectors of the inlet boundary and of the pontoon boundary facing the inlet is 25 deg. The pontoon weighs $1.2168 \cdot 10^7$ kg, has a draft of 0.202λ and uniform density. In some simulations the pontoon is held fixed (0DOF), in others it is allowed to move with 6 degrees of freedom (6DOF), i.e. surge, sway, heave, roll, pitch, and yaw.

The cylinder is surface-piercing, extends from domain bottom to top, has a diameter of $D = 0.91\lambda$, and its center is located at $x = 1.47\lambda$, $y = 1.72\lambda$. The cylinder is held fixed (0DOF).

Forcing zones 1 to 4 from Fig. 87 have different source terms:

Forcing zone 4 damps waves traveling towards the outlet boundary by applying

$$q_x = -\gamma b(\mathbf{x}) u \quad , \tag{116}$$

in Eq. (20) for the x-momentum.

Forcing zones 2 and 3 damp waves traveling towards the domain sides by applying

$$q_y = -\gamma b(\mathbf{x}) v \quad , \tag{117}$$

in Eq. (20) for the y-momentum.

Forcing zone 1 forces the waves towards the incidence wave field by applying

$$\begin{aligned} q_x = \frac{\gamma}{4} b(\mathbf{x})(u_{\text{ref}} - u) \quad , \quad q_y &= \frac{\gamma}{4} b(\mathbf{x})(v_{\text{ref}} - v) \quad , \\ q_z &= \frac{\gamma}{4} b(\mathbf{x})(w_{\text{ref}} - w) \quad , \end{aligned} \tag{118}$$

in Eq. (20) for the x-, y-, and z-momentum, combined with

$$q_\alpha = \frac{\gamma}{4} b(\mathbf{x})(\alpha_{\text{ref}} - \alpha) \quad , \tag{119}$$

in Eq. (21) with $b(\mathbf{x})$ according to Eq. (9), forcing strength γ, Cartesian velocities $\mathbf{v} = (u, v, w)^{\mathrm{T}}$, volume fraction α, and u_{ref}, v_{ref}, w_{ref}, and α_{ref} being the corresponding quantities from the far-field wave according to 5^{th}-order Stokes wave theory. The factor 1/4 in Eqs. (118) and (119) is necessary to obtain forcing of similar strength when applying source terms in 4 governing equations simultaneously as compared to applying forcing only in a single governing equation as described in Sect. 4.1.2.

Simulations are performed for the different *forcing zone arrangements* shown in Fig. 87:

(a) Forcing zone 4: damp x-momentum at the outlet boundary via Eq. (116); even when optimally tuned, wave reflections at the inlet and at the domain sides will be present

(b) Forcing zones 2, 3, and 4: damp x-momentum at the outlet boundary via Eq. (116) and y-momentum at the domain sides via Eq. (117); even when optimally tuned, wave reflections at the inlet will be present

(c) Forcing zones 1, 2, 3, and 4: damp x-momentum at the outlet boundary via Eq. (116) and y-momentum at the domain sides via Eq. (117) and force towards the incidence wave at the inlet boundary via Eqs. (118) and (119); when optimally tuned, wave reflections at all domain boundaries are minimized

Unless mentioned otherwise, the forcing zone thickness is $x_{\mathrm{d}} = 1\lambda$. Simulations are performed for different forcing strengths ($0.0\,\mathrm{s}^{-1} \leq \gamma \leq 131.2\,\mathrm{s}^{-1}$). The results are compared to the theory predictions for forcing zone behavior shown in Fig. 98. Simulations are performed without or with additional turbulence modeling using the standard k-ω-model from Wilcox (1993); where no turbulence modeling is mentioned in the text, the flow is considered laminar and no turbulence model is used.

For the flow simulations, the finite-volume-based commercial flow solver STAR-CCM+ version 11.06.010-R8 from Siemens (formerly CD-adapco) is used. The volume of fluid (VOF) method accounts for the two phases, liquid water and gaseous air, using the high resolution interface capturing scheme (HRIC) as given in Muzaferija and Perić (1999). All discretization approximations are of second order. The linearized equation system is solved by the iterative STAR-CCM+ implicit unsteady segregated solver, using an algebraic multigrid method with Gauss-Seidel relaxation scheme, V-cycles for pressure and volume fraction of water, and flexible cycles for velocity calculation. The under-relaxation factor is 0.9 for velocities and volume fraction and 0.4 for pressure. Eight iterations are performed per time-step; one iteration consists of solving the governing equations for the velocity components, the pressure-correction equation (using the SIMPLE method for collocated grids to obtain the pressure values and to correct the velocities) and the transport equation for the volume fraction of water. Further information on the discretization of and solvers for the governing equations can be found in Ferziger and Perić (2002) or the STAR-CCM+ software manual.

The domain is discretized using a rectilinear grid with local mesh refinement around the free surface. The free surface stays at all times within the region of the finest mesh with > 30 cells per wavelength and > 6 cells per wave height. The computational grid, which consists of $\approx 0.6 \cdot 10^6$ cells for the small domain or $\approx 2.2 \cdot 10^6$ cells for the large domain, is shown in Fig. 100. The discretization was chosen as roughly the coarsest discretization that would be used in engineering practice. The total simulated time is $60\,\mathrm{s} = 12T$ with a time step of $\Delta t = T/500$.

In finite-volume-based flow solvers, discretization errors and iteration errors usually produce a certain amount of numerical diffusion and dispersion; thus the wave's height and phase change the further the wave travels through the domain[19] (see e.g. Larsen et al., 2019; Perić and Abdel-Maksoud, 2015b). Since the wave forces F on the structure are $F \propto H^2$, the change in wave height H has to be compensated to obtain correct results. For this, the change in wave height was determined via computationally inexpensive 2D-flow simulations of wave propagation without the structure using similar discretization (mesh size, time step, etc.) as in the 3D-flow simulations. The loss of wave height was $\approx 0.7\%$ for the small domain and $\approx 3.5\%$ for the large domain.

To obtain the correct wave height at the structure, possible approaches would be to perform the simulations with a considerably finer discretization, which increases the computational effort, or to perform the simulations with correspondingly increased wave height at the inlet. In the present work, an alternative approach is taken: Since the loss of wave height is comparatively small, the forces are first-order-scaled as

$$F = F_{\mathrm{simulated}} \cdot (H/H_{\mathrm{simulated}})^2 \quad , \tag{120}$$

where $F_{\mathrm{simulated}}$ is the force on the structure obtained from the simulation, $H_{\mathrm{simulated}}$ is the wave height that occurs in

[19] This effect is independent of the choice of boundary conditions. Whether or not forcing is used does not influence the change in wave parameters when the wave travels a certain distance within the solution domain.

the simulation at the location of the structure center, H is the intended wave height, and F is the approximation of the force on the structure for the intended wave height H.

7.4 Results for proposed forcing zone arrangement for 3D-flows with strongly reflecting bodies in free-surface waves

Flow simulations are performed for the pontoon as described in Sect. 7.3. First, simulations are performed for the small domain with the pontoon held in fixed position (0DOF). Forcing zone arrangement (c) from Fig. 87 is used, i.e. wave damping at outlet and domain sides combined with forcing towards the incidence wave at the inlet boundary. The forcing zone thickness is $x_\mathrm{d} = 1\lambda$.

Figures 101 and 102 show that the optimum value for forcing strength (here: $\gamma \approx 4.6\,\mathrm{s}^{-1}$) is well predicted by theory (cf. Fig. 98). For close-to-optimum forcing strength γ, a periodic solution is obtained as expected. The more γ deviates from its optimum value, the stronger are influences of undesired wave reflections visible in the results: the solution can become aperiodic and the forces on the body can increase due to the accumulation of reflected wave energy in the solution domain. This illustrates the necessity of tuning the forcing zone parameters.

To assess the validity of the presented results, a grid- and time-step-dependence study was performed for the small domain case. The mesh size in all directions was changed by factor $1/\sqrt{2}$ (finer grid) and by factor $\sqrt{2}$ (coarse grid). Simulations were performed with time-steps $\Delta t = \frac{T}{500}$ (coarse grid), $\Delta t = \frac{T}{\sqrt{2}\cdot 500} \approx \frac{T}{707}$ (original, medium grid), and $\Delta t = \frac{T}{1000}$ (fine grid). For better comparison, Fig. 103 shows the results for optimum forcing setup without any scaling.

Both medium and fine grid produced the desired wave. On the coarse grid, the wave height diminished until it reached the pontoon, resulting in significantly lower forces (up to 8.6% lower force amplitudes) and a slight phase shift due to the change in wave steepness. Medium and fine grid results are nearly identical, with a difference in maximum force amplitude of $< 0.2\%$, and correspond closely to the results in Fig. 101, which were performed on the medium grid but with the coarse time step $\Delta t = \frac{T}{500}$. Thus the loss in wave height for the coarse grid can be mainly attributed to the mesh size. Based on these results, the medium grid was considered sufficient for the present purposes.

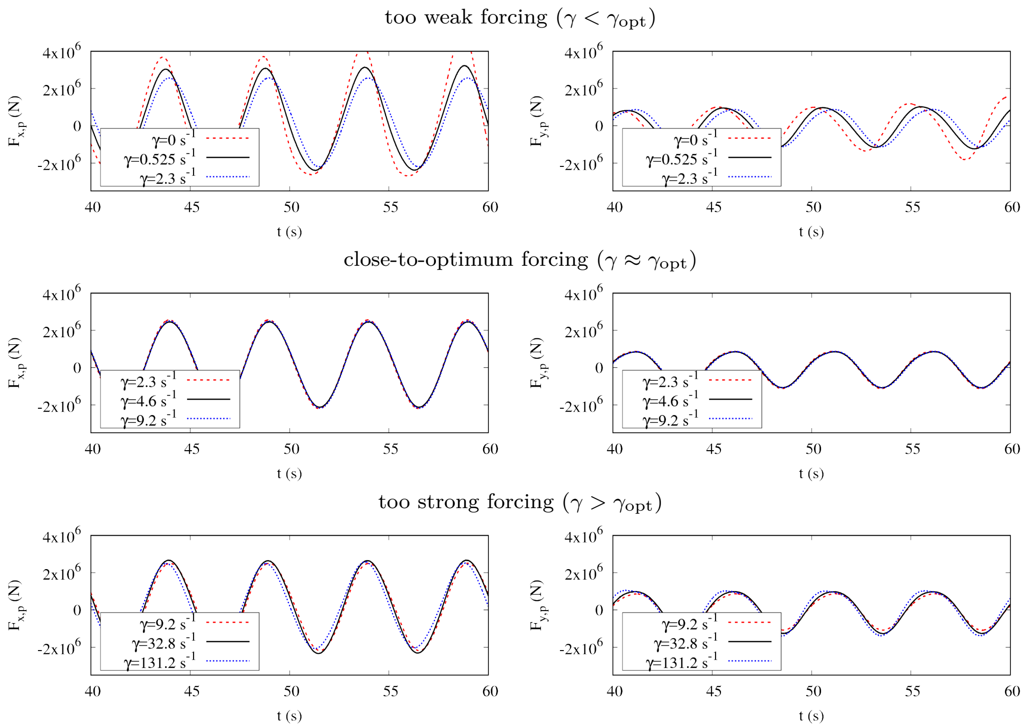

Figure 101: Force components in x- (left) and y-direction (right) integrated over pontoon surface as a function of time; for small domain with zone thickness $x_\mathrm{d} = 1\lambda$ and forcing zone arrangement (c); for close-to-optimum forcing strength ($\gamma_\mathrm{opt} \approx 4.6\,\mathrm{s}^{-1}$), a periodic solution is obtained as expected; for too weak/strong forcing strength γ, undesired reflections influence the results, so forces can increase and become aperiodic

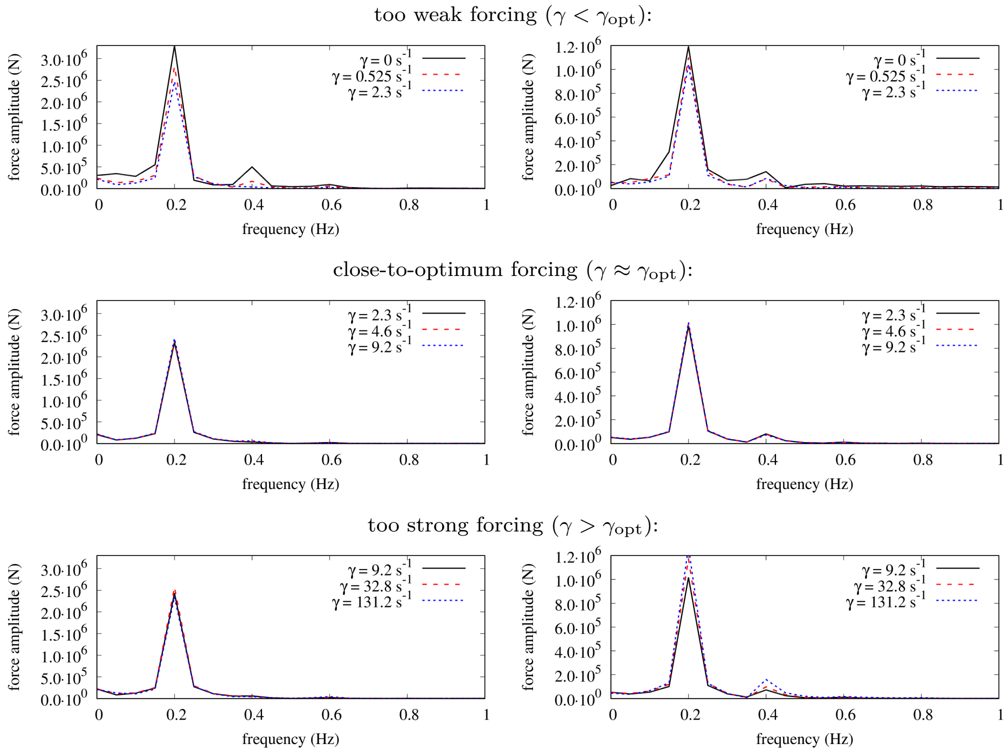

Figure 102: Force amplitude as a function of frequency for the results from Fig. 101; for x- (left) and y-component (right) of the forces integrated over the pontoon; the forces increase the further γ deviates from its optimum, which indicates the accumulation of undesired wave reflections

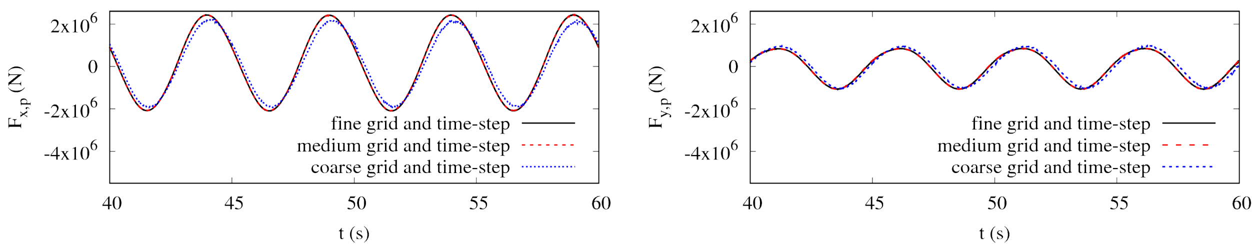

Figure 103: As Fig. 101 except for coarse, medium, and fine grids and time-steps with close-to-optimum forcing ($\gamma = 4.6\,\text{s}^{-1}$)

Figure 104 shows that repeating the simulations from Fig. 101 with turbulence modeling using the standard k-ω-model has no significant influence on the results. Thus the performance of the forcing zones can be considered independent of the use of turbulence models.

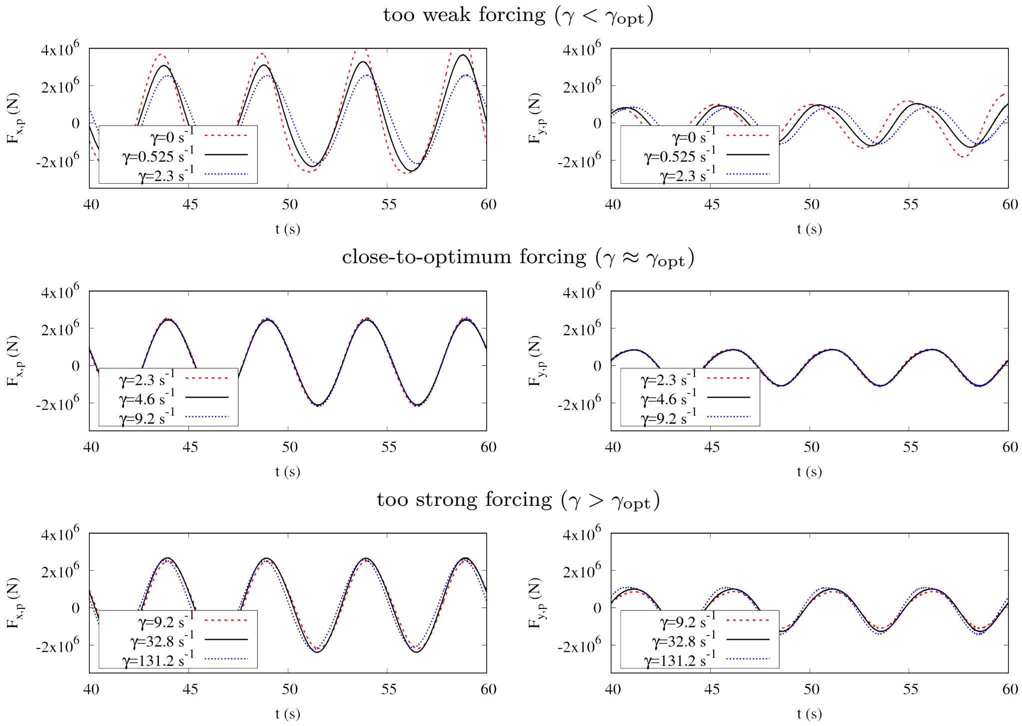

Figure 104: As Fig. 101, except with additional k-ω-turbulence modeling

To investigate the influence of the domain size and the forcing zone thickness, the simulations are repeated for the large domain with increased zone thickness $x_{\mathrm{d}} = 2\lambda$. Again the optimum setting for γ is satisfactorily predicted by the theory as Figs. 105 and 106 show. Further, the range of γ-values, for which undesired wave reflections are reduced satisfactorily, widens as predicted.

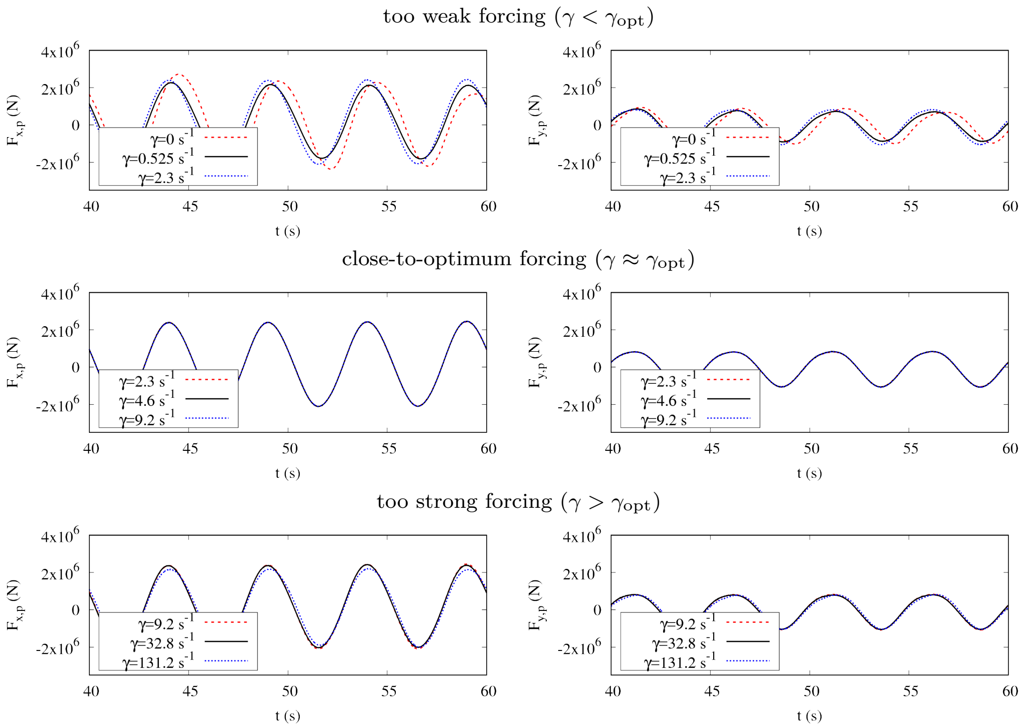

Figure 105: As Fig. 101, except for larger zone thickness $x_{\mathrm{d}} = 2\lambda$

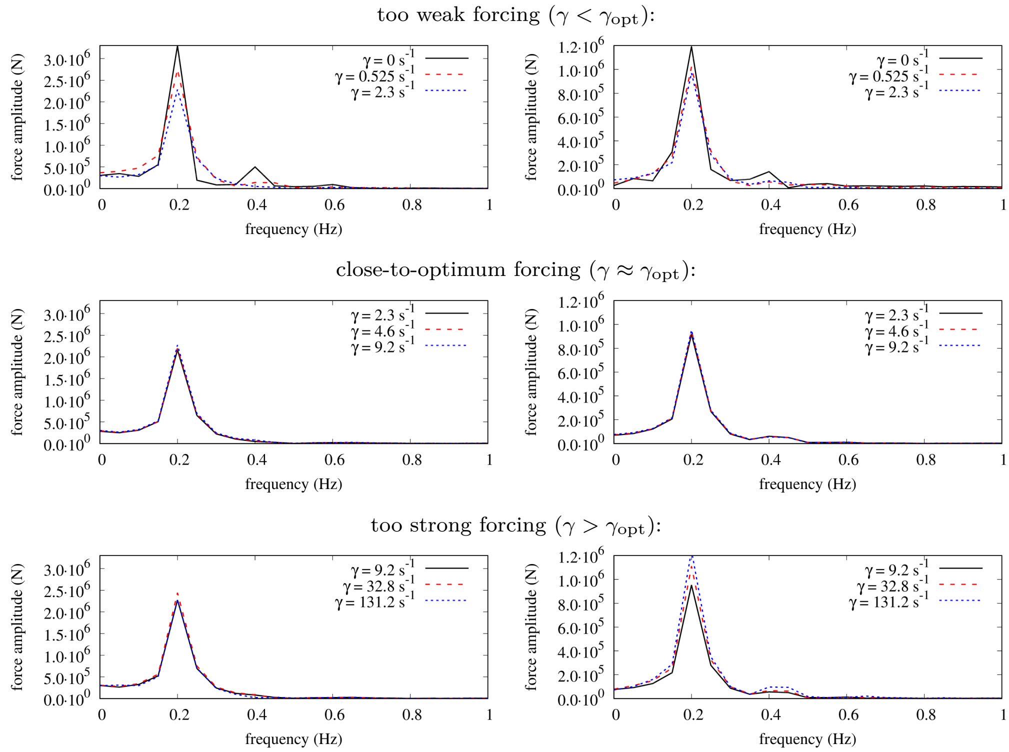

Figure 106: Force amplitude as a function of frequency for Fig. 105; for x- (left) and y-component (right) of the forces integrated over the pontoon

For close-to-optimum forcing strength γ, the differences between the results for the large and the small domain are negligible as Figs. 107 to 109 show. This indicates that undesired wave reflections were satisfactorily reduced on both the small and the large domain. Thus, as expected from the findings in Sects. 5.4 to 5.6, the 1D-theory from Sect. 4.1 can be considered sufficiently accurate for tuning forcing zones in 3D-flow simulations with free-surface waves.

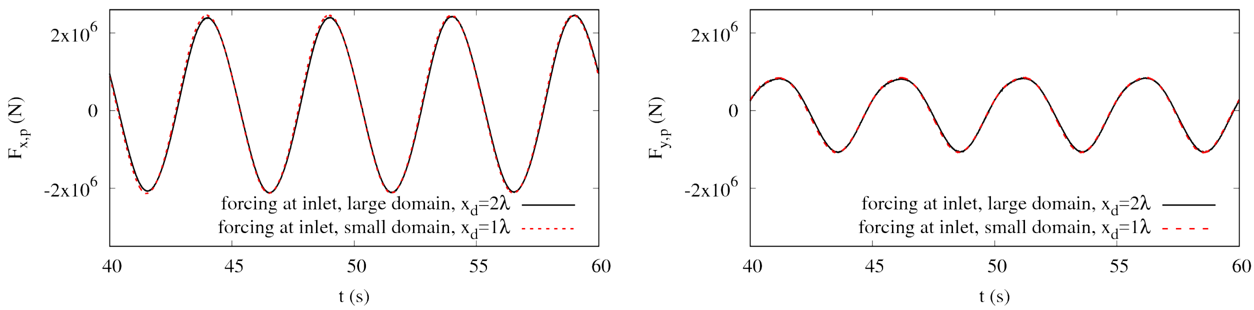

Figure 107: Force components in x- (left) and y-direction (right) integrated over the pontoon surface as a function of time; for large domain with zone thickness $x_{\mathrm{d}} = 2\lambda$ and for small domain with zone thickness $x_{\mathrm{d}} = 1\lambda$, both with forcing zone arrangement (c); the results are nearly identical as Fig. 108 confirms

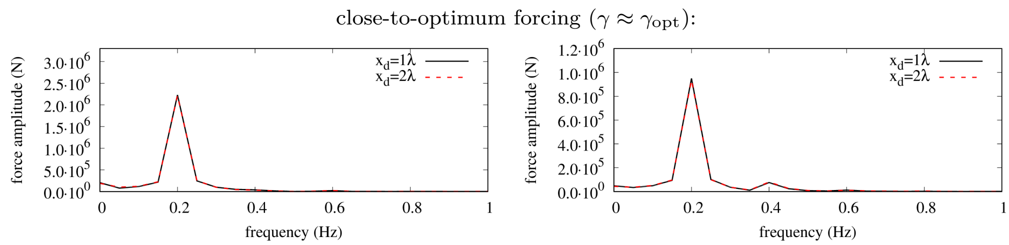

Figure 108: Force amplitude as a function of frequency from FFT of Fig. 107; for x- (left) and y-component (right) of the forces integrated over the pontoon; the largest force amplitude occurs at frequency $f = 0.2\,\mathrm{Hz}$; the largest force amplitude on the small ($x_{\mathrm{d}} = 1\lambda$) and large domain ($x_{\mathrm{d}} = 2\lambda$) differ by less than 0.7% (x-component) and 1.4% (y-component), and the average difference over all force amplitudes per plot is less than 1.2% (x-component) and 1.1% (y-component) in terms of the corresponding maximum force amplitude; thus with correct tuning of the forcing zones, satisfactory results can be obtained already with the small domain

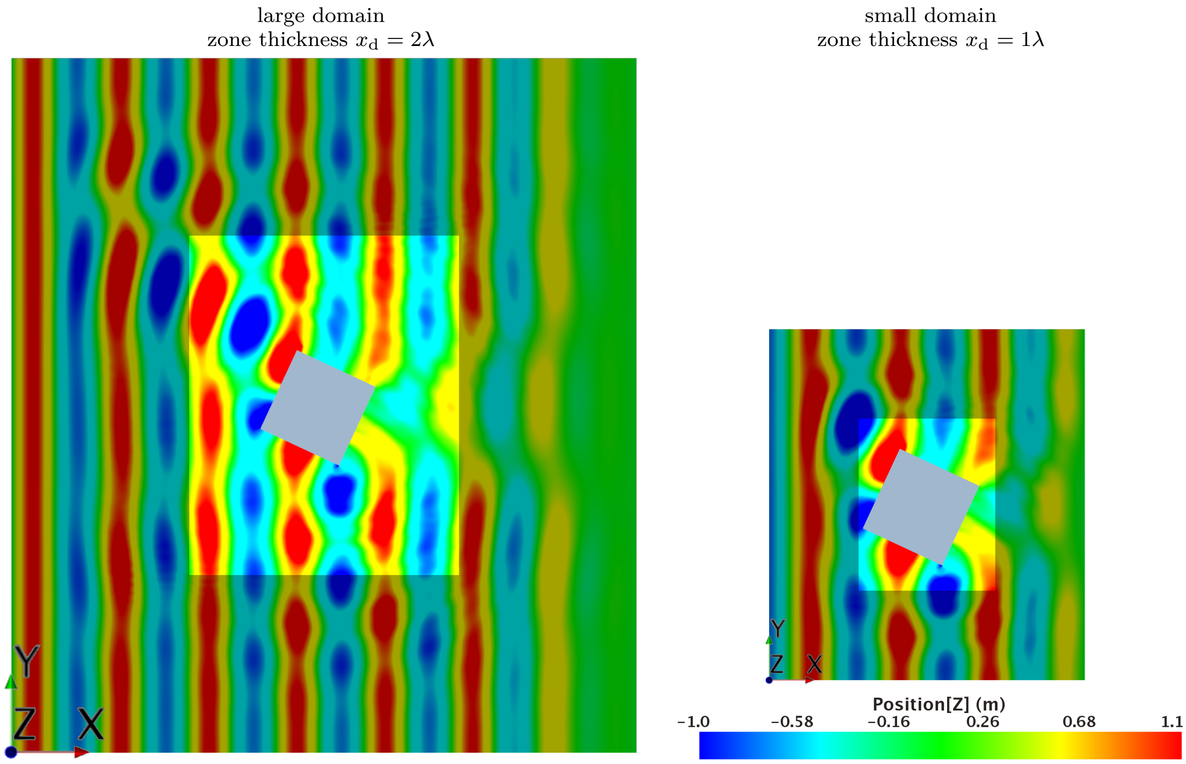

Figure 109: Free-surface elevation at the end of the simulation; the results for the large domain with larger zone thickness ($x_d = 2\lambda$) and the small domain with smaller zone thickness ($x_d = 1\lambda$) are nearly identical in the vicinity of the pontoon; therefore correct tuning of forcing zones enables the use of smaller domains and thus can decrease the computational effort substantially

Therefore the main finding of this section is that *with correct tuning of the forcing zones, satisfactory results can be obtained with smaller domains and thinner forcing zones than commonly used.* In the present case, using the small instead of the large domain in Fig. 109 provided similar results, but reduced the computational effort by more than 72%.

7.5 Results for other forcing zone arrangements in 3D-flows with strongly reflecting bodies in free-surface waves

To investigate the influence of undesired wave reflections at the inlet boundary, the above simulations are repeated with forcing zone arrangement (b) from Fig. 87, i.e. with wave damping at outlet and domain sides, and full reflections at the inlet boundary.

Figures 110 and 111 show that the optimum tuning of forcing strength γ is again well predicted by theory.

Figure 112 shows that, despite the small domain size and full reflections at the inlet boundary, the results differ comparatively little to the previous ones from forcing arrangement (c) (Figs. 101 and 105).

In Sect. 7.4 with forcing arrangement (c), increasing domain size and forcing zone thickness x_d did not significantly change the results; this indicates that undesired wave reflections were satisfactorily minimized.

For forcing arrangement (b) however, increasing domain size and forcing zone thickness x_d changed the results. Figure 113 shows that on the larger domain, the differences to the results from forcing arrangement (c) are $< 1.8\%$, whereas they were $< 5.4\%$ on the smaller domain. This indicates that increasing the distance to the inlet decreased the influence of undesired wave reflections at the inlet, which was expected from the discussion on Fig. 88. However, the close-up in Fig. 114 reveals that the force amplitudes fluctuate significantly with forcing arrangement (b), which indicates that forcing arrangement (c) is indeed more accurate.

On the whole though, the errors due to undesired wave reflections at the inlet with forcing arrangement (b) were comparatively small. This indicates that, for some 3D-flow problems with strongly reflecting bodies in free-surface waves (such as the present case), also with forcing zone arrangement (b) acceptable results can be obtained.

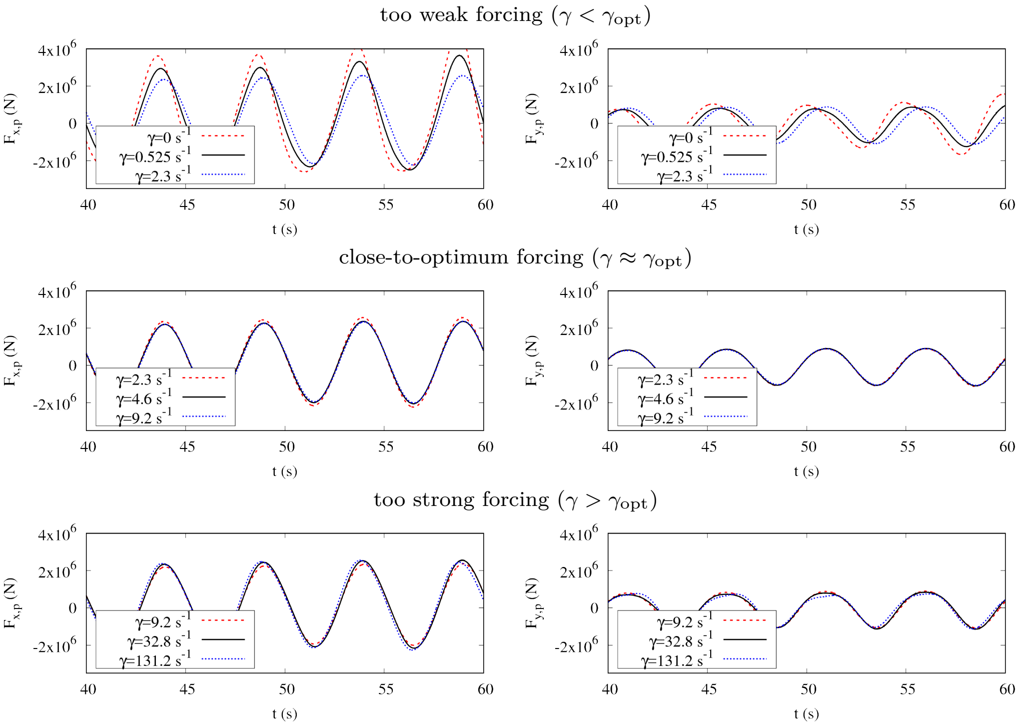

Figure 110: Force components in x- (left) and y-direction (right) integrated over the pontoon surface as a function of time; for small domain with layer thickness $x_{\text{d}} = 1\lambda$ and forcing zone arrangement (b)

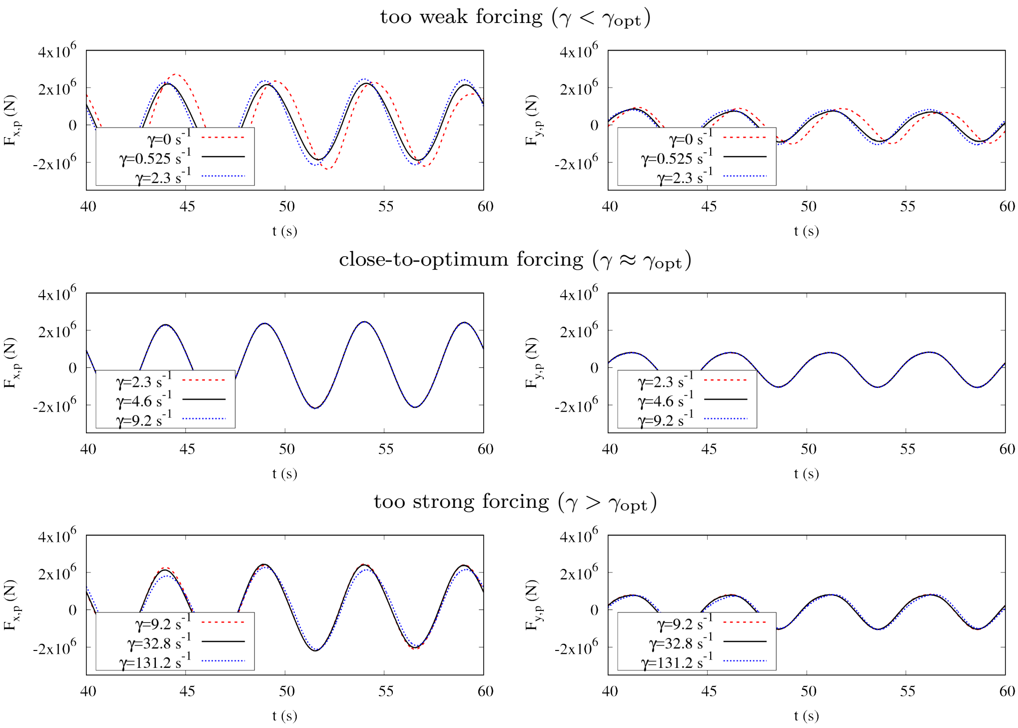

Figure 111: As Fig. 110, except for increased zone thickness $x_{\text{d}} = 2\lambda$

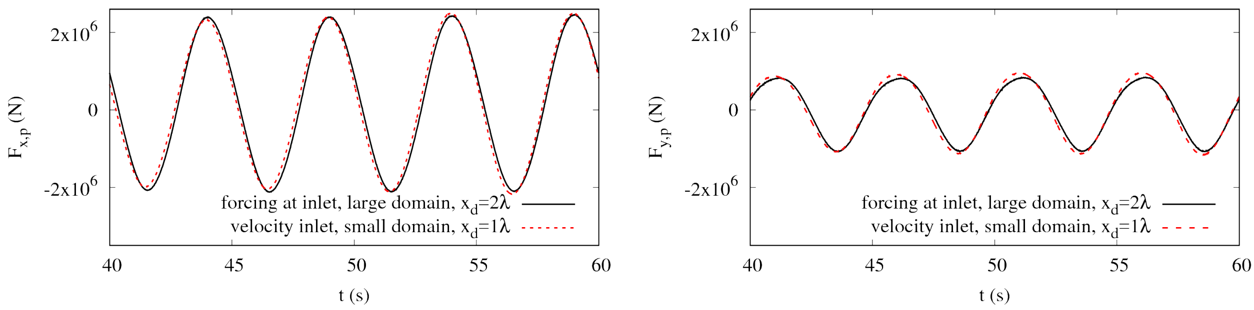

Figure 112: Force components in x- (left) and y-direction (right) integrated over the pontoon surface as a function of time; for small domain with zone thickness $x_{\mathrm{d}} = 1\lambda$ with forcing zone arrangement (b) ('velocity inlet') and large domain with zone thickness $x_{\mathrm{d}} = 2\lambda$ with forcing zone arrangement (c) ('forcing at inlet') at close-to-optimum forcing strength ($\gamma = 4.6\,\mathrm{s}^{-1}$); an FFT-analysis of the above curves shows that for forcing zone arrangements (b) and (c) the results for the force amplitudes differ by $< 5.4\%$ ($F_{\mathrm{x,p}}$) and $< 3.3\%$ ($F_{\mathrm{y,p}}$) in terms of the maximum force amplitude; thus the difference between the simulations with (b) and without (c) undesired wave reflections at the inlet boundary is comparatively small for this case

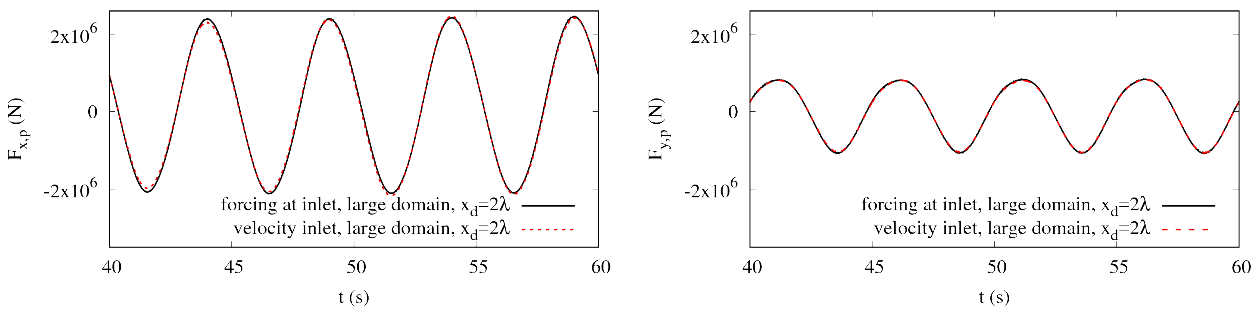

Figure 113: Force components in x- (left) and y-direction (right) integrated over the pontoon surface as a function of time; for large domain with zone thickness $x_{\mathrm{d}} = 2\lambda$; with forcing zone arrangement (b) ('velocity inlet') and (c) ('forcing at inlet') at close-to-optimum forcing strength ($\gamma = 4.6\,\mathrm{s}^{-1}$); an FFT-analysis of the above curves shows that for forcing zone arrangements (b) and (c) the results for the force amplitudes differ by $< 0.9\%$ ($F_{\mathrm{x,p}}$) and $< 1.8\%$ ($F_{\mathrm{y,p}}$) in terms of the maximum force amplitude; thus the difference between the simulations with (b) and without (c) undesired wave reflections at the inlet boundary is comparatively small for this case

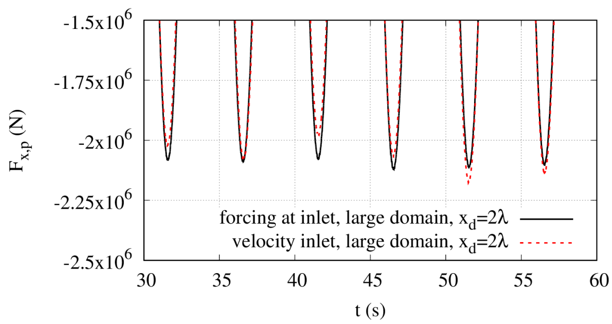

Figure 114: Close-up of left image from Fig. 113; the amplitude of $F_{\mathrm{x,p}}$ varies ca. 10% without (forcing arrangement (b), 'velocity inlet') and only ca. 2% with (forcing arrangement (c), 'forcing at inlet') minimization of undesired wave reflections at the inlet boundary

Figure 115 shows the results for repeating the simulations with the small domain with forcing zone arrangement (a), i.e. wave damping at the outlet in zone 4 and full reflections at the domain sides and at the inlet. The forces are aperiodic and contain significant errors due to undesired wave reflections at the domain sides.

Thus forcing zone arrangement (a) is unacceptable for simulations with strongly reflecting bodies in waves. Forcing zones should be used at least at the domain sides and at the outlet boundary.

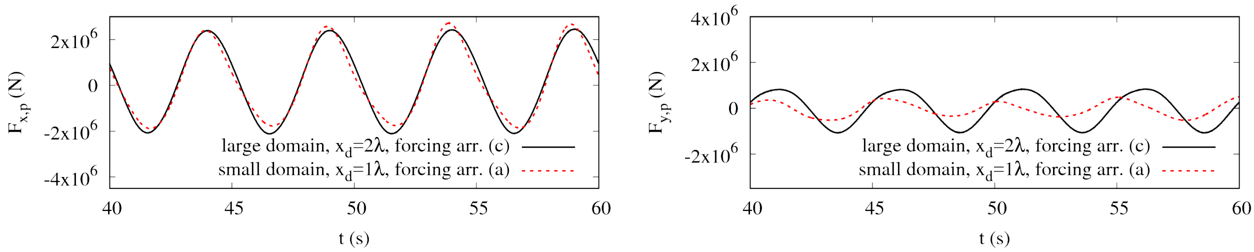

Figure 115: Force components in x- (left) and y-direction (right) integrated over the pontoon surface as a function of time; without (forcing arrangement (a), small domain, zone thickness $x_\mathrm{d} = 1\lambda$) and with (forcing arrangement (c)), large domain, zone thickness $x_\mathrm{d} = 2\lambda$) minimization of undesired wave reflections at inlet and side boundaries, for close-to-optimum forcing ($\gamma = 4.6\,\mathrm{s}^{-1}$); an FFT-analysis of the above curves shows that for forcing zone arrangements (a) and (c) the results for the force amplitudes differ by $< 5.7\%$ ($F_{\mathrm{x,p}}$) and $< 41\%$ ($F_{\mathrm{y,p}}$) in terms of the maximum force amplitude; thus when waves are only damped near the outlet boundary but fully reflected at the other boundaries, undesired wave reflections can have an unacceptably strong influence on the results

The findings from Sect. 6.7 suggest that tuning the forcing zone parameters to the peak wave period and using a slightly larger zone thickness provides a satisfactory reduction of undesired wave reflections for irregular waves. To investigate this, the simulations in the small domain with forcing zone arrangement (b) are repeated with JONSWAP and Pierson-Moskowitz wave spectra (see e.g. DNV, 2014; Hasselmann et al., 1973; Lloyd, 1998).

As discussed in previous sections, flow simulations with irregular waves are especially challenging. First, discretization and iteration errors are different for each wave component, so the wave will propagate differently in the simulation compared to the exact solution. Second, for realistic wave steepnesses linear superposition does not hold, so the wave propagation cannot be exactly described by analytical wave theories; while the correct velocities, pressures and elevations over a given distance of wave propagation may be predicted numerically e.g. by a higher-order nonlinear potential or spectral method as in Gatin et al. (2017), such codes are at the time of writing not always at hand and introducing the results into commercial flow solvers is not always possible or may at least be cumbersome.

Thus for the sake of simplicity, forcing arrangement (b) was used (i.e no forcing at the inlet boundary), since in the above investigations for the given configuration the influence of wave reflections at the inlet was found to be acceptably small (cf. Fig. 112). The significant wave height is $H_\mathrm{s} = H = 3\,\mathrm{m}$ and the peak wave period is $T_\mathrm{peak} = T = 5\,\mathrm{s}$ and an irregular wave is prescribed at the inlet by superposition of 200 linear wave components. The zone thickness is $x_\mathrm{d} = 1\lambda_\mathrm{peak} = 39.6\,\mathrm{m}$ as before; the forcing zone thickness was not increased since the original thickness in the previous simulations was already slightly larger than theoretically required.

Figures 116 and 119 indicate that both for Pierson-Moskowitz- and JONSWAP-spectrum, the theory predicts the optimum forcing strength ($\gamma \approx 4.6\,\mathrm{s}^{-1}$). As before, the differences in the resulting forces are smallest when the forcing strength γ is selected close to its optimum. As previous sections suggest, these differences could be further reduced by increasing the zone thickness and by using forcing arrangement (c) to minimize undesired wave reflections at the inlet boundary.

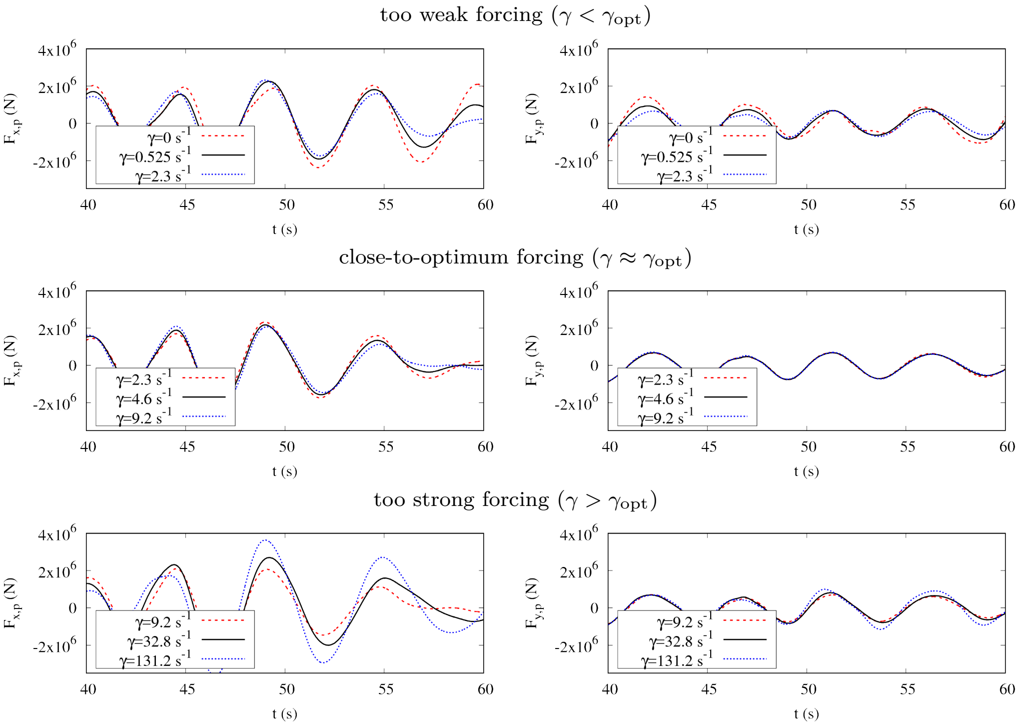

Figure 116: As Fig. 110, except with wave generation based on the Pierson-Moskowitz spectrum

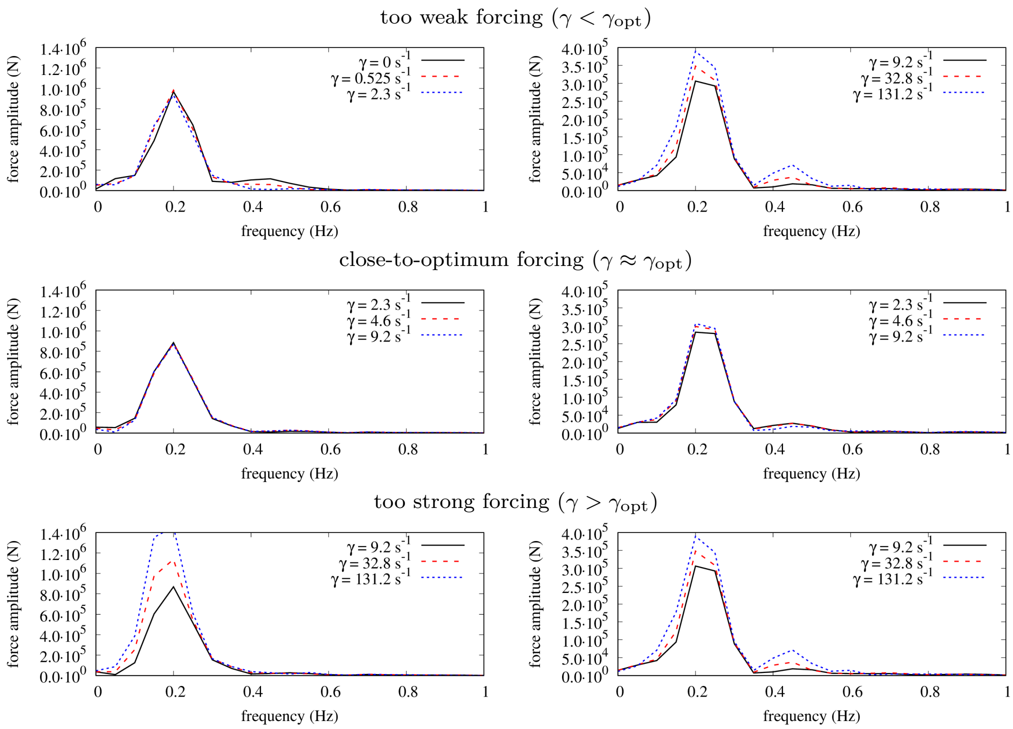

Figure 117: FFT-analysis of the curves from Fig. 116; the force amplitudes in x- (left) and y-direction (right) at the peak frequency $f_{\mathrm{peak}} = 0.2$ Hz differ by $< 10\%$ and $< 18\%$ (too weak forcing), $< 7\%$ and $< 3\%$ (close-to-optimum forcing), $< 69\%$ and $< 28\%$ (too strong forcing)

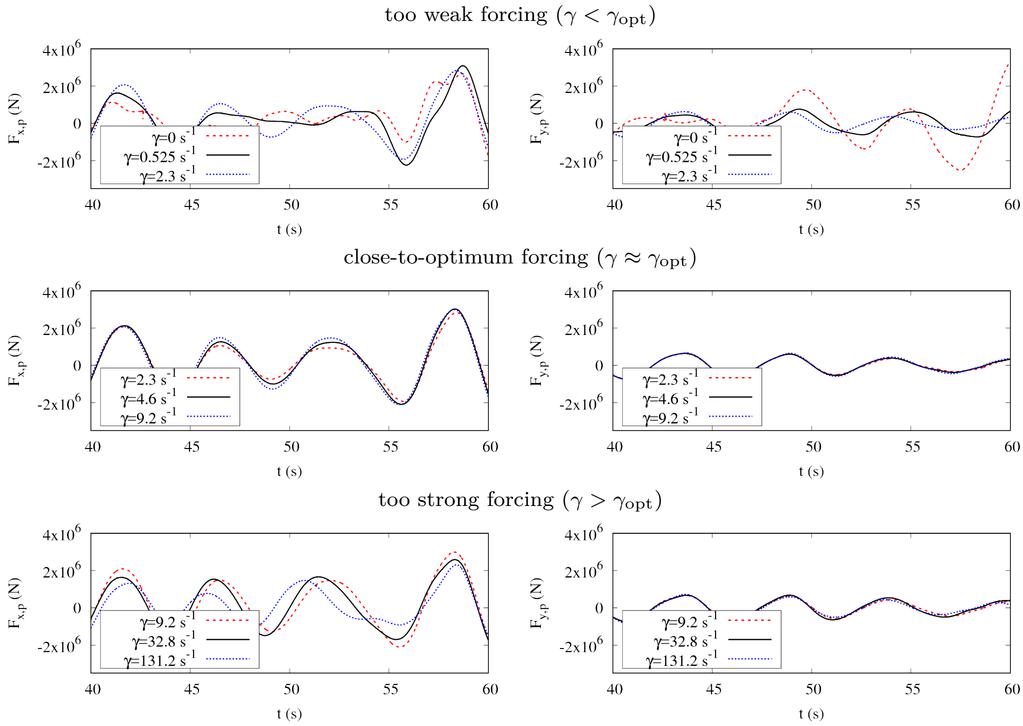

Figure 118: As Fig. 110, except with wave generation based on the JONSWAP spectrum

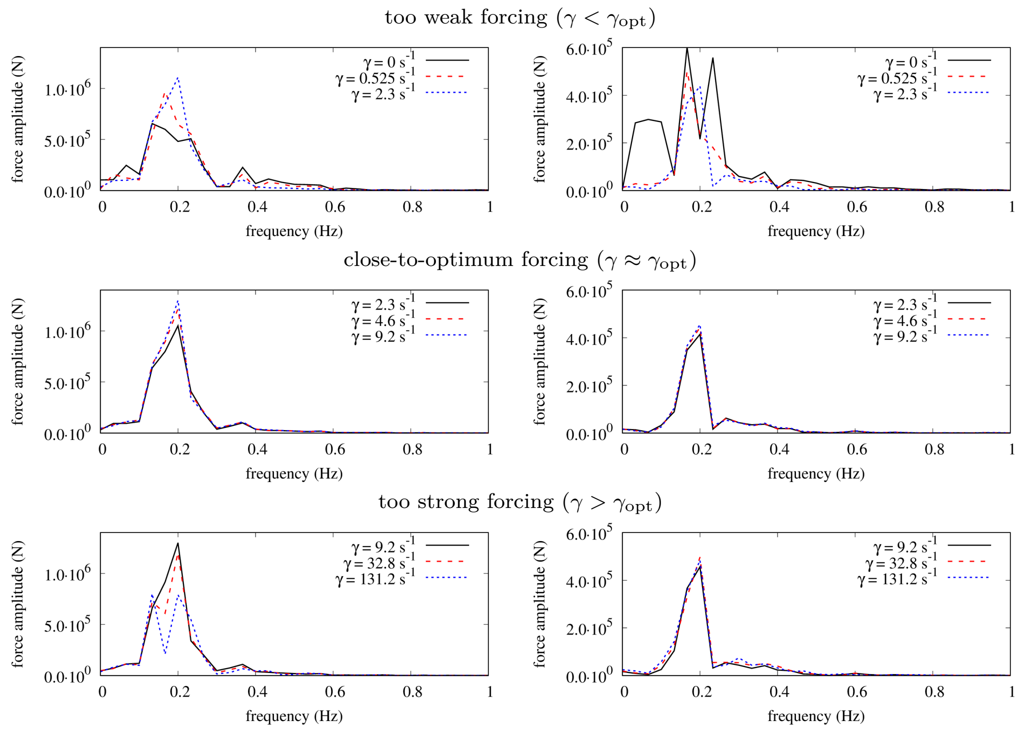

Figure 119: FFT-analysis of the curves from Fig. 118; the force amplitudes in x- (left) and y-direction (right) at the peak frequency $f_{\mathrm{peak}} = 0.2\,\mathrm{Hz}$ differ by $< 119\%$ and $< 94\%$ (too weak forcing), $< 18\%$ and $< 5\%$ (close-to-optimum forcing), $< 65\%$ and $< 9\%$ (too strong forcing)

The simulations with the pontoon held in a fixed position in the small domain with forcing zone arrangement (c) were repeated using an overset mesh with the pontoon in 6DOF-motion. Figures 120 to 122 show that the choice of forcing zone parameters affects the results as before. When forcing strength γ is close to its optimum value, the motions of the platform show smaller differences, which become larger the further γ deviates from its optimum value; note that for too strong damping, where reflection occurs at the entrance to the damping zone, the reflections reach the structure sooner (Fig. 121, bottom image) than for weak damping, where the reflections occur mainly at the domain boundaries. Therefore also the motions of the pontoon are strongly influenced by the forcing zone setup.

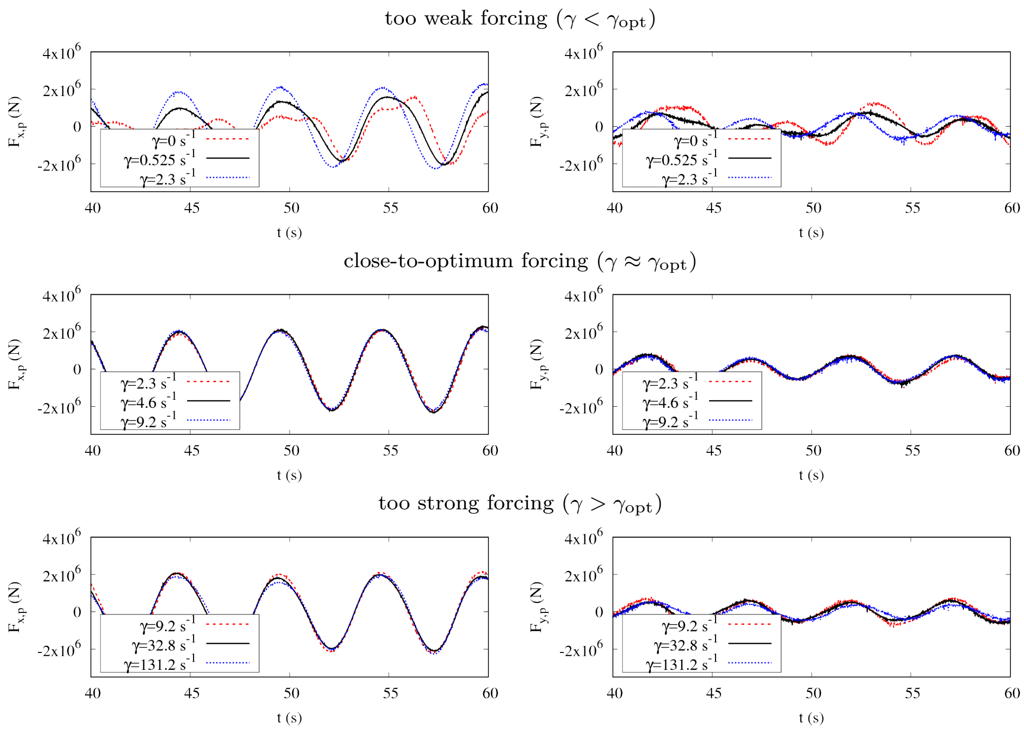

Figure 120: As Fig. 101, except that the pontoon moves unrestrained with six degrees of freedom (6DOF)

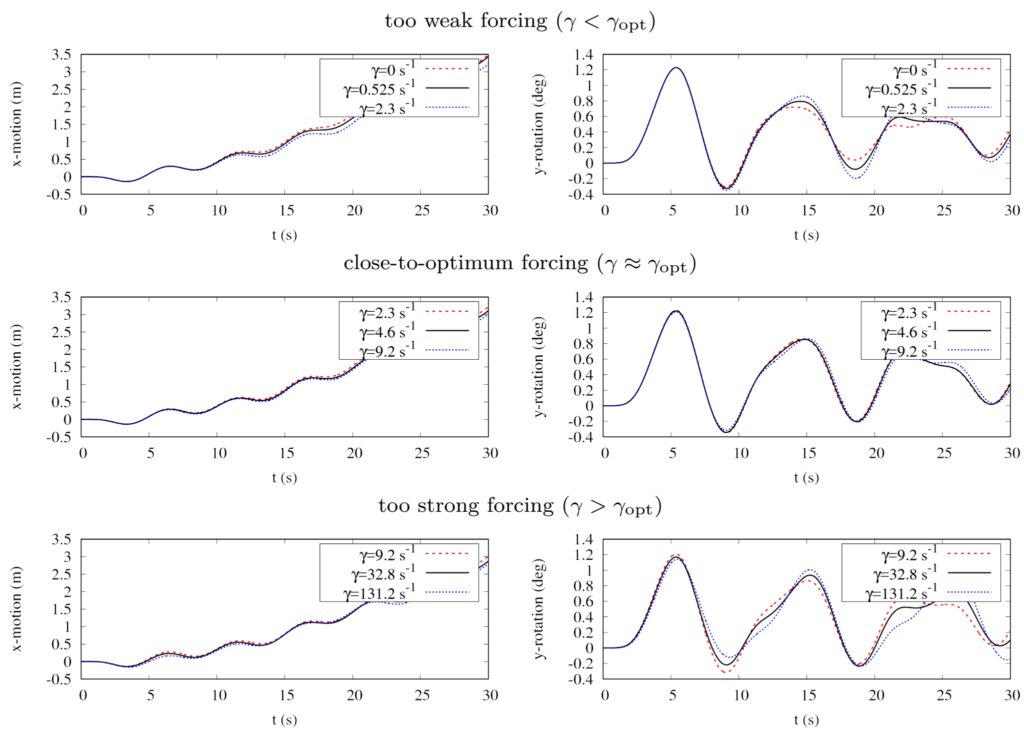

Figure 121: Motion in x-direction (left) and rotation around y-axis (right) of the pontoon from Fig. 120 as a function of time

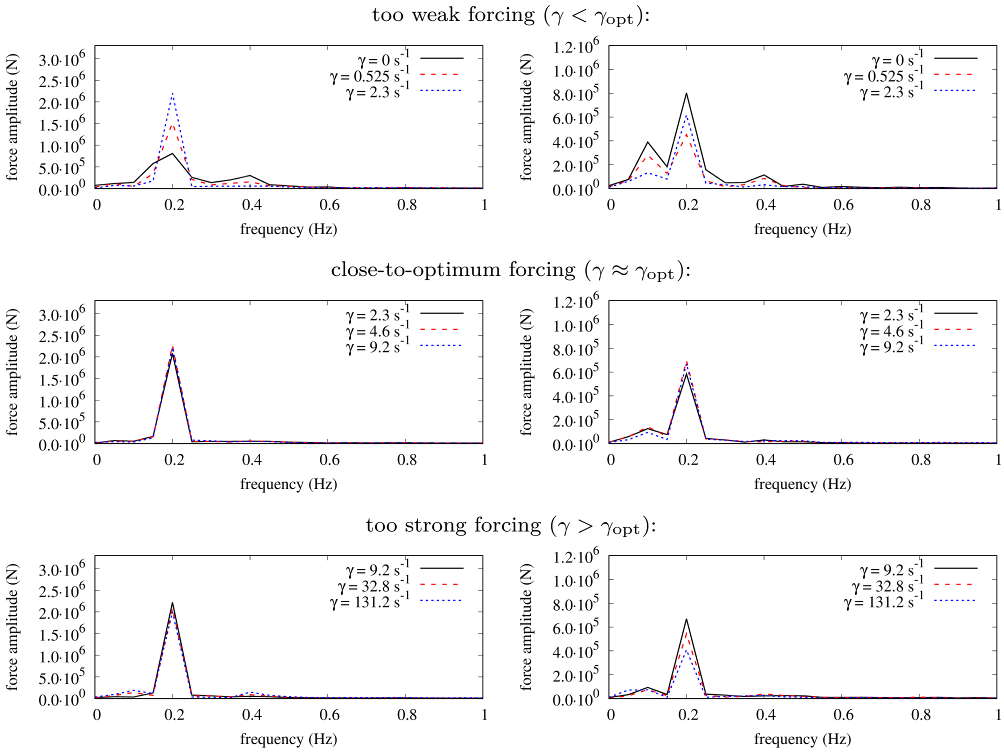

Figure 122: Force amplitude as a function of frequency for Fig. 120; for x- (left) and y-component (right) of the forces integrated over the pontoon floating with six degrees of freedom

In the light of the considerations from Sect. 7.1 it first seemed somewhat surprising that also forcing zone arrangement (b) provided acceptable results in Figs. 110 to 113. With the strongly reflecting pontoon placed so close to the fully reflecting inlet boundary, a stronger influence of undesired reflections could have been expected. The question therefore arose whether forcing zone arrangement (b) can be recommended in general, or whether this depends on the reflecting body and its orientation within the domain?

To answer this question, simulations in the small domain and forcing zone arrangements (b) and (c) were repeated with a fixed cylinder placed within the domain instead of the pontoon, as described in Sect. 7.3. Figure 99 shows the cylinder geometry and surface elevation in the solution domain.

As before, theory predicts the optimum forcing setup well as shown in Fig. 123 for forcing zone arrangement (b). However, repeating the simulations with forcing zone arrangement (c) in Fig. 124 shows large differences between the results for forcing arrangements (b) and (c) at optimum parameter settings; the maximum force amplitudes differ by more than $> 21\%$.

That forcing arrangement (c) produces the correct solution is verified by repeating the simulation in the large domain with thicker forcing zone ($x_{\text{d}} = 2\lambda$). Figure 125 shows that the results for forcing arrangement (c) in small and large domain are nearly identical, indicating that undesired wave reflections were satisfactorily minimized.

This demonstrates that, whereas the pontoon in its 25 deg-position reflected waves primarily sideways as indicated in Fig. 126, the cylinder reflected waves more evenly in all directions; thus more undesired wave reflections from the inlet reached the cylinder. Therefore the investigated pontoon simulations are an example for a case when forcing arrangement (b) can lead to acceptable results, while the cylinder case shows that this does not hold generally, but rather depends on the directional reflection characteristics of the body in waves.

Thus it is generally recommended to use forcing arrangement (c). Arrangement (b) may be used if the body is only weakly reflecting (or even transparent), or if it is strongly reflecting but reflects waves mainly sideways, so that reflections at the inlet are mostly re-reflected towards the damping zones at domain sides or outlet and only insignificantly towards the body in waves.

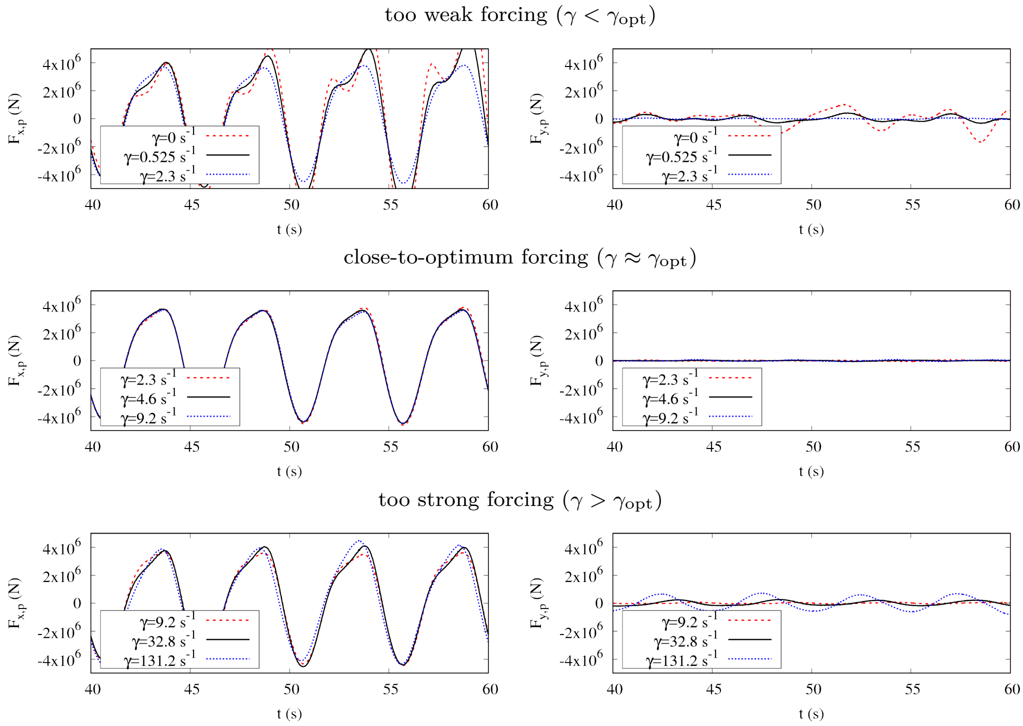

Figure 123: Force components in x- (left) and y-direction (right) integrated over the cylinder surface as a function of time; in small domain with zone thickness $x_{\mathrm{d}} = 1\lambda$ for forcing zone arrangement (b)

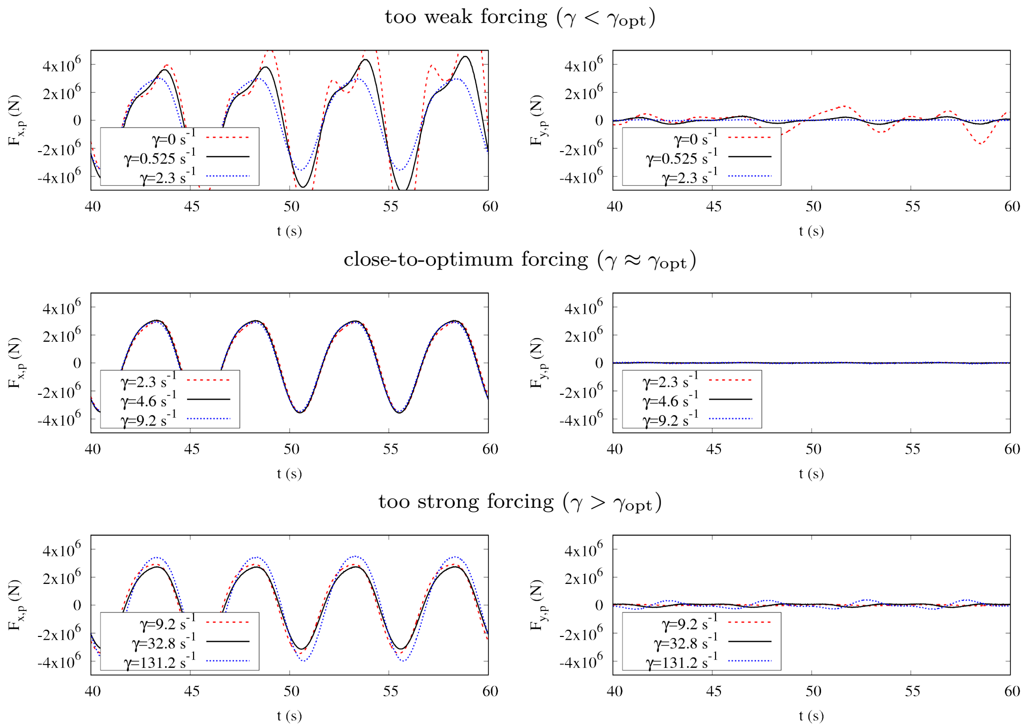

Figure 124: Force components in x- (left) and y-direction (right) integrated over the cylinder surface as a function of time; in small domain with zone thickness $x_{\mathrm{d}} = 1\lambda$ for forcing zone arrangement (c)

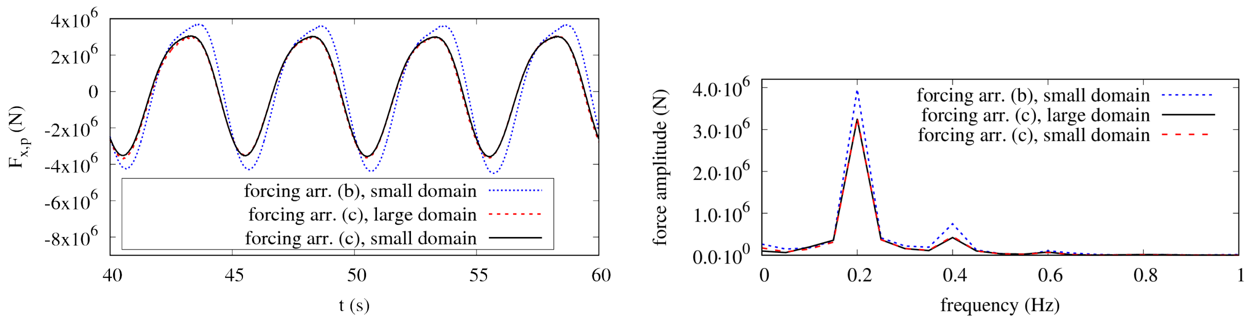

Figure 125: Left: as Fig. 123 at close-to-optimum forcing strength γ for forcing arrangement (b), compared to repeating the simulation with forcing zone arrangement (c) in small and large domain; right: FFT-analysis of the curves in the left plot; for forcing zone arrangement (c), the small and large domain results for the force amplitudes differ by $< 1.1\%$ in terms of the maximum force amplitude; the difference in force amplitudes between forcing zone arrangements (b) and (c) are $< 22\%$ in terms of the maximum force amplitude from forcing zone arrangement (c); thus forcing zone arrangement (b) contains significant errors due to undesired wave reflection at the inlet boundary

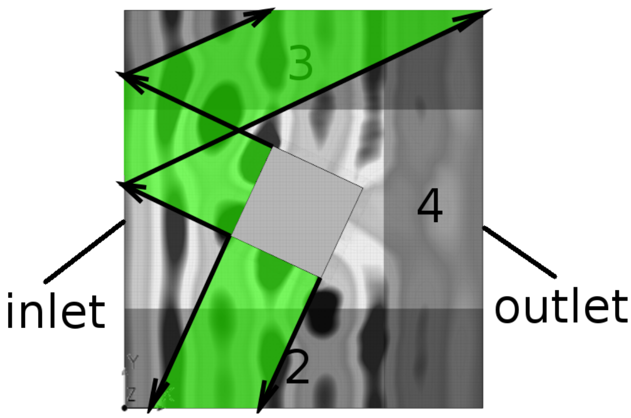

Figure 126: Sketched paths of waves reflected at the pontoon with forcing arrangement (b); although the inlet boundary reflects the waves, they mostly pass into the forcing zones where they are damped without encountering the pontoon again; this is an example where forcing arrangement (b) can be used with good results; however, if the pontoon was turned so that its sides are parallel to the domain sides, or if the pontoon were replaced by the cylinder from Fig. 99, then undesired reflections at the inlet would travel back towards the body in the domain and would cause significant errors as the results from Fig. 125 show

8 Relaxation zones for free-surface waves

Key findings

- Relaxation zones simultaneously blend-out the governing equations and blend-in a specified reference solution
- The theory from Sect. 4.2 satisfactorily predicts reflection coefficients C_R for 2D- and 3D-flow simulations with free-surface waves
- When correctly tuned, relaxation zones and forcing zones produce similar reflection coefficients C_R
- Tuning of the relaxation zones enables the use of smaller domains and thus reduces the computational effort

Sections 8.2 to 8.7 demonstrate that the theory from Sect. 4.2 satisfactorily predicts reflection coefficients for relaxation zones in flow simulations with free-surface waves. Simulations are performed based on the setup in Sect. 8.1 with two different flow solvers, Siemens STAR-CCM+ and the `foam-extend` Naval Hydro Pack. The validation is performed via parameter studies for different blending functions $b(\mathbf{x})$, zone thicknesses x_d, source term magnitudes and reference solutions. Simulations are performed for long-crested waves under shallow-water and deep-water conditions in 2D and for deep-water conditions in 3D with an additional strongly reflecting body within the domain. Based on these findings, recommendations for setting up relaxation zones are given.

When the relaxation zone was tuned using the theory, in all simulations from Sect. 8 held $C_{\mathrm{R,sim}} - C_{\mathrm{R,theory}} < 3.4\%$, with reflection coefficients from simulation results $C_{\mathrm{R,sim}}$ and the corresponding theory predictions $C_{\mathrm{R,theory}}$. Thus the theory predictions were considered to be of satisfactory accuracy for engineering practice.

8.1 Simulation setup

For the 2D-simulations in Sects. 8.2 to 8.6, the solution domain is box-shaped as seen in Fig. 127. The origin of the coordinate system lies at the calm free-surface level, with z pointing upwards and x pointing in wave propagation direction. The domain dimensions are $0\,\mathrm{m} \leq x \leq 24\,\mathrm{m}$, $-2\,\mathrm{m} \leq z \leq 0.24\,\mathrm{m}$ for the simulations with deep water conditions (water depth $h \approx 0.5\lambda$) and $0\,\mathrm{m} \leq x \leq 24\,\mathrm{m}$, $-0.2\,\mathrm{m} \leq z \leq 0.01\,\mathrm{m}$ for the simulations with shallow water conditions ($h \approx 0.05\lambda$). The simulations are performed as quasi-2D, i.e. with only one layer of cells in y-direction and the y-normal boundaries set to symmetry planes. Waves are generated by prescribing volume fraction and velocities according to Rienecker and Fenton's (1981) stream function wave theory (64^{th} order) at the velocity inlet $x = 0$. The deep-water cases had wave period $T = 1.6\,\mathrm{s}$, wavelength $\lambda \approx 4\,\mathrm{m}$ and wave height $H = 0.16\,\mathrm{m}$. The shallow-water cases had wave period $T = 2.893\,\mathrm{s}$, wavelength $\lambda \approx 4\,\mathrm{m}$ and wave height $H = 0.009\,\mathrm{m}$. The waves travel in positive x-direction towards a relaxation zone attached to the pressure outlet boundary at $x = 24\,\mathrm{m}$. At the outlet, pressure and volume fraction are prescribed according to the calm free-surface solution.

The governing equations are Eqs. (23) to (24). In the relaxation zone, the waves are blended towards a reference solution to reduce undesired wave reflections. The relaxation zone parameters were tuned as described in Sect. 4.2. Simulations were performed for different values of zone thickness x_d, different blending functions $b(\mathbf{x})$, and different reference solutions. The bottom boundary had a slip-wall boundary condition and at the top boundary atmospheric pressure was prescribed.

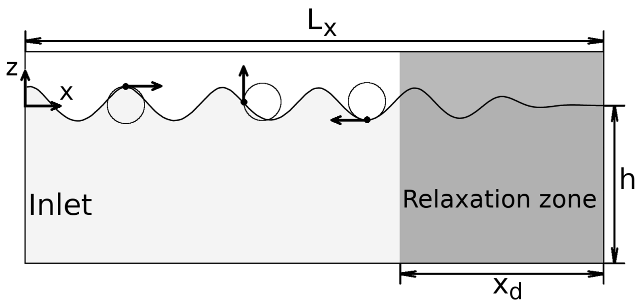

Figure 127: Solution domain filled with air (white) and water (light gray, water depth h), velocity inlet at $x = 0$ and relaxation zone (shaded dark gray) with thickness x_d; three fluid particles (black dots) are sketched with their particle paths (circles) and velocity vectors (arrows)

The simulations in this work were performed using the open-source solver `foam-extend` version 4.1, a community driven fork of the solver OpenFOAM (Weller et al., 1998), combined with the commercial software Naval Hydro Pack. The governing equations are Eqs. (23) to (24), so no turbulence modeling was used. All approximations were of second order. The solvers were conjugate gradient with Incomplete Cholesky preconditioner for pressures, bi-conjugate gradient with ILU0 preconditioner for volume fraction and velocities and the PIMPLE scheme was used with two pressure correction steps per each of the two nonlinear iterations in a given time-step. No under-relaxation was used. In all simulations, the Courant number $C = |\mathbf{v}|\Delta t/\Delta x$ was well below 0.4. Further information on the discretization of and solvers for the governing equations can be found in Ferziger and Perić (2002) and the flow solver manuals.

In Sect. 8.4, selected simulations were repeated with the commercial flow solver STAR-CCM+ version 10.6 by Siemens (formerly CD-adapco), using the grid and simulation setup from Sect. 6.1, except that the forcing zones in STAR-CCM+ were tuned via Eqs. (75) to (77) in such a way that they mimic the behavior of the relaxation zones from the Naval Hydro Pack.

Figure 128 shows the rectilinear grid with local mesh refinement. The free surface stays at all times within the zone with the finest mesh, with 25 (coarse grid), 35 (medium grid), or 50 (fine grid) cells per wavelength λ, and 5 (coarse grid), 7 (medium grid), or 10 (fine grid) cells per wave height H. The grid consists of 12 000 (coarse grid), 27 000 (medium grid), or 48 000 (fine grid) cells. The time-step was $0.01\,\mathrm{s} = T/160$ (coarse grid), $0.0071\,\mathrm{s} = T/226$ (medium grid), or $0.005\,\mathrm{s} = T/320$ (fine grid). The reflection coefficient C_R is calculated via Eq. (34).

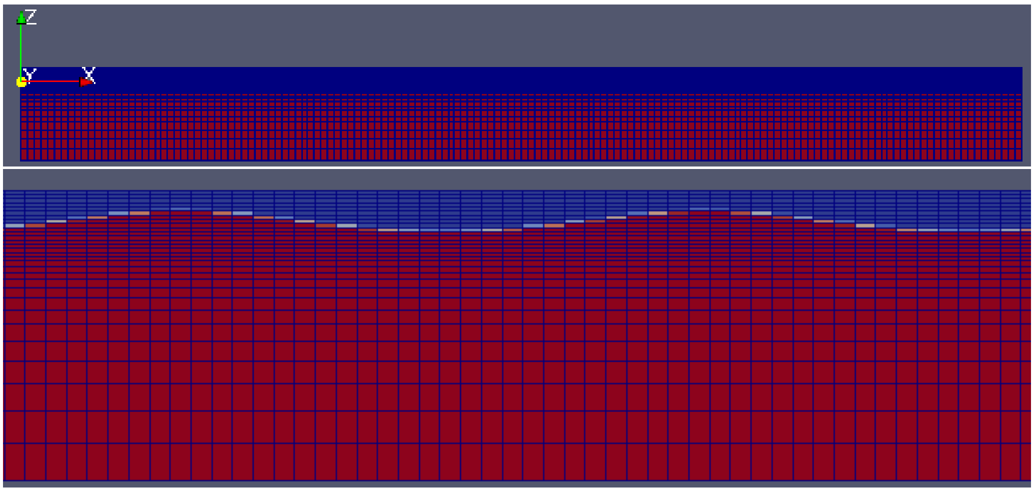

Figure 128: Mesh for 2D simulations with coarse mesh; far view (top) and close-up (bottom); the color denotes the volume fraction (red: water, blue: air)

For the 3D-simulations in Sect. 8.7, the setup is identical to the deep-water 2D simulations, with the following exceptions. The domain has dimensions $0\,\mathrm{m} \leq x \leq 10\,\mathrm{m}$, $0\,\mathrm{m} \leq y \leq 10\,\mathrm{m}$, $-5\,\mathrm{m} \leq z \leq 5\,\mathrm{m}$, so the water depth is $h = 5\,\mathrm{m}$ as seen in Fig. 129. In the center of the domain, a semi-submerged pontoon with dimensions $1\,\mathrm{m} \times 1\,\mathrm{m} \times 1\,\mathrm{m}$ is held in fixed position. It has a draft of $D = 0.5\,\mathrm{m}$ and slip wall boundary conditions. The wave has period $T = 1.6\,\mathrm{s}$, wave height $H = 0.4\,\mathrm{m}$, wavelength $\lambda \approx 4.3\,\mathrm{m}$ and steepness $H/\lambda \approx 71\%$ of the breaking steepness.

The free surface is discretized by 12.9 (coarse grid), 25.8 (medium grid), or 38.7 (fine grid) cells per wavelength λ and 2 (coarse), 4 (medium), or 6 cells per wave height H as shown in Fig. 129. Per wave period 160 (coarse grid), 225 (medium grid), or 320 (fine grid) time steps were used.

The relaxation zone thickness was $x_\mathrm{d} = 3\,\mathrm{m} \approx 0.7\lambda$ and power blending according to Eq. (6) with exponent $n = 0.46$ was used. Simulations are performed for different relaxation parameters $0.001\,\mathrm{s} \leq \tau \leq 1000\,\mathrm{s}$. This setup was expected to be close to the minimum domain size for the simulation of such a strongly reflecting body.

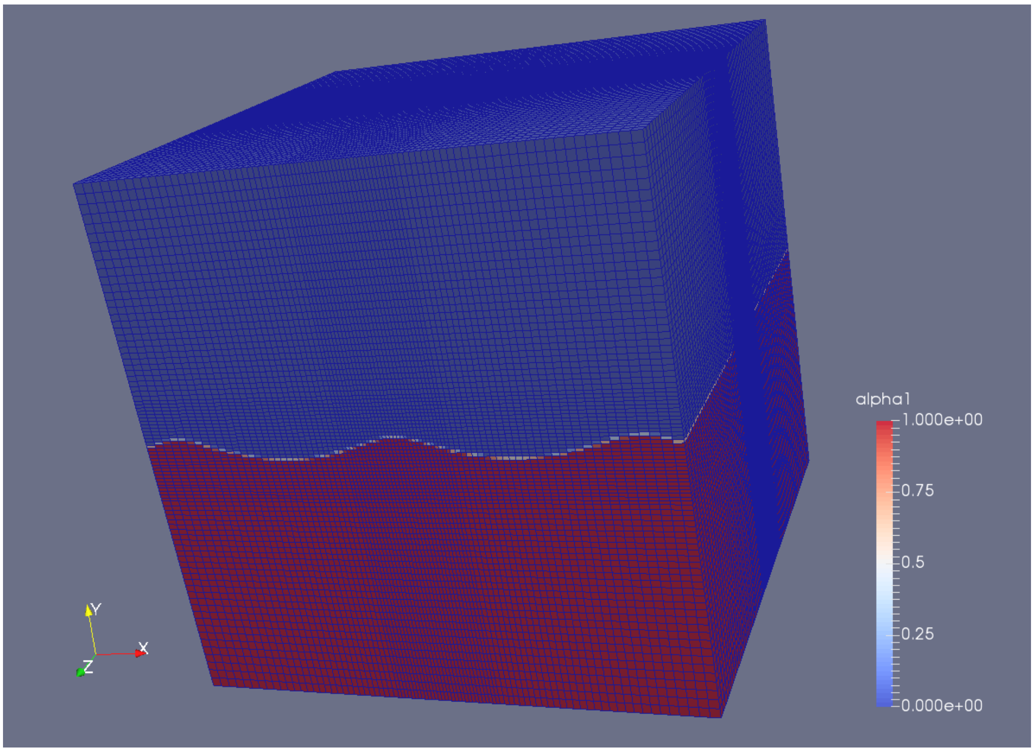

Figure 129: Fine mesh for 3D simulations with initialized volume fraction

8.2 Discretization dependence study for using relaxation zones to damp waves

First, the relaxation zone is set up to damp the waves by setting the hydrostatic solution for the calm free surface as reference solution in Eqs. (23) to (24) using the 2D-flow simulation setup from Sect. 8.1. Exponential blending via Eq. (10) with coefficient $n = 3.5$ is used, which is the default setting in the Naval Hydro Pack. Simulations are performed for different values of zone thickness x_{d} and relaxation parameter τ.

Figure 130 shows that the theory from Sect. 4.1.2 predicts the optimum parameter settings reasonably well, and the theoretical reflection coefficients C_{R} can with good approximation be taken as an upper bound for the recorded values. For the investigated setup, the Naval Hydro Pack default value of τ (i.e. $\tau = \Delta t$; here time step $\Delta t = 0.005\,\mathrm{s}$) is comparatively close to the optimum value of ca. $0.1\,\mathrm{s} \lesssim \tau \lesssim 0.5\,\mathrm{s}$, though not as close as the theory predictions. Further, with the Naval Hydro Pack default setting $\tau = \Delta t$ the reflection coefficients will increase for finer time steps, since Sect. 4.4 showed that the reflection behavior of relaxation zones can be considered independent of the discretization, which is supported by the results in Fig. 131. For example for a time step of $\Delta t \lesssim 1 \cdot 10^{-3}\,\mathrm{s}$, the same reduction of undesired wave reflections, that would be obtained with default settings for a relaxation zone thickness $x_{\mathrm{d}} = 1\lambda$, can be obtained for a zone thickness of only $x_{\mathrm{d}} = 0.5\lambda$ when τ is tuned according to theory.

For many engineering applications though, the results suggest that setting $\tau = \Delta t$ when using the default blending function should provide acceptable reduction of undesired wave reflections, if the zone thickness is chosen sufficiently large; for $x_{\mathrm{d}} \geq 1.0\lambda$, reflection coefficients of $C_{\mathrm{R}} < 10\%$ can be expected. Since the time step $\Delta t \propto T$ with wave period T, the default value for τ in the Naval Hydro Pack also scales correctly (cf. Eq. (12)), so that the default coefficients provide acceptable 'black box' default settings.

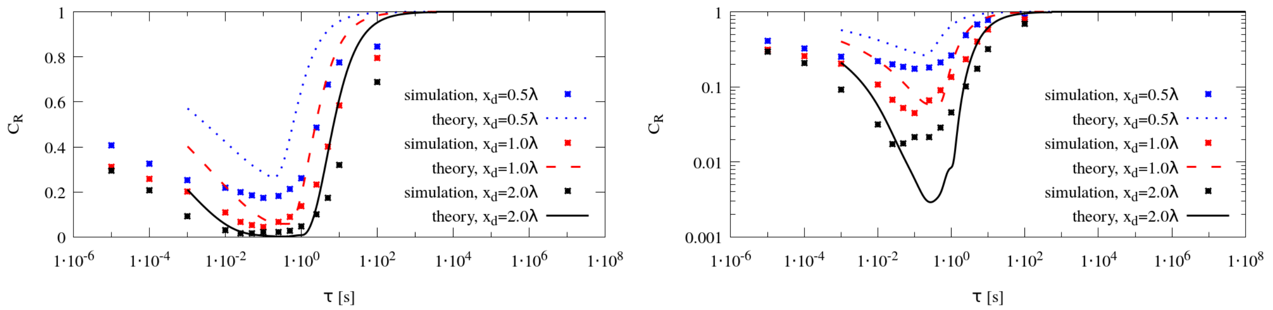

Figure 130: Theory predictions and simulation results for reflection coefficient C_R as a function of relaxation parameter τ, for deep-water waves with period $T = 1.6\,\mathrm{s}$; for different relaxation zone thickness x_d, exponential blending via Eq. (10) with exponent $n = 3.5$ and coarse discretization; for all simulation results $C_{\mathrm{R,sim}}$ and corresponding theory predictions $C_{\mathrm{R,theory}}$ holds $C_{\mathrm{R,sim}} - C_{\mathrm{R,theory}} < 3.8\%$; for the forcing strength $\tau \leq \tau_{\mathrm{opt,theory}}$ closest to the theoretical optimum value $\tau_{\mathrm{opt,theory}}$ holds $C_{\mathrm{R,sim}} - C_{\mathrm{R,theory}} < 1.9\%$

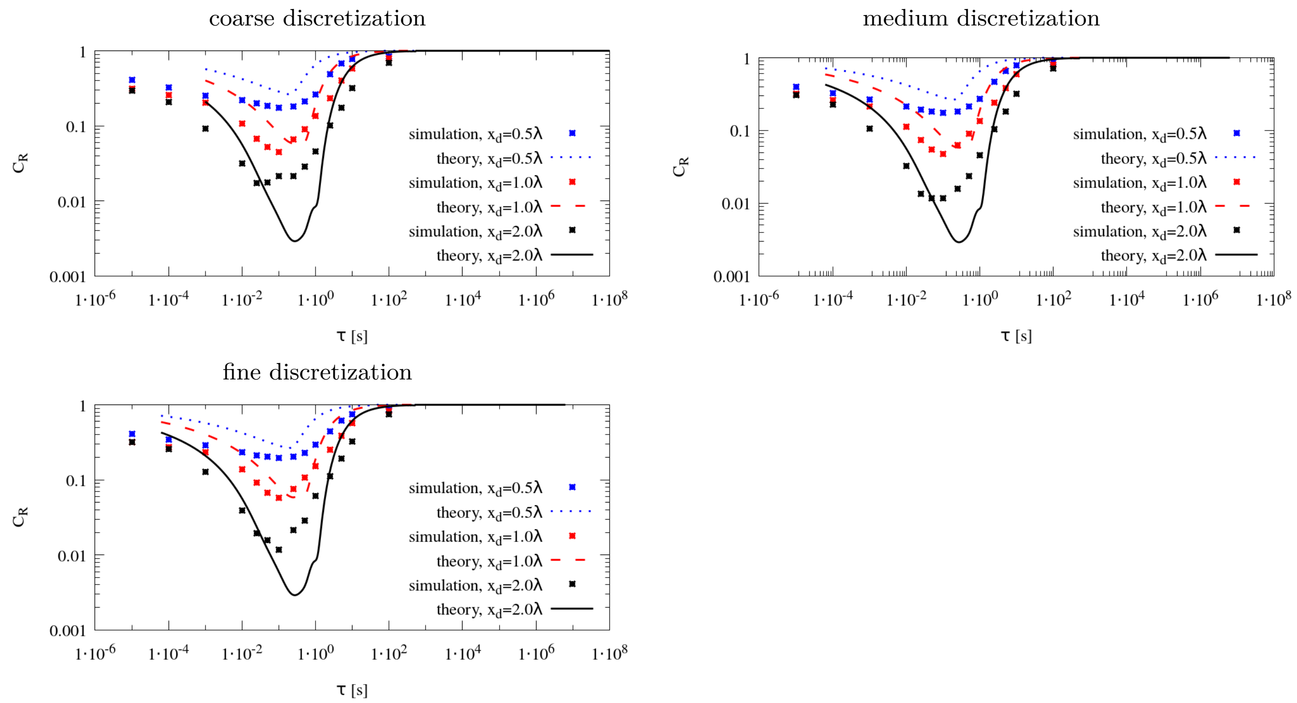

Figure 131: As Fig. 130, except for coarse, medium, and fine discretization; as theory suggests, results can be considered discretization-independent for practical discretizations; for all simulation results $C_{\mathrm{R,sim}}$ and corresponding theory predictions $C_{\mathrm{R,theory}}$ holds $C_{\mathrm{R,sim}} - C_{\mathrm{R,theory}} < 5.3\%$; for the relaxation parameter $\tau \leq \tau_{\mathrm{opt,theory}}$ closest to the theoretical optimum value $\tau_{\mathrm{opt,theory}}$ holds $C_{\mathrm{R,sim}} - C_{\mathrm{R,theory}} < 1.9\%$

8.3 Using relaxation zones to damp waves in shallow water

The theory in Sect. 4.2 was derived to hold for all water depths and Fig. 132 confirms that the predictions are of satisfactory accuracy also for shallow water depths. Compared to the deep-water case, the simulation results for the reflection coefficient C_R are lower for smaller-than-optimum values of relaxation parameter τ, but show no substantial qualitative difference otherwise.

Recently, Carmigniani and Violeau (2018) used forcing zones for horizontal and vertical velocities to damp regular waves in finite-difference-based flow simulations for linearized Navier-Stokes-equations; they observed a decrease in the optimum value of the source term strength for decreasing water depth. In contrast, the present results show no significant dependence of the optimum value of relaxation parameter τ on the water depth.

However, one should point out that in Figs. 130 to 136 the optimum τ from the simulation results is sometimes slightly larger or smaller than theory predicts. The relaxation parameter for the simulation result with the lowest reflection coefficient C_R took values within $\tau_{\mathrm{opt,sim}} \in [\frac{1}{12}\tau_{\mathrm{opt,theory}}, 2\tau_{\mathrm{opt,theory}}]$, where $\tau_{\mathrm{opt,theory}}$ denotes the theoretically predicted optimum τ-value.

Since there did not seem to be a clear trend in these deviations and since they were comparatively small, this detail seems to be of minor importance for engineering practice.

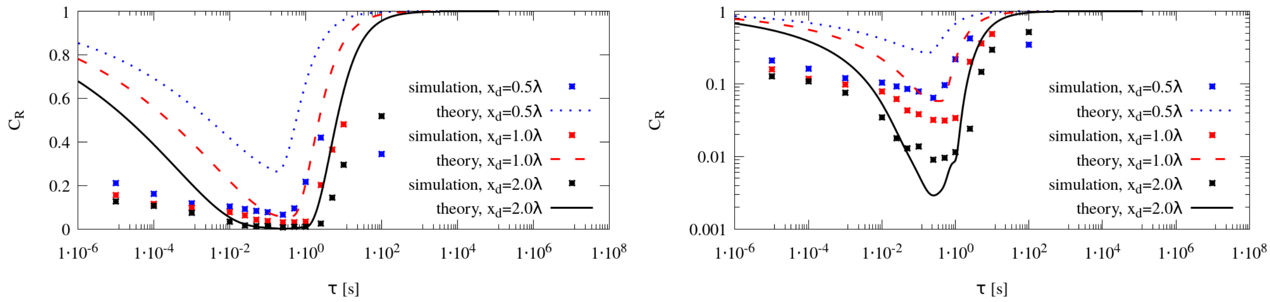

Figure 132: As Fig. 130, except for shallow water waves with period $T = 2.893\,\mathrm{s}$; for all simulation results $C_{\mathrm{R,sim}}$ and corresponding theory predictions $C_{\mathrm{R,theory}}$ holds $C_{\mathrm{R,sim}} - C_{\mathrm{R,theory}} < 0.8\%$; for the forcing strength $\tau \leq \tau_{\mathrm{opt,theory}}$ closest to the theoretical optimum value $\tau_{\mathrm{opt,theory}}$ holds $C_{\mathrm{R,sim}} - C_{\mathrm{R,theory}} < 0.5\%$

8.4 Comparison to relaxation zone in a different flow solver

Similar to the way in which Sect. 4.2 extended the theory for forcing zones to relaxation zones, the behavior of relaxation zones can be 'modeled' using forcing zones. To demonstrate this, simulations for the wave from Sect. 8.2 are repeated with a different flow solver, STAR-CCM+ by Siemens. STAR-CCM+ does not have relaxation zones implemented, but forcing zones according to Eqs. (18) and (19) are available.

To obtain relaxation-zone-like behavior, Eqs. (75) and (76) are introduced as source terms in Eqs. (18) and (19). This formulation has the disadvantage that at the domain boundary holds $b(\mathbf{x}) = 1$, so that $q_i, q_\alpha \to \infty$. Thus stability problems must be expected when relaxation parameter $\tau \to 0$ and when the cell sizes close to the domain boundary are small. The STAR-CCM+ simulations indeed blew up for small τ values, which is the reason for the missing data points ($\tau \leq 10^{-2}\,\mathrm{s}$) in Figs. 133 and 134. These stability issues are due to the different implementation of forcing zones and relaxation zones, so using one approach to 'mimic' the other would theoretically give the same results, but practically can be significantly less stable for certain settings by allowing source terms to become extremely large.

Note that no stability issues occur when using forcing zones (Eqs. (18) to (21)) or relaxation zones (Eqs. (23) and (24)) in the way they were intended, as the results in Sect. 6 demonstrate. Further, comparing the present results to the ones from Sect. 6 indicates that forcing zones and relaxation zones both work equally satisfactory when correctly set up.

Figures 133 and 134 show that the results of the two different codes agree well. Thus one can confidently expect both the present results and the theory from Sect. 4 to be applicable to all computational fluid dynamics (CFD) solvers using any implementation of relaxation zones.

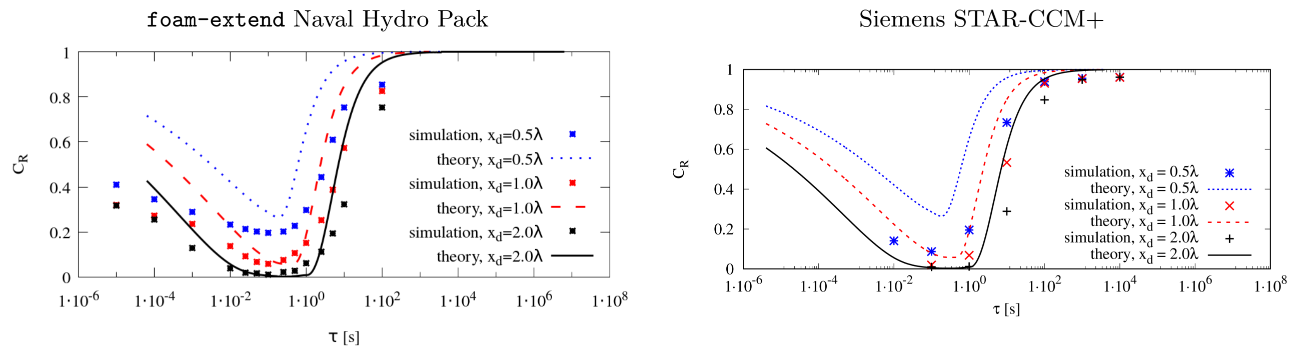

Figure 133: Theory predictions and simulation results from two different CFD codes for reflection coefficient C_{R} as a function of relaxation parameter τ, for deep-water waves with period $T = 1.6\,\mathrm{s}$; for fine discretization, exponential blending via Eq. (10) with exponent $n = 3.5$, and different relaxation zone thickness x_{d}

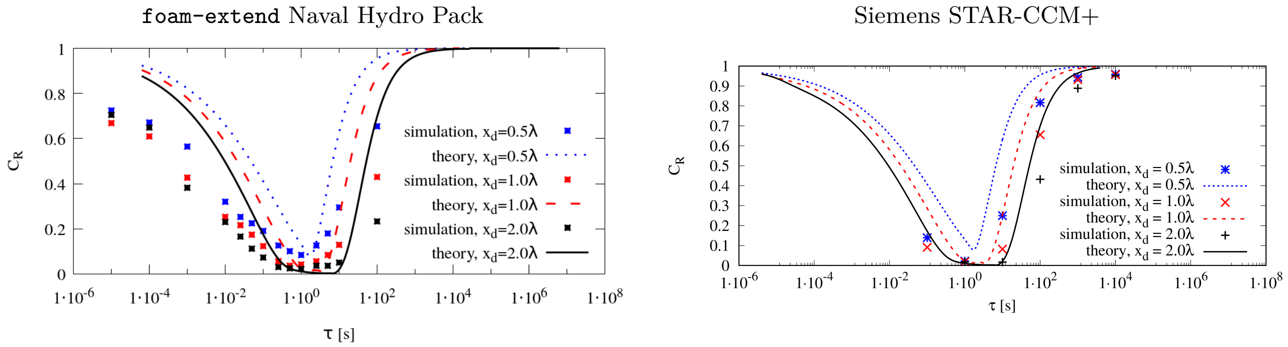

Figure 134: As Fig. 133, except that linear blending according to Eq. 6 with $n = 1$ was used; for all simulation results $C_{\mathrm{R,sim}}$ and corresponding theory predictions $C_{\mathrm{R,theory}}$ holds $C_{\mathrm{R,sim}} - C_{\mathrm{R,theory}} < 3.9\%$; for the forcing strength $\tau \leq \tau_{\mathrm{opt,theory}}$ closest to the theoretical optimum value $\tau_{\mathrm{opt,theory}}$ holds $C_{\mathrm{R,sim}} - C_{\mathrm{R,theory}} < 3.4\%$

8.5 Relaxation towards background wave vs. relaxation towards calm water solution

In practice, the reference solution in relaxation zones is often the far-field wave. Thus the simulations from Sect. 8.2 were repeated with the reference solution set to the stream function solution for the far-field wave.

Figure 135 shows that, although Sects. 8.2 and 8.5 use substantially different reference solutions, again the optimum value for relaxation parameter τ is well predicted. Compared to Fig. 130 though, the values for reflection coefficient C_{R} are much lower. Further, in Fig. 135 reflection coefficient C_{R} is lower for the finer discretization than for the coarser discretization. This was expected, since the closer the solution within the simulation domain is to the reference solution, the smaller will the reflections become, since $(u_{i,\mathrm{ref}} - u_i) \to 0$ and $(\alpha_{\mathrm{ref}} - \alpha) \to 0$ in Eqs. (23) and (24).

However, in practice the wave entering the relaxation zone usually does not correspond to the far-field wave, because it will be modified by wave reflecting bodies or discretization and iteration errors within the domain. Thus for the general case of forcing towards the far-field wave, one should rather expect reflection coefficients C_{R} as in Fig. 131.

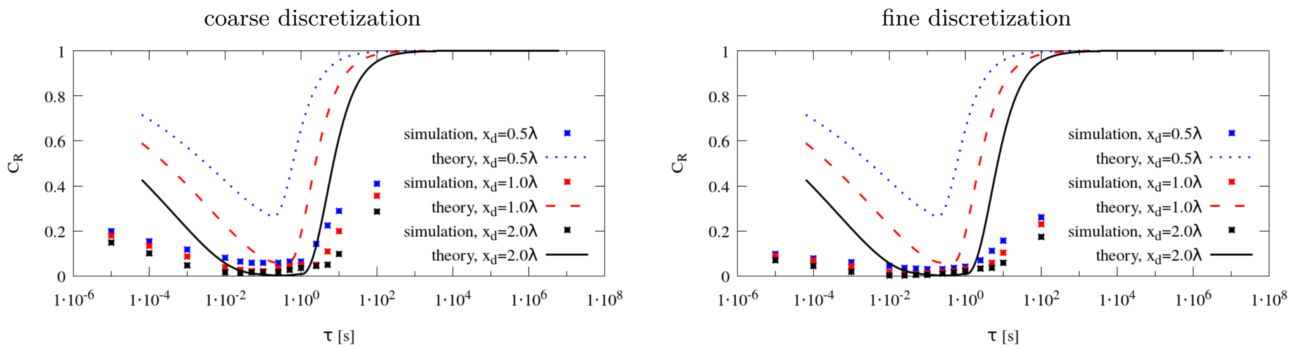

Figure 135: As Fig. 130, except for relaxation towards the far-field wave; for all simulation results $C_{\mathrm{R,sim}}$ and corresponding theory predictions $C_{\mathrm{R,theory}}$ holds $C_{\mathrm{R,sim}} - C_{\mathrm{R,theory}} < 2.9\%$; for the forcing strength $\tau \leq \tau_{\mathrm{opt,theory}}$ closest to the theoretical optimum value $\tau_{\mathrm{opt,theory}}$ holds $C_{\mathrm{R,sim}} - C_{\mathrm{R,theory}} < 1.6\%$

8.6 Influence of choice of blending function

The simulations from Sect. 8.2 were repeated using different blending functions. Figure 136 shows results for power blending according to Eq. (6) for different relaxation parameter τ, different zone thickness x_{d}, and different coefficients n. The results show good agreement between simulation and theory, indicating that the theory is a suitable tool for tuning the relaxation zone parameters.

For $\tau \to \infty$ the relaxation source terms vanish to zero, so one would expect that the solution behaves as if there were no relaxation zone; this would result in a standing wave (i.e. $C_{\mathrm{R}} \approx 1$), since the outlet boundary is nearly perfectly reflecting. Instead, the reflection coefficients remained significantly lower than 1, which becomes more pronounced for smaller values of n. It is possible that this is due to the term $(1 - b(\mathbf{x}))$ on the left hand side of the governing equations, since if there is no reference solution to blend over to, then the blending out of the flow solution may behave like a damping. Note though that such large values of τ are not of practical interest since they cannot be used for combined generation and damping of waves as is illustrated in Sect. 8.7 in Figs. 139 and 140. Thus answering this question was considered outside the scope of this study and remains open for further research.

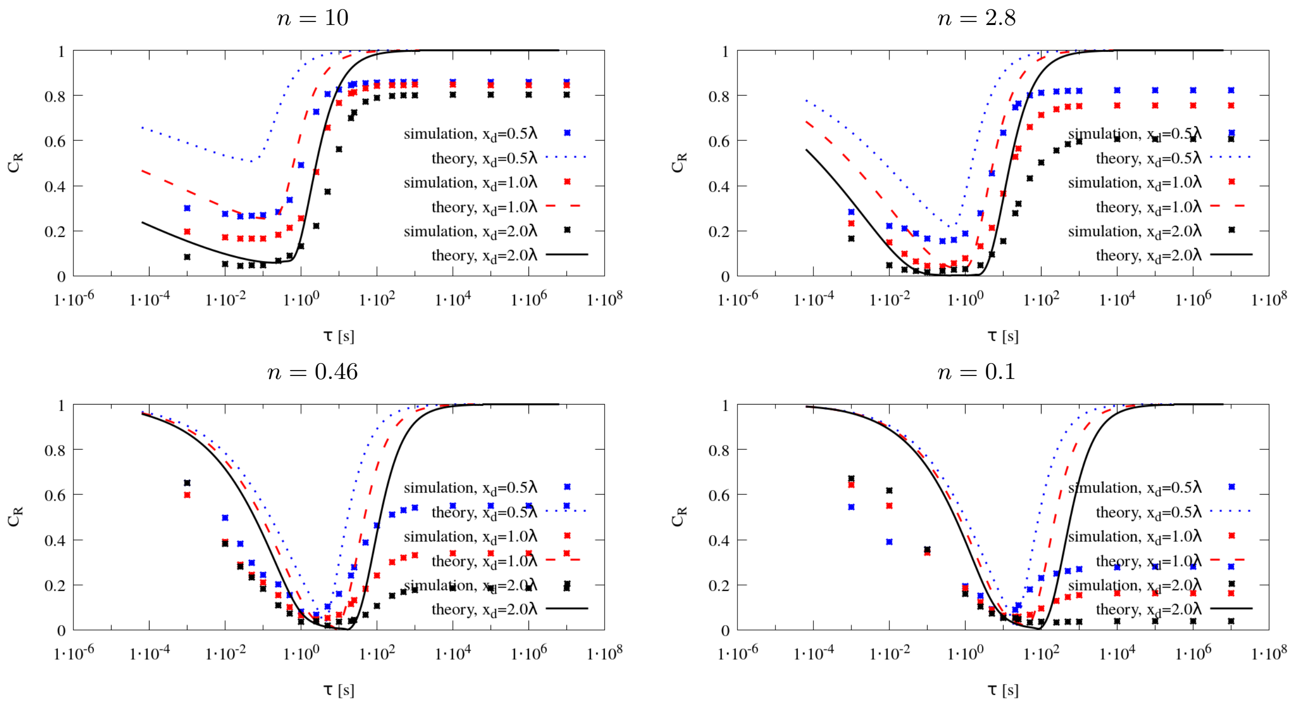

Figure 136: As Fig. 130, except for power blending via Eq. (6) with different values for exponent n; theory predicts the shift in optimum value for τ when changing exponent n; for all simulation results $C_{\mathrm{R,sim}}$ and corresponding theory predictions $C_{\mathrm{R,theory}}$ holds $C_{\mathrm{R,sim}} - C_{\mathrm{R,theory}} < 8.4\%$ ($n = 0.1$), $< 4.7\%$ ($n = 0.46$), $< 4.2\%$ ($n = 2.8$), and $< 2.3\%$ ($n = 10$); for the forcing strength $\tau \leq \tau_{\mathrm{opt,theory}}$ closest to the theoretical optimum value $\tau_{\mathrm{opt,theory}}$ holds $C_{\mathrm{R,sim}} - C_{\mathrm{R,theory}} < 2.7\%$ ($n = 0.1$), $< 3\%$ ($n = 0.46$), $< 2.0\%$ ($n = 2.8$), and $< -1.5\%$ ($n = 10$)

Not only do the optimum values for τ and the curves for reflection coefficient C_{R} as a function of τ change as seen in Fig. 136, but also the optimum choice of coefficient n depends on the zone thickness x_{d} as Figs. 137 and 138 demonstrate.

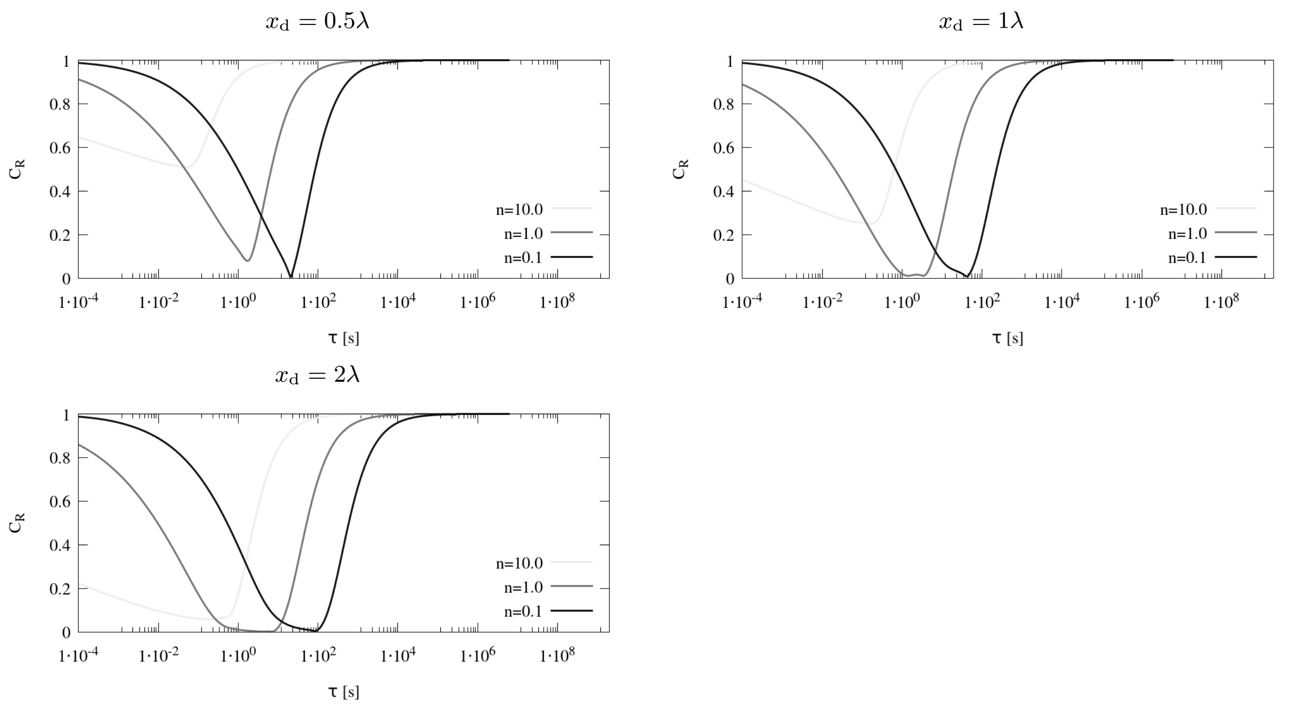

Figure 137: Theory predictions for reflection coefficient C_{R} as a function of relaxation parameter τ for deep-water waves with period $T = 1.6\,\mathrm{s}$; for power blending according to Eq. (6) with different values for exponent n

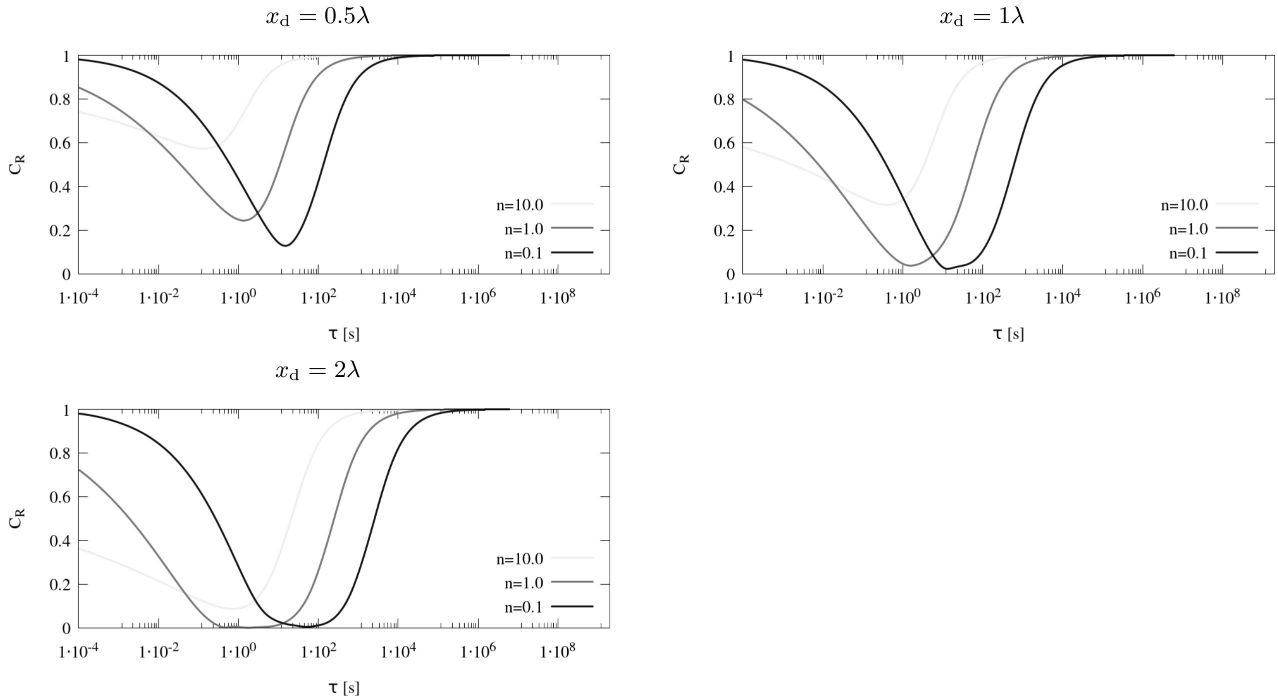

Figure 138: As Fig. 137, except for $\cos^{2n}$-blending according to Eq. (7) with different values for exponent n; the optimum exponent n increases with increasing zone thickness x_{d}

For the investigated blending functions, the larger the relaxation zone thickness x_{d} becomes, the larger becomes the optimum value for n. For practical choices of x_{d}, the tendency seems to be that n should be > 1 for $x_{\mathrm{d}} \gtrsim 1.5\lambda$, whereas for $x_{\mathrm{d}} \lesssim 1.0\lambda$ then n should be < 1.

The complexity of the curves for $C_{\mathrm{R}}(\tau)$ suggests that no simple empirical relationship can be found to determine the optimum setting. Further, depending on the investigated wave spectrum a different tuning of the reflection-reducing characteristics of the relaxation zone may be appropriate. Thus it is recommended to use the theory to tune the forcing zone parameters to the wave of interest before each simulation.

It remains to say that by correctly tuning the relaxation zone parameters, the reduction of undesired wave reflections can be significantly improved, so that when correctly tuned already with a zone thickness of $0.5\lambda \leq x_{\mathrm{d}} \leq 1.0\lambda$ (depending on the intended reflection coefficient) satisfactory results can be obtained, whereas with default settings an at least two to three times larger zone thickness would be required for the same reduction of undesired reflections.

8.7 Results of 3D-flow simulations with relaxation zones

To investigate the validity of the present findings for practical 3D-flow simulations, the flow around a strongly reflecting semi-submerged pontoon subjected to steep deep-water waves is simulated with the setup from Sect. 8.1. The solution domain was selected intentionally small, with relaxation zones attached to all vertical domain boundaries with a zone thickness of only $x_{\mathrm{d}} \approx 0.7\lambda$. With respect to the tuning for the optimum blending function from Sect. 8.6, a power blending according to Eq. (6) with coefficient $n = 0.46$ was used. According to the theory prediction, a relaxation parameter of $\tau = 2.5\,\mathrm{s}$ should provide a satisfactory reduction of undesired wave reflections ($C_{\mathrm{R}} \approx 5\%$), while values larger or smaller by a factor of $10^{\pm 1}$ should produce significant reflections.

If reflections are satisfactorily reduced, then a periodic solution is expected to occur after several wave periods, and long-time simulations are possible without the accumulation of errors due to undesired wave reflections. Figure 139 shows that indeed such periodic results are obtained for the optimum setting. As shown in Fig. 140, too large values of τ damp not only undesired reflections but also the incident wave, while too small values produce wave reflections at the entrance to the relaxation zone, as can also be seen from the aperiodicity and change of amplitude of the forces on the pontoon.

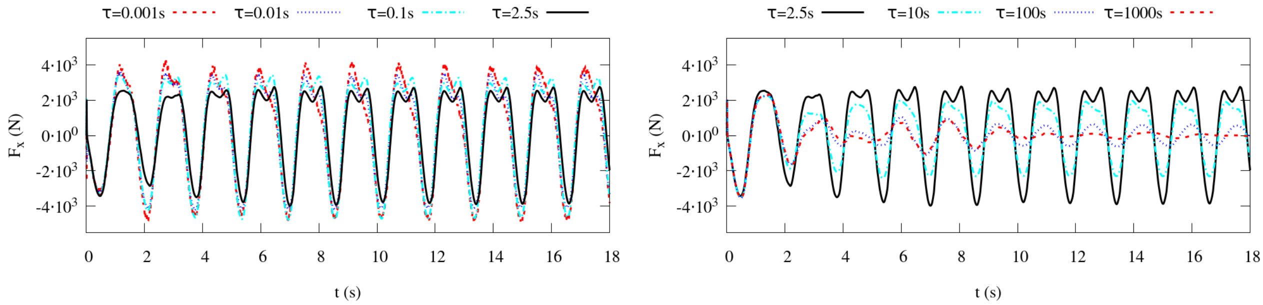

Figure 139: Force component in x-direction integrated over the pontoon surface as a function of time t for the *medium grid*; with relaxation zone thickness $x_{\mathrm{d}} \approx 0.7\lambda$, power blending with exponent $n = 0.46$ and different values of relaxation parameter τ; theory predicts an optimum of $\tau = 2.5\,\mathrm{s}$, for which a periodic solution is obtained; the further τ deviates from the theoretical optimum, the stronger are the visible influences of undesired wave reflections in the results

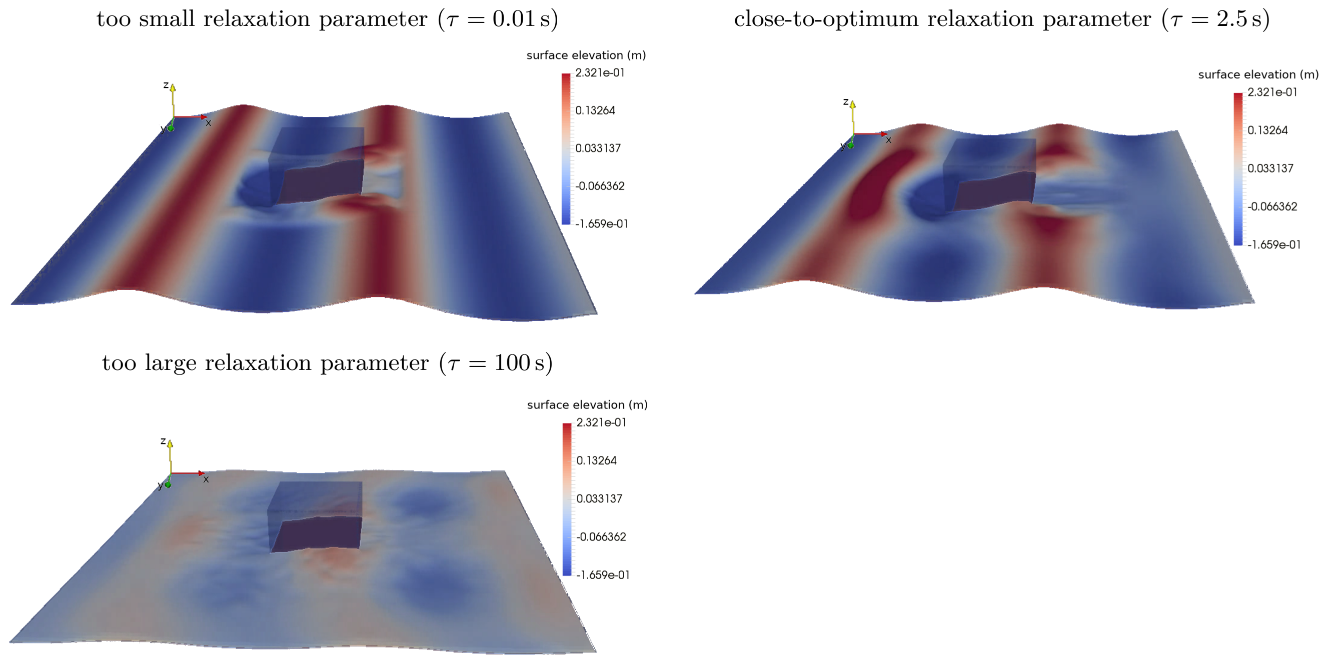

Figure 140: Simulation results for free-surface elevation at $t \approx 15\,\mathrm{s}$ with too small ($\tau = 0.01\,\mathrm{s}$), too large ($\tau = 100\,\mathrm{s}$), and close-to-optimum ($\tau = 2.5\,\mathrm{s}$) choice of relaxation parameter τ; for $\tau = 0.01\,\mathrm{s}$, the blending towards the far-field wave is too strong, so that reflection occurs mainly at the entrance to the relaxation zone; for $\tau = 100\,\mathrm{s}$, the blending towards the far-field is too weak, so that the far-field wave is not sustained; for $\tau = 2.5\,\mathrm{s}$, the waves reflected at the pontoon decay smoothly over the whole relaxation zone as intended

Figure 141 shows that the correct tuning of the relaxation zone enables a periodic solution for simulations over arbitrarily long simulation times.

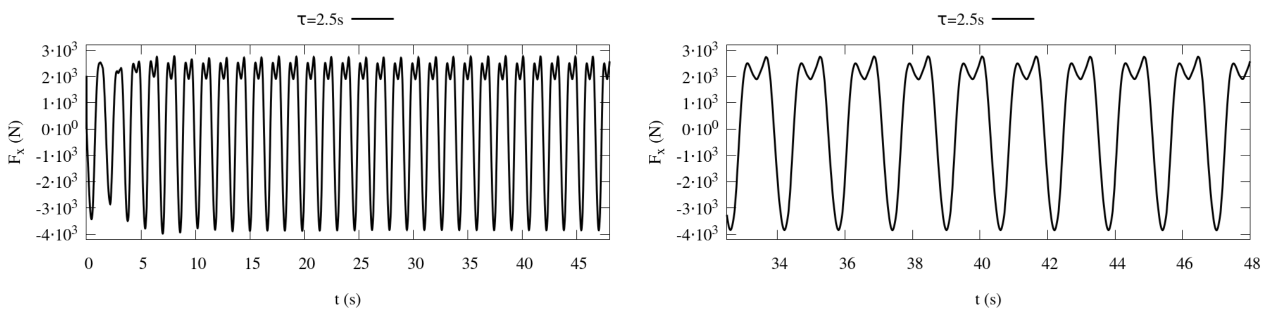

Figure 141: As Fig. 139, except for longer simulation duration; with close-to-optimum relaxation ($\tau = 2.5\,\mathrm{s}$), simulations were performed for $30T$ without noticeable accumulation of reflections

Figures 142 and 143 show that the difference between medium and fine grid is comparatively small, but for the coarse grid the force amplitudes are ≈ 10% lower. For the present purposes all grids were considered suitable to demonstrate the benefits of tuning relaxation zones to the wave parameters.

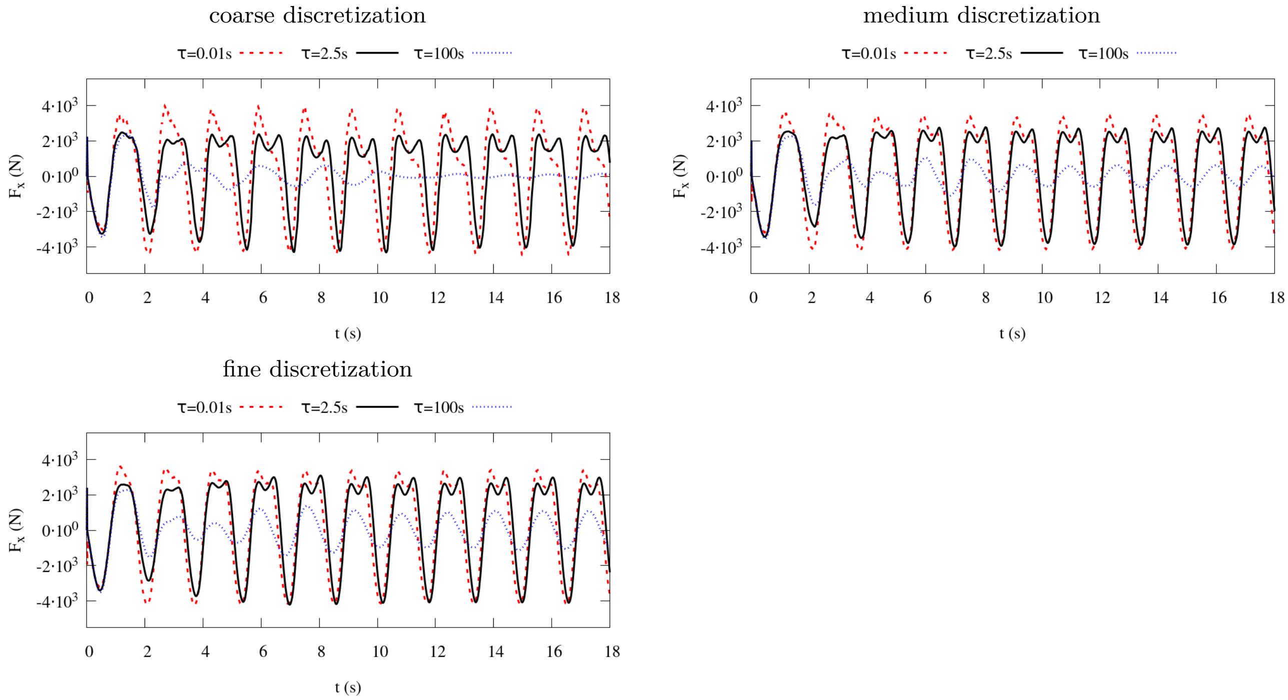

Figure 142: As Fig. 139, except for coarse, medium and fine discretization

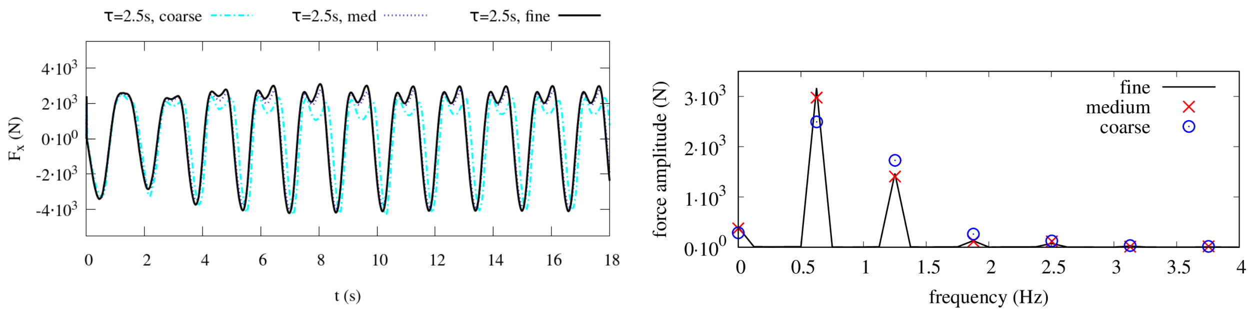

Figure 143: Left: as Fig. 139, except for close-to-optimum relaxation parameter τ on coarse, medium and fine discretization; right: force amplitude as a function of frequency for FFT-analysis of the curves from the left plot during time interval $10\,\mathrm{s} \leq t \leq 18\,\mathrm{s}$; the difference between the coarse and fine discretization are significant (all differences are $< 660\,\mathrm{N}$, which corresponds to over 20% of the first harmonic's amplitude); the difference between the medium and fine discretization are small (all differences are $< 190\,\mathrm{N}$, which corresponds to ≈ 6% of the first harmonic's amplitude), so already the medium discretization is considered acceptable for the present purposes

9 Discussion and Outlook

Key findings

- Forcing zones are not 'ad-hoc' approaches, but can be well described mathematically via the presented theory
- For practical discretizations, forcing zones behave roughly independent of the discretization and flow solver used
- Although the theory was extended to cover oblique wave incidence in 2D/3D, already the 1D-version of the theory suffices for tuning forcing zones in typical 2D-/3D-flow simulations
- For future research, application of the presented theory to other wave propagation mediums in expected to be promising

As described in Sect. 1, forcing zones had been considered to be 'heuristic' or 'ad-hoc' approaches. Possibly because they are often used in complex flows for which there is no analytical solution, such as flows with nonlinear waves or turbulence, it was questioned whether there was a mathematical foundation to these approaches. Thus at the time of writing it is still common practice to use forcing zones with their case-dependent parameters set to the solver's default values or tuned by trial and error, which often does not provide the intended reduction of undesired wave reflections.

In Sect. 4, a theory was presented which can predict the reflection coefficients C_{R} and the flow within the forcing zone, and thus can be used to optimally tune the forcing zone before performing the flow simulations. The comparison to simulation results in Sects. 5 to 8 for various linear and highly nonlinear flow problems demonstrates that forcing zones are not 'ad-hoc' approaches, but can be well described mathematically. As predicted by theory, for practical discretizations the forcing zones were found to behave independent of the chosen discretization scheme, its order, the mesh size, the time-step size, and also of the used flow solver. The theory shows that the influence of the wave parameters on the optimum choice of forcing zone parameters is quite complex and cannot be fully captured by simple empirical formulas.

The benefit of the theory for engineering practice was verified via flow simulations of typical ocean engineering applications of strongly reflecting bodies subjected to free-surface waves. As demonstrated especially in Sects. 7 and 8, tuning forcing zones using the theory enables the use of smaller domains and thinner forcing zones than commonly used, which can substantially reduce the computational effort. The theory has been extended to predict reflection coefficients for oblique wave incidence in 2D-/3D-flows in Sect. 4.5. However, the findings from Sects. 5.4, 5.5, 7 and 8.7 demonstrate that already the 1D-theory from Sects. 4.1 to 4.3 provides a decent estimate for the upper limit of the overall reflection coefficient for typical flow simulation setups with 2D- and 3D-wave-propagation. A simple, user-friendly, open-source software to evaluate the theory was published along with this work. Thus it is recommended to use the theory in engineering practice.

Although the theory was developed for flow problems with free-surface waves in ocean engineering and shipbuilding applications, it was shown to hold also for (hydro-)acoustic wave propagation in gases and liquids. The present findings suggest that the theory will also hold for wave propagation in other mediums. Thus the application of the present approach to forcing zones in other research fields is expected to be promising. Computer simulations of wave propagation phenomena are carried out in various disciplines within mathematics, physics and engineering, and for various single- or multiphase mediums, including gases (Colonius and Lele, 2004; Hesthaven, 1998; Hu, 1996; Hu, 2008; Lorenzzetti and Wang, 1986; Marburg and Nolte, 2008), liquids (Bodony, 2006; McDonald, 2003; Modave et al., 2010; Zhang et al., 2014), non-porous (Appelö and Kreiss, 2006; Collino and Tsogka, 2001; Komatitsch and Martin, 2007; Komatitsch and Tromp, 2003; Semblat et al., 2011) as well as porous (Straughan, 2008; Zeng et al., 2001) solids, and fields (e.g. gravitational (Novak and Bonazzola, 2004; Rinne et al., 2007) or electromagnetic (Abarbanel and Gottlieb, 1998; Berenger, 1994; Berenger, 1996; Gedney, 1996; Katz et al., 1994; Petropoulos at al., 1998; Turkel and Yefet, 1998).

Aside from wave phenomena, forcing zones have also been used in an ad-hoc manner to damp other flow phenomena, for example to reduce reflections of Kármán vortex streets, vortex pairings, or turbulent flows at the outlet domain boundary (Andersson et al., 2004; Bogey et al., 2000; Enger et al., 2014; Manning and Lele, 2000; Spalart, 1989; Wanderley and Levi, 2005; Wang et al., 2006). The present findings suggest that it could be worthwile to investigate whether the present theory could be modified to enable the tuning of forcing zones for such applications as well.

Thus the present work opens up an interesting new research field, i.e. the theoretical investigation of forcing zones over various fields, with many intricate aspects that deserve further study; some of these are discussed in the following.

9.1 Forcing strength γ

Key findings

- Theory predictions and simulation results for the optimum value of forcing strength γ agreed closely in most cases
- Differences by more than factor $2^{\pm 1}$ were attributed to background noise in the scheme for detecting reflection coefficient C_R, increased flow complexity when forcing transverse velocity components and the existence of multiple local minima for thicker forcing zones
- For close-to-optimum tuning of γ, simulation results for reflection coefficient C_R were never more than 3.4% larger than theory predictions

For all (hydro-)acoustic wave simulation results, the optimum value $\gamma_\mathrm{opt,sim}$ of the forcing strength γ was $\gamma_\mathrm{opt,sim} \in [\frac{1}{2}\gamma_\mathrm{opt,theory}, 2\gamma_\mathrm{opt,theory}]$ in terms of the optimum value $\gamma_\mathrm{opt,theory}$ predicted by theory (cf. Sect. 5). Considering that the flow simulations were performed for forcing strengths $\gamma_{i+1} = 2\gamma_i$ where index i corresponds to the i^th simulation from each parameter study, and that several results indicate close agreement between theory predictions and simulation results close to the theoretical optimum value of γ (cf. e.g. Figs. 16 and 20), for flows with (hydro-)acoustic waves the theory predictions for the optimum choice of forcing strength γ can be expected to be of satisfactory accuracy for practical purposes.

For most free-surface wave simulation results, $\gamma_\mathrm{opt,sim} \in [\frac{1}{2}\gamma_\mathrm{opt,theory}, 2\gamma_\mathrm{opt,theory}]$ held as well (cf. Sects. 6 to 8). However, there were a few exceptions, which were attributed to the following causes.

First, since reflection coefficients $C_\mathrm{R} \lesssim 1\%$ could not be detected reliably (cf. Sects. 3 and 6.2), for forcing zone thickness $x_\mathrm{d} = 2\lambda$ the simulation results formed a plateau with $C_\mathrm{R} \approx 1\%$ over several γ-values (cf. e.g. Figs. 51, 62 and 78). There, the differences between the C_R-values were in the order of $\mathcal{O}(0.1\%)$. These differences were assumed to be due to background noise in the scheme for determining C_R, and it was found that the lowest value of C_R could lie anywhere on the plateau, i.e. not necessarily on the theoretically predicted optimum. There appeared to be no clear trend where on the plateau the lowest C_R-value would occur and this held independently of the water depth as shown in Sects. 6.2 and 6.8. A detailed investigation of this phenomenon was considered out of the scope of the present study and is left for future research.

Second, when applying forcing source terms (also) in the equation for the vertical fluid velocity w, it was found, especially for $\gamma \gg \gamma_\mathrm{opt,theory}$, that simulation results for reflection coefficient C_R could be significantly lower than theory predictions (cf. e.g. Sects. 6.3 to 6.5). Consequently, for zone thickness $x_\mathrm{d} = 2\lambda$ the plateau formed by simulation results with $C_\mathrm{R} \approx 1\%$ over several γ-values widens and extends to larger γ-values than in the case of forcing of the horizontal fluid velocities. This holds for relaxation zones as well, and since relaxation parameter $\tau \propto \gamma^{-1}$ the range with $C_\mathrm{R} \approx 1\%$ therefore extends to smaller τ-values than predicted by theory (cf. e.g. Figs. 131 and 136). Another configuration which can lead to such behavior is forcing of both volume fraction α and horizontal velocities in shallow water (cf. e.g. Figs. 74 and 79).

Third, for larger zone thicknesses such as $x_\mathrm{d} = 2\lambda$ the theoretical curve for reflection coefficient C_R as a function of γ may have several local minima. Thus depending on the choice of γ-values for which simulations are performed, the lowest simulation result for C_R did not always occur for the γ-value next to the global theoretical minimum of C_R; in some cases (cf. e.g. Fig. 51) it occurred for a γ-value close to a local theoretical minimum.

Thus for Figs. 51, 58, 60, and 61 held $\gamma_\mathrm{opt,sim} \in [\frac{1}{4}\gamma_\mathrm{opt,theory}, 4\gamma_\mathrm{opt,theory}]$, for Figs. 64 and 74 held $\gamma_\mathrm{opt,sim} \in [\frac{1}{2}\gamma_\mathrm{opt,theory}, 12\gamma_\mathrm{opt,theory}]$, for Fig. 80 held $\gamma_\mathrm{opt,sim} \in [\frac{1}{2}\gamma_\mathrm{opt,theory}, 33\gamma_\mathrm{opt,theory}]$, and for Figs. 130 to 136 held $\tau_\mathrm{opt,sim} \in [\frac{1}{12}\tau_\mathrm{opt,theory}, 2\tau_\mathrm{opt,theory}]$, where as before $\gamma_\mathrm{opt,sim}$ and $\tau_\mathrm{opt,sim}$ are the forcing strength and relaxation parameter for the simulation result with the lowest reflection coefficient C_R in the corresponding figure, and $\gamma_\mathrm{opt,theory}$ and $\tau_\mathrm{opt,theory}$ are the theoretically predicted optimum values.

Even in the cases when theory predictions and simulation results for the optimum value of forcing strength γ differed by an order of magnitude, the simulated reflection coefficient $C_\mathrm{R,sim}$ at the theoretically predicted optimum setting for forcing strength γ or relaxation parameter τ was for all simulations $< 3.4\%$ larger than the corresponding theoretically predicted reflection coefficient $C_\mathrm{R,theory}$, as shown in Sect. 9.7. Therefore also for flow simulations with free-surface waves, the theory predictions for the optimum forcing strength γ can be considered of satisfactory accuracy for engineering practice. Thus tuning forcing strength γ and relaxation parameter τ via the theory from Sect. 4 is recommended.

9.2 Zone thickness x_d

Key findings

- Increasing the forcing zone thickness tends to decrease the reflection coefficient C_R and to widen the range of wavelengths that are satisfactorily damped
- For certain combinations of blending function $b(\mathbf{x})$ and zone thickness x_d, reflection coefficients of $C_\mathrm{R} < 1\%$ can be achieved with comparatively thin forcing zones ($x_\mathrm{d} < 0.5\lambda$), though only for a narrow range of wavelengths
- To ensure reliable minimization of undesired wave reflections, the use of thicker forcing zones ($1\lambda \lesssim x_\mathrm{d} \lesssim 2\lambda$) is recommended for engineering practice

Sections 5.3 and 7.1 show that increasing the zone thickness x_d tends to reduce the reflection coefficient C_R at optimum tuning of forcing strength γ and also widens the range of wavelengths for which satisfactory reduction of undesired wave reflections will occur. However, it also increases the domain size and therefore the computational effort, thus the choice of zone thickness x_d corresponds to finding a compromise between ensuring reliable minimization of undesired wave reflections and keeping the computational effort as low as possible.

An interesting phenomenon is that, for monochromatic waves and certain combinations of blending function $b(\mathbf{x})$ and zone thickness x_d, exceptionally effective absorption was observed in Sect. 5.3, which can be seen as negative peaks in the left images of Fig. 27. For these settings, reflection coefficients C_R at optimum tuning can be several orders of magnitude lower than they would be if the zone thickness were increased or decreased by a few percent. By utilizing this phenomenon, satisfactory minimization of undesired wave reflections can be obtained using very thin forcing zones; for example, reflection coefficients of $C_\mathrm{R} < 1\%$ can be realized for a zone thickness of $x_\mathrm{d} \approx 0.3\lambda$, cf. the first negative peak in the top image of Fig. 27. Figure 20 shows that such negative peaks can indeed be realized in flow simulations. However, the use of such thin forcing zones is in general not recommended. The reason for this is that this phenomenon is highly sensitive to the wavelength of the incoming wave. As shown in Sect. 7.1, discretization and iteration errors can lead to a change in wavelength in finite-volume-based flow simulations, which then could lead to significantly larger reflection coefficients than expected. Thus such a tuning could lead to false decisions and animate inexperienced users to apply too thin forcing zones in cases where this is not suitable. However, the phenomenon may be utilized as a favorable effect when the forcing zones are selected sufficiently thick, so that also with modifications of the wavelength due to numerical errors satisfactory forcing is ensured. Then this phenomenon may be used for example to improve the damping of the peak wave period or some other relevant period for irregular waves. Future research is expected to yield further insights into why this phenomenon occurs, how it can be evoked, whether it can be tuned to reduce undesired wave reflections for two or more different wave periods at the same time, and whether a similar phenomenon can be achieved by combining grid stretching and forcing zones.

Reliable minimization of undesired wave reflections is typically more important than the last few percent of computational efficiency, since such reflections can lead to substantial errors in the simulation results. Moreover, despite the overall remarkable agreement between theory predictions and simulation results in this work, there were some cases, for example nonlinear (Fig. 39) or irregular (Fig. 77) waves, for which theory was observed to slightly under-predict reflection coefficient C_R. It is therefore strongly recommended not to 'over-tune' the forcing zone, but rather to use slightly thicker zones than theoretically necessary. Typically, increasing the zone thickness by $x_\mathrm{d} = 0.5\lambda$ to $x_\mathrm{d} = 1\lambda$ does not substantially increase the computational effort, but it increases confidence that undesired reflections will be satisfactorily reduced.

For typical ocean engineering applications, it is therefore recommended to select the zone thickness as $1.2\lambda \leq x_\mathrm{d} \leq 2\lambda$, depending on the expected flow complexity; when tuning the forcing zone according to the theory from Sect. 4, reflection coefficients of $C_\mathrm{R} \lesssim 1\%$ can be expected with exponential blending as shown in Fig. 27. Experienced users of the theory may achieve similar reflection coefficients with zone thicknesses of $0.5\lambda \leq x_\mathrm{d} \leq 1.2\lambda$.

9.3 Blending function $b(\mathbf{x})$

Key findings

- Quadratic, cosine-squared or exponential blending $b(\mathbf{x})$ produced comparable reflection coefficients C_{R}
- Constant and linear blending functions $b(\mathbf{x})$ typically produced larger reflection coefficients C_{R} than quadratic, cosine-squared or exponential blending
- Results indicate that the optimum choice for blending function $b(\mathbf{x})$ depends on the zone thickness and on the investigated wave spectrum

Consider the case for constant blending $b(\mathbf{x}) = 1$, where wave reflections theoretically can only occur at the entrance to the forcing zone and at the domain boundary to which the zone is attached. Within the forcing zone the wave is attenuated by absorption due to the source terms. Require that the forcing zone should produce a reflection coefficient of $C_{\mathrm{R}} < 1\%$. Evaluating the theory shows that, with optimum tuning of forcing strength γ, this is achieved by all zone thicknesses $x_{\mathrm{d}} \geq 30.2\lambda$ in terms of wavelength λ, as well as for selected zone thicknesses below 30λ when especially favorable interference occurs as discussed in Sect. 9.2.

In contrast, for exponential blending via Eq. (9), where partial wave reflections occur throughout the zone, $C_{\mathrm{R}} < 1\%$ is achieved by all zone thicknesses $x_{\mathrm{d}} \geq 1.04\lambda$ when optimally tuned, and for a zone thickness of $x_{\mathrm{d}} = 10\lambda$ the reflection coefficients are three orders of magnitude lower than for constant blending. Figure 144 demonstrates that the choice of blending function $b(\mathbf{x})$ can have a significant influence on the zone thickness required to obtain satisfactory reduction of undesired wave reflections, and that blending functions $b(\mathbf{x})$ that gradually fade-in the source terms are typically more effective than constant blending functions.

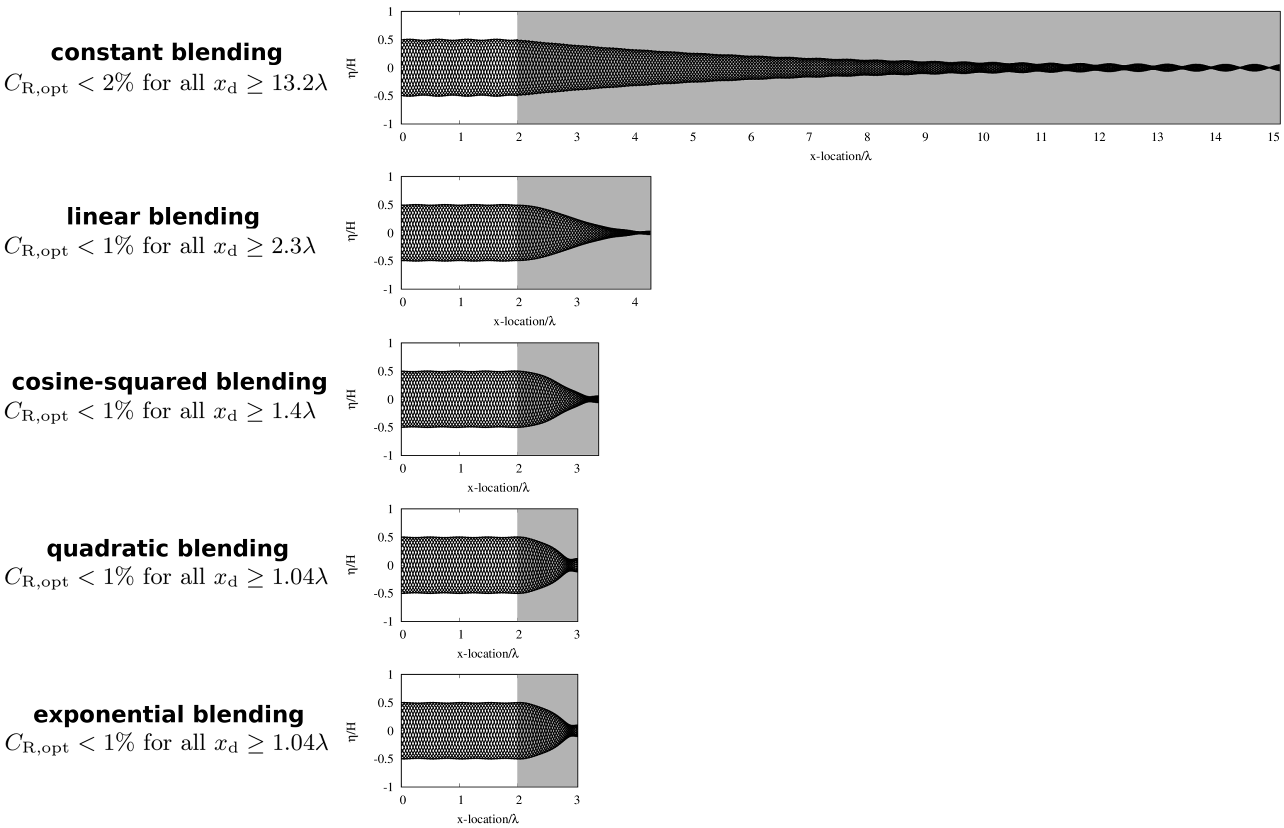

Figure 144: Theory prediction for surface elevation η per wave height H in the vicinity of a forcing zone (shaded gray) as a function of x-location in wave propagation direction per wavelength λ for several time instances during a wave period; each plot represents the optimum tuning of forcing strength γ for the given zone thickness x_{d} and blending function $b(\mathbf{x})$, where zone thickness x_{d} takes the smallest value for which holds that $C_{\mathrm{R}} < 2\%$ (constant blending) or $C_{\mathrm{R}} < 1\%$ (other blending functions) for all larger zone thicknesses, given than γ ist optimally tuned; for constant (Eq. (3)), linear (Eq. (4)), $\cos^2$ (Eq. (7)), quadratic (Eq. (5)), and exponential (Eq. (9)) blending

The results from Sects. 5.2, 5.3, and 7.1 indicate that quadratic (Eq. (5)), cosine-squared (Eq. (7)), and exponential (Eq. (9)) blending $b(\mathbf{x})$, even though these functions differ significantly, produce nearly equivalently satisfactory reduction of undesired wave reflections, with perhaps a slight preference for exponential blending $b(\mathbf{x})$. Thus it is recommended to use blending via Eqs. (5) to (10), whereas constant or linear blending via Eqs. (3) and (4) should not be used.

Note though that these findings do not directly apply to relaxation zones and the same holds vice versa, since when formulating relaxation zones as a special case of forcing zones as in Sect. 4.2, then using linear blending $b(\mathbf{x})$ via Eq. (4) corresponds indeed to an effective blending of $b(\mathbf{x})/\left(1 - b(\mathbf{x})\right)$. Thus for relaxation zones, linear blending $b(\mathbf{x})$ can be an effective choice.

The findings in Sects. 8.6 and 8.7 demonstrate that there is no single optimum blending function $b(\mathbf{x})$ which applies for all cases. Rather, the choice of optimum blending depends on the zone thickness x_d and on how broad-banded the investigated wave spectrum is, i.e. how broad the range of γ-values should be for which satisfactory absorption is to be obtained. This indicates that the 'perfect' choice of blending function $b(\mathbf{x})$ has to be made case-dependently.

The present theory can be evaluated fast enough so that parameter studies for different choices of blending $b(\mathbf{x})$ can be performed within seconds on a standard desktop computer, and thus a suitable blending $b(\mathbf{x})$ can be selected.

Future research could be directed towards automation of the selection of a suitable $b(\mathbf{x})$ and investigation of the influence of $b(\mathbf{x})$ on the occurrence of local minima for reflection coefficient C_R for different forcing strengths γ.

9.4 Influence of wave nonlinearity and how forcing zones reduce reflections

Key findings

- The mechanisms behind how forcing zones reduce undesired wave reflections are
  - wave absorption
  - partial wave reflections, which occur where $\nabla b(\mathbf{x}) \neq 0$
  - destructive interference of these reflections
- For close-to-optimum tuning, forcing zones 'split' nonlinear waves into many approximately linear wave components that interfere destructively; thus forcing zone behavior for nonlinear waves was well predicted via linear theory

The results from Sects. 5.6 and 6.6 demonstrate that the theory from Sect. 4 satisfactorily predicts reflection coefficients C_R of forcing zones for highly nonlinear waves. It was found that the wave's nonlinearity had a negligible influence on the accuracy of the theory's predictions. Since the theory was derived based on linear wave theory, the question arises how can its predictions be so accurate also for highly nonlinear waves?

This question can be answered based on the findings from Sects. 4, 5.6 and 6.6, which show that forcing zones reduce undesired wave reflections via three mechanisms: wave absorption, partial wave reflection occurring everywhere within the forcing zone where $\nabla b(\mathbf{x}) \neq 0$ (cf. Figs. 17, 52, and 63), and destructive interference of these partial wave reflections (cf. Fig. 68). The present findings demonstrate that all three mechanisms need to be considered to accurately predict the optimum forcing strength γ and the corresponding reflection coefficient C_R for a given blending function $b(\mathbf{x})$ and zone thickness x_d.

Figure 145 illustrates that when a forcing zone is optimally tuned, then the wave height gradually decreases within the forcing zone and partial wave reflections occur throughout the whole forcing zone with small amplitude; thus when optimally tuned, forcing zones 'split up' nonlinear waves into many approximately linear wave components, which interfere destructively due to their phase differences.

This behavior characterizes a key difference between forcing zone approaches and boundary-based wave absorption techniques (cf. Sect. 1.1) such as absorbing boundary conditions or active wave absorption: Boundary-based approaches can neither utilize partial wave reflections nor their destructive interference, since they act only at the boundary. This explains why forcing zones, despite their simple formulation, are capable of damping even highly nonlinear waves in complex flow problems, where high-order boundary-based wave damping approaches would fail.

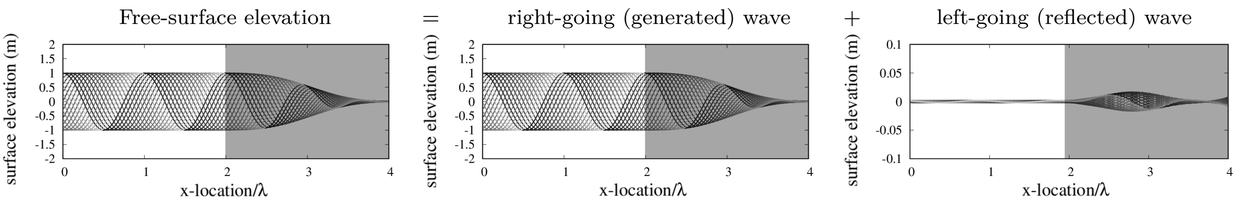

Figure 145: Theory prediction for surface elevation as a function of x-location at several time instances during one wave period (left), decomposed into generated (middle) and reflected wave components (right, with zoomed-in vertical axis); for a forcing zone (shaded gray) with thickness $x_\mathrm{d} = 2\lambda$ in terms of wavelength λ, blending via Eq. (9), and close-to-optimum tuning of forcing strength γ; as seen in the right image, the wave is reflected with comparatively low amplitude at the domain boundary $x/\lambda = 4$ and at first looses amplitude when traveling in negative x-direction until ca. $x/\lambda \approx 3.7$, which could be explained by absorption; however, the following increase in the amplitude of the left-going wave until ca. $x/\lambda \approx 2.8$ cannot be explained by absorption, thus it is due to the occurrence of partial wave reflections; since these occur throughout the forcing zone and with different phases, the partially reflected waves can be expected to interfere destructively

The aforementioned mechanisms are further confirmed by the simulation results in Appendix A and the agreement between theory predictions and simulation results in Sects. 5 to 8, and explain why, when correctly tuned, forcing zones produced similar reflection coefficients regardless whether the investigated waves were linear or highly nonlinear.

9.5 Choice of governing equations in which forcing source terms are introduced

Key findings

- For forcing of longitudinal fluid momentum, theory predictions are nearly accurate
- For forcing of transversal fluid momentum, theory predictions provide an estimate of the upper limit for the reflection coefficient
- Theory predicts optimum forcing zone parameters and corresponding reflection coefficients with satisfactory accuracy for engineering practice
- For close-to-optimum tuning, similar reflection coefficients were obtained regardless in which governing equations forcing source terms were applied

When applying forcing source terms in the conservation equation for the momentum in longitudinal (i.e. in wave propagation) direction, then the theory predictions for reflection coefficients, free-surface elevation, velocities, and vorticity within the whole forcing zone are nearly perfectly accurate as demonstrated in Sects. 5 and 6.2.

When applying forcing source terms (also) in the conservation equation for the transversal momentum for dispersive mediums (i.e. vertical momentum for free-surface waves in intermediate- or deep-water conditions), then the flow within the forcing zone becomes more complex, so that some flow details are not fully described by the theory anymore. As Sects. 6.2 to 6.5 show, for some choices of forcing strength γ the simulation results for reflection coefficient C_{R} were then lower than the theory predictions. Note though that this effect occurred mainly for impractical forcing parameter settings (cf. discussion in Sect. 6.2). However, the relevant flow features appeared to be predicted by the theory, since the optimum choice of the forcing zone parameters and the corresponding reflection coefficients were predicted with satisfactory accuracy for engineering practice.

In this work, when forcing was applied simultaneously in several governing equations, the same forcing strength γ was used for all equations. Section 4.1.2 shows that applying forcing to several equations can be related to the case of applying forcing in a single equation. Also from the results from Sects. 5 and 6.2 no preference towards applying source terms in certain governing equations is made out; as long as forcing strength γ is optimally tuned, the resulting reflection coefficients appear to be similar as Fig. 146 implies. The present findings indicate that this also holds for relaxation zones from Sects. 2.3, since relaxation zones can be considered as a special case of forcing zones as shown in Sect. 4.2.

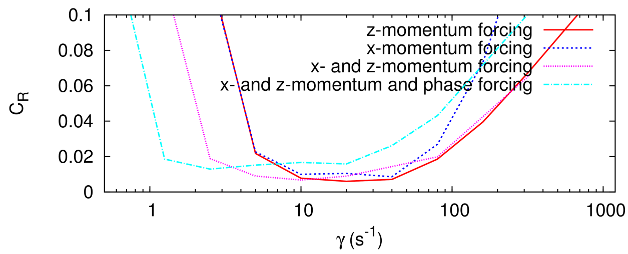

Figure 146: Reflection coefficient C_{R} as a function of forcing strength γ, from Perić and Abdel-Maksoud (2016b)

9.6 Choice of forcing zone arrangements for 2D- and 3D-flows

Key findings

- Different combinations of forcing zones can be used to successfully minimize undesired wave reflections
- Forcing fluid momentum and volume fraction towards the far-field wave solution can create flow disturbances for forcing zones tangential to the wave propagation direction
- For 3D-flow simulations with bodies subjected to long-crested far-field waves, a forcing zone arrangement was presented which does not produce the aforementioned flow disturbances

Section 7.1 showed that 'forcing zone arrangements' in 3D-flow simulations can differ in the choice of governing equations to which source terms are applied, the choice of reference solutions towards which the flow is forced, and the choice of domain boundaries to which forcing zones are attached. It was found that usually several different forcing arrangements can produce satisfactory results for a given flow problem.

However, Sects. 7.1 and 7.2 demonstrated that even when correctly tuned, some forcing arrangements, such as forcing of velocities u_i and volume fraction α towards the far-field wave, can produce undesired flow disturbances. These occur when waves travel tangential to the forcing zone and additionally the computed flow, including changes in wave height and phase due to numerical diffusion and dispersion, does not match the prescribed reference solution. Further research is necessary to quantify the errors due to such disturbances. The present results suggest that to reduce these disturbances such forcing arrangements require finer discretizations than commonly used, and thus a larger computational effort. If the reference solution is inaccurate, as e.g. when using low-order wave theories as reference solution, then such disturbances cannot be controlled by refining the discretization.

For long-crested far-field waves, forcing arrangements have been presented for which the above discrepancies or disturbances do not occur. Examples are the approach by Chen et al. (2006) or the forcing arrangement proposed in Sects. 7.1 and 7.4. The latter is computationally more efficient and is thus recommended.

Although not the topic of the present investigation, the present findings indicate that the case of short-crested far-field waves can be treated as follows. One option is to select the solution domain as small and the far-field solution as accurate as possible. Such a far-field solution can be obtained e.g. from a higher-order spectral method or a nonlinear potential flow solver. Apply forcing towards the velocities and volume fraction of the far-field solution near all vertical domain boundaries. Since this approach can produce flow disturbances as outlined above, a finer than commonly used discretization may be required to ensure that no significant disturbances occur. Alternatively, an approach along the lines of Chen et al. (2006) could be constructed. However, this is not entirely straight-forward, since the first simulation in Chen et al. (2006) was designed for long-crested wave propagation, and it is not obvious how the simulation could be performed with a superposition of multiple waves with arbitrary propagation directions. However, often for realistic directional wave energy spectrums the majority of the wave energy is distributed over wave propagation directions close to one primary direction (Lloyd, 1998). In such cases, the intended wave energy spectrum may be simplified by only considering waves with propagation direction $\mu \pm 45\,\text{deg}$, where μ is the primary wave propagation direction. By prescribing the directional wave generation to a single domain boundary and applying wave damping zones to all other boundaries, the first simulation can be carried out, and from here the approach again follows Chen et al. (2006). Thus the approach is also suitable for coarse discretizations. Future research is necessary to develop and investigate these and possibly also further forcing zone arrangements for short-crested waves.

9.7 Accuracy of theory predictions

Key findings

- For forcing of longitudinal fluid momentum, the average difference between theory predictions and simulation results for reflection coefficient C_{R} was less than 4.3% in all simulations
- Even for settings far from optimum, no simulation result for C_{R} was more than 10.5% larger than theory predicted
- For close-to-optimum tuning, simulation results for C_{R} were never more than 3.4% larger than theoretically predicted, and in most cases $C_{\mathrm{R,sim}} - C_{\mathrm{R,theory}}$ was $< 2\%$

As discussed in Sect. 9.5, the accuracy of the theory predictions depends on which governing equations forcing source terms are applied to. First, consider those simulations from the present work where theory closely predicts the reflection coefficients C_{R}, such as when forcing is applied to the fluid momentum directed in wave propagation direction.

Figure 147 shows the upper limit of the average difference between theory predictions and simulation results for all figures from the present work, except for those where significant differences between theory predictions and simulation results were to be expected. Not included are figures which show overall reflection coefficients for flows with 2D- and 3D-wave-propagation, figures which show results for simultaneous wave generation and damping in a forcing zone, figures which show results for forcing of (also) vertical fluid momentum or of all fluid momentum as well as volume fraction α, and figures which show results for relaxation zones; in these cases, the findings from Sects. 5 to 8 show that, even if for these figures the theory successfully predicts the optimum tuning of the forcing zone, further away from the optimum settings the simulation results for reflection coefficient C_{R} can e.g. be significantly lower than the theory predictions.

For the results in Fig. 147, theory and simulation results differ on average less than 2%, with three exceptions: For the highly nonlinear sound waves in Fig. 39, the theory slightly underpredicts the reflection coefficients resulting in an average difference of $< 2.1\%$. For the highly nonlinear free-surface waves in Fig. 62, the wave steepness is so large that wave breaking occurs in a few simulations where forcing strength is $\gamma \ll \gamma_{\mathrm{opt}}$ or $\gamma \gg \gamma_{\mathrm{opt}}$ relative to the optimum value γ_{opt}, which increases the average difference to $< 3.1\%$. For the shallow water free-surface waves in Fig. 78, reflection coefficients were, especially for thinner zones, lower than predicted by theory; this favorable effect resulted in an average difference of $< 4.2\%$.

Thus Fig. 147 indicates that for the depicted flows the theory predictions based on Sect. 4 on average agree closely with the simulation results.

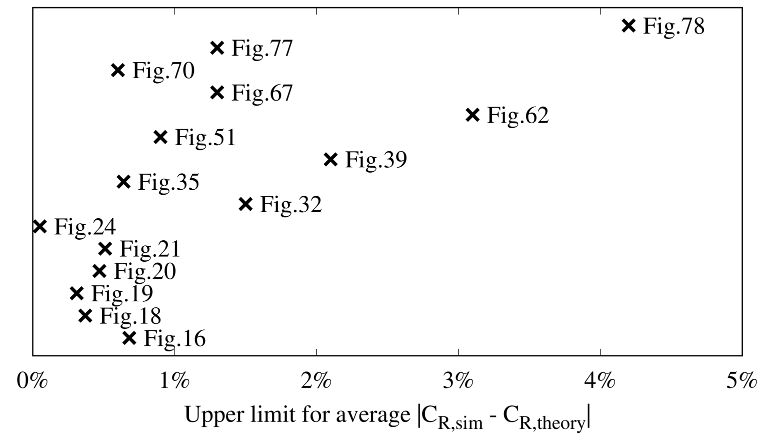

Figure 147: For each of the above figures (i.e. Figs. 16, 18, ...), the location of the cross (**x**) marks the upper limit of $\overline{|C_{\mathrm{R,sim}} - C_{\mathrm{R,theory}}|}$, with reflection coefficient obtained from simulation results ($C_{\mathrm{R,sim}}$) and according to theory prediction ($C_{\mathrm{R,theory}}$) for the same forcing strength γ; the average is taken over all simulation results and corresponding theory predictions belonging to the same curve, after which its absolute value is calculated; the upper limit applies to all curves in the figure; for most figures holds $\overline{|C_{\mathrm{R,sim}} - C_{\mathrm{R,theory}}|} < 2\%$, which indicates close agreement between simulation results and theory predictions

For engineering practice, it is desired that simulation results for reflection coefficient C_{R} should not substantially exceed theory predictions. Figure 148 shows that for all considered flow simulations, the simulated results for reflection coefficients were never more than 10.5% larger than the corresponding theory predictions. Indeed, the simulated reflection coefficients exceeded the theory predictions by more than 5% only for a few simulations in the following figures:

For the highly nonlinear sound waves in Fig. 39, simulation results exceeded theory predictions most severely for the smallest forcing zone thickness ($x_{\mathrm{d}} = 0.5\lambda$) by $< 8.3\%$, for larger zone thicknesses this reduced to $< 5.5\%$.

In Fig. 45, when using forcing zones to simulate standing (hydro-)acoustic waves, for one simulation with a forcing strength γ nearly an order of magnitude lower than its theoretical optimum value the theory underpredicted the reflection coefficient by 10.5%; for close-to-optimum tuning, however, differences between theory predictions and simulation results were well below 1%.

For the highly nonlinear free-surface waves in Fig. 62, the wave steepness was so large that for a few simulations wave breaking occurred, which led to results for C_{R} being $< 7.4\%$ larger than theory predictions for a few simulations with forcing strength γ several orders of magnitude away from its optimum value.

For the relaxation zones in Fig. 131, simulation results for C_{R} exceeded theory predictions by $< 5.3\%$ for relaxation parameters τ nearly an order of magnitude larger than its theoretical optimum.

In Fig. 136, the relaxation zones with blending exponent $n = 0.1$ rapidly blended-in the source terms (i.e. $b(\mathbf{x})$ changes from 0 to 0.5 in the first 1% of the relaxation zone), so that for zone thickness $x_{\mathrm{d}} = 0.5\lambda$ the simulation results for C_{R} exceeded the theory predictions for one τ-value by $< 8.4\%$. With increasing zone thickness the difference decreased to $< 2.6\%$ for zone thickness $x_{\mathrm{d}} = 2\lambda$. Also for larger exponents n the difference decreased, so that for $n = 10$ no simulation results exceed theory predictions by more than 2.3% for all zone thicknesses.

In the present work, a wide range of different flow problems have been investigated. These include irregular waves, highly nonlinear waves, oblique wave incidence in 2D and 3D, simultaneous wave generation and wave damping, a wide range of forcing zone parameters, as well as deep and shallow water conditions. In this regard it seems remarkable that simulation results were found to be at all times either comparatively close to or lower than theory predictions. Thus keeping in mind the above uncertainties if comparable cases are investigated, the theory may be used with confidence even for forcing zone settings far from their theoretical optimum.

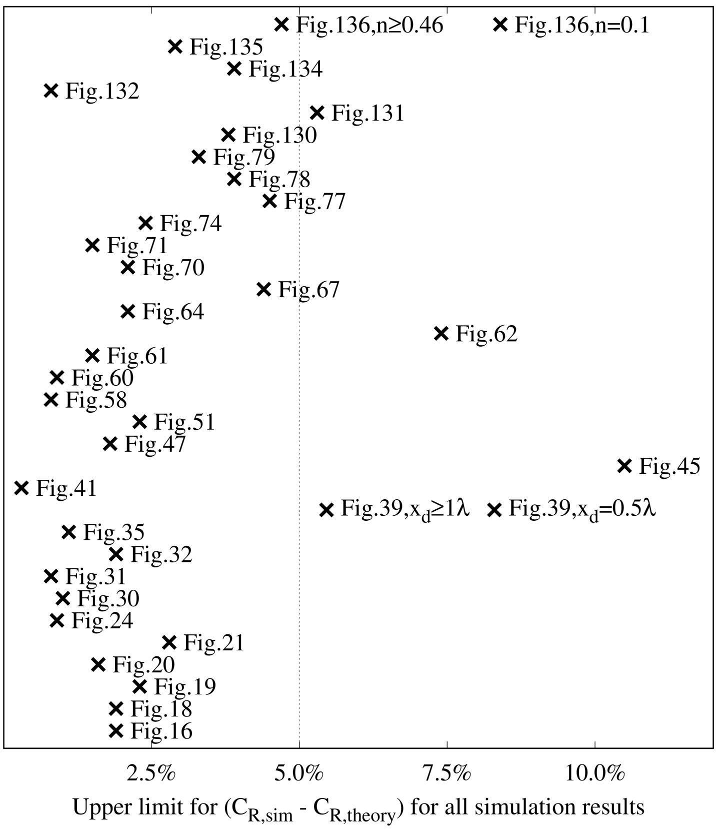

Figure 148: For each of the above figures (i.e. Figs. 16, 18, ...), the location of the cross ($\mathbf{x}$) marks the upper limit for $C_{\mathrm{R,sim}} - C_{\mathrm{R,theory}}$, i.e. for every simulation result ($C_{\mathrm{R,sim}}$) and the corresponding theory prediction ($C_{\mathrm{R,theory}}$) for reflection coefficient C_R in that figure, the value of $C_{\mathrm{R,sim}} - C_{\mathrm{R,theory}}$ remains below the threshold given in the above plot; in this work, no simulation result for reflection coefficient $C_{\mathrm{R,sim}}$ was more than 10.5% larger than the corresponding theory prediction $C_{\mathrm{R,theory}}$, and in most figures $C_{\mathrm{R,sim}} - C_{\mathrm{R,theory}}$ was below 5%, indicating that the theory from Sect. 4 rarely overpredicts the reflection coefficient significantly

Figure 149 shows that, if the forcing zone is tuned close to the theoretical optimum setting, then simulation results for reflection coefficients ($C_{\mathrm{R,sim}}$) were at most < 3.4% larger than the corresponding theory predictions ($C_{\mathrm{R,theory}}$).

For all flow simulations with (hydro-)acoustic waves and forcing zones in Sect. 5 held $C_{\mathrm{R,sim}} - C_{\mathrm{R,theory}} < 1\%$, except for forcing of highly nonlinear waves with zone thickness $x_{\mathrm{d}} \leq 1\lambda$ in Fig. 39 with 1.7%.

For all flow simulations with free-surface waves and forcing zones from Sect. 6 held $C_{\mathrm{R,sim}} - C_{\mathrm{R,theory}} < 2\%$, except for forcing of x-momentum with small zone thickness $x_{\mathrm{d}} = 0.25\lambda$ in Fig. 51 with 2.4% and for forcing of highly nonlinear waves with forcing of x- and z-momentum as well as volume fraction α in Fig. 64 with 2.1%.

For all flow simulations with free-surface waves and relaxation zones from Sect. 8 held $C_{\mathrm{R,sim}} - C_{\mathrm{R,theory}} < 2\%$, except for forcing with less effective blending functions as investigated in Figs. 134 and 136, where values up to < 3.4% were recorded.

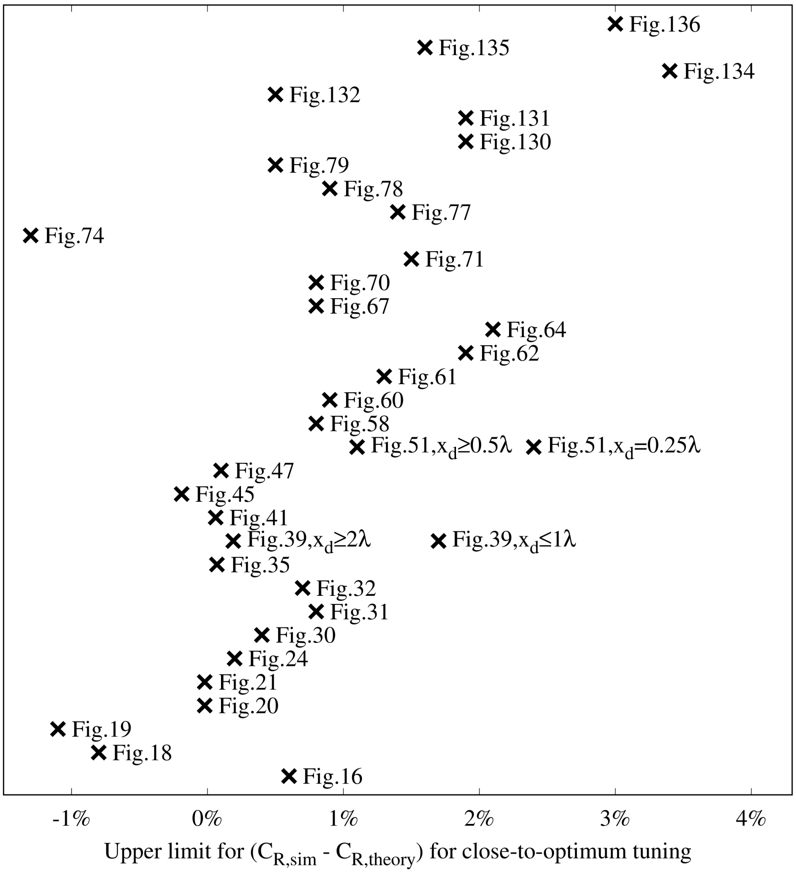

Figure 149: For each of the above figures (i.e. Figs. 16, 18, ...), the location of the cross (**x**) marks the upper limit for $C_{\mathrm{R,sim}} - C_{\mathrm{R,theory}}$ with the parameters of the forcing zone tuned close to the theoretical optimum; with reflection coefficient obtained from simulation results ($C_{\mathrm{R,sim}}$) and according to theory prediction ($C_{\mathrm{R,theory}}$) for the same forcing strength γ; for each curve per figure, $C_{\mathrm{R,sim}} - C_{\mathrm{R,theory}}$ is evaluated at the forcing strength $\gamma \geq \gamma_{\mathrm{opt,theory}}$ closest to the theory prediction $\gamma_{\mathrm{opt,theory}}$ of the optimum value for forcing strength γ; for relaxation zones, $C_{\mathrm{R,sim}} - C_{\mathrm{R,theory}}$ is evaluated at the relaxation parameter $\tau \leq \tau_{\mathrm{opt,theory}}$ closest to the theory prediction $\tau_{\mathrm{opt,theory}}$ of the optimum value for relaxation parameter τ; the results show that when the forcing zone was tuned using the theory from Sect. 4, simulation results were never more than 3.4% larger than theoretically predicted, and in most cases $C_{\mathrm{R,sim}} - C_{\mathrm{R,theory}}$ was < 2%, which demonstrates that the theory predictions are of satisfactory accuracy for typical engineering purposes

Consider tuning a forcing zone via the theory from Sect. 4. Assume that the theoretical reflection coefficient is $C_{\mathrm{R,theory}} <$ 0.6%, and that the worst-case from Fig. 149 holds with $C_{\mathrm{R,sim}} - C_{\mathrm{R,theory}} < 3.4\%$. Thus follows that the simulation results for reflection coefficient are $C_{\mathrm{R,sim}} < 4\%$. As discussed in Sect. 3, the energy E_{refl} of the reflected wave relative to the energy E of the generated wave is $E_{\mathrm{refl}}/E_{\mathrm{gen}} \approx C_{\mathrm{R}}^2$. Inserting $C_{\mathrm{R,sim}} < 4\%$ gives $E_{\mathrm{refl}}/E_{\mathrm{gen}} < 0.0016$. Therefore, the wave energy reflected back into the domain parts of interest is less than 0.16% of the energy of the generated wave, which can be considered negligible for typical engineering purposes.

Thus the present results indicate that for typical ocean engineering and shipbuilding applications, the theory from Sect. 4 predicts the optimum values for the forcing zone parameters and the corresponding reflection coefficients with satisfactory accuracy for engineering practice. Therefore, the theory is recommended for the tuning of forcing zones in typical flow problems with (hydro-)acoustic waves or free-surface waves, as was demonstrated for typical ocean engineering and shipbuilding applications (cf. Sects. 7, 8.7 and Appendix B).

Given the demonstrated accuracy of the theory predictions, future work to further increase the accuracy of the theoretical predictions seems promising.

First, it could be attempted to derive the theory from Sect. 4 for forcing in the equations for vertical fluid momentum and/or volume fraction, with the intention to predict the corresponding complex flow behaviors. Examples of such complex flow behaviors include the occurrence of net mass flux into the forcing zone for forcing of vertical fluid momentum as observed in Fig. 59, or the reflection of waves with inverted surface elevation for forcing of volume fraction as observed in Fig. 68.

Second, for (hydro-)acoustic waves the derivation might be attempted for different nonlinear wave equations, and accordingly for free-surface waves the application of nonlinear wave theories may improve predictions. This may be used to assess in more detail the accuracy of the theory for flows with nonlinear waves, and investigate whether there are further challenging nonlinear flow problems for which reflection coefficient C_{R} is under-predicted by theory.

Third, investigations over a wide range of Mach numbers could be performed, although applications to such flows does not suggest a strong variation in optimum tuning of the forcing zone parameters as the example in Appendix B suggests.

Fourth, the derivation could also be extended to unsteady reference flow solutions, to provide further theoretical foundation why the optimum forcing zone parameters were found to be nearly independent of the choice of reference solution.

The above investigations may require more complicated derivations, increased computational effort, longer evaluation times, and might possibly be more complicated to use if they require more knowledge about the investigated flow from the user.

Finally, further results from flow simulations are necessary to assess in more detail the forcing zone behavior with rogue or breaking ocean waves (Perić et al., 2015; Perić and Abdel-Maksoud, 2016), and also with different types of (hydro-)acoustic wave distortion than in Sect. 5.6.

10 Conclusion

In this thesis, a theory was presented which predicts the reflection coefficients and the flow within forcing zones in finite-volume-based flow simulations with (hydro-)acoustic waves and free-surface waves.

The theory is intended to be used to optimize the forcing zone's case-dependent parameters before performing the flow simulation. It was derived to hold with good approximation for every continuous or discontinuous blending function $b(\mathbf{x})$ and is based on a generic forcing zone formulation, so that it can easily be applied to many existing implementations in different flow solvers. To facilitate the use of the presented theory in the scientific community, computer programs to evaluate the theory for free-surface and (hydro-)acoustic waves have been published as free software.

The main mechanisms behind how forcing zones reduce undesired wave reflections were shown to be wave absorption, partial wave reflection occurring throughout the forcing zone where $\nabla b(\mathbf{x}) \neq 0$, and the destructive interference of the partially reflected waves. All three mechanisms need to be considered to accurately predict the optimum forcing strength γ and the corresponding reflection coefficient C_{R} for a given blending function $b(\mathbf{x})$ and zone thickness x_{d}. For close-to-optimum tuning, partial wave reflections occur throughout the forcing zone so that the amplitudes of these reflected waves are small compared to the amplitude of the wave that entered the forcing zone. Thus forcing zones 'split up' nonlinear waves into many low-amplitude (i.e. nearly linear) wave components which can then cancel via destructive interference. This mechanism explains why, when correctly tuned, forcing zones produced similar reflection coefficients regardless whether the investigated waves were linear or highly nonlinear.

Further, it was found that there exists no general optimum setup for the parameters in the forcing zone formulation. Instead, the optimal choice of parameters is case-dependent and differs depending on the intended reflection coefficient C_{R} and the investigated wave energy spectrum.

In 3D-flow simulations, different 'forcing zone arrangements' can be used, which differ in the choice of the governing equations to which forcing source terms are applied, the reference solution towards which the flow is forced, and the domain boundaries to which forcing zones are attached. Different types of forcing zones can be combined in a simulation, and several combinations can produce satisfactory results. However, it was shown that some forcing zone arrangements produce flow disturbances when waves travel tangential to the forcing zone and when there is a mismatch between the computed flow and the reference solution.

For long-crested far-field waves, an efficient forcing zone arrangement was proposed which does not produce such flow disturbances: The flow near the inlet boundary is forced towards the incidence wave, to generate the desired wave while minimizing undesired reflections at the inlet. Near the domain sides, the boundary-normal velocities are gradually forced to zero, thus the waves generated at the inlet pass through these zones undisturbed, whereas waves traveling towards the domain sides (e.g. due to reflections at a body within the domain) are damped. At the outlet boundary, all waves are damped by forcing the boundary-normal velocities towards zero or, in the presence of currents, by forcing the flow towards the calm-surface solution for the flow with currents. This forcing zone arrangement reliably reduced undesired wave reflections in several flow simulations for typical ocean engineering and shipbuilding applications with strongly reflecting bodies subjected to free-surface waves. The results showed that the presented forcing arrangement with optimization of the forcing zone parameters according to the theory enables the use of smaller domains and thinner forcing zones than those commonly used, which can substantially reduce the computational effort.

The theory predictions were demonstrated to be of satisfactory accuracy for forcing zones in 1D-, 2D- and 3D-flow simulations with (hydro-)acoustic waves and free-surface waves, with regular and irregular, linear and highly nonlinear wave propagation, normal or oblique wave incidence, both in dispersive (free-surface waves in deep-water conditions) and non-dispersive (free-surface waves in shallow-water conditions; sound waves in an ideal gas and in liquid water) mediums, for different forcing zone parameters, for forcing in different governing equations, for forcing towards different reference solutions, and for forcing zones applied to different domain boundaries. As predicted by theory, for practical discretizations the forcing zones were found to behave independent of the chosen discretization scheme, its order, the mesh size, the time-step size, and also of the used flow solver.

When the forcing zone was tuned using the developed theory, the simulation results for reflection coefficient C_{R} were in most cases smaller or nearly equal to those predicted by theory, but never more than 3.4% larger. The developed theory is therefore suitable for optimization of the forcing zone parameters for flow simulations with (hydro-)acoustic or free-surface waves.

A Appendix: (Hydro-)acoustic wave propagation through thin constant-blending forcing zone in the domain center

Key findings

- At every location within the forcing zone where $\nabla b(\mathbf{x}) \neq 0$, waves are partially reflected
- At every location within the forcing zone where $\nabla b(\mathbf{x}) = 0$, no wave reflection occurs
- The amount of transmission, reflection and absorption depends on the value of forcing strength γ

This section investigates the reflection and transmission behavior of a thin forcing zone. The results are the basis for some of the assumptions used in the derivation in Sect. 4. The setup for the flow simulations in this section is as described in Sect. 5.1, with domain size $L_x = 6\lambda$, given in relation to wavelength λ. The following exceptions apply.

Figure 150 shows a sketch of the domain. The forcing zone is based on Eq. (31) and is located in the middle of the domain, with $b(x) = 1$ for the cell located at $x = 3\lambda$ and $b(x) = 0$ for all other cells, i.e. the forcing zone is one cell thick with constant blending. The cell size is $\Delta x = \frac{\lambda}{30}$, so the thickness of the zone is $x_\mathrm{d} = \frac{\lambda}{30}$. The reference solution is set to $u_\mathrm{ref} = 0$ to damp the waves. Simulations are performed for five wave periods T with a time step of $\Delta t = \frac{T}{100}$ and for different forcing strengths γ.

The simulations are performed once with liquid water, and once with an ideal gas as fluid. The main differences are that the speed of sound is larger in water, so the domain and the cell sizes were scaled to fit $\Delta x = \frac{\lambda}{30}$ and $L_x = 6\lambda$. Further, the amplitude of the pressure fluctuation at the wave-maker is 10 Pa for the ideal gas (in air, this would correspond to ≈ 113 dB(SPL)) and 1000 Pa in water (≈ 180 dB(SPL)).

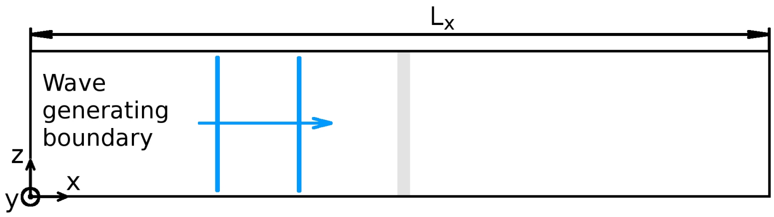

Figure 150: Sketch of the computational domain with wave-maker at $x = 0$ m and 1-cell-thick forcing zone (shaded gray)

The wave is generated at the wave-maker boundary $x = 0$ m during the time interval $0 \leq t \leq 1T$. After this, the pressure at boundary $x = 0$ is set to the reference pressure. Thus only a sinusoidal wave pulse of one wavelength (cf. Fig. 151 bottom) is created, which travels in positive x-direction.

When it reaches the one-cell forcing zone at $x = 3\lambda$, the wave is partly transmitted, absorbed and reflected, the percentage of which depends on the forcing strength γ. The energy of the generated wave is obtained by integrating the wave energy in the whole domain at time instance $t = 2T$, when the wave is fully generated and has not yet encountered the forcing zone, via $E_\mathrm{tot}|_{t=2T} = \int_A \int_0^{6\lambda} E_\mathrm{kin} + E_\mathrm{pot}\,\mathrm{d}x\,\mathrm{d}A|_{t=2T}$, with kinetic and potential energy evaluated via Eq. (38) and cross-section area $A = \Delta y \Delta z$ of the quasi-1D simulation domain.

At time $t = 5T$, the wave has fully encountered the forcing zone, and the reflected part of the wave is on the interval $0 \leq x < 3\lambda$ whereas the transmitted part of the wave is on the interval $3\lambda < x \leq 6\lambda$ as shown in Fig. 151 bottom. By computing the wave energy in the corresponding domain parts, the reflected component E_R, the transmitted component E_T and the absorbed component E_A of the total energy of the generated wave, normalized by the total energy of the generated wave $E_\mathrm{tot}|_{t=2T}$, are obtained via

$$E_\mathrm{R} = \frac{\int_A \int_0^{3\lambda} E_\mathrm{kin} + E_\mathrm{pot}\,\mathrm{d}x\,\mathrm{d}A|_{t=5T}}{\int_A \int_0^{6\lambda} E_\mathrm{kin} + E_\mathrm{pot}\,\mathrm{d}x\,\mathrm{d}A|_{t=2T}} \quad , \tag{121}$$

$$E_\mathrm{T} = \frac{\int_A \int_3^{6\lambda} E_\mathrm{kin} + E_\mathrm{pot}\,\mathrm{d}x\,\mathrm{d}A|_{t=5T}}{\int_A \int_0^{6\lambda} E_\mathrm{kin} + E_\mathrm{pot}\,\mathrm{d}x\,\mathrm{d}A|_{t=2T}} \quad , \tag{122}$$

$$E_\mathrm{R} + E_\mathrm{T} + E_\mathrm{A} = 1 \quad , \tag{123}$$

with wavelength λ, time t, wave period T, location x in wave propagation direction, kinetic and potential energies E_{kin} and E_{pot} evaluated via Eq. (38), and cross-section area $A = \Delta y \Delta z$.

Figure 151 shows that the simulation results for E_{T}, E_{R}, E_{A} for the ideal gas and liquid water are nearly identical, despite the different mediums and wavelengths. Thus with a single-cell forcing zone of thickness $\lambda/30$, roughly 50% of the energy of the incoming wave can be absorbed at optimum setting of γ; as expected, for γ set close-to-optimum, i.e. $\gamma = 20480\,\mathrm{s}^{-1}$ in bottom image of Fig. 151, this results in a transmitted and a reflected wave with roughly the same velocity amplitude $\approx \frac{1}{2}u_{\mathrm{a}}$, where u_{a} is the velocity amplitude of the initially generated wave. Via the scaling of $\gamma_{\mathrm{opt}} \propto \omega$ and $x_{\mathrm{d}} \propto \lambda$ given in Sect. 2.2, these results can be applied to a wave of any period, which would correspond to a sideways shifting of the curves in Fig. 151.

The similar forcing zone behavior (i.e. the values for E_{T}, E_{R} and E_{A}) for gas and liquid suggests that the present findings could also apply in other wave propagation mediums such as solids. The theory from Sect. 4 suggests that, if the forcing zone formulation can be traced back to the generic formulation in Eq. (2), and if the wave period T and wavelength λ are known, then no further information about the wave propagation medium are required to predict reflection coefficient C_{R}.

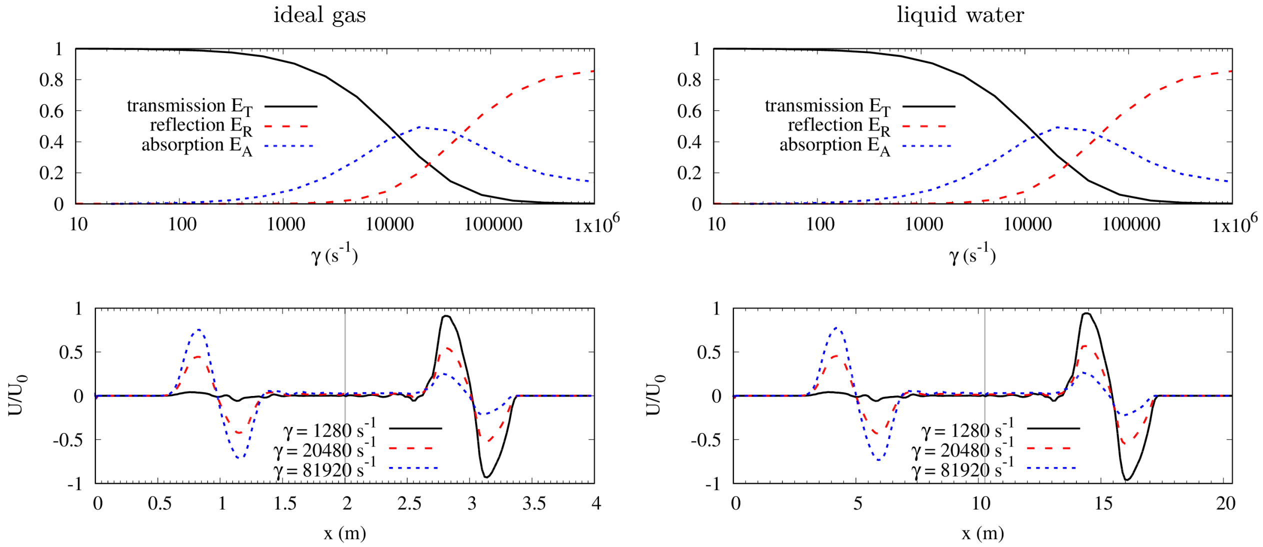

Figure 151: Propagation of a wave with period $T = 0.002\overline{27}\,\mathrm{s}$ in an ideal gas (left) and liquid water (right) through a thin forcing zone (shaded gray) positioned roughly in the domain center; for forcing via Eq. (31) with constant blending via Eq. (3) and zone thickness $x_{\mathrm{d}} = \lambda/30$; top: transmitted ($E_{\mathrm{T}}$), reflected ($E_{\mathrm{R}}$), and absorbed ($E_{\mathrm{A}}$) components of the total energy as a function of forcing strength γ; bottom: velocity in the domain at time $t = 5T$ for forcing strengths $\gamma = 1.28 \cdot 10^3\,\frac{1}{\mathrm{s}}$ (mostly transmission), $\gamma = 2.048 \cdot 10^4\,\frac{1}{\mathrm{s}}$ (roughly equal transmission and reflection) and $\gamma = 8.192 \cdot 10^4\,\frac{1}{\mathrm{s}}$ (mostly reflection)

Figure 152 shows that similar results as before in Fig. 151 are obtained when the simulations are repeated with finer discretization but same zone thickness $x_{\mathrm{d}} = \frac{\lambda}{30}$. This shows that the original discretization (selected as roughly the coarsest discretization that would be used in engineering practice) was sufficient to capture the forcing zone behavior, although the finer discretization has a smoother wave resolution. It also supports the finding from Sect. 4.4, that the behavior of the forcing zone can thus be considered independent of the discretization for most practical configurations.

Simulations with 8 or 2 times refined discretization, as well as corresponding simulations with ideal gas as fluid were conducted and showed the same behavior, and thus are not depicted. Since the forcing zone thickness $x_{\mathrm{d}} = \frac{\lambda}{30}$ was maintained, the forcing zone contains more than one cell for the finer discretized simulations. As this does not affect the result, it follows that no reflection occurs at the interfaces between cells in which the forcing strength γ is the same, which is equivalent to $\nabla b(\mathbf{x}) = 0$; further, reflection occurs at the interface between two cells if there holds $\nabla b(\mathbf{x}) \neq 0$.

Considering Figs. 151 and 152, it is remarkable that the energy absorption is so large for such a thin zone. However, literature (e.g. Israeli and Orszag, 1981) and the discussion in Sect. 9.3 indicate that the damping performance (i.e. the decrease in C_{R}) will improve comparatively slowly when increasing the zone thickness x_{d} for the constant blending used ($b(\mathbf{x}) = 1$); Israeli and Orszag (1981) suggest for a related case that at least a zone thickness of $x_{\mathrm{d}} > 15\lambda$ is required to obtain reflection coefficient $C_{\mathrm{R}} < 1\%$, and the discussion in Sect. 9.3 shows that, for precisely this case, to obtain

$C_\mathrm{R} < 1\%$ requires a zone thickness of $x_\mathrm{d} \geq 30.2\lambda$ with optimum tuning[20] of forcing strength γ, and that the damping can be substantially improved by gradually increasing the blending function $b(x)$ within the zone as found in Sects. 5.3 and 7.1.

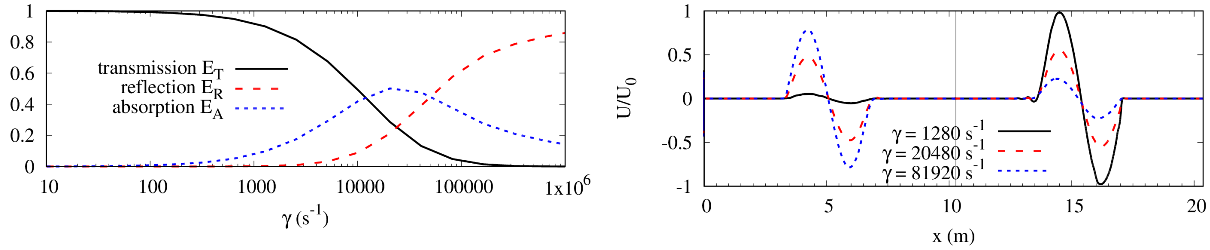

Figure 152: As in Fig. 151 for water, except for 4 times smaller cells size Δx and time step Δt; thus instead of 1 cell in Fig. 151, the above forcing zone contains 4 cells; the forcing zone's reflection, transmission, and absorption characteristics are nearly identical to those from Fig. 151, which demonstrates that in the parts of the forcing zone where $\nabla b(\mathbf{x}) = 0$, no wave reflection occurs

[20]The exception to this statement are those smaller x_d-values, for which the especially favorable interference (cf. Fig. 27) occurs; however, for these zone thicknesses the reflection coefficient C_R can be highly sensitive to the wavelength as discussed in Sect. 9.2.

B Appendix: Tuning forcing zones to improve convergence for ship resistance computations

Key findings

- Applying forcing zones near all vertical domain boundaries can improve the convergence of ship resistance computations
- When performing simulations in model and full scale, the forcing strength must be correctly scaled to ensure that the solution converges in a similar manner
- If the forcing strength is not scaled, the solution may not converge
- It is recommended to tune the forcing zones to the period and wavelength of the transversal wave in the ship wake

This section compares results from model and full scale resistance computations in 3D of the Kriso container ship (KCS) at Froude number 0.26. The simulations in this section are based on the simulations reported in detail in Enger et al. (2010). For detailed information on the setup and discretization, the reader is referred to Enger et al. (2010). In the following, only a brief overview of the setup and differences to the original simulations are given for the sake of brevity. The present model-scale simulations differ only in the forcing zone setup (and slight modifications of the used grid) from the fine grid simulation in Enger et al. (2010). The KCS is fixed in its floating position at zero speed. To simulate the hull being towed at speed U, this velocity is prescribed at the inlet domain boundaries and the hydrostatic pressure of the undisturbed water surface is prescribed at the outlet boundary behind the ship. The domain is initialized with a flat water surface and flow velocity U for all cells. As time accuracy is not in the focus here, the first-order implicit Euler scheme is used for time integration. The k-ϵ turbulence model by Launder and Spalding (1974) is used. The computational grid consists of roughly 3 million cells. The pressure components of the drag and vertical forces are compared, which are obtained by integrating the x-component for the drag and z-component for the vertical component of the pressure forces over the ship hull. The simulation starts at time $t = 0\,\mathrm{s}$ and is stopped at time $t_{\mathrm{end}} = 90\,\mathrm{s}$.

The Kelvin wake of the ship can be decomposed into a transversal and a divergent wave component. The wave damping setup is based on the ship-evoked transversal wave (wavelength $\lambda_{\mathrm{t}} \approx 3.1\,\mathrm{m}$). The wave period is calculated from the wave's phase velocity c, which equals the ship speed U, via $T = \lambda_{\mathrm{t}}/c$. Forcing zones for vertical momentum according to Eq. (20) with reference solution $w_{\mathrm{ref}} = 0$ and with exponential blending according to Eq. (9) have been attached to all vertical domain boundaries with zone thickness $x_{\mathrm{d}} = 2.3\lambda_{\mathrm{t}}$ and forcing strength $\gamma = f_1 = 22.5\,\mathrm{s}^{-1}$. This setup provided convergence of drag and vertical forces in model scale. Figure 153 shows the wake pattern for the finished simulation. The results for the forces are in agreement with the findings from Enger et al. (2010). The obtained resistance coefficient $C_{\mathrm{T,sim}} = 3.533 \cdot 10^{-3}$ compares well with the experimental data ($C_{\mathrm{T,exp}} = 3.557 \cdot 10^{-3}$, 0.68% difference to $C_{\mathrm{T,sim}}$) by Kim et al. (2001) and to the simulation results by Enger et al. (2010) ($C_{\mathrm{T,Enger}} = 3.561 \cdot 10^{-3}$, 0.11% difference to $C_{\mathrm{T,exp}}$).

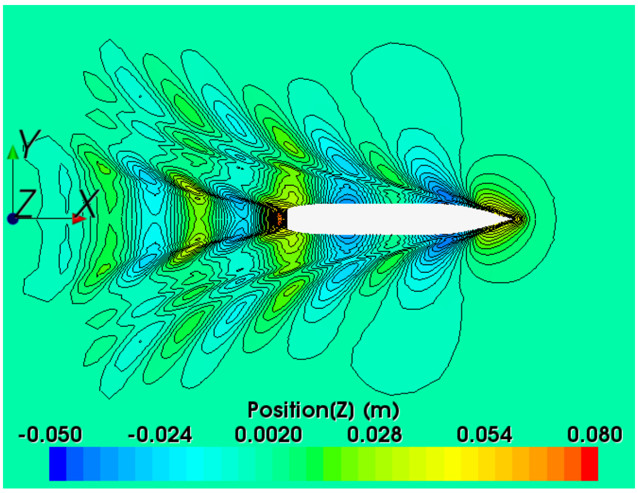

Figure 153: Wave profile for model scale ship with $f_1 = 22.5\,\mathrm{s}^{-1}$ for converged solution

Additionally, full scale simulations are performed with Froude similarity. The scaled velocity and ship dimensions are shown in Table 1. The grid is similar to the one for the model scale simulation except scaled with factor 31.6.

Table 1: KCS parameters

scale	waterline length L (m)	service speed U (m/s)
model	7.357	2.196
full	232.5	12.347

To obtain similar wave damping as in model scale, zone thickness x_d was scaled according to Eq. 13 by factor 31.6 and forcing strength $\gamma = f_1$ was scaled according to Eq. 16; the correctly scaled f_1 value for the full scale simulation is thus $f_{1,\,\mathrm{full}} = f_{1,\,\mathrm{model}} \cdot \omega_\mathrm{full}/\omega_\mathrm{model} = 22.5\,\mathrm{s}^{-1} \cdot 1/\sqrt{31.6} \approx 4\,\mathrm{s}^{-1}$. Additionally, the full scale simulations were performed with the same forcing strength as in the model scale simulations, i.e. $f_1 = 22.5\,\mathrm{s}^{-1}$. Otherwise the setup corresponds to the one from the model scale simulation.

Figure 154 shows drag and vertical forces as a function of time when both model and full scale simulations are performed with the same value for damping coefficient f_1. In contrast to the model scale forces, the full scale forces oscillate and a converged solution is not obtained for the full scale case.

In contrast, Fig. 155 shows that indeed similar wave damping is obtained when forcing strength f_1 is correctly scaled, since in both cases the forces converge in a qualitatively similar fashion. Note that a perfect match of the curves in Fig. 155 is not expected, since Froude-similarity is given, but not Reynolds-similarity. Thus although the pressure components of the forces on the ship converge to the same values (if scaled with L^3), the amplitude and frequency of the force oscillation is different.

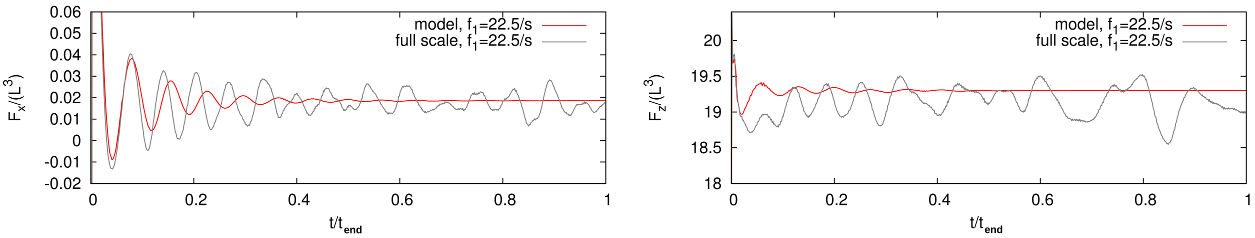

Figure 154: Drag (left image) and vertical (right image) pressure forces on ship as a function of time for model (red) and full scale (gray); for the full scale simulation, the same forcing strength $f_1 = 22.5\,\mathrm{s}^{-1}$ as in the model scale simulations is used; since f_1 is not correctly scaled, the wave damping is not similar and the full scale simulation does not converge

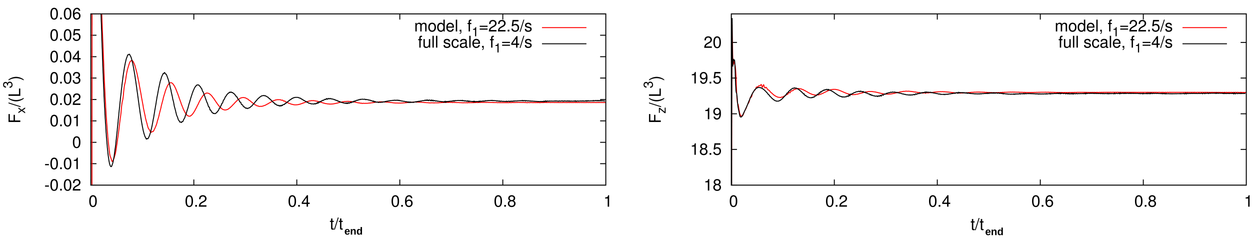

Figure 155: As Fig. 154, except that the forcing strength f_1 in the full scale simulation is correctly scaled to provide similar wave damping as in the model scale simulation, and thus forces converge in a similar manner

References

[1] Abarbanel, S., & Gottlieb, D. (1998). On the construction and analysis of absorbing layers in CEM. Applied Numerical Mathematics, 27(4), 331-340.

[2] Andersson, N., Eriksson, L. E., & Davidson, L. (2004). A study of Mach 0.75 jets and their radiated sound using large-eddy simulation. In 10th AIAA/CEAS Aeroacoustics Conference (p. 3024).

[3] Appelö, D., & Kreiss, G. (2006). A new absorbing layer for elastic waves. Journal of Computational Physics, 215(2), 642-660.

[4] Arai, M., Paul, U. K., Cheng, L. Y., & Inoue, Y. (1993). A technique for open boundary treatment in numerical wave tanks. Journal of the Society of Naval Architects of Japan, 1993(173), 45-50.

[5] Benacchio, T., & Bonaventura, L. (2013). Absorbing boundary conditions: a spectral collocation approach. International Journal for Numerical Methods in Fluids, 72(9), 913-936.

[6] Berenger, J. P. (1994). A perfectly matched layer for the absorption of electromagnetic waves. Journal of computational physics, 114(2), 185-200.

[7] Berenger, J. P. (1996). Perfectly matched layer for the FDTD solution of wave-structure interaction problems. IEEE Transactions on antennas and propagation, 44(1), 110-117.

[8] Bodony, D. J. (2006). Analysis of sponge zones for computational fluid mechanics. Journal of Computational Physics, 212(2), 681-702.

[9] Bogey, C., Bailly, C., & Juvé, D. (2000). Numerical simulation of sound generated by vortex pairing in a mixing layer. AIAA journal, 38(12), 2210-2218.

[10] Brorsen, M., & Helm-Petersen, J. (1999). On the reflection of short-crested waves in numerical models. In Coastal Engineering 1998 (pp. 394-407).

[11] Cao, Y., Beck, R. F., & Schultz, W. W. (1993). An absorbing beach for numerical simulations of nonlinear waves in a wave tank. In Proc. 8th Intl. Workshop Water Waves and Floating Bodies (pp. 17-20).

[12] Carmigniani, R. A., & Violeau, D. (2018). Optimal sponge layer for water waves numerical models. Ocean Engineering, 163, 169-182.

[13] Chen, H. C., Yu, K., & Chen, S. Y. (2006). Simulation of Wave Runup Around Offshore Structures by a Chimera Domain Decomposition Approach. In Civil Engineering in the Oceans VI (pp. 267-280).

[14] Choi, J., & Yoon, S. B. (2009). Numerical simulations using momentum source wave-maker applied to RANS equation model. Coastal Engineering, 56(10), 1043-1060.

[15] Clauss, G., Lehmann, E., & Östergaard, C. (1992). Offshore structures: volume I: conceptual design and hydromechanics. Springer, London.

[16] Clément, A. (1996). Coupling of two absorbing boundary conditions for 2D time-domain simulations of free surface gravity waves. Journal of Computational Physics, 126(1), 139-151.

[17] Collino, F., & Tsogka, C. (2001). Application of the perfectly matched absorbing layer model to the linear elastodynamic problem in anisotropic heterogeneous media. Geophysics, 66(1), 294-307.

[18] Colonius, T. (2004). Modeling artificial boundary conditions for compressible flow. Annu. Rev. Fluid Mech., 36, 315-345.

[19] Colonius, T., & Lele, S. K. (2004). Computational aeroacoustics: progress on nonlinear problems of sound generation. Progress in Aerospace sciences, 40(6), 345-416.

[20] Cooley, J. W., & Tukey, J. W. (1965). An algorithm for the machine calculation of complex Fourier series. Mathematics of computation, 19(90), 297-301.

[21] Cruz, J. (ed.) (2008). Ocean wave energy: current status and future prespectives. Springer Series in Green Energy and Technology, Berlin.

[22] DNV (DET NORSKE VERITAS AS) (2014). Environmental conditions and environmental loads. Link (accessed 15 March 2018): `http://rules.dnvgl.com/docs/pdf/DNV/codes/docs/2014-04/RP-C205.pdf`

[23] Eça, L., Vaz, G., & Hoekstra, M. (2010). Code verification, solution verification and validation in RANS solvers. In Proc. ASME 2010 29th International Conference on Ocean, Offshore and Arctic Engineering (pp. 597-605). American Society of Mechanical Engineers, Shanghai, China.

[24] Enger, S., Perić, M., & Perić, R. (2010). Simulation of flow around KCS-hull. In Proceedings from Gothenburg 2010 – A Workshop on Numerical Ship Hydrodynamics, Gothenburg.

[25] Enger, S., Perić, M., & Monteiro, H. (2014). Coupling of 3D numerical solution method based on Navier-Stokes equations with solutions based on simpler theories. In Proc. XXXV Iberian Latin, American Congress on Comp. Meth. in Eng., ABMEC, Fortaleza, CE, Brazil.

[26] Fenton, J. D. (1985). A fifth-order Stokes theory for steady waves. Journal of waterway, port, coastal, and ocean engineering, 111(2), 216-234.

[27] Ferziger, J. H., & Perić, M. (2002). Computational methods for fluid dynamics. Springer Science & Business Media.

[28] Feynman, R. P., Leighton, R. B., & Sands, M. (2011). The Feynman lectures on physics, Vol. I: The new millennium edition: mainly mechanics, radiation, and heat (Vol. 1). Basic books.

[29] Gatin, I., Vukčević, V., & Jasak, H. (2017). A framework for efficient irregular wave simulations using Higher Order Spectral method coupled with viscous two phase model. Journal of Ocean Engineering and Science, 2(4), 253-267.

[30] Gedney, S. D. (1996). An anisotropic perfectly matched layer-absorbing medium for the truncation of FDTD lattices. IEEE transactions on Antennas and Propagation, 44(12), 1630-1639.

[31] Givoli, D. (2004). High-order local non-reflecting boundary conditions: a review. Wave motion, 39(4), 319-326.

[32] Goda, Y., & Suzuki, Y. (1977). Estimation of incident and reflected waves in random wave experiments. In Coastal Engineering 1976 (pp. 828-845).

[33] Guignard, S., Grilli, S. T., Marcer, R., & Rey, V. (1999). Computation of shoaling and breaking waves in nearshore areas by the coupling of BEM and VOF methods. In The Ninth International Offshore and Polar Engineering Conference. International Society of Offshore and Polar Engineers.

[34] Ha, T., Lin, P., & Cho, Y. S. (2013). Generation of 3D regular and irregular waves using Navier–Stokes equations model with an internal wave maker. Coastal Engineering, 76, 55-67.

[35] Hasselmann, K., Barnett, T.P., Bouws, E., Carlson, H., Cartwright, D.E., Enke, K., Ewing, J.A., Gienapp, H., Hasselmann, D.E., Kruseman, P. & Meerburg, A. (1973). Measurements of wind-wave growth and swell decay during the Joint North Sea Wave Project (JONSWAP). Ergänzungsheft 8-12.

[36] Hesthaven, J. S. (1998). On the analysis and construction of perfectly matched layers for the linearized Euler equations. Journal of computational Physics, 142(1), 129-147.

[37] Higuera, P., Lara, J. L., & Losada, I. J. (2013). Realistic wave generation and active wave absorption for Navier–Stokes models: Application to OpenFOAM®. Coastal Engineering, 71, 102-118.

[38] Hirt, C. W., & Nichols, B. D. (1981). Volume of fluid (VOF) method for the dynamics of free boundaries. Journal of computational physics, 39(1), 201-225.

[39] Hu, F. Q. (1996). On absorbing boundary conditions for linearized Euler equations by a perfectly matched layer. Journal of computational physics, 129(1), 201-219.

[40] Hu, F. Q. (2004). Absorbing boundary conditions. International Journal of Computational Fluid Dynamics, 18(6), 513-522.

[41] Hu, F. Q. (2008). Development of PML absorbing boundary conditions for computational aeroacoustics: A progress review. Computers & Fluids, 37(4), 336-348.

[42] Hu, Z., Tang, W., Xue, H., Zhang, X., & Guo, J. (2015). Numerical simulations using conserved wave absorption applied to Navier–Stokes equation model. Coastal engineering, 99, 15-25.

[43] Hughes, S. A. (1993). Laboratory wave reflection analysis using co-located gages. Coastal Engineering, 20(3-4), 223-247.

[44] IAPWS (International Association for the Properties of Water and Steam) (2007). Revised release on the IAPWS industrial formulation 1997 for the thermodynamic properties of water and steam. IAPWS Secretariat, Lucerne, Switzerland (available at www.iapws.org).

[45] Isaacson, M. (1991). Measurement of regular wave reflection. Journal of Waterway, Port, Coastal, and Ocean Engineering, 117(6), 553-569.

[46] Israeli, M., & Orszag, S. A. (1981). Approximation of radiation boundary conditions. Journal of computational physics, 41(1), 115-135.

[47] Jacobsen, N. G., Fuhrman, D. R., & Fredsøe, J. (2012). A wave generation toolbox for the open-source CFD library: OpenFoam®. International Journal for Numerical Methods in Fluids, 70(9), 1073-1088.

[48] Jasak, H., Vukčević, V., & Gatin, I. (2015). Numerical simulation of wave loading on static offshore structures. In CFD for Wind and Tidal Offshore Turbines (pp. 95-105). Springer, Cham.

[49] Jose, J., Choi, S. J., Giljarhus, K. E. T., & Gudmestad, O. T. (2017). A comparison of numerical simulations of breaking wave forces on a monopile structure using two different numerical models based on finite difference and finite volume methods. Ocean Engineering, 137, 78-88.

[50] Katz, D. S., Thiele, E. T., & Taflove, A. (1994). Validation and extension to three dimensions of the Berenger PML absorbing boundary condition for FD-TD meshes. IEEE microwave and guided wave letters, 4(8), 268-270.

[51] Kim, M. W., Koo, W., & Hong, S. Y. (2014). Numerical analysis of various artificial damping schemes in a three-dimensional numerical wave tank. Ocean Engineering, 75, 165-173.

[52] Kim, J., O'Sullivan, J., & Read, A. (2012). Ringing analysis of a vertical cylinder by Euler overlay method. In ASME 2012 31st International Conference on Ocean, Offshore and Arctic Engineering (pp. 855-866). American Society of Mechanical Engineers.

[53] Kim, J., Tan, J. H. C., Magee, A., Wu, G., Paulson, S., & Davies, B. (2013). Analysis of ringing response of a gravity based structure in extreme sea states. In ASME 2013 32nd International Conference on Ocean, Offshore and Arctic Engineering (pp. V007T08A077-V007T08A077). American Society of Mechanical Engineers.

[54] Kim, W. J., Van, S. H., & Kim, D. H. (2001). Measurement of flows around modern commercial ship models. Experiments in fluids, 31(5), 567-578.

[55] Komatitsch, D., & Martin, R. (2007). An unsplit convolutional perfectly matched layer improved at grazing incidence for the seismic wave equation. Geophysics, 72(5), SM155-SM167.

[56] Komatitsch, D., & Tromp, J. (2003). A perfectly matched layer absorbing boundary condition for the second-order seismic wave equation. Geophysical Journal International, 154(1), 146-153.

[57] Larsen, J., & Dancy, H. (1983). Open boundaries in short wave simulations—a new approach. Coastal Engineering, 7(3), 285-297.

[58] Larsen, B. E., Fuhrman, D. R., & Roenby, J. (2019). Performance of interFoam on the simulation of progressive waves. Coastal Engineering Journal, 61(3), 380-400.

[59] Launder, B., & Spalding, D. (1974). The numerical computation of turbulent flows. Computer Methods in Applied Mechanics and Energy, 3, 269-289.

[60] Lerch, R., Sessler, G., & Wolf, D. (2009). Technische Akustik: Grundlagen und Anwendungen. Springer-Verlag, Berlin.

[61] Lloyd, A. R. J. M., (1998). Seakeeping: ship behavior in rough weather. Seakeeping, 6 Trueman Square, Andover, Hampshire, United Kingdom.

[62] Lorenzzetti, J. A., & Wang, J. D. (1986). On the use of wave-absorbing layers in the treatment of open boundaries in numerical coastal circulation models. Applied Mathematical Modelling, 10(5), 339-345.

[63] Mani, A. (2012). Analysis and optimization of numerical sponge layers as a nonreflective boundary treatment. Journal of Computational Physics, 231(2), 704-716.

[64] Manning, T., & Lele, S. (2000). A numerical investigation of sound generation in supersonic jet screech. In 6th Aeroacoustics Conference and Exhibit (p. 2081).

[65] Mansard, E. P., & Funke, E. R. (1980). The measurement of incident and reflected spectra using a least squares method. In Coastal Engineering 1980 (pp. 154-172).

[66] Marburg, S., & Nolte, B. (2008). Computational acoustics of noise propagation in fluids: finite and boundary element methods (Vol. 578). Berlin: Springer.

[67] Mayer, S., Garapon, A., & Sørensen, L. S. (1998). A fractional step method for unsteady free-surface flow with applications to non-linear wave dynamics. International Journal for Numerical Methods in Fluids, 28(2), 293-315.

[68] McCormick, M. E. (2007). Ocean wave energy conversion. Dover Publications, Inc., New York.

[69] McDonald, A. (2003). Transparent boundary conditions for the shallow-water equations: Testing in a nested environment. Monthly weather review, 131(4), 698-705.

[70] McKee, R., Elsäßer, B., & Schmitt, P. (2018). Obtaining reflection coefficients from a single point velocity measurement. Measurement, 6(2), 1-11.

[71] Mei, C. C., Stiassnie, M., & Yue, D. K. P. (1989). Theory and applications of ocean surface waves: part 1: linear aspects, part 2: nonlinear aspects. World Scientific, New Jersey.

[72] Meyer, J., Graf, K., & Slawig, T. (2017). A new adjustment-free damping method for free-surface waves in numerical simulations. In VII International Conference on Computational Methods in Marine Engineering, MARINE 2017.

[73] Michell, J. H. (1893). XLIV. The highest waves in water. The London, Edinburgh, and Dublin Philosophical Magazine and Journal of Science, 36(222), 430-437.

[74] Modave, A., Deleersnijder, É., & Delhez, É. J. (2010). On the parameters of absorbing layers for shallow water models. Ocean Dynamics, 60(1), 65-79.

[75] Moin, P. (2010). Fundamentals of engineering numerical analysis. Cambridge University Press.

[76] Muzaferija, S., & Perić, M. (1999). Computation of free surface flows using interface-tracking and interface-capturing methods. In Mahrenholtz, O., Markiewicz, M. (Eds.), Nonlinear Water Wave Interaction (pp. 59-100). WIT Press, Southampton.

[77] Myers, A., Pyle Jr, R. W., Gilbert, J., Campbell, D. M., Chick, J. P., & Logie, S. (2012). Effects of nonlinear sound propagation on the characteristic timbres of brass instruments. The Journal of the Acoustical Society of America, 131(1), 678-688.

[78] Novak, J., & Bonazzola, S. (2004). Absorbing boundary conditions for simulation of gravitational waves with spectral methods in spherical coordinates. Journal of Computational Physics, 197(1), 186-196.

[79] Park, J. C., Kim, M. H., & Miyata, H. (1999). Fully non-linear free-surface simulations by a 3D viscous numerical wave tank. International Journal for Numerical Methods in Fluids, 29(6), 685-703.

[80] Park, J. C., Kim, M. H., & Miyata, H. (2001). Three-dimensional numerical wave tank simulations on fully nonlinear wave–current–body interactions. Journal of Marine Science and Technology, 6(2), 70-82.

[81] Park, J. C., Zhu, M., & Miyata, H. (1993). On the accuracy of numerical wave making techniques. Journal of the Society of Naval Architects of Japan, 1993(173), 35-44.

[82] Patankar, S. (1980). Numerical heat transfer and fluid flow. McGraw-Hill Book Company, New York.

[83] Perić, M. (2015). Steigerung der Effizienz von maritimen CFD-Simulationen durch Kopplung verschiedener Verfahren. In Jahrbuch der Schiffbautechnischen Gesellschaft, 109. Band (pp. 69-76), Schiffahrts-Verlag "Hansa" GmbH & Co. KG, Hamburg.

[84] Perić, R., & Abdel-Maksoud, M. (2015). Assessment of uncertainty due to wave reflections in experiments via numerical flow simulations. In The Twenty-fifth International Ocean and Polar Engineering Conference (ISOPE). International Society of Offshore and Polar Engineers.

[85] Perić, R., & Abdel-Maksoud, M. (2015b). Generation of free-surface waves by localized source terms in the continuity equation. Ocean Engineering, 109, 567-579.

[86] Perić, R., & Abdel-Maksoud, M. (2016). Reliable damping of free-surface waves in numerical simulations. Ship Technology Research, 63(1), 1-13.

[87] Perić, R., & Abdel-Maksoud, M. (2016b). Damping of free surface waves - state of the art and future developments. Proc. 19th Numerical Towing Tank Symposium (NuTTS), St Pierre d'Oléron, France.

[88] Perić, R., & Abdel-Maksoud, M. (2018). Analytical prediction of reflection coefficients for wave absorbing layers in flow simulations of regular free-surface waves. Ocean Engineering, 147, 132-147.

[89] Perić, R., Abdel-Maksoud, M. (2018b). Reducing undesired wave reflection at domain boundaries in 3D finite-volume-based flow simulations via forcing zones. In Proceedings of the 32$^{\text{nd}}$ Symposium on Naval Hydrodynamics, Hamburg, Germany.

[90] Perić, R., Hoffmann, N., & Chabchoub, A. (2015). Initial wave breaking dynamics of Peregrine-type rogue waves: a numerical and experimental study. European Journal of Mechanics-B/Fluids, 49, 71-76.

[91] Perić, R., Vukčević, V., Abdel-Maksoud, M., & Jasak, H. (2018). Tuning the case-dependent parameters of relaxation zones for flow simulations with strongly reflecting bodies in free-surface waves. arXiv preprint arXiv:1806.10995.

[92] Petropoulos, P. G., Zhao, L., & Cangellaris, A. C. (1998). A reflectionless sponge layer absorbing boundary condition for the solution of Maxwell's equations with high-order staggered finite difference schemes. Journal of Computational Physics, 139(1), 184-208.

[93] Richardson, L. F. (1911). IX. The approximate arithmetical solution by finite differences of physical problems involving differential equations, with an application to the stresses in a masonry dam. Phil. Trans. R. Soc. Lond. A, 210(459-470), 307-357.

[94] Richardson, L. F., & J Arthur Gaunt, B. A. (1927). VIII. The deferred approach to the limit. Part I. Single lattice. Part II. Interpenetrating lattices. Phil. Trans. R. Soc. Lond. A, 226(636-646), 299-361.

[95] Rienecker, M. M., & Fenton, J. D. (1981). A Fourier approximation method for steady water waves. Journal of Fluid Mechanics, 104, 119-137.

[96] Rinne, O., Lindblom, L., & Scheel, M. A. (2007). Testing outer boundary treatments for the Einstein equations. Classical and Quantum Gravity, 24(16), 4053.

[97] Romate, J. E. (1992). Absorbing boundary conditions for free surface waves. Journal of computational Physics, 99(1), 135-145.

[98] Schäffer, H. A., & Klopman, G. (2000). Review of multidirectional active wave absorption methods. Journal of waterway, port, coastal, and ocean engineering, 126(2), 88-97.

[99] Schäffer, H. A., & Skourup, J. (1997). Active absorption of multidirectional waves. In Coastal Engineering 1996 (pp. 55-66).

[100] Schmitt, P., & Elsaesser, B. (2015). A review of wave makers for 3D numerical simulations. In Marine 2015 6th International Conference on Computational Methods in Marine Engineering.

[101] Semblat, J. F., Lenti, L., & Gandomzadeh, A. (2011). A simple multi-directional absorbing layer method to simulate elastic wave propagation in unbounded domains. International Journal for Numerical Methods in Engineering, 85(12), 1543-1563.

[102] Spadoni, A., & Daraio, C. (2010). Generation and control of sound bullets with a nonlinear acoustic lens. Proceedings of the National Academy of Sciences, 107(16), 7230-7234.

[103] Spalart, P. R. (1989). Direct numerical study of leading-edge contamination. Fluid Dynamics of Three-Dimensional Turbulent Shear Flows and Transition, 5-1.

[104] Straughan, B. (2008). Stability and wave motion in porous media (Vol. 165). Springer Science & Business Media.

[105] Troch, P., & De Rouck, J. (1999). An active wave generating–absorbing boundary condition for VOF type numerical model. Coastal Engineering, 38(4), 223-247.

[106] Turkel, E., & Yefet, A. (1998). Absorbing PML boundary layers for wave-like equations. Applied Numerical Mathematics, 27(4), 533-557.

[107] Ursell, F., Dean, R. G., & Yu, Y. S. (1960). Forced small-amplitude water waves: a comparison of theory and experiment. Journal of Fluid Mechanics, 7(1), 33-52.

[108] Vukčević, V., Jasak, H., & Malenica, Š. (2016). Decomposition model for naval hydrodynamic applications, Part I: Computational method. Ocean Engineering, 121, 37-46.

[109] Vukčević, V., Jasak, H., & Malenica, Š. (2016b). Decomposition model for naval hydrodynamic applications, Part II: Verification and validation. Ocean engineering, 121, 76-88.

[110] Wanderley, J. B., & Levi, C. (2005). Vortex induced loads on marine risers. Ocean Engineering, 32(11-12), 1281-1295.

[111] Wang, M., Freund, J. B., & Lele, S. K. (2006). Computational prediction of flow-generated sound. Annu. Rev. Fluid Mech., 38, 483-512.

[112] Wei, G., Kirby, J. T., & Sinha, A. (1999). Generation of waves in Boussinesq models using a source function method. Coastal Engineering, 36(4), 271-299.

[113] Weller, H. G., Tabor, G., Jasak, H., & Fureby, C. (1998). A tensorial approach to computational continuum mechanics using object-oriented techniques. Computers in physics, 12(6), 620-631.

[114] Wilcox, D. C. (1993). Turbulence modeling for CFD (Vol. 2, pp. 103-217). La Canada, CA: DCW industries.

[115] Wöckner-Kluwe, K. (2013). Evaluation of the unsteady propeller performance behind ships in waves. PhD thesis at Hamburg University of Technology (TUHH), Schriftenreihe Schiffbau, 667, Hamburg.

[116] Zeng, Y., He, J., & Liu, Q. (2001). The application of the perfectly matched layer in numerical modeling of wave propagation in poroelastic media. Geophysics, 66(4), 1258-1266.

[117] Zhang, Y., Kennedy, A. B., Panda, N., Dawson, C., & Westerink, J. J. (2014). Generating–absorbing sponge layers for phase-resolving wave models. Coastal Engineering, 84, 1-9.